Photodissociation Imaging studies of Molecular Oxygen and Sulfur

Photodissociation Imaging studies of Molecular Oxygen and Sulfur

Proefschrift

ter verkrijging van de graad van doctor
aan de Radboud Universiteit Nijmegen,
op gezag van de rector magnificus, prof. dr. Th.L.M. Engelen,
volgens besluit van het college van decanen
in het openbaar te verdedigen op woensdag 8 juli 2015,
om 10:30 uur precies

door

Zahid Farooq
Geboren op 1 december 1977
te Faisalabad, Punjab, Pakistan

Promotor: Prof. dr. D. H. Parker

Manuscriptcommissie: Prof. dr. W.J. van der Zande
Prof. dr. ir. G.C. Groenenboom
Prof. dr. C. Western (University of Bristol, UK)

Photodissociation Imaging studies of Molecular Oxygen and Sulfur

Doctoral Thesis

to obtain the degree of doctor
from Radboud University
on the authority of the Rector Magnificus, prof. dr. Th.L.M. Engelen,
according to the decision of the Council of Deans
to be defended in public on Wednesday, July 8, 2015
at 10:30 hours

by

Zahid Farooq
born on December 1, 1977
in Faisalabad, Punjab, Pakistan

Supervisor:	Prof. dr. D. H. Parker
Doctoral Thesis Committee:	Prof. dr. W.J. van der Zande
	Prof. dr. ir. G.C. Groenenboom
	Prof. dr. C. Western
	(University of Bristol, UK)

Contents

Chapter 1

Introduction

Abstract

This thesis is based on a series of experimental investigations using the velocity map imaging technique which was carried out at the Radboud University Nijmegen. The goal of the research is to improve our understanding of photodissociation dynamics of molecular oxygen and molecular sulfur excited by laser radiation in the ultraviolet region. The emphasis is on photodissociation of singlet oxygen and singlet sulfur which are metastable electronically excited states. The high intensity of the laser radiation necessary for these studies is found to drive additional multi-photon processes which produce signals that overlap the singlet oxygen and singlet sulfur signals. It was thus necessary to understand these multi-photon processes and the work proceeds to study multiphoton dissociation of molecular oxygen and molecular sulfur via two-photon excitation of Rydberg states in a wide energy range using ultraviolet laser photons. In the following sections of this chapter a few key concepts of the experiments will be explained, followed by an overview of the following chapters contained in this thesis.

1.1 Photodissociation

Photodissociation and fragmentation of a molecule due to the absorption of light is among the most fundamental of all chemical processes. While these types of unimolecular reactions have great significance in the fields of astrophysics and atmospheric chemistry, they also provide a set of systems ideally suited to test our understanding of molecular dynamics. The last 40 years have shown a dramatic growth in the number and degree of sophistication of such investigations. The advent of laser technology has made the most important contribution to rapid advances in this field. [1]

A photodissociation event can be viewed as a half collision: whereas a full collision is concerned with two particles coming initially together from far away to form products via an intermediate complex, photodissociation starts already with a bound molecule which is excited to an excited state before breaking apart into fragments. When a generic molecule AB absorbs one or more photons the following processes can occur: photodissociation, ionization, dissociative ionization, ion pair formation, radiative decay and collisional relaxation.

1. $AB + nhv \rightarrow AB^* \rightarrow A + B$ photodissociation
   $\rightarrow A + B^*$ with formation of metastable B*
2. $\rightarrow AB^+ + e^-$ ionization
3. $\rightarrow A + B^+ + e^-$ dissociative ionization
4. $\rightarrow A^- + B^+$ ion-pair formation
5. $\rightarrow AB^* + hv$ radiative decay
6. $\rightarrow AB^* + C \rightarrow AB + C$ collisional relaxation

Photodissociation results in the formation of neutral fragments or their combination with electronically excited fragments, which can be ionized by one or more photons. Photoionization leads to formation of AB^+ ions which may be in our studies dissociated by one or more photons. The AB^* complex may also fall back to the ground state under emisson of a photon (fluorescence). In this research our techniques are most sensitive to the photodissociation, ionization and dissociative ionization pathways.

During photodissociation the bond between A and B (atomic or molecular constituents) is broken and neutral fragments fly apart. The energy required from the lowest possible rotational level of the ground vibrational state, labeled $X(v=0)$, to break the AB bond is called the dissociation energy (D_0), where the subscript 0 refers to the lowest energy dissociation channel.

Molecular photodissociation can proceed via two processes:

1. Direct dissociation by absorption to a repulsive state or to the repulsive wall of a bound state. Bond breaking takes place in a very short time (10^{-13}—10^{-14}s).
2. Indirect photodissociation by excitation to a bound state followed by a predissociation process. This depends on the coupling strength between the bound excited state and various possible dissociating state(s).In this case the process takes more time, typically >10^{-13}s.

In addition, photoionization is a process in which the photon energy is used to eject an electron out of its orbital leaving the AB^+ ion in a state having certain values of vibrational and rotational quantum numbers. The minimum energy required to emit an electron is called the ionization potential (IP).

Photoionization can also be divided into two processes:

1. In direct ionization, the electron leaves the molecule immediately, on the fs timescale.
2. In the case of indirect ionization (or autoionization) a transient intermediate state AB^* lies above the ionization potential and can therefore decay into the ionization continuum.

The combination of photodissociation and ionization is named dissociative ionization. This process requires more energy, because now the bond of the AB^+ ion needs to be broken. When the excited intermediate state of AB^* is a repulsive state in the ion the process will be called direct dissociation ionization. Otherwise, the process is called indirect dissociative ionization.

1.1.1 Kinetics of photofragmentation

The main part of the total photon energy for n photons ($E = nh\nu$) in the process of photodissociation is utilized to break the bond between A and B. This bond breaking requires the dissociation energy, (D_0). The rest of the energy is distributed over the internal energy of the atoms E_{int} and the kinetic energy of the photofragments, E_{kin}.

$$E_{int}(AB) + nh\nu = E_{int}(A) + E_{int}(B) + E_{kin}(A) + E_{kin}(B) + D_0 \quad (1.1)$$

The total kinetic energyE_{kin} delivered in the reaction, also known as the total kinetic energy release (TKER), is given by:

$$E_{kin} = E_{kin}(A) + E_{kin}(B) = \frac{1}{2}m_A v_A^2 + \frac{1}{2}m_B v_B^2 \quad (1.2)$$

Where m is the mass of the fragment and v is the velocity. This equation can be combined with the equation of conservation of linear momentum:

$$m_A v_A + m_B v_B = 0 \tag{1.3}$$

These two equations result in partitioning of the total kinetic energy release (TKER) between the individual fragments:

$$E_{kin}(\mathrm{A}) = \frac{m_B}{m_A+m_B} E_{kin} \tag{1.4}$$

Experimentally, the kinetic energies of fragments can be determined in various ways. In this thesis the velocity map imaging technique has been applied, which is further detailed in Chapter 2.

1.1.2 Angular Distributions

Angular distributions of photofragments provide important information about dissociation dynamics.[2,3,4,5,6] These depend on the both the laser polarization and the symmetries of the electronic states that are involved in the dissociation process. The transition dipole of an allowed one-photon transition between two electronic states of diatom is either parallel or perpendicular to the diatom axis, depending on the symmetry properties of the initial and final state. For one-photon dissociation, the angular distribution of the photodissociation products [7,8] is described by:

$$I(\theta) = \frac{1}{4\pi}[1 + \beta P_2(\cos\theta)] \tag{1.5}$$

where $P_2(x) = \frac{1}{2}(3x^2 - 1)$ is the 2nd order Legendre Polynomial, θ is the angle between the polarization of dissociation light and the recoil direction (i.e. the recoil velocity vector of the fragment) and β is the anisotropy parameter where $(-1 < \beta < 2)$. The limiting values of -1 to 2, correspond to purely perpendicular and parallel transitions, respectively. For example, the diatomic molecule electronic transitions $\Sigma - \Sigma$ and $\Pi - \Pi$ are parallel transitions, but $\Pi - \Sigma$ is a perpendicular transition. An isotropic distribution is characterized by $\beta = 0$. In the case of a parallel transition, the transition dipole moment vector $\boldsymbol{\mu}$ lies in the direction of internuclear axis of the diatom and the angular distribution $I(\theta)$ is proportional to $\cos^2\theta$. For a perpendicular transition $\boldsymbol{\mu}$ lies perpendicular to the internuclear axis and the angular distribution $I(\theta)$ is proportional to $\sin^2\theta$. In the axial recoil limit, an intermediate value of β indicates that both parallel and perpendicular transitions are being simultaneously excited.

Determination of the anisotropy parameter for different nascent O atoms channels after photodissociation of O_2 provides information on the symmetry of the O_2 excited states and their lifetime with respect to rotation.[2] The limiting values of β usually appear only if the dissociation is significantly faster than the time for a complete rotation of the molecule, which is called direct photodissociation. Therefore, measuring

the value of β also provides information on the type of dissociation and the mixing of electronic states with different symmetries involved in the excitation step.

For multiphoton absorption processes, the angular distribution is described by an expansion in Legendre Polynomials. For two-photon photodissociation process the result becomes

$$I(\theta) = \frac{1}{4\pi}[1 + \beta P_2(\cos\theta) + \gamma P_4(\cos\theta)] \quad (1.6)$$

If an intermediate state dominates in the two-photon excitation step, the angular distribution will be influenced strongly by that state, and the excitation can be regarded as stepwise. If there is no dominating intermediate state, second order perturbation theory prescribes a weighted summation over all intermediate states: the closer a state is with respect to the one-photon level, the stronger its participation in the excitation process.[9]

1.2 Molecules studied in this thesis

Over the last two decade, our group has been involved in the study of fragmentation and ionization of small molecules. In this thesis, we studied the photodissociation dynamics of molecular oxygen and molecular sulfur in order to improve the fundamental understanding of the excitation processes in these important molecules.

1.2.1 Molecular oxygen and its photochemistry

Molecular oxygen, O_2, is a unique and fascinating molecule that plays a pivotal role in many processes that take place on Earth. Of the light elements that are the building blocks of nature, oxygen is unique in having three stable forms that are common in both the atmosphere and laboratory: $O(^3P)$, O_2 and O_3.[10] The reactive and photosensitive nature of O_2(due to absorption in the so-called Schumann-Runge band ($B\ ^3\Sigma_u^- \leftarrow X\ ^3\Sigma_g^-$), 7-9 eV, see the right side of Figure 1.1, protects the surface of Earth from harmful UV solar radiation and is the primary step in the formation of ozone (O_3). In fact, photodissociation of O_2 accounts for the primary formation of ozone in Earth's atmosphere and other processes important for the photochemical balance in the atmosphere. The highly forbidden oxygen Herzberg bands ($A\ ^3\Sigma_u^+ \leftarrow X\ ^3\Sigma_g^-$; $A'\ ^3\Delta_u \leftarrow X\ ^3\Sigma_g^-$; $c\ ^1\Sigma_u^- \leftarrow X\ ^3\Sigma_g^-$) lying to lower energy than the Schumann-Runge bands and not visible on the linear scale of Fig. 1.1, also affect the propagation of near-ultraviolet radiation through the atmosphere. Next to that, oxygen chemistry is of the greatest importance in processes such as combustion. As a result,O_2 photodissociation is of great interest to many investigators.

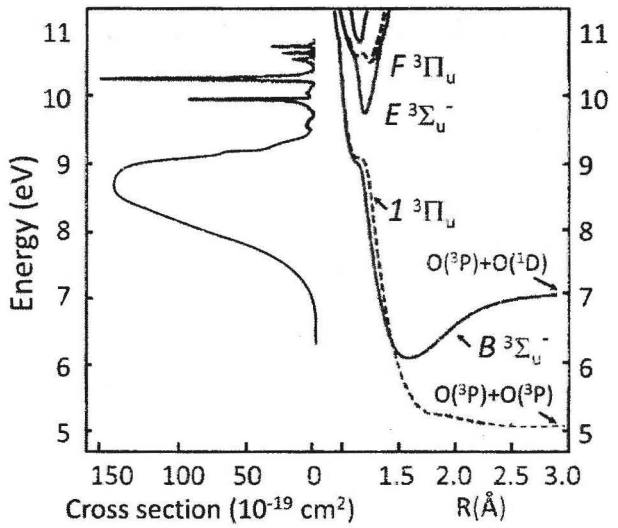

Figure 1.1. Right side: Absorption spectrum of O_2 in the 5-11 eV regions. Left side: Corresponding potential energy curves for states involved in the allowed electronic transitions from the ground state of O_2.

1.2.2 Electronic states of O_2

Despite its apparent simplicity, the O_2 molecule exhibits a number of rather unusual properties with respect to spectroscopy, magnetic behavior, energy transfer processes and chemical reactivity. These peculiarities are a consequence of the open-shell electronic structure of oxygen molecule. Two oxygen atoms, each with six outer electrons, are bound, leading to the electronic configuration:

$$O_2(X^3\Sigma_g^-, a\ ^1\Delta_g, b\ ^1\Sigma_g^+): \quad \underbrace{(1\sigma_g^2)(1\sigma_u^2)}_{\text{inner orbitals}}\ \underbrace{(2\sigma_g^2)(2\sigma_u^2)(3\sigma_g^2)(1\pi_u^4)(1\pi_g^2)}_{\text{valence orbitals}}$$

With the exception of the first two degenerate anti-bonding $\pi_{g,x}$ and $\pi_{g,y}$ orbitals, all molecular orbitals (MOs) are doubly occupied. As with atomic oxygen, there are three different 'valence' states corresponding to different arrangement of these electrons. It was Mulliken who predicted that this special electronic configuration should give rise to three energetically close-lying electronic states, the triplet ground state and the excited Σ and Δ singlet states.[11] Later, Mulliken specified the electronic states as the $^3\Sigma_g^-$ triplet ground state and $^1\Sigma_g^+$ and $^1\Delta_g$ excited singlet states[12]. Finally, Ellis and Kneser [13] discovered the $^1\Delta_g \leftarrow {}^3\Sigma_g^-$ transition in an absorption experiment, identifying $O_2(a\ ^1\Delta_g)$ as the metastable O_2 species, which is now commonly called singlet oxygen. The other singlet state is denoted by $O_2(b\ ^1\Sigma_g^+)$. Both of these are long-lived metastable

states (under collision-free conditions) which are also important in atmospheric chemistry.

The outer $1\pi_g$ shell of O_2 is open with only two of the four electrons occupied, whereas all the inner valence shells are filled. Ionization of a $1\pi_g$ electron yields the doublet ground state $X(^2\Pi_g)\, O_2^+$, whereas removal of an electron from the other shell yields both quartet and doublet states $A(^2\Pi_u)$ and $a(^4\Pi_u)$.[14] These, and other electronic states of O_2^+ are obtained by removing an electron from the following orbitals:

$$O_2^+ \underbrace{X(^2\Pi_g)}_{(1\pi_g)^{-1}},\ \underbrace{A(^2\Pi_u) + a(^4\Pi_u)}_{(1\pi_u)^{-1}},$$

$$\underbrace{B(^2\Sigma_g^-) + b(^4\Sigma_g^-)}_{(3\sigma_g)^{-1}},\underbrace{C(^2\Sigma_u^-) + c(^2\Sigma_u^-)}_{(2\sigma_u)^{-1}},\ \underbrace{^2\Sigma_g^- + d(^4\Sigma_g^-)}_{(2\sigma_g)^{-1}}$$

The potential energy curves corresponding to the above-listed valence states of O_2 and O_2^+ are shown in left part of Fig. 1.2.

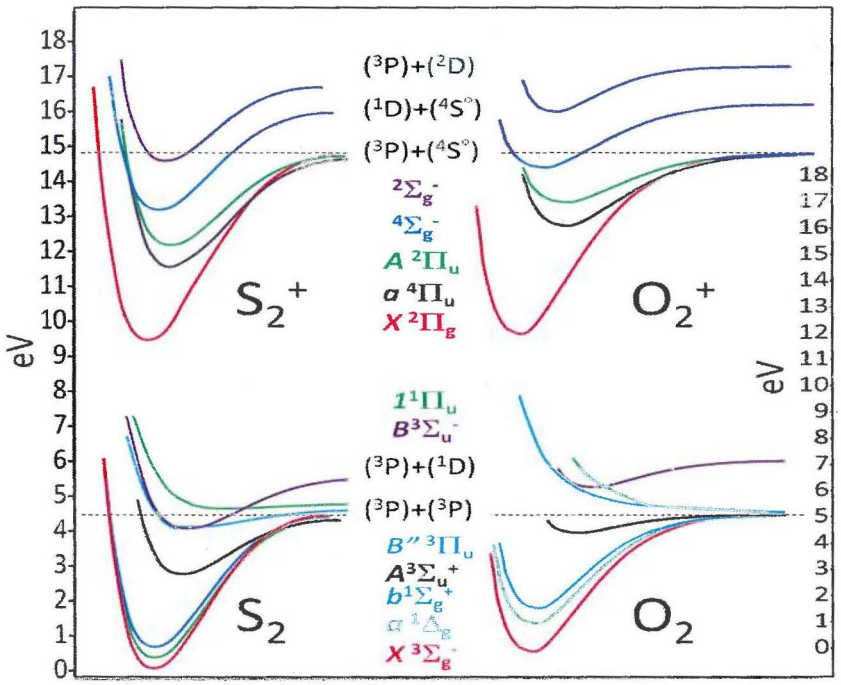

Figure 1.2: Potential energy curves for selected electronic states of S_2 and S_2^+ versus O_2 and O_2^+. The two sets of curves are scaled on the vertical (energy) axis to the same atomic ionization potential and on the horizontal (atom-atom separation) axis to the same width of the ground electronic state energy well. The lower(upper) horizontal dashed line indicates the

lowest dissociation energy of the ground state of the neutral (ionic) molecule.

1.2.3 Singlet Oxygen

Over the last 40 years or so, it has been established that singlet oxygen is important in a wide range of disciplines. Singlet oxygen is a useful synthetic "reagent", it can contribute to degradation of polymers, it is involved in chemistry of atmosphere, it is responsible for sunburn and photo-bleaching phenomena, it plays a significant role in response of plants to stress and it is an integral component of events that result in cell death in photodynamic therapy. The roles played by singlet oxygen in biological systems have been a long interest to the community. Of course, this interest is fueled by the fact that singlet oxygen is an important reactive intermediate in many biological processes.[15]

As already described above, Mullikan described the ground state of oxygen as a spin triplet ground state $^3\Sigma_g^-$ with two unpaired electrons distributed in the highest occupied orbitals.[11,12,16] As such, it often exhibits radical-like behavior in chemical reactions. The first excited state, $a\ ^1\Delta_g$, has a rich chemistry that is distinctly different from the second excited state, $b\ ^1\Sigma_g^+$. These singlet states result from a rearrangement of the electron spins within the two highest orbitals. The $a\ ^1\Delta_g$ state is 0.997 eV above the ground state; both electrons are paired in a single orbital, leaving the other vacant. In contrast, the $b\ ^1\Sigma_g^+$ state comes from spin pairing electrons in different orbitals and is 1.627 eV above the ground state.

Three different optical transitions are possible between the $X\ ^3\Sigma_g^-$ ground state and the $a\ ^1\Delta_g$ and $b\ ^1\Sigma_g^+$ singlet states, all of them are forbidden as electric-dipole transitions, due to the even (gerade) parity of the electronic states. Further restrictions exist for singlet $\leftrightarrow$ triplet and $\Sigma \leftrightarrow \Delta$ transitions.[17] In our laboratory we produced ground and vibrationally excited singlet oxygen $O_2(a\ ^1\Delta_g)$ by a ring type pulsed electric discharge. In thesis we studied the photodissociation of singlet oxygen $O_2(a\ ^1\Delta_g)$ via the so-called Chamberlain continua ($A\ ^3\Sigma_u^+, A'\ ^3\Delta_u \leftarrow a\ ^1\Delta_g$) in the region from 200 to 240 nm using velocity map imaging. In this work, one-color and two-color experiments were performed whose description is given in detail in chapter 3.

1.2.4 Molecular Sulfur

Molecular Sulfur (S_2) is an important intermediate in combustion processes of sulfur containing molecules and in the chemistry of

planetary atmosphere.[18] The S_2 radical exists in molecular clouds and interstellar space.[19] We can also find S_2 molecules in various natural and industrial plasmas containing sulfur compounds. There are many good reasons for our experimental interest in diatomic sulfur. As for O_2, the photoexcitation and photoemission in the Ultraviolet-Visible(UV) region are limited in S_2 by strict symmetry rules. Also, the compound is hazardous and also a pollutant in the atmosphere; hence the dissociation of S_2 is an important aspect. Furthermore, S_2 is a molecule about which much is yet to be studied by experiment. Finally, it is interesting to compare S_2 with O_2, since molecular sulfur is structurally similar to the well-studied oxygen molecule. The MOs of S_2 are entirely analogous to

$$S_2(X^3\Sigma_g^-, a\ ^1\Delta_g, b\ ^1\Sigma_g^+)\ (1\sigma_g^2)(1\sigma_u^2)(2\sigma_g^2)(2\sigma_u^2)(3\sigma_g^2)$$
$$(1\pi_u^4)(1\pi_g^4)(3\sigma_u^2)(4\sigma_g^2)(4\sigma_u^2)(5\sigma_g^2)(2\pi_u^4)(2\pi_g^2)$$

those of O_2, although the valence MOs for S_2 are constructed from the 3s and 3p atomic orbitals of sulfur. As S_2 has the same number of valence electrons as O_2, by analogy to our discussion of O_2 we would expect S_2 to show more or less the same photodissociation behavior as O_2.

1.2.5 Singlet Sulfur

The progress of our research on singlet molecular oxygen has given us motivation to explore the chemistry of the analogous sulfur species, singlet diatomic sulfur. Singlet sulfur has been found to be involved in various physical, chemical and biological processes as well in many disease processes. Although singlet diatomic sulfur has been known to exist in molten sulfur and vaporized sulfur, relatively a few studies on its chemistry have been reported because of the lack of convenient generation methods. Like molecular oxygen, there are two kinds of singlet sulfur. $S_2(a\ ^1\Delta_g)$ has an energy of only 0.583 eV above that of the ground state while the $(b\ ^1\Sigma_g^+)$ energy is 1.05 eV. The two singlet sulfur states have different lifetimes.

Singlet S_2 is normally formed when sulfur compounds such as H_2S or OCS are photolyzed. In our laboratory we generated singlet sulfur with a ring-type pulsed electric discharge to produce ground and vibrationally excited singlet sulfur $S_2(a\ ^1\Delta_g, b\ ^1\Sigma_g^+)$ by a ring type pulsed electric discharge. In this thesis we studied the photodissociation of singlet sulfur$S_2(a\ ^1\Delta_g, b\ ^1\Sigma_g^+)$ via the $(\tilde{B}''\ ^3\Pi_u^+, \tilde{B}\ ^3\Sigma_u^+ \leftarrow a\ ^1\Delta_g)$and $(\tilde{B}''\ ^3\Pi_u^+ \leftarrow b\ ^1\Sigma_g^+)$ transition in the ultraviolet wavelength region using velocity map imaging. In this work, one-color and two-color experiments were performed whose description is given in chapter 4.

1.3 Differences between the potential energy curves of O_2 and S_2

While O_2 and S_2 have identical electronic valence structures, there are significant differences in the potential energy curves of the two molecules. Particularly, the potential energy curves for the bound states are more strongly bound in S_2 than those of O_2. The difference is further depicted in figure 1.2 below. The three S_2 Herzberg states: $A\,^3\Sigma_u^+$, $A'^3\Delta_u$ and $c\,^1\Sigma_u^-$ (named Herzberg I, II and III, respectively as Herzberg bands) are more strongly bound. Furthermore, the upper level of well-known SR bands, the $B(^3\Sigma_u^-)$ state is located at lower energy in S_2, with bound levels lying below the first dissociation limit. For O_2, the repulsive state ($1\,^3\Pi_u$) correlates with ground electronic states of atomic oxygen (which is equivalent to the S_2 $B''(^3\Pi_u)$ state) lies in O_2^+ above the first dissociation limit and repulsive in character. Likewise, the $1\,^1\Pi_u$ state of O_2 is repulsive but becomes very weakly bound in S_2. A comparison of the photodynamics of O_2 with those of isovalent S_2 molecule is also topic of discussion in this thesis.

Our initial goal in this research was to compare the one-photon photodynamics of the O_2 and S_2 molecules by detecting nascent O or S atoms. In these studies it became immediately clear that additional photofragment signals arising from multi-photon absorption are observed. Because these signals overlap the one-photon signals it was necessary to also understand the multiphoton processes. Furthermore, the photodynamics observed following absorption of three ultraviolet photons can be compared with those for one-photon absorption at the same equivalent energy. Three-photon absorption (with roughly the same selection rules as one-photon absorption) can thus provide extra information on O_2 and S_2 photodynamics in the extreme ultraviolet wavelength regions. Our studies of multiphoton absorption in O_2 and S_2 are described in Chapters 4 and 5, respectively.

1.4 Beyond the valence MO description

The description of the electronic structure of O_2 and S_2 given thus far is often referred to as the valence structure of the molecule, with all valence states correlating at long internuclear distance to some combination of two 'valence' O(^{3}P,^{1}D,^{1}S) atoms. A large number (62!) of different valence electronic states arise from the combinations of these three O atom states,[15] the ground state ,$X^3\Sigma_g^-$, is one of four (of the 62) with $^3\Sigma_g^-$ symmetry. Of the 62 states only 8 show clear bound-state character, the majority are thus repulsive states. Electric dipole selection rules allow absorption from the ground state only to 3 possible $^3\Sigma_u^-$ and 5

possible $^3\Pi_u$excited states. Thus, only 8 of the possible 61 final states are accessible by allowed transitions from the ground electronic state and only two are accessible in the (vacuum) ultraviolet region.[20] However, valence-valence interactions, particularly spin-orbit coupling, can mix the symmetry character of these excited states, revealing a few more of the hidden electronic states by slightly relaxing the strict optical selection rules.

1.4.1 Valence-Valence Interactions

An electric-dipole-forbidden transition can borrow intensity from electric-dipole-allowed transitions of the O_2 and S_2 molecules through, in principle, spin-orbit and orbit-rotation interactions with both the upper and lower states of each transition. These interactions have been discussed in detail by Mineav and coworkers [21]and in the work from our group by Buissje et al [22] for the Herzberg transitions of O_2. Owing to the cold rotational state distributions in our experiments, it was argued that spin-orbit interactions play the dominant role. For the studies described in this thesis we also limit discussion to spin-orbit interactions.

First-order spin-orbit interactions in a spin-forbidden transition between an initial state $|i\rangle$ and a final state $|f\rangle$ result in an effective transition moment as given by Field and Lefebre-Brion[23]:

$$\langle f|\boldsymbol{\mu}|i\rangle = \sum_{k\neq i}\frac{\langle f|\boldsymbol{\mu}|k\rangle\langle k|\mathbf{H}^{SO}|i\rangle}{E_i-E_k} + \sum_{k\neq f}\frac{\langle f|\mathbf{H}^{SO}|k\rangle\langle k|\boldsymbol{\mu}|i\rangle}{E_f-E_k} \qquad (1.6)$$

Where $\mathbf{H}^{so}$ and $\boldsymbol{\mu}$ are the spin-orbit and electric-dipole operators, respectively, the $E_{i,k,f}$are electronic-state energies, and the sums are over all states $|k\rangle$ that are dipole-connected to either the initial or final states. For an allowed electric dipole transition to a continuum (from the terms $\langle f|\boldsymbol{\mu}|i\rangle$ in 1.6) our imaging studies determine the amount of parallel ($\Delta\Lambda = \Delta\Omega = 0$) and perpendicular ($\Delta\Lambda = \Delta\Omega = \pm1$) character. Spin-orbit coupling takes place between the same Ω levels of two different states ($\Delta\Omega = 0$). The first term on the right hand side of equation 1.6 describes spin-orbit coupling with the lower state and the second with the upper state of the transition.

In this thesis a number of spin-orbit induced transitions in O_2 and S_2 are studied, two coupling pathways are illustrated in Fig. 1.2 for the optically allowed but weak ($1\,^3\Pi_u \leftarrow X\,^3\Sigma_g^-$) transition (upper panel) and the optically forbidden ($B\,^3\Sigma_u^- \leftarrow b\,^1\Sigma_g^+$) transition (lower panel). Spin-orbit coupling of the $1\,^3\Pi_u$ state with the $\tilde{B}\,^3\Sigma_u^+$ state can take place in both the ($\Omega = 0^+$) and ($\Delta\Omega = \pm1$) levels of the $1\,^3\Pi_u \leftarrow X\,^3\Sigma_g^-$ transition, but the $\Delta\Omega = \pm2$ of the $1\,^3\Pi_u$ state cannot couple, and indeed in the bound-bound

transition to this state in S_2 these levels are missing.[24] While the dominant component of the optically allowed $B\ ^3\Sigma_u^- \leftarrow X\ ^3\Sigma_g^-$ transition is the ($\Delta\Omega = \pm 1$) component. Buissje, Lewis and coworkers[22] showed for the $b \leftarrow B$ transition in O_2,the SO pathway is via $X\ ^3\Sigma_g^-$-$b\ ^1\Sigma_g^+$ coupling, which is only possible via $\Omega = 0^+$.

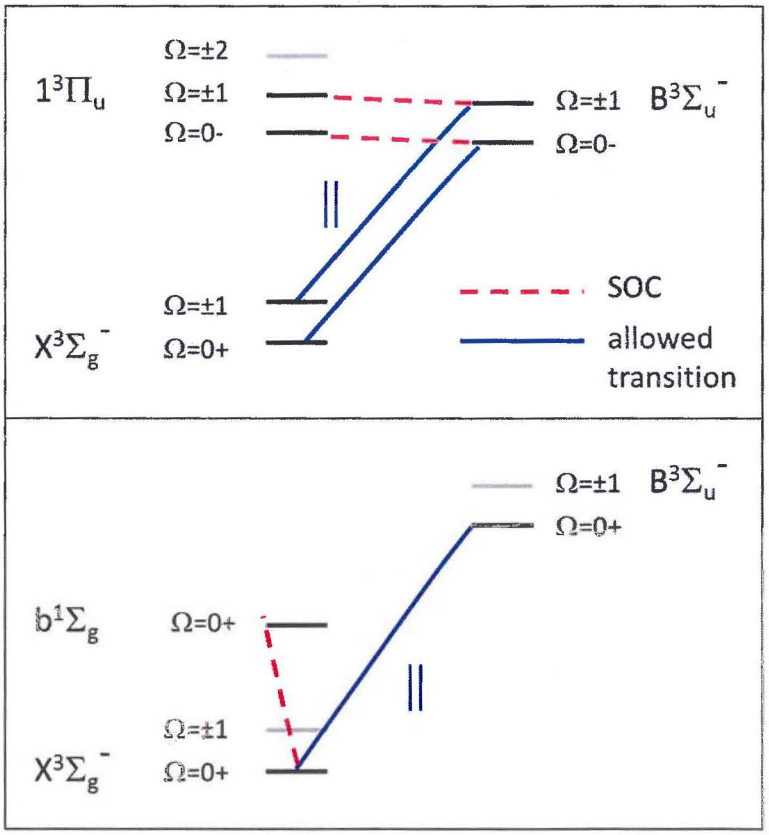

Figure 1.3: Spin-orbit coupling pathways for a weak (upper panel) and a forbidden (lower panel) transition of O_2 and S_2.

1.4.2 Rydberg states

The already complex spectroscopy of O_2 and S_2 becomes even more complicated when considering molecular Rydberg states.the two sharp and strong higher energy absorption bands shown in Fig. 1.1, for example, are transitions to the 3p Rydberg states of O_2. Rydberg states are excited states present in any molecule (or atom). According to Herzberg, "More and more highly excited states are obtained by bringing an electron from one of the orbitals filled in the ground state to higher

and higher orbitals. These higher atomic orbitals are more and more atomic orbitals and therefore give rise to Rydberg series of electronic states whose limit corresponds to the complete removal of the electron considered, i.e. to an ionization limit, IP, of the molecule." The energy of Rydberg states can be expressed as:

$$E_n = I_P - \frac{R_m}{(n-\delta)^2} \tag{1.7}$$

where I_P is the ionization potential to which the series converges when $n \to \infty$ of the neutral molecule (or atom) and is called Rydberg series limit, n is called the principal quantum number having positive integer values, δ is the quantum defect,which is characteristic of a particular Rydberg series and which depends on the orbital angular momentum quantum number l of the Rydberg electron. R_m is the mass-scaled Rydberg constant taking into account the finite mass of the nucleus$R_m = R_\infty \left(\frac{M}{m_e+M}\right)$, where $R_\infty = 109737.318\ \text{cm}^{-1}, M$ is the mass of molecule(or atom) and m_e is the mass of electron.[25] Electronic Rydberg series converge to all excited rotational or vibrational states of the ground electronic state of ion and also to the electronically excited ro-vibrational states of the ion.

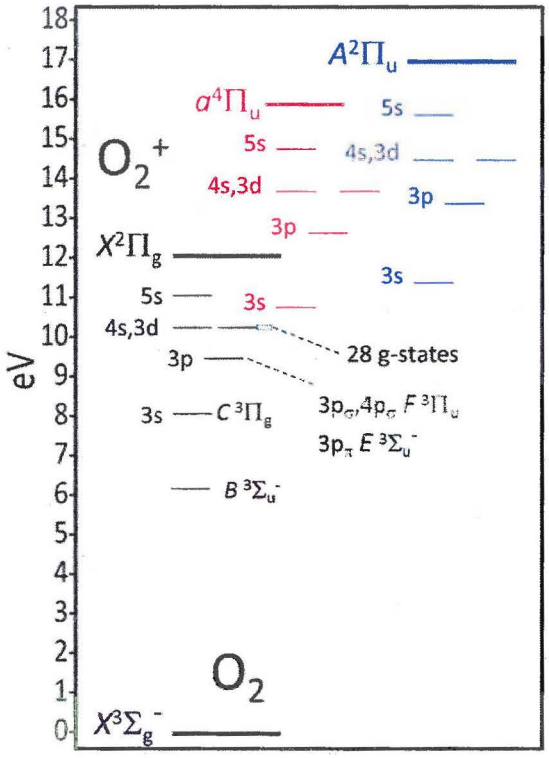

Figure 1.4: Energy level diagram for the v=0 levels of the lower Rydberg states of O_2.

The Rydberg energy level structure of O_2 is plotted schematically in Fig. 1.3, where only the lowest vibrational level of each state is shown for the lower members of Rydberg series *nl* correlating to the $X(^2\Pi_g)$, $a(^4\Pi_u)$, and $A(^2\Pi_u)$ states of O_2^+. The energy positions of the above-mentioned *E* and *F* states are indicated along with the *B(v=0)* valence state. As seen in the figure, the lowest lying Rydberg states correlating to the higher energy $a(^4\Pi_u)$ and $A(^2\Pi_u)$ states of O_2^+ overlap with higher energy members of states correlating with the ground state of O_2^+. The *l*=even Rydberg-*X* states are of g symmetry and thus are optically forbidden while the *l*=odd Rydberg-*X* states have ungerade symmetry and some of these states, such as the 3p states *E* and *F*, are reached by strong optically allowed transitions (Fig. 1.1).

In terms of bond length and well depth, Rydberg states resemble the electronic state of the ion to which they correlate. Fig. 1.4 shows schematic potential energy curves for O_2 where three Rydberg states

arising from the lowest Rydberg orbital (the 3s united atom orbital, which has σ_g symmetry) are added (dashed lines) which correlate each with the lowest three electronic states of the O_2^+ ion.

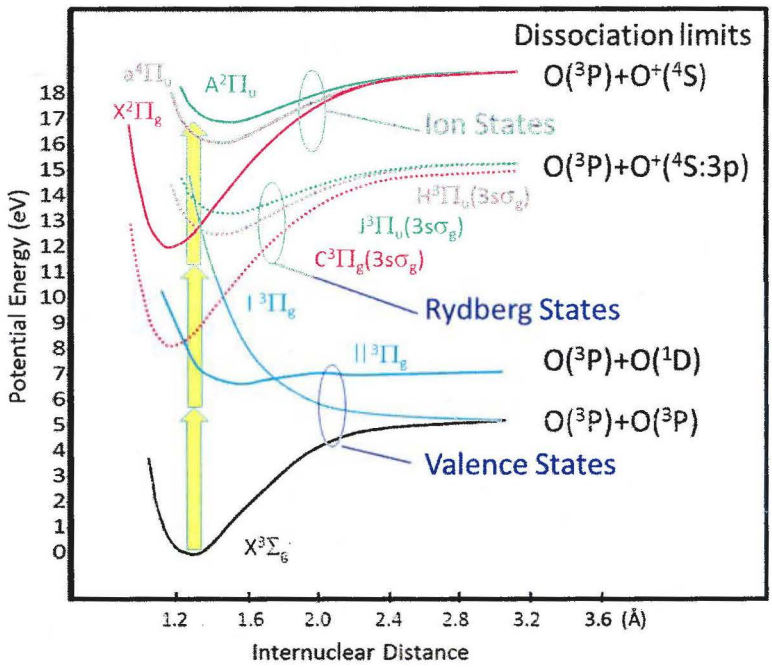

Figure 1.5: Selected potential energy curves for several Valence, Rydberg, and Ion states of O_2 in the diabatic (non-crossing) picture.

The first two dissociation limits of O_2 and S_2, D_0 and D_1, correspond to $O(^3P)+O(^3P)$ and $O(^3P)+O(^1D)$, respectively (Fig. 1.4) while the highest valence dissociation limit D_5, producing two $O(^1S)$ atoms, lies 8.379 eV above D_0 and thus 8.379+5.117=13.496 eV above the ground state of O_2. This significantly exceeds 12.078 eV, the ionization potential of O_2. We can thus expect that the higher energy valence states of O_2 will overlap the ionic states of O_2 and particularly the Rydberg states of the molecule, these are lower energy precursors of the ionic states.

In terms of photodissociation, a simple definition is that a molecular Rydberg state correlates with dissociation products with one 'valence' and one electronically excited O atom. For these high-lying states *prediction* of the dissociation limit of a Rydberg state is not simple, the limits indicated for the Rydberg states in Fig. 1.3 are speculative. [26]At higher energies the absorption spectrum can become extremely crowded with multiple Rydberg series converging to various limits. In the simplest picture, however, only a handful of Rydberg series are optically allowed

from the ground state, these are again excited states of $^3\Sigma_u^-$ and $^3\Pi_u$ symmetry.

The studies described in this thesis employ intense UV laser light can which easily cause multi-photon excitation to and through the Rydberg states of O_2 and S_2. With 5.5 eV photons (wavelength ~225 nm) a typical three-photon excitation in O_2 is depicted as vertical arrows in Fig. 1.4. The first photon interacts in the dissociation continuum of the $A\ ^3\Sigma_u^+$ state (Fig. 1.2), the second photon reaches Rydberg states converging on the X-state of the ion, and the third photon can cause direct ionization to the X, and a (and for higher photon energies the A-) states of the ion, or excite Rydberg states converging to higher electronic states of O_2^+.

1.4.3 Rydberg-Valence Interactions

For diatomics, the potential energy curves of the electronic states do not cross, unless permitted by symmetry. If the electronic states have different symmetry elements, say Σ or Π, u or g, singlet or triplet, there is no restriction on whether the potential energy curves can cross and the electronic states must be degenerated at the point of crossing. If the electronic states are of the same symmetry, the degeneracy is forbidden for any internuclear distance. The potential energy curves repel and the result is an avoided crossing.[27] The amount of repulsion between two crossing states of the same symmetry is determined by an electrostatic interaction; if this interaction is extremely weak, the states effectively cross each other; with a strong interaction the repulsion between the curves greatly changes their shape in the crossing region.

Avoided crossing is observed even for states from the only valence manifold. For example in Fig. 1.4, two valence states ($|\ ^3\Pi_g$ and $\|\ ^3\Pi_g$) must undergo avoided crossing, and these two also cross the lowest 3s Rydberg state labeled $C^3\Pi_g$ ($3s\sigma_g$). It is tempting treat the Rydberg and valence manifolds of states independently, which assumes a very weak perturbation in the avoided crossing picture or, better; the interactions of valence and Rydberg states is treated as a local perturbations at the crossing regions. This latter approach[28] is called the diabatic picture as illustrated in panel a) of Figure 1.5 for a manifold of valence states crossing a manifold of Rydberg states, all states having the same symmetry. In the limit where there is strong interaction between Rydberg and valence states the non-crossing rule results in a complex pattern, this is called the adiabatic approach as illustrated in panel (b) of Figure 1.5. The Rydberg series mixes with the valence repulsive state series, which can lead to rapid predissociation. This predissociation due to valence-Rydberg mixing is observed in many molecules and occurs

especially in O_2 and S_2 due to the large number of repulsive states present in these molecules.

With strong Rydberg-valence interactions the upper states (red curves in Fig 1.5.b) correlate with excited atom products; dissociation to these products is abbreviated as ND or neutral dissociation in Fig 1.5b. This adiabatic picture can be used to explain why excited atom products are observed near their energetic threshold, with low kinetic energy release. However, the complex pattern leads to quite disturbed or irregular spectra, which is not usually observed for the Rydberg states for O_2.

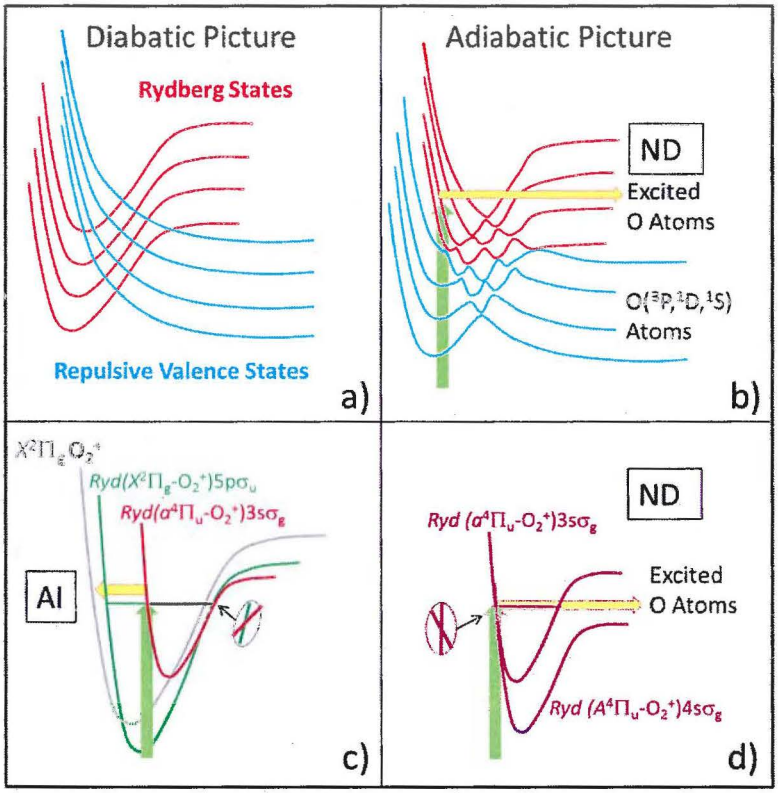

Figure 1.6: Diabatic (a) and adiabatic (b) schemes for Rydberg-Valence state mixing. In panel b) excitation to the upper state leads to neutral dissociation (ND) to produce electronically excited atoms. In panels c)) a diabatic scheme shows crossing at the outer walls of two Rydberg state converging to different states of the ion, leading to autoionization (AI), and d) shows crossings at the inner walls leading to ND.

1.5 Neutral dissociation versus Autoionization in O_2 and S_2

Along with ND of a diatomic molecule the molecule can also eject an electron (autoionization, labeled AI in Fig. 1.5c).[29] These two processes might also occur on the same time scale since autoionization takes place in time scales around 10^{-12} to 10^{-16} seconds whereas the predissociation occurs for time scales shorter than 10^{-13} seconds.

An alternative explanation to panel b of Fig.1.5 for the behavior of ND and AI in O_2 by Ehresmann and coworkers[26] is illustrated in panels c) and d). Here, the optically excited high energy molecular Rydberg state is crossed by another Rydberg state correlating to a different electronic state of the ion. In the ND picture of panel d) the optically excited state is crossed at the inner turning point of the potential by a Rydberg state converging to a higher electronic state of O_2, this Rydberg state correlates with the observed threshold excited atoms. At the outer turning point the state can be crossed by a Rydberg state converging to a lower electronic state of O_2^+. This state can lead to strong autoionization (AI), with production of a wider range of vibrational states of the ion, as is also observed. These fascinating and complex mechanisms will be described in more detail in Chapters 5 and 6.

1.6 Outline of this Thesis

In this study, measurements were carried out on two different species on same experimental setup. We studied bound-free transitions of molecular oxygen (O_2) and molecular sulfur (S_2) by detecting the speed and angular distributions of photofragments atoms using the velocity map imaging technique. The introduction has described photodissociation and the most important features of the diatomic molecules oxygen and sulfur including their metastable states, in and beyond the simple valence MO picture.

In chapter 2, a description is given of the equipment used in the experiments as well as the basic setup for VMI. General aspects of the various experiments described in this thesis will be discussed. Background information regarding velocity map imaging and experimental details about the setup are presented and the theory needed for the interpretation of experiments will be discussed here.

Chapter 3 presents the study of UV photodissociation of singlet oxygen $O_2(a\,^1\Delta_g)$ in the energy region from 200 to 240 nm by velocity map imaging. In our group a significant number of experimental studies have already been carried out to probe the complex nature of molecular oxygen. In past studies, our group has reported the photodissociation of

O_2 via the Herzberg $(A, A', c \leftarrow X)$, Schumann-Runge $(B \leftarrow X)$ and Parker $(B \leftarrow b)$ continua. In the current study, one-color and two-color experiments were performed to dissociate singlet oxygen $O_2(a\ ^1\Delta_g)$ via the Chamberlain continua $(A\ ^3\Sigma_u^+, A'\ ^3\Delta_u \leftarrow a\ ^1\Delta_g)$ with subsequent detection of$O(^3P_{j=0,1,2,3})$ fragments.

Chapter 4 deals with the photodissociation of singlet sulfur$S_2(a\ ^1\Delta_g, b\ ^1\Sigma_g^+)$. We probed the photodissociation of singlet sulfur $S_2(a\ ^1\Delta_g, b\ ^1\Sigma_g^+)$ via $(\widetilde{B}''\ ^3\Pi_u^+, \tilde{B}\ ^3\Sigma_u^+ \leftarrow a\ ^1\Delta_g)$ and $(\tilde{B}''\ ^3\Pi_u^+ \leftarrow b\ ^1\Sigma_g^+)$ transitionsin the ultraviolet region using velocity map imaging.

Chapter 5 deals with the multiphoton dissociation of molecular oxygen $O_2(X\ ^3\Sigma_g^-)$ via two-photon resonant Rydberg states. Superexcited states of molecular oxygen have been accessed at three photon level via two-photon resonant Rydberg states. The various decay process of superexcited states of molecular oxygen are studied. Competition between autoionization and neutral dissociation were observed at third photon level. Furthermore, one and two-photon dissociation of ground and vibrationally excited $O_2^+(X^2\Pi_g)$ is also topic of discussion in this chapter.

Finally, the last section of the thesis, chapter 6, presents the multiphoton dynamics of diatomic sulfur S_2 using three-photon excitation with light in the ultraviolet-visible region by using a single laser. In a previous study by our group, we probed the one-photon dissociation of S_2 in two-color experiment using velocity mapped imaging. In that pump and probe laser experiment, the bond energy of S_2 was also significantly revised. This work is extension of that work. At the three-photon level, superexcited states of S_2, labeled S_2^{**}, are reached via two resonant states. Competition between autoionization and neutral dissociation of S_2^{**} has been investigated by extracting the TKER distribution of the S^+ ions.

References

1. R. Levine and R. Bernstein, Molecular Reaction Dynamics and Chemical Reactivity. (Oxford University Press, New York 1987).
2. A. S. Bracker, E. R. Wouters, A. G. Suits, Y. T. Lee and O. S. Vasyutinskii, Phys. Rev. Lett. **80**, 1626 (1998).
3. A. S. Bracker, E. R. Wouters, A. G. Suits and O. S. Vasyutinskii, J. Chem. Phys. **110**, 6749 (1999).
4. T. P. Rakitzis, S. A. Kandel, A. J. Alexander, Z. H. Kim and R. N. Zare, Science **281**, 1346 (1998).
5. T. P. Rakitzis and R. N. Zare, J. Chem. Phys. **110**, 3341 (1999).

6. G. G. Balint-Kurti, A. J. Orr-Ewing, J. A. Beswick, A. Brown and O. S. Vasyutinskii, J. Chem. Phys. **116**, 10760 (2002).

7. S. N. Dixit and V. McKoy, J. Chem. Phys. **82**, 3546 (1985).

8. K. Wang and V. McKoy, J. Chem. Phys. **95**, 4977 (1991).

9. R. N. Zare, Mol. Photochem. **4**, 1 (1972).

10. T. G. Slanger and R. A. Copeland, Chem. Rev. **103**, 4731 (2003).

11. R. S. Mulliken, Phys. Rev. **32**, 186 (1928).

12. R. S. Mulliken, Rev. Mod. Phys. **4**, 1 (1932).

13. J. Ellis and H. Kneser, Z. Phys **86**, 583 (1933).

14. W. J. van Der Zande, W. Koot, J. Peterson and J. Los, Chem. Phys. **126**, 169 (1988).

15. L. Zhao, *Singlet Oxygen*. (University of Lowa, Lowa city, 2001).

16. C. S. Foote, J. S. Valentine, A. Greenberg and J. F. Liebman, *Active oxygen in chemistry*. (Springer, 1995).

17. G. Herzberg, *Molecular Structure and Molecular Spectra I. Spectra of Diatomic Molecules*. (1950).

18. P. W. Frederix, C.-H. Yang, G. C. Groenenboom, D. H. Parker, K. Alnama, C. M. Western and A. J. Orr-Ewing, J. Phys. Chem. A **113**, 14995 (2009).

19. S. J. Kim, M. F. A'Hearn and S. M. Larson, Icarus **87**, 440 (1990).

20. R. P. Saxon and B. Liu, J. Chem. Phys. **67**, 5432 (1977).

21. B. Minaev and L. Yashchuk, Opt. & Spectro. **95**, 553 (2003).

22. B. Buijsse, W. Van Der Zande, A. Eppink, D. Parker, B. Lewis and S. Gibson, J. Chem. Phys. **108**, 7229 (1998).

23. H. Lefebvre-Brion, *Perturbations in the spectra of diatomic molecules*. (Elsevier, 1986).

24. M. E. Green and C. M. Western, J. Chem. Phys. **104**, 848 (1996).

25. T. F. Gallagher, *Rydberg Atoms*. (Cambridge University Press, 2005).

26. P. V. Demekhin, V. L. Sukhorukov, H. Schmoranzer and A. Ehresmann, J. Chem. Phys. **132**, 9 (2010).

27. J. von Neumann and E. Wigner, Phys. Z **30**, 467 (1929).

28. J. Dehmer, A. Parr, S. Southworth and G. Marr, Vol. 2Elsevier, Amsterdam, 241 (1987).

29. B. Lewis, S. Gibson, S. Banerjee and H. Lefebvre-Brion, J. Chem. Phys. **113**, 2214 (2000).

Chapter 2

Experimental methods

Abstract

In this chapter an overview is given of the instruments and experimental techniques which were used in this thesis to obtain a fundamental insight into dynamical processes in oxygen and sulfur. Some of the main characteristics of the conventional velocity map imaging setup will be detailed here.

2.1 Velocity map imaging

In the past 25 years, instrumental improvements and innovations have increased the sensitivity and selectivity of imaging experiments. Chandler and Houston pioneered this new field by inventing the so-called ion imaging method[1]. The availability of position sensitive detectors (based on microchannel plates) and charge coupled device (CCD) cameras enabled the detection of the full three dimensional velocity distribution of ions or electrons. This has opened the detailed study of all kinds of dynamical studies, such as photodissociation processes, reactive scattering, rotational excitation by inelastic scattering, often controlled or initiated by the application of a pulsed laser source. After creating ions or electrons (e.g. by ionizing fragments or product molecules) they used a uniform electric field to extract these into a time-of-flight tube towards the imaging detector. They used a flat repeller plate and a single extraction electrode covered by a fine mesh grid to create this uniform field.

Later, a major improvement to the ion imaging technique (i.e, velocity map imaging, VMI) was achieved by Eppink and Parker[2]. They improved the resolution of the imaging technique by exchanging the grid electrode with two open electrodes, which created a tunable electrostatic lens. Velocity map imaging has emerged over the past 15 years as a powerful means of studying dissociation and ionization processes as well as scattering processes in crossed molecular beams setups. This experimental technique was employed in this work to study the reaction dynamics of molecular oxygen (O_2) and molecular sulfur (S_2). A number of methods have been developed to probe various properties of the scattered products of a chemical event. The VMI technique in combination with resonance enhanced multiphoton ionization (REMPI) scheme has become a widely used method to study laser–molecule interactions. The reasons why the VMI technique has become the most effective method are manifold: the Newton spheres are superimposed, open lenses without grids are used for the electrodes, and the removal of any sensitivity to the precise birthplace of the ion also means that a large starting volume can be used. This allows lower ion densities and thus reduces blurring from effects of space charge, *i.e*, the mutual repulsion of ions of like charges. Grids lower the lens transmission and perturb the ion trajectories. Space charge, the bane of ion measurement, changes the nascent velocity of the investigated species[3]. Velocity map imaging (VMI) works directly for ionic Newton spheres formed in processes such as photoionization,[2,4] photodissociation of state-selected cations,[5] electron impact ionization,[6] photo-detachment,[7,8,9]and ion-molecule reactions.[10] For other experiments such as photodissociation,[11] inelastic[12], or reactive scattering, and deflection of molecular beams by a laser formed lens,[13] the initially

formed neutral Newton spheres are converted to ions and then velocity-mapped.

Velocity map imaging can be explained in four simple steps.

- Firstly, create the Newton spheres by photodissociation
- Secondly, convert the photofragments to ions by laser ionization
- Thirdly, project the ionic Newton spheres to a 2D detector
- Lastly, recover the three-dimensional information from the 2D image.

A standard velocity map imaging setup contains ion optics (for the extraction field), a time of flight (TOF) tube and a 2-dimensional position sensitive detector, which consist of two microchannel plates and a phosphor screen followed by a charge-coupled device (CCD) camera. The main theme of VMI is to extract ions with the same velocity vector using ion optics and to focus them onto the same pixel position at the 2-D detector, irrespective of the position where these ions were formed. The resulting ions are extracted from the focus of the ions lens, the voltages of which are set (i.e. the ratio of voltages applied to the repeller and extractor electrodes is adjusted to find the sharpest image) so as to achieve velocity map imaging conditions. After passing through a field-free time-of-flight (TOF) tube all ions with the same mass-to-charge ratio will arrive at the detector at the same time.

2.1.1 Scaling properties in VMI

The velocity map imaging method yield images of selected charged particles in the form of rings, where the ring radius is a measure for the kinetic energy of the measured particles. How the image radius and energies scale in the experiment is described in the following. Let us for this purpose consider a photodissociation process of a molecule AB via an intermediate excited complex AB*,

$$AB + h\nu \rightarrow AB^* \rightarrow A + B + TKER \tag{2.1}$$

The total kinetic energy release (TKER) is the total excess energy left over after subtracting the bond energy of the molecule AB and the internal energies of the dissociation products A and B, thus

$$TKER = h\nu - D_0(AB) - E_{int}(A) - E_{int}(B) \tag{2.2}$$

Conversation of momentum and energy results in kinetic energy partitioning of the TKER among the two fragments according to

$$KER_A = \left(\frac{m_B}{m_{AB}}\right) \cdot TKER \tag{2.3}$$

$$KER_B = \left(\frac{m_A}{m_{AB}}\right) \cdot TKER \tag{2.4}$$

where $\left(\frac{m_A}{m_{AB}}\right)$ and $\left(\frac{m_B}{m_{AB}}\right)$ are referred to as mass partitioning factors. In photoionization the photoelectron receives essentially all TKER because mass of electron is very small as compared to the mass of fragments, whereas in photodissociation of a homonuclear diatomic molecule such as O_2 the TKER is equally shared between the two product O atoms. Note that the velocities and kinetic energies scale with the same mass ratio according to

$$\frac{v_A}{v_B} = \frac{T_A}{T_B} = \frac{m_B}{m_A} \tag{2.5}$$

The situation is depicted in Figure (2.1). Each photodissociation or photoionization event produces two partner fragments flying with equal momentum in opposite directions in the center of mass frame. Repetition of many of these evens results in the formation of Newton spheres. The size and surface pattern of these Newton spheres yield the energy and angular distributions of the molecule. The size of the Newton sphere is directly proportional to the speed of the fragments. Every particle A falls somewhere on a Newton velocity sphere A and the same holds for B. Speed and angular distributions in VMI are usually described by these Newton spheres.[14]

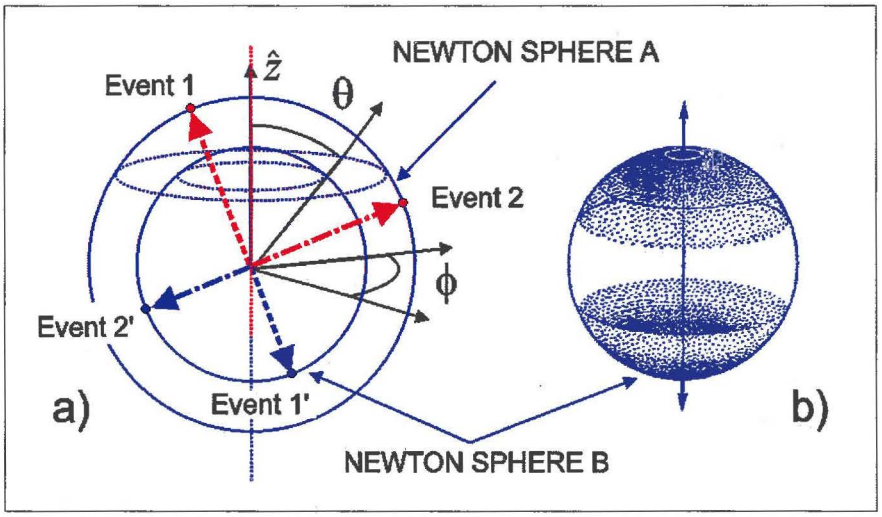

Figure 2.1: (a) two dissociation events are shown, which are distributed on two Newton spheres A and B. (b) After collection of many events, each Newton sphere shows a particular angular distribution.

Generally the extraction voltages used are in the order of kilovolts, which is much larger than the TKER in most cases. This results in the Newton sphere becoming flattened (or 'pancaked') before it reaches the imaging detector. The resulting image is thus a nice 2D projection (or 'crush' image) of the 3D Newton sphere. In order to get a feeling for the image size we want to derive formulas for the time-of-flight (TOF), and the radius R of the image. We assume first – for reasons of simplicity – the original ion imaging setup existing of a single extraction region and a time-of-flight tube, shown in Fig. 2.2.

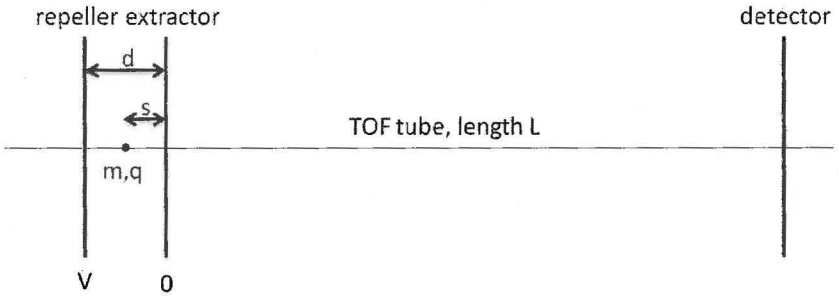

Figure 2.2: Ion imaging setup.

In this figure the repeller voltage is V, the extractor (grid) electrode is at ground and the distance between them is d. An ion of mass $m = m_A$ or m_B and charge q starts at position$s$, and the TOF tube has a length L. Thus the potential energy at the starting point is

$$E_{pot} = q\left(\frac{s}{d}\right)V \tag{2.6}$$

This energy is transferred into kinetic energy of the ion in the TOF tube $E_{kin} = \frac{1}{2}m_{A,B}v_t^2$, thus the ion gets a translational speed

$$v_t = \sqrt{\frac{2qVs}{m_{A,B}d}} \tag{2.7}$$

If we neglect the time spent in the extraction region we find from $TOF = L/v_t$ the following expression for the time of flight:

$$TOF = L\sqrt{\frac{m_{A,B}d}{2qVs}} \tag{2.8}$$

So the time of flight is proportional to the length of the TOF tube. Further it scales with $\sqrt{m/q}$, which is a common feature for mass spectrometers, and allows for an easy identification is different masses on basis of the time of flight.

The image radius directly follows from the expansion speed of the fragment Newton spheres through the simple relationship $R_{A,B} = TOF \cdot v_{A,B}$ and $v_{A,B} = \sqrt{2KER_{A,B}/m_{A,B}}$. This leads to the expression

$$R_{A,B} = L\sqrt{\frac{KER_{A,B}d}{qVs}} \tag{2.9}$$

Thus, the image size is mass independent, and scales with $\sqrt{KER}$ for each fragment. These two characteristic scaling properties are used experimentally for an easy calibration: an image with 1 eV KER will always appear at the same radius, for a specific setting of the repeller voltage V and laser position s.

The ratio between the fragment image radii can be found from

$$\frac{R_A}{R_B} = \frac{\sqrt{KER_A}}{\sqrt{KER_B}} = \sqrt{\frac{m_B}{m_A}} \tag{2.10}$$

In the discussion above we assumed the ion imaging setup, which has a homogeneous and flat electric field in the extraction region. In that case, the relation $R = v \cdot TOF$ is approximately true (remember we neglected the time spent in the extraction region); therefore it's possible to determine the speed of any fragment by measuring the time of flight and the image size. However, for VMI this is not true anymore. Due to the open electrodes the extraction field acts as an ion lens and the electric field lines are curved, which results in a magnification faction N, i.e.:

$$R = N \cdot v \cdot TOF \tag{2.11}$$

Fortunately this magnification factor is a constant for all images as long as the repeller/extraction voltage ratio and original laser position s are kept the same. Experimentally this feature of VMI implies the need for a calibration of the apparatus. This can be done easily by taking a calibration image of a process for which all channels appear in rings with known TKER. A well-known example of such a calibration image is the O^+ image at the (2+1) REMPI transition via the $3d\pi(^3\Sigma_{1g}^-)$ Rydberg state at 225 nm. Analogous to the description above, a ring with 1 eV KER will always appear at the same radius, so we can rewrite equation (2.9) as

$$R_{A,B} = NL\sqrt{\frac{KER_{A,B}d}{qVs}} \tag{2.12}$$

From this equation it is found that

$$KER_{A,B} = c \cdot R_{A,B}^2 \tag{2.13}$$

With c the calibration constant.

2.1.2 Extracting TKER distributions in VMI

How does this work in the experiment? Suppose you are detecting particles A and you want to determine their TKER distribution. The steps to take are then:

1. Take a crush image of A^+ ions by gating the MCP detector at the right time of flight, and by integrating the events over many laser shots.
2. Reconstruct the slice image from the crush image using an inversion program[15].
3. Extract the speed distribution from the reconstructed slice image by integrating over all angles. The speed distribution is then given by

$$I(R) = \int_0^{\pi} R \sin\theta \; I(R,\theta) d\theta \tag{2.14}$$

Where $I(R,\theta)$is the intensity in the reconstructed image, in polar coordinates.

4. Plot $I(R)/R$ versus R^2 to get from the speed distribution to the energy distribution. The $1/R$ factor comes from the Jacobian for the transformation from speed to kinetic energy. This is important if you need to compare the intensities between different channels, for instance to obtain branching ratios. The total intensity for a channel is obtained from the speed distribution by integrating this over a range of radii $[R_1, R_2]$. This yields

$$I_{tot} = \int_{R_1}^{R_2} I(R)\, dR \tag{2.15}$$

Because $KER = K = cR^2$ it follows $dK = 2cRdR \Longrightarrow dR = 1/(2cR)dK$ this integral transforms to:

$$I_{tot} = 1/2c \int_{K_1=cR_1^2}^{K_2=cR_2^2} \frac{I(R)}{R} dK \tag{2.16}$$

and thus the$1/R$ factor.

5. Scale the horizontal axis using the calibration coefficient c, which yields $K_A = cR_A^2$ on this axis. Usually this yields the kinetic energy release KER_A in units of electron volts [eV].
6. Finally the horizontal axis is rescaled using the mass partitioning factor to yield the TKER distribution, thus $TKER = \frac{M}{m_B} cR^2$.

2.1.3 Ion cloud deformation

Up to now we have neglected what happens in the extraction region. We will now have a more detailed look how this works out for the topics

pancaking and *turn-around time*. The principle of the situation is sketched in figure 2.3.

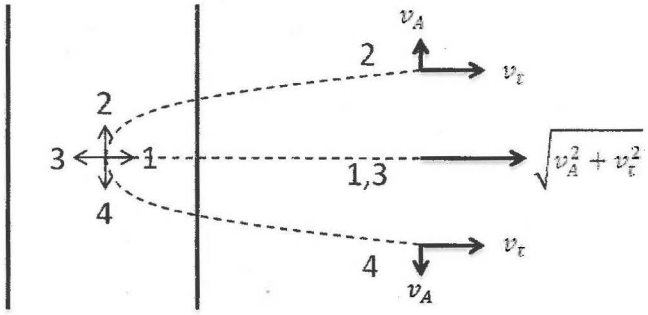

Figure 2.3: Initial velocities for four trajectories directed at 0°, 90°, 180° and 270° with respect to the TOF axis lead to different velocities in the TOF tube.

After photodissociation, fragments are ejected with starting speed v_A in all directions (1,2,3 and 4). Particles perpendicular to the TOF axis (2 and 4) maintain their velocity components v_A perpendicular and $v_t = \sqrt{2qVs/md}$ parallel to the TOF axis.

The particles along the TOF axis (1 and 3) will have a final velocity in the TOF tube according to the sum of the initial potential and kinetic energy, $K_{tot} = \frac{1}{2}mv_{tot}^2 = \frac{qVs}{d} + KER = \frac{1}{2}mv_t^2 + \frac{1}{2}mv_A^2$, therefore all particles will have the same *total* velocity $v_{tot} = \sqrt{v_A^2 + v_t^2}$. However, the velocity *component* parallel to the TOF axis is larger for trajectory 1 and 3 than for 2 and 4. This will lead to a deformation of the ion cloud when it passes through the TOF tube. In the extreme case, particles 2 and 4 will lag behind 1 and 3 if the TOF tube is long enough. The question is now how large this deformation effect can be.

The separation in space between particles 1 and 3 is constant and determined only by the turn-around time in the acceleration region. Solving the equations of motion inside the extraction region it can be shown that the turn-around time is given by

$$t_r = \frac{2v_A md}{qV} \tag{2.17}$$

which leads to a spatial separation Δz between particles 1 and 3 of

$$\Delta z = t_r\sqrt{v_A^2 + v_t^2} \tag{2.18}$$

Let's consider a number example to see how large these effects are on the deformation of the ion cloud. In the photodissociation of methyl iodide

(CH_3I) the fragments are A=CH_3 (methyl) and B=I (iodine). So we have $m_A = 15u$, $q = 1e$. Let's futher assume $V = 2000\,V$, $s = \frac{1}{2}d\,, d = 15$ mm, $L = 1$ m, $KER_A = 1$ eV. This leads to an expansion speed of $v_A = 3\,597$ m/s; $v_t = 113\,423$ m/s ;$t_r = 8.36$ ns; $\Delta z = 0.95$ mm.

For $L = 1$ m we have about $8.8\,\mu s$ time of flight, which leads to the following final positions in mm: $(r_1, z_1) = (0, 998.62)$; $(r_2, z_2) = (31.6, 998.12)$; $(r_3, z_3) = (0,\ 997.67)$; $(r_4, z_4) = (-31.6,\ 998.12)$.

From these numbers it is clear that the ion cloud is extremely flat (pancaked), with a pancake thickness of only 1.5 % of the pancake/image diameter. Also the deformation effect is only slight (~9.8%), which means that the trajectories 2 and 4 are only slightly lagging behind 1 and 3. Note that in most experiments, the TOF tube is less than 1 m, which further reduces this effect.

In conclusion, in VMI the ion cloud is deformed into a flat pancake before hitting the detector. The resulting image therefore represents a neat projection of the three dimensional velocity distributions, which reveals nested crushed Newton spheres for all fragmentation channels involved.

2.1.4 More deviations from perfection

In the typical VMI experiment the all-important features to optimize are energy resolution, linearity of radius with speed, extraction of reliable branching ratios and angular distributions. As will be described in the following sections, especially the thermal transverse speed distribution of the molecular beam and the ion recoil in the ionization process will be important parameters in the experiment which can reduce the attainable energy resolution.

Because the speed and energy resolution directly depend on the spatial resolution of an image, these are directly limited by the MCP detector resolution and the CCD camera resolution. Each ion which reaches the first MCP plate will emit up to 10^4 electrons, which hit multiple channels of the second MCP. The output of 10^6 – 10^7 electrons are accelerated toward the phosphor screen, which emits a localize flash of ~150 μm diameter for each detected ion. The localized flashes on the MCP detector are recorded for each laser shot by the CCD camera, which typically covers an area of 3x3 pixels for a 640x480 pixels camera. Using an event counting routine the ultimately attainable resolution can be determined by centroiding (i.e., finding the center-of-mass of the signal) to sub-pixel resolution. This leads to a spatial resolution around 30 μm, on a detector of 40 mm diameter.

It follows that the intrinsic spatial resolution of the imaging detector – CCD camera system is not the limiting factor for most cases. Also the linearity of image size with expansion speed has been shown to be quite well-behaved,[2] which pointed out that VMI is a reliable method for extraction speed and angular distributions, and branching rations from images. Other small aberration effects (spherical and chromatic aberrations) are described elsewhere into more detail ,[16] but we can restrict ourselves here to mention the method is not limited by these small effects for the purposes applied in this thesis.

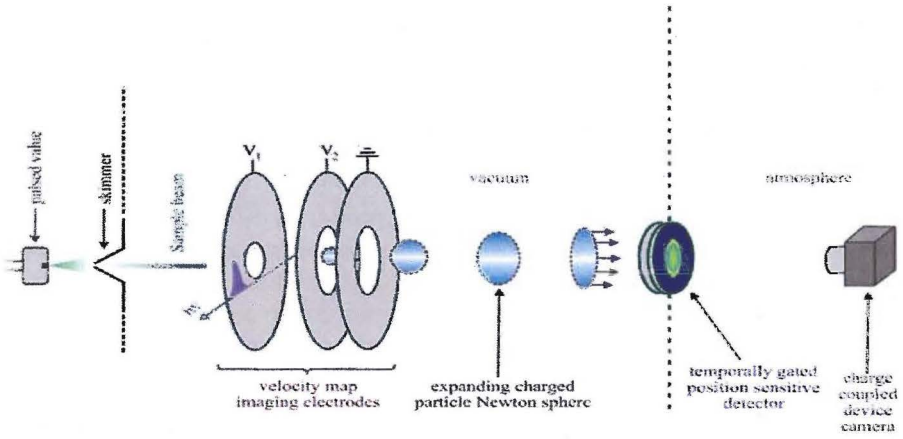

Figure 2.4: Velocity mapped imaging setup.

2.1.5 Slice Imaging

A major drawback in imaging techniques is its limiting energy resolution. Although in velocity map imaging technique the energy resolution has been improved, the analysis velocity mapped images still relies on cylindrical symmetry of the measured distribution and the inverse Abel transform to extract a slice through the three dimensional distribution. Inversion methods introduce artificial noise into the reconstructed image, especially along the symmetry axis, which can lead to a loss of experimental resolution. Because the equatorial slice through the image contains the full angular and translational energy information, it would be preferable if only this central part could be recorded directly in the imaging experiments. This is called slice imaging. Gebhardt*et al.*[17] developed a slice imaging method for photofragments studies and experimentally proved that slicing can be combined with the high resolution advantages of velocity mapping. They used a delayed pulsed extraction field, which spreads the ion arrival time over an interval of about 500 ns. By gating the microchannel plate and applying 40 ns high voltages pulses, they measured time slices of the ion packet. This delay

extraction approach to slicing is similar in concept, although different in technique, to the laser sheet approach developed by Suzuki and coworkers [18] in an ion imaging set up. They used a probably focused probe laser to ionize a slice through the centre of the neutral product sphere. This method is known as "sheet-sheet" slicing. Then, Suits and coworkers[19] developed a "dot-dot" raster method for slice imaging. In this method, both the dissociation and probe lasers are focused with spherical lenses. A horizontal stripe through the sliced image is formed, so the probe laser beam must be repeatedly moved up and down through the neutral sphere to recover the full image. In our own group, Chestakov *et al.*[20] invented optical "sheet dot" slicing where the dissociation laser is focused by a cylindrical lens and the probe laser by a spherical lens. In this method, the entire slice is captured without displacing the probe laser beam. It has been observed that in the "sheet dot" slicing method, for difficult REMPI schemes the higher flux of the 'dot' focused probe laser can yield signal under conditions where a cylindrically focused 'sheet' laser beam cannot. Close after the first slicing paper, Kopin Liu[21] and coworkers and Suits and coworkers developed a so-called DC slicing method where the electrostatic lens contains extra electrodes. The ions are created in a low electric field to allow the ion cloud to expand before hitting the detector. The main goal in DC and pulsed field slicing is to adjust the apparatus conditions so as to achieve a longer ion packet arrival time, while at the same time maintaining VMI conditions. When the arrival time is long enough, a short voltage pulse at the detector can be used to record selectivity the center of the ion packet.[3]

Slicing of image is also possible without modifying the velocity map imaging setup, as explained by Chestakov *et al.*[20] Photodissociation and ionization take place in field free conditions and subsequently a pulsed voltage is applied to the repeller and extractor electrodes around a microsecond after the formation of ions. The time delay permits the ion cloud to expand sufficiently before the beginning of extraction. Since extraction starts when the ions are dispersed in the space, the velocity focusing and the time focusing conditions are no longer fulfilled simultaneously. The voltage is adjusted in order to provide velocity focusing and ions of the same mass arrive at the detector over an extended period of time (up to ~400 ns) depending on the projection of their initial speed on the axis perpendicular to the detector. The detector is gated by a high voltage pulse with a short period of time (~25 ns) in order to extract the middle slice of ion cloud. The short time gate of detector allows detection of only the middle slice of ion sphere. The shape of high voltage pulse is critical for the ion lens and for the MCP gating as well. The rise time of the voltage pulse for ion lens should be short (~20 ns). The MCPs detector combined with phosphor screen, convert each signal ion event into light spot. A charged couple device (CCD) camera

records the ion image from the phosphor screen and a PC accumulated and stored the image for analysis.

In this thesis most experiments were performed with velocity map imaging, because of the easy usage and validity of the method. Above all, the attainable energy resolution was good enough for the purposes investigated. The applicability of slice imaging was confirmed in Chapter 4, where singlet oxygen images were obtained using both VMI and slice imaging.

2.2 *Resonance enhanced multiphoton ionization (REMPI)*

Velocity map imaging is generally combined with the resonance enhanced multiphoton ionization (REMPI) detection scheme, which has the advantage of detecting the full three dimensional velocity distributions with mass and state selectivity. It is this powerful combination which has led to the success of the VMI method. REMPI is extremely sensitive and a valuable method to investigate reaction dynamics or photodissociation processes. In a REMPI scheme a neutral atom/molecule absorbs one or more photons from a laser field and is excited to an intermediate electronic state. If the photon flux in the laser field is high enough the electronically excited molecule can then absorb additional photons sufficient to excite the molecule above its ionization potential (IP). The ionization process occurs immediately if the energy of the observed photon exceeds the IP. This multiphoton excitation of molecules allows us to access electronically excited states inaccessible by one photon techniques. It also allows us to study high lying electronically excited Rydberg states which are otherwise only accessible using vacuum ultra violet (VUV) light.

Resonance enhanced two or three-photon ionization is needed for state-selective detection. In most of our experiments a (2+1) REMPI scheme was used. Here, the first two photons resonantly excited an intermediate electronic state of a molecule (i.e., Rydberg states for O_2 and S_2 molecules) and a third photon of the same wavelength causes a transition into the ionization continuum. It has been assumed in imaging experiments that conversion of neutral fragments to ionic fragments using the standard VMI technique does not significantly change the nascent velocity distribution of the neutral species. In the REMPI process the nascent species is converted to an ion plus electron, the electron recoils with essentially all the excess energy in the process and the original velocity of the neutral remains unchanged. However small, this contribution is still significant in the overall apparatus function, limiting the attainable

energy resolution in VMI. Ion recoil distorts the energy distributions mainly for the light species with small kinetic energies.

2.3 Instrumental overview

In this chapter the instrumental overview is presented. A schematic diagram showing the complete view of our velocity map imaging (VMI) setup is shown in Figure 2.4.

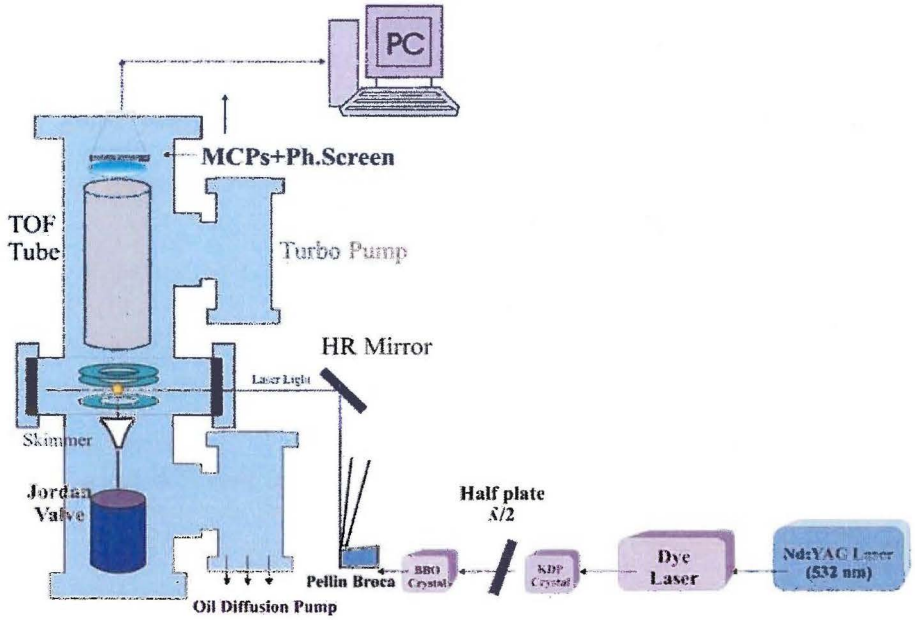

Figure 2.5: Schematic diagram of our VMI setup.

2.3.1 Vacuum System

The VMI experimental setup consists of a source chamber (typical pressure ~10^{-7} mbar; with molecular beam operating ~10^{-5} mbar) and a detection chamber (also ~10^{-7} mbar and is less than 10^{-6} mbar with the molecular beam running). Both chambers are differently pumped and separated by a skimmer with a 2 mm diameter aperture. A gate valve is located between these two chambers for the convenience of venting and pumping each region separately. The source chamber contains the pulsed valve and the detection chamber contains the electrostatic lens, the time of flight (TOF) tube and the 2-D position-sensitive charged particle detector. To guarantee a sufficiently low background pressure, the source chamber is pumped by an oil diffusion pump, while the detection chamber is pumped by a 100 l/s turbo molecular pump. Both pumps are backed by

a mechanical pump at a backing pressure of 1×10^{-2} mbar. In this way the molecular beam is created with collision free conditions are achieved which are very important for the study of dynamical processes for single molecules.

The molecular beam containing O_2 and S_2 is efficiently cooled by the supersonic expansion and propagates through the skimmer (2 mm diameter) 20 mm downstream from the nozzle. The molecular beam is directed towards the detector and the distance between the nozzle and the interaction region is 80 mm. The beam is further collimated by a 2 mm hole in the center of the repeller electrode. In this classical VMI setup the electrostatic lens consists of three electrodes (repeller, extractor with 20 mm inner diameter and ground electrode with 20 mm inner diameter) each with central apertures to allow the molecular beam to pass through them.[2] The interaction between the molecular beam and laser light takes place between repeller and extractor electrodes in the detection chamber.

2.3.2 Molecular Beam

For the production of the molecular beam of oxygen and sulfur, a pulsed valve (Jordan Company) is used. The operation of this valve is based on current-loop mechanism (i.e., magnetic repulsion within a strip in a single loop, closing off an O-ring). The Jordan valve is used because it is stable, and has a short (~60 μsec), intense pulse and fast rise time. The properties of the molecular beam (beam intensity, temperature and length) can be changed by setting the valve current and backing pressure.

Supersonic expansions have been used for many years to translationally and rotationally cool gas-phase species. In a supersonic expansion, vibrational cooling is rarely achieved. This is generally not a problem for diatomic molecules because the vibrational constant is large and the molecules are mostly populated in the ground vibrational state within the source gas. For large molecules, Suzuki introduced a different approach,[22] by adding a few percent isobutene in the sample gas (5 % N_2O seeded in Ar) in order to enhance the vibrational cooling of N_2O by energy transfer. A supersonic expansion is achieved when a high pressure (1 to 6 bar backing pressure) gas is expanded through a small orifice (400-1200 micron) into a vacuum. Since the gas is actually a mixture of buffer gas (like helium) with a small percentage of the molecule we want to probe, the molecules undergo many collisions with the buffer gas. In these collisions the molecule cools, losing most of its vibrational and rotational energy. This situation is ideal for doing spectroscopy because we have greatly reduced the number of transitions the molecule can undergo. In

addition, it is ideal for studying clusters because if the molecule has too much energy the clusters will fall apart.

The molecular beam is either directed parallel to the TOF axis (on-axis beam) or perpendicular to the TOF axis (off-axis beam). The output results obtained with both configurations are similar. In our experimental setup, the molecular beam is directed towards the detector as shown in figure 2.4. When the beam is directed towards the detector, the transverse velocity spread within the molecular beam is important. In our case the distance from the nozzle to the ionization region is 80 mm; the length of the ionization region after a 2 mm collimator at the repeller is 2.2 mm; the speed of an O_2 molecular beam at room temperature is around 735 m/s. Thus the transverse velocity spread is estimated to be 2.2 mm / 80 mm × 735m/s = 20.21 m/s. This can be reduced by using a carrier gas of a higher mass or by lowering the nozzle temperature to make a slower beam. Increasing the distance between valve and interaction region or reducing the collimator diameter on the repeller will also reduce the transverse velocity spread. However, this will lead to a reduced number density at the interaction region.

For a molecular beam directed parallel to the detector face, the longitudinal velocity spread is important, and is generally large. This is defined by the speed ratio, which depends on the quality of the supersonic expansion. Typically the velocity spread is at least a few tens of m/s.[16] The beam speed and speed ratio can be measured directly when the beam is parallel to the detector.

In our work, molecular beams of oxygen and sulfur were produced. If the gas molecules are cooled sufficiently in the supersonic expansion, the terminal velocity of the molecular beam can also be assumed by the following equation:[23,24]

$$v_\infty = \sqrt{\frac{2C_pT}{N_a m}} = \sqrt{\left(\frac{2kT}{m}\right)\left(\frac{\gamma}{\gamma-1}\right)} \qquad (2.19)$$

Where C_p, T and m are the mean heat capacity, temperature of valve and mean mass. Further $C_p = \left(\frac{\gamma}{\gamma-1}\right)R$ whereγ is the adiabatic coefficient C_p/C_v and R is the gas constant having value R = 8.314472 J/(mol K) [this is connected to Boltzmann's constant $k = R/N_A$, where N_A is Avogadro's number which yields k = 1.38065×10^{-23} JK^{-1}]. For a diatomic molecule the adiabatic constant is $\gamma = 7/5$. For molecular oxygen the mass 32×1.667×10^{-27} kg, the terminal velocity of molecular beam of oxygen at room temperature (T= 298 K) should be 734.8 m/s. For ^{4}He the terminal velocity becomes 1760 m/s and for ^{40}Ar it is 556 m/s.

During the experiment, the speed of the molecular beam can be chosen by varying the distance of both valve and skimmer (i.e, the distance between

valve and skimmer is kept fixed) with respect to the detection region. By measuring the two timings with respect to the two different positions, the speed of the molecular beam is simply $\Delta s/\Delta t$.

2.3.3 Pulsed electric discharge

Pulsed discharge sources are known to produce rotationally cold but vibrationally excited species, so production of vibrationally excited species is often observed when using these electric discharge sources. In some cases, a pulsed discharge source of short duration is considered as a reliable and effective source of populating low-lying metastable states of molecular oxygen. A pulsed discharge source for oxygen and sulfur molecules has been investigated and is characterized in this section.

A ring type discharge source[25] was used in the O_2 and S_2 experiments. For the SH or OH radical sources produced by a discharge of H_2S seeded in Xe and H_2O seeded in Ar, respectively, the rotational cooling after the discharge is substantial and the vibrational temperature is estimated to be round about 2000 K.[26] For the production of the S_2 radicals, a pulsed ring discharge source (with 4 mm diameter) is used. Two different gas mixtures, OCS and H_2S in Ar, are used to produce S_2. In the case of OCS seeded in Ar, a large background of S atoms has been observed, so in the current study a H_2S/Ar mixture has been used. First of all, 20% H_2S gas is seeded in argon at a backing pressure of 2 bar which is led to the pulsed valve (Jordan Company) with 0.4 mm diameter orifice. This gas expands through the nozzle into the source chamber to produce a cold, pulsed molecular beam. Just in front of the nozzle, 2.5 mm downstream, a stainless steel ring (4 mm diameter, 0.5 mm thickness) is mounted, as shown in figure 2.5. At each gas pulse passing the voltage on the ring is pulsed to a positive high voltage (~1000 V) which produces an electrical discharge between the ring and the grounded nozzle for the production of S_2. The production of S_2 radicals is dependent on the width, delay and voltage of the pulse applied to the ring. It is observed that a positive voltage (~1000V, 10 μs) is more suitable for a high production of S_2 radicals as compared to a negative voltage (which is more suitable for the production of SH). In addition to this, a filament is placed adjacent to the ring discharge and a current of around 1.5 ampere is passed through it. This glowing filament emits electrons that help to initiate and stabilize the discharge.

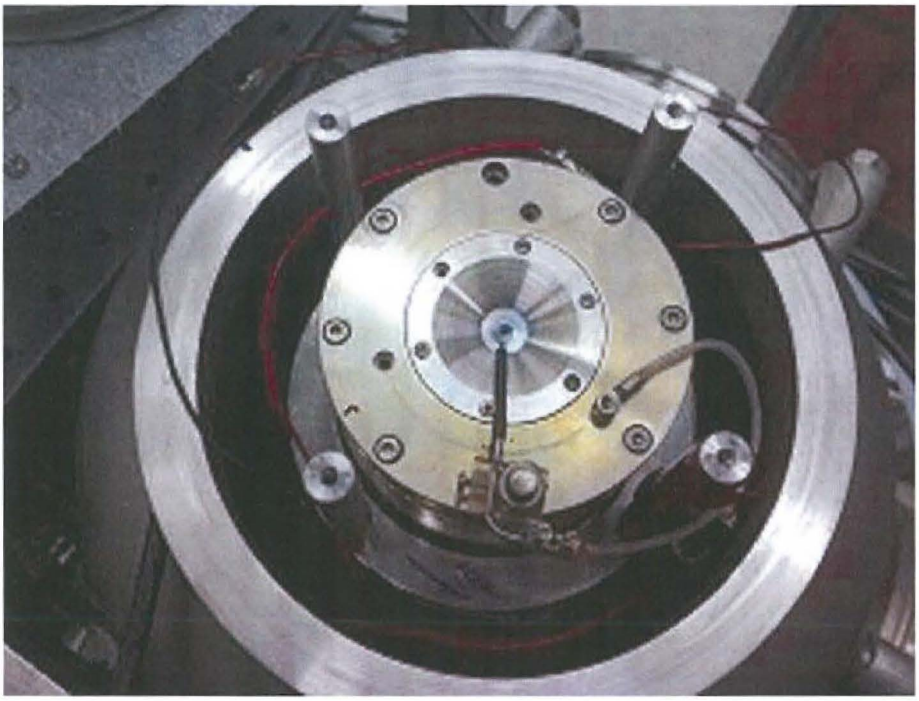

Figure 2.6: Photograph of the discharge setup.

In the case of molecular oxygen (O_2), the low-lying metastable $a(^1\Delta_g)$ state can be populated by this ring type discharge source. There are number of methods for the formation of singlet oxygen. Both physical and chemical methods (i.e., photosensitization, microwave and radiofrequency discharge and energy transfer methods) can generate singlet oxygen but unfortunately no reliable source for formation of singlet oxygen has been reported. In our experiment we produced singlet oxygen $a(^1\Delta_g)$ by using this ring type high voltage pulsed discharge. A high voltage is applied for a small duration (~16 μs) which should be shorter than opening duration (~60 μs) of the Jordan valve.

Next to the production of singlet oxygen, a lot of excited oxygen species (i.e. radicals/molecules) are present in the beam. All these species give rise to background signal, which makes the measurement very difficult. In order to get rid of these background signals, we adjusted the duration of the discharge to less than three to four times time of the molecular propagation time from nozzle to skimmer. All fast ions which are produced in the discharge completely fly away whereas excited species passed only a few centimeters after the nozzle for expanding and cooling. As a result, we obtained a strong signal from cold oxygen radical with minimum background.

In our experiments, an electric discharge was used in pulsed mode instead of continuous mode. In order to understand the difference between a discharge with continuous voltage and pulsed voltage applied to the ring, the time scales of the different processes during the discharge are very critical. Let's assume, to illustrate this, a thermal speed of the molecular beam to be 500 m/s. So the time the molecules fly from the nozzle to the skimmer (where the main cooling takes place) is given by:

$$t_{\text{neutrals}} = \frac{L}{v} = \frac{0.05}{500} = 100\ \mu\text{s} \tag{2.20}$$

During the discharge a lot of ions and free electrons appear as well as excited molecules and radicals. All produced charged particles accelerate in the electric field of the ring and reach high speeds. Because the voltage at the ring is negative for oxygen, positive ions accelerate in the direction of the beam propagation. Their speed can be determined by:

$$u_{\text{ions}} = \sqrt{\frac{2eV}{m}} = 5.10^5 \text{m/s} \tag{2.21}$$

and the time for these ions to reach the skimmer is:

$$t_{\text{ions}} = \frac{0.05}{5{\cdot}10^5} = 0.01\ \mu\text{s} \tag{2.22}$$

If these ions meet with some other particle when flying to the skimmer it can excite that particle. So, ions can collide with the particles, which passed through the ring almost 100 μs before. The collisions between ions and particles take place at the end of the cooling region, therefore excitation by the collision particle can be still take place even after passing through the skimmer, and can have rovibrational temperatures much higher than the cooled particles.

If the time of discharge has a value comparable with time of flight between the nozzle and the skimmer, all those processes will take place. It means that we will have not only cooled particles in the beam, but also a number of hot molecules excited by collisions with fast ions from the discharge. It is in fact the same situation when a continuous voltage is used. In that case the duration of discharge is almost the same as the beam duration, and comparable with the time of flight between nozzle and skimmer. In our experiments, however, the duration of the discharge was less than a third of t_{neutrals}, so by the time the neutrals reach the interaction region all ions already have passed it due to their high speeds.

2.3.4 Laser system

For the detailed investigation of the O_2 and S_2 spectral features, a tunable light source in the visible-ultraviolet region with sufficiently narrow bandwidth is required. Tunability and narrow bandwidth are

$$O_2 \xrightarrow{h\nu} O(^3P_2) + O(^3P_J) \quad (2.23)$$

$$O_2 \xrightarrow{2h\nu} O(^3P_J) + O(^1D_2) \quad (2.24)$$

In the calibration image three rings appear: the inner ring the of the image corresponds to one-photon dissociation in Herzberg continuum, leading to channel $O(^3P_2)+O(^3P_j)$ where the O atom total kinetic energy release is 0.38 eV. The other two outer rings correspond to two photon dissociation leading to $O(^3P_2)$ $+O(^1D_2)$, and $O(^3P_2)+O(^3P_j)$, where the O atom kinetic energy release (KER) is 3.91 and 5.88 eV, respectively. These quantities are calculated using $KER = (h\nu - D_0(O_2) - E_{int})/2$, where $h\nu = 5.494$ eV, $D_0(O_2) = 5.117$ eV, and E_{int} the internal energy of the O state.

References

1. D. W. Chandler and P. L. Houston, J. Chem. Phys. **87**, 1445 (1987).
2. A. T. J. B. Eppink and D. H. Parker, Rev. Sci. Instrum. **68**, 3477 (1997).
3. M. N. R. Ashfold, N. H. Nahler, A. J. Orr-Ewing, O. P. J. Vieuxmaire, R. L. Toomes, T. N. Kitsopoulos, I. A. Garcia, D. A. Chestakov, S.-M. Wu and D. H. Parker, Phys. Chem. Chem. Phys. **8**, 26 (2006).
4. C. Bordas, F. Paulig, H. Helm and D. L. Huestis, Rev. Sci. Instrum. **67**, 2257 (1996).
5. M. Beckert, S. J. Greaves and M. N. R. Ashfold, Phys. Chem. Chem. Phys. **5**, 308 (2003).
6. P. W. Harland, B. R. Cameron, M. Bart and M. O. Pearce, Rev. Sci. Instrum. **73**, 2398 (2002).
7. A. Sanov and W. Carl Lineberger, Phys. Chem. Chem. Phys. **6**, 2018 (2004).
8. A. V. Davis, R. Wester, A. E. Bragg and D. M. Neumark, J. Chem. Phys. **118**, 999 (2003).
9. R. Mabbs, E. Surber and A. Sanov, Analyst **128**, 765 (2003).
10. E. L. Reichert, G. Thurau and J. C. Weisshaar, J. Chem. Phys. **117**, 653 (2002).
11. D. H. Parker, Advanced Series of Phys. Chem. 10A & 10B (World Scientific Publishing Co. Ltd.Singapore,2000).

12. K. T. Lorenz, D. W. Chandler, J. W. Barr, W. W. Chen, G. L. Barnes and J. I. Cline, Science **293**, 2063 (2001).

13. H. S. Chung, B. S. Zhao, S. H. Lee, S. Hwang, K. Cho, S.-H. Shim, S.-M. Lim, W. K. Kang and D. S. Chung, J. Chem. Phys. **114**, 8293 (2001).

14. D. H. Parker and A. T. J. B. Eppink, in *Imaging in Molecular Dynamics; Technology and Applications (A User's Guide)*, edited by B. J. Whitaker (Cambridge University Press, Cambridge, 2003).

15. V. Dribinski, A. Ossadtchi, V. A. Mandelshtam and H. Reisler, Rev. Sci. Instrum. **73**, 2634 (2002).

16. W. Malcom, Radboud University, Nijmegen, 2004.

17. C. R. Gebhardt, T. P. Rakitzis, P. C. Samartzis, V. Ladopoulos and T. N. Kitsopoulos, Rev. Sci. Instrum. **72**, 3848 (2001).

18. K. Tonokura and T. Suzuki, Chem. Phys. Lett. **224**, 1 (1994).

19. D. Townsend, M. P. Minitti and A. G. Suits, Rev. Sci. Instrum. **74**, 2530 (2003).

20. D. A. Chestakov, S.-M. Wu, G. Wu, D. H. Parker, A. T. Eppink and T. N. Kitsopoulos, J. Phys. Chem. A **108**, 8100 (2004).

21. J. J. Lin, J. Zhou, W. Shiu and K. Liu, Rev. Sci. Instrum. **74**, 2495 (2003).

22. T. Nishide and T. Suzuki, J. Phys. Chem. A **108**, 7863 (2004).

23. D. Miller, *Free Jet Source in Atomic and Molecular Beam Methods* (Oxford University Press, Oxford, 1988).

24. W. Christen, K. Rademann and U. Even, J. Phys. Chem. A **114**, 11189 (2010).

25. M. Van Beek and J. Ter Meulen, Chem. Phys. Lett. **337**, 237 (2001).

26. D. C. Radenovic, A. J. van Roij, D. A. Chestakov, A. T. Eppink, J. J. ter Meulen, D. H. Parker, M. P. van der Loo, G. G. Groenenboom, M. E. Greenslade and M. I. Lester, J. Chem. Phys. **119**, 9341 (2003).

Chapter 3

Photodissociation of Singlet Oxygen in the UV region

Abstract

Photodissociation of singlet oxygen, $O_2\, a^1\Delta_g$, by ultraviolet radiation in the region from 200 to 240 nm has been investigated using velocity map imaging of the atomic oxygen photofragments. Singlet oxygen molecules are generated in a pulsed discharge and studied by one-laser photodissociation and detection around 226 nm as well as two color photodissociation at various wavelengths in the range from 200 to 240 nm. A simple model of the discharge on and off signal indicates efficient conversion of $O_2\, X^3\Sigma_g^-$(v=0) in the parent beam to $O_2\, a^1\Delta_g$(v=0-2). Minute amounts of highly excited vibrational levels of ground state $O_2\, X^3\Sigma_g^-$(v>0) are detected but no evidence is found for production of the $O_2\, b\ ^1\Sigma_g^+$ state. Over the decreasing wavelength range 240-200 nm the $a^1\Delta_g$-state signal relative to the $X^3\Sigma_g^-$(v=0) signal decreases strongly. Around 226 nm the $a^1\Delta_g$(v=0-2) states averaged branching ratio percentage for O(^{3}P$_j$ j=2:1:0) is found to be 56 : 36 : 8 (±5%), respectively. The anisotropy parameter for photodissociation of $a^1\Delta_g$(v=0-2) averages to β=1.3±0.4. The $a^1\Delta_g$(v=0) photodissociation cross section is found to 3-10 times stronger than theory predicts. Furthermore, the photodissociation image shows a strong parallel character, (i.e., transition moment parallel to the molecular axis) while theory predicts a predominantly negative character.

3.1 Introduction

Molecular oxygen, O_2, is a fascinating[1] molecule involved in many processes occurring on Earth. Oxygen plays a pivotal role in the maintenance of life, and in mechanisms by which life is extinguished and materials destroyed. Many of these mechanisms are photochemically driven, making photodissociation, the first step in photochemistry, an interesting topic for fundamental research[2]. Over the past years our group has investigated several aspects of the photodissociation of isolated O_2 and weakly bound O_2–X van der Waals complexes in the ultraviolet region[2-11]. In this study we investigate photodissociation of the $O_2\, a(^1\Delta_g)$ state; also known as 'singlet oxygen', in the 200-240 nm region. Singlet oxygen has a rich chemistry[12] which is distinctly different from that of the ground triplet state of $O_2\, X^3\Sigma_g^-$. While to our knowledge there is no previous publication of an experimental study of the photodissociation of this state, an upper limit of 8×10^{-22} cm^2 for the absorption cross section of $O_2 a(^1\Delta_g)$ in the wavelength region 190–290 nm has been estimated[13]. Comparisons of our data with previous predictions by theory[14, 15] reveal a number of unexpected aspects of singlet oxygen photodissociation.

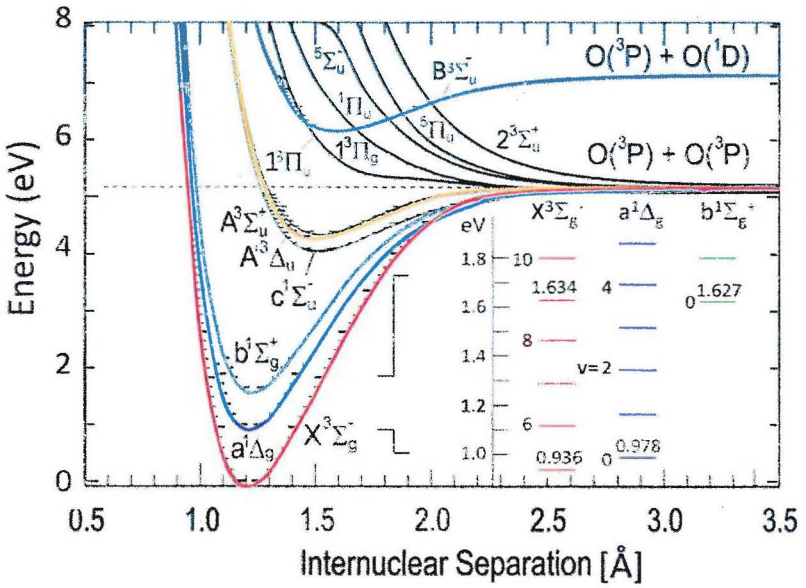

Figure 3.1: Potential energy curves for the lower electronic valence states of molecular oxygen[16,17]; the curves most relevant for this study are highlighted in color. The inset shows the energy positions (from Ref. 18) of states populated in the discharge beam. States with energy spacing comparable to the experimental resolution are indicated by their energy in eV.

A large amount of knowledge about the spectroscopic and dynamic properties of O_2 is encoded in the potential energy curves[16,17] of the lowest valence electronic states shown in Figure 1. O_2 is unique in its high number of electronic states and absence of allowed electric dipole transitions between the lower states[18]. The only electric dipole allowed triplet-triplet absorption of the O_2 molecule near the first dissociation limit is the Schumann-Runge (SR) $B^3\Sigma_u^- \leftarrow X^3\Sigma_g^-$ transition. All other transitions from the ground state O_2 and from the two low-lying metastable spin singlet electronic states, $a^1\Delta_g$ and $b^1\Sigma_g^+$, are very weak. For all three lowest energy states, the very small absorption strength is due to spin-orbit and spin-rotation coupling with optically allowed electronic states lying at higher energy[14, 18, 19].

The next three upper excited electronic states: $c^1\Sigma_u^+$, $A'^3\Delta_u$, and $A^3\Sigma_u^+$ are known collectively as the Herzberg states. Excitation to the Herzberg states, labeled as Herzberg I, II, and III for the $A^3\Sigma_u^+$, $c^1\Sigma_u^+$, and $A'^3\Delta_u \leftarrow X^3\Sigma_g^-$ are symmetry-forbidden transitions, respectively, appear as very weak, narrow-line bands between 270 and 242 nm. Franck-Condon overlap determines the spectral envelope of the transitions from the lower $X^3\Sigma_g^- a^1\Delta_g$, and $b^1\Sigma_g^+$ states of O_2. As can be seen in Figure 1, these states overlap optimally with the unbound parts of the potential energy curves of the Herzberg states (and the higher-lying $B^3\Sigma_u^-$ state) causing the absorption curve to peak in the broad, weak continuum between 242 and ~180 nm, where the Herzberg I continuum provides the largest cross section from the electronic ground state, rising from 86% at 242 nm to 94% at 198 nm[4].

The $X^3\Sigma_g^- \leftarrow a^1\Delta_g, b^1\Sigma_g^+$ transitions with radiative lifetimes of 4000 s and 150 s respectively[18], are electric-dipole forbidden both by orbital and spin selection rules, but can be induced by magnetic-dipole and electric quadrupole interactions. The very weak magnetic dipole oscillator strength of the $b^1\Sigma_g^+ \leftarrow X^3\Sigma_g^-$ transition around 762 nm is due to admixture of ground state character via spin-orbit coupling to the b state.[20] The lowest excited metastable $a^1\Delta_g$ state is remarkably long-lived, also under collision conditions, and the density of oxygen molecules excited in this state is usually determined spectroscopically by $X^3\Sigma_g^- \leftarrow a^1\Delta_g$ emission at 1268 nm. Rotational structure of these bands clearly reveals a magnetic dipole nature of both transitions[18].

The transitions starting from the $a^1\Delta_g$ state to the $c^1\Sigma_u^+$, $A'^3\Delta_u$, and $A^3\Sigma_u^+$ Herzberg states are collectively labeled in this paper as the Chamberlain bands; this name applies specifically to the $A'^3\Delta_u \leftarrow a^1\Delta_g$ component. These bands provide a means for probing singlet oxygen and for understanding singlet oxygen photodynamics on exposure to ultraviolet light. Photoexcitation of singlet oxygen in the UV, the topic of

this investigation, is predicted to be of similar strength as photodissociation by UV excitation from the ground state. In view of the low steady-state singlet oxygen concentrations it may thus be unimportant in atmospheric photochemistry.

In our laboratory we study bound-free transitions of O_2 by detecting the speed and angle distribution of the photofragment $O(^3P_{j=2,1,0})$ or $O(^1D_{j=2})$ atoms using the velocity map imaging technique[21], where j indicates the atomic fine-structure state using the notation of Ref. 4. The quantum state of a product atom is determined by state-selective detection of one atom; from the measured speed distribution, momentum conservation yields the quantum state of the other atom. The angular distribution of the photodissociation products is described by:

$$I(\theta) = \frac{1}{4\pi}[1 + \beta P_2(\cos\theta)] \qquad (4.4)$$

where $P_2(x) = \frac{1}{2}(3x^2 - 1)$ is the 2nd order Legendre Polynomial, θ is the recoil angle with respect to the polarization axis and β is the anisotropy parameter $(-1 < \beta < 2)$.$I(\theta)$is an important observable that can elucidate the amount of parallel (β=2) and perpendicular (β=-1) character in an electronic transition to a continuum state, information that is unattainable using conventional spectroscopic techniques[4]. In contrast to the case of electric dipole-allowed transitions, where one matrix element dominates the transition probability, the situation is different forthe weaker forbidden transitions of O_2. Here, intensity is borrowed from allowed transitions through one or several second-order pathways with either parallel or perpendicular character. Ifthe nature of the optical excitation is a mixture of paralle land perpendicular pathways, then this will be reflected in the photofragment angular distribution. In this way, angular distributions form a diagnostic tool which is of particular interest in the study of forbidden bound-free transitions. We show here that the product O-atom speed and angular distributions yields unique information on the UV photodissociation of singlet oxygen.

The Herzberg continuum arising from excitation of $O_2\, X^3\Sigma_g^-$(v=0) begins at 242.3 nm, the lowest energy dissociation threshold D_0= 5.117eV, which corresponds to production of two $O(^3P_2)$ atoms; the Schumann Runge continuum (SRC) begins at the second threshold, D_1, at 7.084 eV (175.0 nm),corresponding to $O(^3P_2)+O(^1D)$ products. An overview of the UV absorption spectrum of the $X^3\Sigma_g^-$, $a^1\Delta_g$ and $b^1\Sigma_g^+$ states of O_2, which are all essentially due to continuum absorption, is summarized in Figure 2.

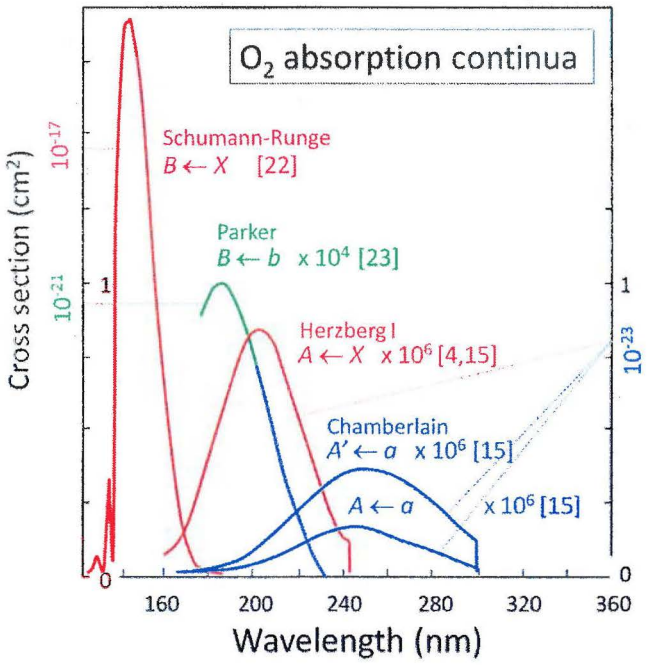

Figure 3.2: Compilation of the dissociation continua of O_2 in the UV-VUV region, using the color coding of Fig. 1. The Schumann-Runge continuum, with maximum value of $7x10^{-17}$ cm^2 is adapted from Ref. 22, the Parker continuum spectrum with maximum of $1x10^{-21}$ cm^2, was calculated by Lewis et al in Ref. 23, the Herzberg I continuum with maximum of $9x10^{-24}$ cm^2, measured by Buijsse et al in Ref. 4 and is similar to the spectrum shown here, which was calculated by Saxon and Slanger in Ref. 15 and scaled to the experimental absorption spectrum. The Chamberlain continua shown here are also taken from Ref. 15.

The bound-bound Schumann-Runge bands begin with the (0,0) band at 202.5 nm with a narrow-line peak intensity of ~$4.5x10^{-23}$ cm^2 (Ref. 24) and continue to 175 nm where they connect smoothly in intensity with the SRC, which peaks at ~142 nm with a very large cross section of ~$1.7x10^{-17}$ cm^2. The $B^3\Sigma_u^- \leftarrow b^1\Sigma_g^+$ transition, first reported experimentally by our group[5] and analyzed by Lewis et al.[23] and Minaev[25], is almost 200 times weaker than the SRC and peaks at ~185 nm with a predicted cross section of ~$1x10^{-21}$ cm^2. Our group[4] has also reported the experimental deconvolution of the three Herzberg continua; the dominant $A(^3\Sigma_u^+) \leftarrow X(^3\Sigma_g^-)$ transition, shown in Figure 2, has a measured maximum cross section of ~$9x10^{-24}$ cm^2 around 200 nm. The Chamberlain continuum has only been studied by theory. Klotz and Peyerimhof[14] reported *ab initio* calculations of forbidden transitions in O_2. Their data was used by

Saxon and Slanger [15] to predict the absorption continua from the $X^3\Sigma_g^-$, $a^1\Delta_g$ and $b^1\Sigma_g^+$ states. The calculations of Ref.15 for the $A^3\Sigma_u^+ \leftarrow X^3\Sigma_g^-$ Herzberg continuum and the $A^3\Sigma_u^+ \leftarrow a^1\Delta_g$ and $A'^3\Delta_u \leftarrow a^1\Delta_g$ Chamberlain continua are shown to scale in Figure 2. The $A'^3\Delta_u \leftarrow a^1\Delta_g$ transition, first described experimentally in atmospheric emission studies by Chamberlain[26], is predicted to be strongest, with a cross section of ~4×10^{-24} cm^2 peaking at 250 nm. Calculations of the $A^3\Sigma_u^+ \leftarrow b^1\Sigma_g^+$, and $A'^3\Delta_u \leftarrow b^1\Sigma_g^+$ transitions by Saxon and Slanger[15] yield continua that are even weaker and peak at longer wavelengths (>300 nm) than those explored in this study. Transitions to the upper $c^1\Sigma_u^+$ state are weak for both the Herzberg and Chamberlain continua and are not mentioned further more in this paper.

The goal of the present experiment is to study photodissociation of the $a^1\Delta_g$ state of singlet oxygen. Our previous study[5] of photodissociation of the $b^1\Sigma_g^+$ state used O_2 ($X^3\Sigma_g^-$,v=0, J) rotational state selective photoexcitation of the $X^3\Sigma_g^-$ state by intense narrow-band pulsed radiation at ~762 nm to the $b^1\Sigma_g^+$ state, followed by both photodissociation and detection of the O(^{3}P) and O(^{1}D) fragments at 226 and 205 nm, respectively. Direct excitation of the $a^1\Delta_g$ state was not possible due to the extremely low cross section for the $a^1\Delta_g \leftarrow X^3\Sigma_g^-$ transition. Instead, we use a pulsed electric discharge taking place during the supersonic expansion of pure O_2 or a 10% O_2/Ar mixture from a pulsed nozzle to produce excited oxygen molecules. Electric discharges have been used as a means of generating metastable molecules in the gas phase since the early 1900s. Such dischargesproduce rotationally cold but vibrationally hot beams of NO, OH[28], SH[29], S_2[30], etc. In the case of molecular oxygen, in addition to formation of vibrationally hot $O_2X^3\Sigma_g^-$(v>0)a discharge can produce the low-lying metastable $a^1\Delta_g$ and $b^1\Sigma_g^+$ states. Houston and coworkers[31], for example, have studied Rydberg transitions from the $a^1\Delta_g$ and $b^1\Sigma_g^+$ states of O_2 formed in a low pressure microwave discharge. From Figure 2, however, it is predicted that in the 240-200nm region we study, the Herzberg I continuum is stronger than the $a^1\Delta_g$ state continua. It should thus be difficult to study photo-dissociation of the $a^1\Delta_g$ state in a molecular beam containing mainly $X^3\Sigma_g^-$ (v=0) with only small concentrations of singlet oxygen.

3.2 Experimental setup

The experiments were carried out using a velocity map imaging (VMI) setup which has been described in detail elsewhere[6]. Pure oxygen gasor a 10% O_2/Ar mixture at a backing pressure of 2 bar was led to a pulsed valve (Jordan Company) with a 0.4 mm diameter orifice. Just in front of

the nozzle, 2.5 mm downstream, a stainless steel ring (4 mm diameter, 0.5 mm thickness) was mounted. During each passing gas pulse, the voltage on the ring was pulsed to a negative high voltage (-1000 V DC) which produced an electrical discharge between the ring and the grounded nozzle for the production of singlet oxygen. The production efficiency was dependent on the width, delay and voltage of the pulse applied to the ring. It was observed that a negative voltage pulse (-1000V, 10 μs) was more suitable for a high production of singlet oxygen as compared to a positive voltage (which is more suitable for the production of, *e.g.*, S_2, from a discharge in H_2S[30]). A 0.5 mm diameter tungsten filament was placed adjacent to the discharge ring and a current of around 1.5 A was passed through it. This glowing filament emitted electrons that helped to initiate and stabilize the discharge. This electrode had to be cleaned after a period of a few weeks to restore the discharge efficiency.

The discharge measurably depletes the population of ground state O_2 in the beam showing a 2 to 5-fold decrease in the O_2 (v=0,low J) signal when the discharge is 'on'. The degree of depletion increases with the applied voltage difference (negative). Products are $O(^3P_2)$ atoms and vibrationally and electronically excited but rotationally cold O_2 molecules. A scan of the two-photon resonance enhanced multiphoton ionization (REMPI)of the $3d4s\,^3\Sigma_{1g}^-$ Rydberg state at 225.0 nm[11]shows that the remaining ground state O_2 molecules in the beam are rotationally quite cold (T_{rot}~30 K) with the discharge on. In this work, photodissociation of a mixture of low rotational states, primarily N=1,3, and 5, of ground and electronically excited $O_2$is reported. Compared to rotational states, vibrationally excited states state do not relax effectively in the supersonic beam[27, 28]. We note that previous studies of pulsed discharge beams of OH[28], SO[32] and NO[27] found vibrational populations for the ground electronic state that can be roughly described by temperatures of 2000, 1000 and 6500 K, respectively.

The pulsed discharge beam was passed through a 2 mm diameter skimmer, forming a collimated molecular beam that was directed along the axis of a time of flight(TOF) spectrometer. Further downstream from the skimmer in the collision-free zone, the molecular beam passed through a 2mm hole in the repeller plate of the velocity mapping ion optics assembly and crossed at right angles the laser beam.

Radiation in the 215-240 nm range (1-4 mJ/pulse) was generated by a frequency-doubled dye laser pumped by the third harmonic of a Nd:YAG laser. Radiation below 215 nm was generated using a frequency doubled pulsed Nd:YAG laser (Spectra-Physics DCR-3A) operating at a repetition rate of 10 Hz to pump a dye laser (NarrowScan) which was operated at various wavelengths by using different dyes including Coumarine 47 and

a mixture of Sulforhodamine B and DCM dyes in order to cover a wavelength range of 600 to 625nm.Subsequently, frequency doubling was achieved by an angle-tuned KDP/BBO (beta-barium borate) crystal yielding ~4mJ/pulse in the 300-312nm range. A wave plate(ALPHALAS GmbH) and a BBO crystal following the KDP crystal were used to triple the frequency of the dye laser which produced a power of 0.7-0.8 mJ/pulse and ~0.6 cm^{-1} line width in the 200 to 208nm range. The polarization was further purified using a Brewster angle polarizer and is usually fixed with the electric field $\vec{E}$ of the linearly polarized laser beam set parallel to the face of the imaging detector (labeled here as V polarization). The laser beam was then focused into the interaction region between the repeller and extractor by means of a 15 cm focal length spherical lens. In the two color experiments, one Nd:YAG pumped dye laser was used for dissociation in the 203-240 nm wavelength region and a second Nd:YAG pumped dye laser was used to probe the O($^3P_{j=0,1,2}$) fragments. The pump and probe laser beams were separated in time by ~20 ns and carefully overlapped spatially.

O($^3P_{j=0,1,2}$) atoms were detected via (2+1) REMPI) via the $3p\ ^3P$state at 226.233, 226.060, and 225.654 nm, respectively. O(^1D) photofragments were also detected by (2+1) REMPI via the $^1F \leftarrow {}^1D$ and $^1P \leftarrow {}^1D$ transitions at 203.815 nm and 205.473 nm, respectively. During image acquisition, the probe laser wavelength was scanned over the Doppler profile of the REMPI transitions in order to ensure equal detection sensitivity of all product velocities. Atomic oxygen ions formed by state-selective REMPI are velocity mapped onto an imaging detector containing of a pair of 40mm Chevron microchannel plates (MCPs) coupled with a P47 phosphor screen. Mass selection is achieved by gating the voltage on the front MCP at the arrival time of the mass of interest. The image on the phosphor screen was captured by a charge coupled device (CCD) camera mounted behind the phosphor screen. Ion images appearing on the phosphor screen at each laser shot were subsequently sent to a PC for signal processing (thresholding, event counting and accumulation). Crushed images were averaged over typically 20,000 laser shots which were then inverted using the BASEX[33] inversion algorithm incorporated in the acquisition software (Davis, Lavision). The speed and angular distributions are extracted from customized routines running under Davis.

In some of the experiments a slicing technique was employed using delayed extraction described by Chestakov *et al*[34]. Photodissociation and ionization take place in field-free conditions, and pulsed voltages are applied to the repeller and extractor electrodes ~1 μs after formation of the ions. The detector is gated by a high voltage pulse supply with short period of time (~ 25 ns) in order to detect the middle slice of the Newton

sphere. Slicing selects a cut through the Newton sphere of dissociating molecules. Slicing was found to yield slightly better resolution than crushing.

3.3 Results

3.3.1. Images and Calibration

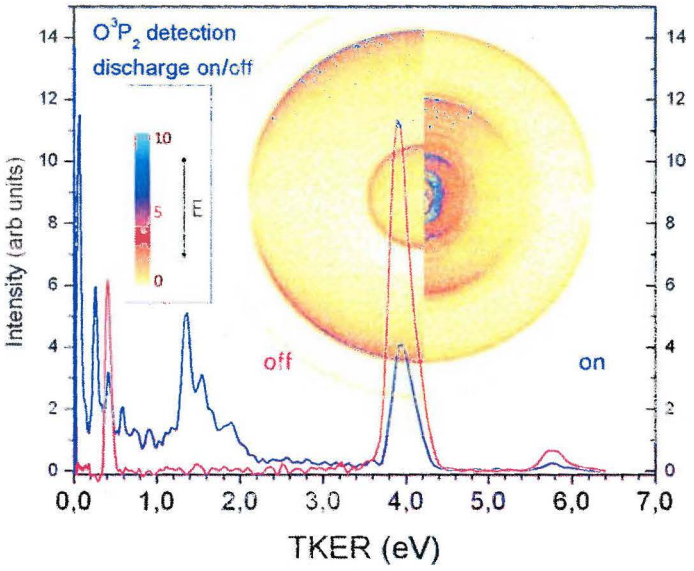

Figure 3.3: Raw O($^3P_2$) images with discharge 'off' (left side) and 'on' (right side). In the inset a color bar code for intensity is shown along with the direction of the linearly polarized laser $\vec{E}$ field, which lies parallel to the detector face (V polarization). Superimposed on the images are the corresponding kinetic energy distributions. The peak at zero total kinetic energy release (TKER) corresponding to cold O($^3P_2$) atoms is undercounted by the event centroiding software used to average the image.

A typical velocity mapped image of O($^3P_2$) atoms formed by photodissociation of a beam of 10% O_2/Ar with the discharge 'off' and 'on' is shown in Figure 3. Also shown in Fig. 3 is the total kinetic energy release (TKER) curve obtained by integrating the Basex-inverted image I(θ,r) over the angular distribution to obtain I(r) with r the image radius (velocity), weighting I(r) by the integration factor $1/r$, and plotting I(r)/r versus r^2. With the discharge off, three peaks with well-known total kinetic energy release (TKER) are observed[11] which are used to calibrate the TKER curves. Because the fragments have equal mass, the oxygen atoms each acquire half of the release energy, i.e. KER = TKER/2. The

calibration signals correspond to the one-photon process $O_2 + 1h\nu \rightarrow O(^3P_2) + O(^3P_j)$, and the two-photon processes $O_2 + 2h\nu \rightarrow O(^3P_2) + O(^1D_2)$ and $O_2 + 2h\nu \rightarrow O(^3P_2) + O(^3P_j)$. At the $O(^3P_2)$ detection wavelength (225.654 nm, 5.4944 eV), the dissociation channels are observed at 0.377 eV TKER for the one-photon process and at 3.905 eV TKER and 5.871 eV TKER for the two-photon processes. The two-photon channels become dominant at laser pulse energies higher than 2 mJ. In the present study the pulse energy is below 1 mJ/pulse and the two-photon channels are weak, but still useful for initial calibration of the kinetic energy release (KER) of the product O(^{3}P) atoms. An additional calibration was provided by a two-color study with photodissociation of the discharge beam of O_2 using a F_2 laser, which yields a strong $O(^3P_2,^1D)$ probe laser signal at 0.78 eV TKER[6].

In Figure 4 discharge images using a single laser for dissociation and detection of $O(^3P_j$, j=2, 1, and 0) are compared; the corresponding TKER curves are shown in Figure 5. In Figures 6 and 7 two-color pump-probe images and TKER curves for the discharge beam are shown for $O(^3P_2)$ probe of 217 nm and 239 nm dissociation (pump), respectively.

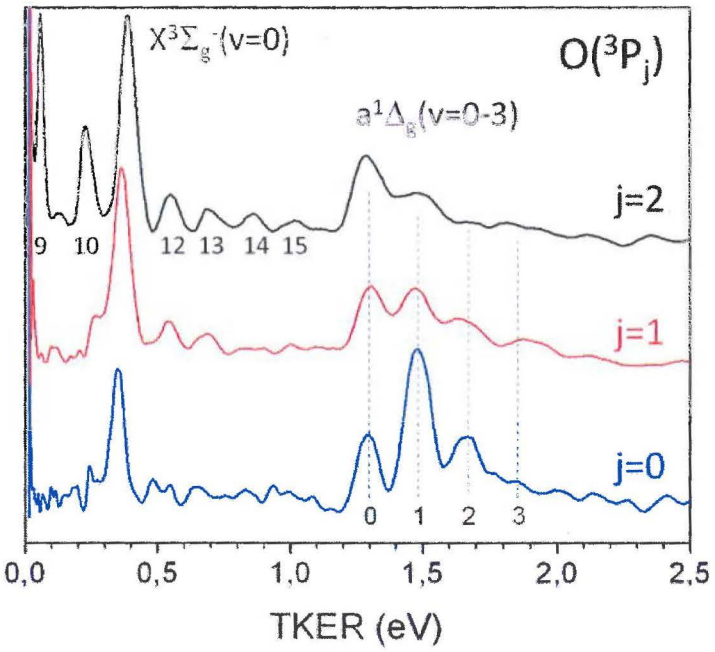

Figure 3.4: Raw $O(^3P_j$, j=2,1,0) images 226.233, 226.060, and 225.654 nm using milder discharge conditions (less depletion) than those of Fig. 3. See the caption of Fig. 3 for other details.

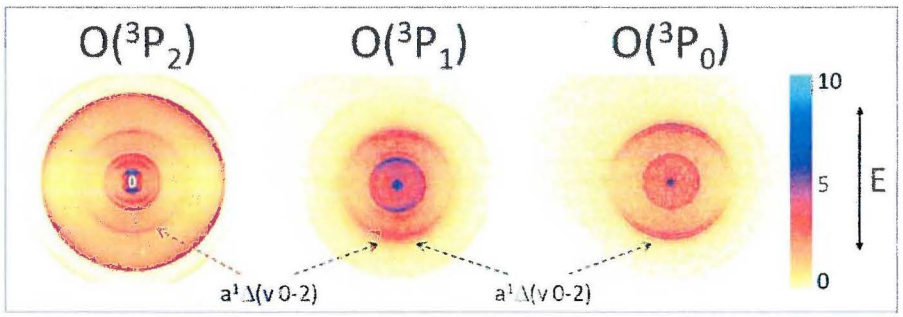

Figure 3.5: TKER curves extracted from the three $O(^3P_j)$ j= 2,1,0 images shown in Figure 4. Positions of the signals for photodissociation of $X^3\Sigma_g^-(v=9\text{-}15)$ in the 0-1 eV range and $X^3\Sigma_g^-(v=0)$ at 0.377 eV are indicated along with the $a(^1\Delta_g)(v=0\text{-}3)$ peaks.

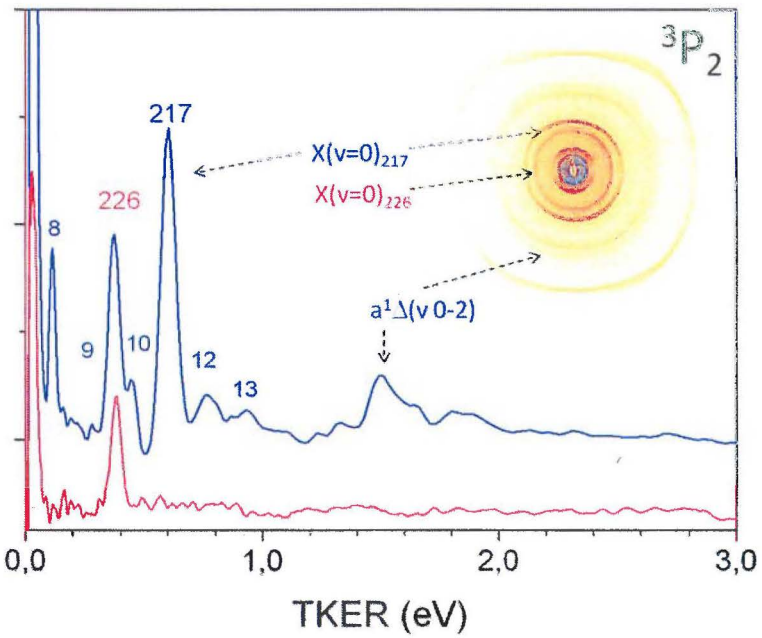

Figure 3.6: Sliced image using two color dissociation of O_2 at 217nm with detection of $O(^3P_2)$ at 226 nm. The polarization of the detection laser is set to H (perpendicular to the detector plane) in order to decrease the amount of detection laser signal. Note that in the signal from only the H polarized detection laser (lower trace) the $X^3\Sigma_g^-(v=0)$ peak, labeled 226 in the TKER curve and the image, is still present compared to the other peaks seen in the J=2 curve of Fig. 5, taken with V polarization. The highest velocity

ring becomes too large for the ion lens with slicing, and is slightly distorted. Discharge conditions are similar to those used in Figure 4.

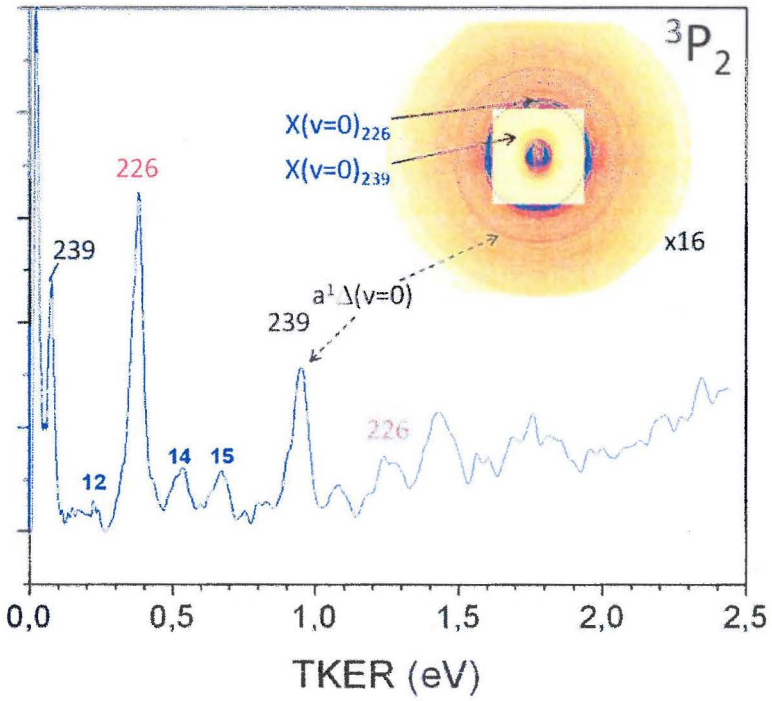

Figure 3.7: Same conditions as Figure 6, with dissociation at 239 nm. The middle part of the image is presented at 16x less gain to show the relative strength of the cold atom signal.

Two-color studies are particularly challenging because a probe laser signal (Fig.3) will appear alongside signal from the pump laser, resulting in many overlapped rings. Since the probe laser must be sufficiently intense to drive the 2+1 REMPI O atom detection process, we rotate the polarization of the probe laser to lie perpendicular to the detector (labeled here H polarization) and employ the time-delay slicing method[34] to obtain Figs. 6 and 7. The lower trace, labeled 226, in Fig. 6 is the probe laser only signal with H polarization, where essentially only the $X^3\Sigma_g^-$ (v=0) peak at 0.377 eV from Equ. 1 is observed above background. Slicing detects only the central part of the Newton sphere of product ions as they

arrive at the detector. Using H polarization, the central part of a β=2 sphere does not contain fragments in a sliced image. It is noted that using slicing a β=-1 sphere will appear similar to a β=2 sphere rotated by 90°, and a β=0 sphere will yield the same isotropic ring in both H and V polarizations. We find that the $X^3\Sigma_g^-$ (v=0) peak is much less reduced in intensity than the other peaks using V polarization (Fig. 3)implies that the other peaks have beta values larger than β=0.6, known[4] for $O(^3P_2)$ detection following photodissociation of $O_2X^3\Sigma_g^-$ (v=0) at 226nm. Data for the column VH β* in Table 1 is taken at the $a^1\Delta_g$(v=0) peak but contains a significant contribution by the H-polarized detection laser.Because the VH β* data is roughly constant over the range of dissociation wavelengths and the background from the detection laser is also constant, it appears that the β value for $a^1\Delta_g$(v=0) itself does not change greatly over the same range.

Under favorable conditions where accidental overlap of the pump and probe laser signals in the TKER distribution is minimal we managed to obtain sliced two-color images using VV polarization, which resulting in a β value at 230 nm dissociation in Table 1. β values for the peaks seen in the 1.0-2.0 eV TKER region of Fig. 3, which we ascribe to photodissociation of $a^1\Delta_g$ state O_2 based on the TKER values are listed in Table 1.

Table 3.1: Angular anisotropy β parameters observed by detection of $O(^3P_j)$ atoms from the photodissociation of O_2 $a(^1\Delta_g)$ (v=0-2) at the listed dissociation wavelengths. Uncertainties are estimated from a combination of repeated measurements and the quality of fit to the β equation. With V polarization the electric field of the linearly polarized dissociation laser is parallel to the plane of the imaging detector; H polarization is perpendicular to the detector plane.

Dissociation Wavelength (nm)	atom	VH β*	VV β a(v=0)	β a(v=1)	β a(v=2)
239	$O(^3P_2)$	0.4±0.2			
230	$O(^3P_2)$	0.5±0.2	1.3±0.2		
228	$O(^3P_2)$	0.35±0.2			
225.65	$O(^3P_2)$		1.7±0.2	1.3±0.2	0.4±0.2
226.06	$O(^3P_1)$		1.3±0.4	1.3±0.4	1.1±0.4
226.23	$O(^3P_0)$		1.5±0.6	1.5±0.6	1.0±0.6

Dissociation Wavelength (nm)	atom	VH β*	VV β a(v=0)	β a(v=1)	β a(v=2)
223	$O(^3P_2)$	0.6±0.2			
223	$O(^3P_1)$	0.6±0.2			
217	$O(^3P_2)$	0.6±0.2			
205	$O(^3P_2)$	0.2±0.4			
* combined a(v=0) signal and background produced by the detection laser with H polarization					

3.3.2 Parent beam depletion and cold $O(^3P_j)$ atom production

With the discharge turned on, the three peaks in Fig. 3 corresponding to the parent molecules $X^3\Sigma_g^-$ (v=0) (the only peaks observed with the discharge off) decrease by a factor of ~2.5, while a very intense signal appears at the middle of the detector corresponding to zero velocity $O(^3P_2)$ atoms, and new rings appear in the middle part of the image. Images of the zero velocity or 'cold atom' signal are distorted due to space charge and undercounted in intensity due to saturation of the detector and to overlap of events in the event counting software. Setting the electrostatic lens away from velocity mapping to spread the signal over the detector in order to avoid saturation we can compare the integrated area of the peaks in the 1-2 eV TKER region of Fig. 3 (which we later ascribe to photodissociation of $O_2 a^1\Delta_g$-state) to the area of the cold O^3P atom signals. For both a mild discharge with 30% depletion of the $O_2X^3\Sigma_g^-$ (v=0) signal (Figs. 4-7) and a more intense discharge with 70% depletion (Fig. 3) the cold atom signal is roughly 100 times stronger than the signals attributed to photodissociation of the O_2 $a^1\Delta_g$ state. While $O(^3P)$ is detected directly, in order to detect $O_2a^1\Delta_g$ it must first be converted to $O(^3P)$ by photodissociation. A conversion efficiency of 1% would then indicate equal amounts of O_2 $a^1\Delta_g$ and cold $O(^3P)$ atoms. The cold atom signal is substantially smaller for $O(^3P_1)$ than for $O(^3P_2)$, and the $O(^3P_0)$ cold atom signal is much smaller than that for $O(^3P_1)$, showing little distortion or evidence for undercounting. We conclude that the supersonic expansion cools the fine-structure distribution of the $O(^3P_j)$ atoms down to the $O(^3P_2)$ state. Nearly no cold $O(^1D)$ is found.

Formation and photodissociation of ozone or larger $O_{n>2}$ molecules possibly formed in the discharge is expected to yield fragments with kinetic energy release. The absence of signal from higher masses than O_2^+

with non-zero TKER values suggests that formation and photodissociation of ozone or larger molecules is unimportant.

3.3.3 Photodissociation of discharge-excited O_2

Assignment of the higher velocity signals arising from the discharge requires first a consideration of the energy resolution of the apparatus, which in the present case is limited by space charge effects due to the cold $O(^3P_j)$ atoms, and electron recoil in the 2+1 REMPI detection process[28]. Extensive experience with O_2 dissociation and ionization processes allows us to estimate a practical resolution of 0.02 eV for peaks with TKER < 2eV. This is insufficient for rotational resolution but a factor of ten better than the vibrational energy spacing of $O_2X^3\Sigma_g^-$ (v) (Fig. 1). Shown in the inset of Fig. 1 are the energy positions of nearly iso-energetic vibrational levels of the $X^3\Sigma_g^-, a^1\Delta_g, b\ ^1\Sigma_g^+$ states[18]. For example, $b\ ^1\Sigma_g^+$(v=0) and $X^3\Sigma_g^-$ (v=9) are not distinguishable by their TKER if both states dissociate to the same final limit. The $a^1\Delta_g$(v=0) and $X^3\Sigma_g^-$ (v=5) levels are quite close, especially taken into account the differences in the internal energies of the $O(^3P_{1,0})$ fragments. Formation of $O(^3P_1)$ or $O(^3P_0)$ lowers the TKER by 0.0196 and 0.0281 eV, respectively, compared to formation of $O(^3P_2)$. An additional complication is that a higher energy initial state that dissociates to the second dissociation limit $D_1[O(^3P_2)+O(^1D)]$ can overlap signal from an initial state lying 1.967 eV lower in energy which dissociates to D_0, where 1.967 eV is the $O(^3P_2)$-$O(^1D)$ energy spacing. The $X^3\Sigma_g^-$ (v=11) state dissociating to D_1 and $X^3\Sigma_g^-$ (v=0) dissociating to $D_0[O(^3P_2)+O(^3P_2)]$ yield $O(^3P_2)$ atoms with essentially the same TKER.

Consider the following possible pathways 1-5 for photodissociation of vibrationally or electronically excited O_2 at 225.65 nm (5.4944 eV) with $O(^3P_2)+O(^3P_2)$ or $O(^3P_2)+O(^1D)$ as products for D_0 and D_1 respectively

1. $X\ ^3\Sigma_g^-(v<9)+h\nu$ (Herzberg continuum), diss. to D_0 limit (v=0 TKER: 0.377 eV)
2. $X\ ^3\Sigma_g^-(v=5)+h\nu \rightarrow B\ ^3\Sigma_u^-(v=4)$ (SR band), prediss. to D_0 limit (TKER:1.313 eV)
3. $X\ ^3\Sigma_g^-(v>8)+h\nu \rightarrow B\ ^3\Sigma_u^-$ (SR continuum), diss. to D_1 limit (v=11TKER: 0.378eV)
4. $b\ ^1\Sigma_g^+(v=0)+h\nu \rightarrow B\ ^3\Sigma_u^-$ (Parker continuum), diss. to D_1 limit (TKER: 0.0370eV)
5. $a\ ^1\Delta_g(v=0,1,2)+h\nu \rightarrow A'\ ^3\Delta_u$ (Chamberlain continuum), diss. to D_0 limit (v=0 TKER: 1.327 eV)

Pathway 1) **One-photon dissociation of the $X\ ^3\Sigma_g^-$ state O_2via the Herzberg continuum**: Below $X\ ^3\Sigma_g^-$ (v=9) one-photon dissociation

between 242 and 200 nm produces O (^3P) atoms exclusively. Photodissociation of $X\ ^3\Sigma_g^-$(v=0) in the Herzberg continuum between 242 and 200 nm has a well-known[4] signature in the velocity map image of the O(^3P)product atoms. The angular distribution parameter beta is positive, ranging from β= 0.8 at 205 nm to 0.4 at 240 nm. At 226 nm the branching ratio fraction for O(^{3}P$_j$) j= 2:1:0 formation was found[4] to be 0.68 : 0.25 : 0.07. The optical signature is mixed in character due to the complex pattern of spin-orbit coupling giving strength to the $X\ ^3\Sigma_g^- \rightarrow A\ ^3\Sigma_u^+, A'\ ^3\Delta_u, c\ ^1\Delta_u$ transitions. The TKER and β values for photodissociation of $X^3\Sigma_g^-$ (v=0) observed in the images shown in Figs 3 and 4 at 226 nm and Figs 6 and 7 for 217 and 239 nm, respectively, match the expected values quantitatively with the discharge off. With the discharge on, the TKER values are in agreement but the β value is not reliable due to contributions from underlying signals.

Pathway2) **Predissociation of bound levels of the $B^3\Sigma_u^-$state** should also be considered, where these $B^3\Sigma_u^-(v')$ levels could be populated by accidental resonance of the wavelength of the dissociation laser with highly structured $B^3\Sigma_u^-(v')\leftarrow X\ ^3\Sigma_g^-(v'')$ bound-bound transitions. Predissociate produces two O (^3P) atoms. The $B^3\Sigma_u^-(v'=4)\leftarrow X(v''=5)P_{15}R_{13}$ transition is, for example, nearly resonant with 225.654 nm (vacuum) light, as seen in the spectrum from Leahy et al [35]. The $P_{15}R_{13}$ transition has been studied by direct excitation from the ground state, i.e., $B^3\Sigma_u^-(v'=4)\leftarrow X\ ^3\Sigma_g^-$ (v=0) using a tunable ArF excimer laser followed by imaging detection of O ($^3P_2$) atoms[7]. The $9' \leftarrow 7''$ and $12' \leftarrow 8''$ transitions are also close to resonance with 225.654 nm. It was found in our previous study[7], however, that exact resonance was necessary, i.e., mistuning by a few cm^{-1} led to no resonant signal.

Pathway 3) **Photodissociation via the Schumann-Runge (SR) continuum:** Vibrational states $X\ ^3\Sigma_g^-$(v>8) when excited by a 5.4994 eV photon have enough energy to reach the optically allowed Schumann-Runge (SR) continuum, Fig. 2, which has an optical signature of $\beta = 2$. The $B\ ^3\Sigma_u^-$ states correlates adiabatically with D$_1$, the second dissociation channel [O(^{1}D)+O(^{3}P$_j$)] where j=2 is the major component. Gordon and coworkers[36] found the ratio O(^{3}P$_j$) j= 2:1:0 as 0.90 : 0.08 : 0.02, which was confirmed in our subsequent studies [3,6]. In the images shown in Figs 3, 4, 6, and 7 for O(^{3}P$_2$) detection a clear set of rings in the TKER region of 0-2 eV matching the energy spacing expected for photodissociation of $X\ ^3\Sigma_g^-$ (v>8) is observed. Vibrational quantum numbers of the peaks observed using O(^{3}P$_2$) detection are labeled in Fig. 5.

These $X^3\Sigma_g^-$ (v>8) signals from the discharge have been described briefly in a previous publication[6] and interesting trends in their beta parameter will be presented in a subsequent publication. With single laser

photodissociation and O(^{1}D) detection at 203.815 nm and 205.473 nm only the $X^3\Sigma_g^-$ (v>6) signals are observed, no peaks corresponding to photodissociation of $a^1\Delta_g$ or $b\ ^1\Sigma_g^+$ states could be identified.

We point out the apparently strong intensity of these $X^3\Sigma_g^-$ (v>0) peaks is due to the very large cross section of the SR continuum (Fig. 2). If we assume a vibrational temperature for the discharge of 2000K (as found for OH formed in a water discharge under similar conditions[28]) the signal for photodissociation of $X^3\Sigma_g^-$(v=12) (TKER 0.54 eV) arises from molecules with a fractional population of only ~3×10^{-6}. Saxon and Slanger[37] have calculated the $B\ ^3\Sigma_u^- \leftarrow X^3\Sigma_g^-$ dissociation cross section for $X^3\Sigma_g^-$ (v=12) at 226 nm as ~5×10^{-19} cm^2 for the SR continuum (leading to O(^{3}P)+O(^{1}D) products). The dissociation cross section for the $A\ ^3\Sigma_u^+ \leftarrow X^3\Sigma_g^-$(v=0) of the Herzberg I continuum at 226 nm is 3×10^{-24}cm^2 (Fig. 2). It is thus not surprising that pathway 1 for $X^3\Sigma_g^-$(v=0) and pathway 3 for $X^3\Sigma_g^-$ (v=12) yield comparable signals, even though the population of the highly vibrationally excited $X^3\Sigma_g^-$(v>0) states is quite small. Because saturation of the $X^3\Sigma_g^-$ (v=12) dissociation step is likely at our laser flux, a more quantitative analysis of the $X\ ^3\Sigma_g^-$(v>0) population is not possible.

As for the lowest vibrationally excited levels $X^3\Sigma_g^-$(v = 1, 2) no significant signal is found for two-photon dissociation of $X^3\Sigma_g^-$ (v = 1, 2) in the discharge 'on' image. Apparently, the population of discharge-produced $X^3\Sigma_g^-$(v = 1, 2) is small for the lowest v levels. A similar conclusion was drawn for discharges of NO molecules[27]. We conclude that the total population of $X\ ^3\Sigma_g^-$(v>0) is a minor (<2%) fraction of excitation products due to the discharge.

Pathway 4) **Photodissociation of the $b\ ^1\Sigma_g^+$-state** at 226 nm takes place through the B -state continuum, producing near the threshold for photodissociation exclusively O(^{3}P$_2$)+O(^{1}D) products with $\beta = 2$. The TKER is quite small (0.037 eV), and if signal exists it will be obscured by the strong signal at the center of the O(^{3}P$_2$) image arising from cold atoms produced in the discharge. We note that the $b\ ^1\Sigma_g^+$(v=0) and $X^3\Sigma_g^-$(v=9) levels are essentially iso-energetic. The $X^3\Sigma_g^-$ (v=9) signal strength changes considerably at different dissociation wavelengths due to oscillation in their Franck-Condon factors (FCF)[37]. We observe such a behavior; consider peak labeled 9 in Figs 4 and 6. Peak 9 is strong at 226 nm, weaker at 223 nm (not shown) and at 217nm it is very weak, presumably due to a small FCF. The near disappearance of signal at the position of peak 9 means that there is no significant amount of $b\ ^1\Sigma_g^+(v = 0)$ in the discharge beam.

The above shows that the peaks in the TKER curves can be unambiguously interpreted. Below we come to the core of the results on singlet oxygen.

3.3.4 *Photodissociation of* O_2 $a\,^1\Delta_g(v = 0,1,2)$

The relatively strong signals in the 1-2 eV TKER distribution in Fig. 4 are assigned by their peak positions as photodissociation of the $a^1\Delta_g$-state of O_2: $a\,^1\Delta_g(v = 0,1,2) + h\nu \rightarrow A'\,^3\Delta_u, A^3\Sigma_u^+$ via the Chamberlain continua to limit D_0. At the shorter wavelengths studied, 200-205 nm, the D_1 limit is accessible for photodissociation of $a^1\Delta_g$ (v=0) but no signal for this channel is observed; although a weak signal could be obscured by other signals. Also, photodissociation at 157 nm, does not yield signal attributable to $a^1\Delta_g$-state dissociationto D_0nor D_1. However, a small $O(^1D)$ signal due to photodissociation of $X^3\Sigma_g^-$ (v=5) in the discharge by two 157nm photons was seen, which indicates the experiment is reasonably sensitive to weakly populated excited states. These observations suggest that D_0 is the primary dissociation limit for $a^1\Delta_g$-state photodissociation in the UV-VUV region.

In this section we present data concerning the vibrational state dependence for $a^1\Delta_g$ -state photodissociation, the relative branching between O^3P_jproducts, the wavelength dependence of the $a^1\Delta_g$ -state signal, and the angular anisotropy (β) for the $a^1\Delta_g$-state photodissociation process.

1. **The vibrational state dependence for photodissociation of $a^1\Delta_g(v)$** seen in the TKER curves of Fig. 5, which is quite reproducible and the same for both discharge conditions, shows an interesting variation in peak heights at the different O^3P_j detection wavelengths for the signals from photodissociation of $a^1\Delta_g$(v=0,1, and 2). The relative branching into the three O^3P_j product channels is anomalous, particularly for $O(^3P_0)$ detection the $a^1\Delta_g$ (v = 1) signal is a factor of 2-3 stronger than that seen in the curve for $O(^3P_2)$ detection. While the $a^1\Delta_g$ (v)-state dependent photodissociation cross sections at 217 and 239 nm shown in Figs 6 and 7 reflects a strong variation in FCF, the relative vibrational signal strengths at 226 nm should not reflect changes in FCFs with these very similar dissociation wavelengths of 226.233, 226.060, and 225.654 nm. It seems also unlikely that the vibrational state has an effect on the relative cross sections to the three Herzberg states. A different $O(^3P_j)$-state branching ratio for each vibrational level is also unlikely. As stated earlier, the same pattern is seen for both 30% and 70% depletion conditions, which makes overlap with

signal from $X^3\Sigma_g^-$ (v>0) is not likely. Finally, the beta signature of any other overlapping process must also be quite positive since the trends in beta for $a^1\Delta_g$(v=0-2) photodissociation listed in Table 1 are similar. Although we have no explanation for the irregularity in O(^{3}P$_j$) signal from the different $a^1\Delta_g$(v) states, the present evidence suggests that the variation is due to differences in the $a^1\Delta_g$(v) dynamics.

2. **The j-state branching** between the O(^{3}P$_j$) products in the beam can be roughly estimated from the one-color O(^{3}P$_j$) images obtained at 226 nm, shown in Fig. 3, where the laser intensity and the number of laser shots averaged are the same. $X^3\Sigma_g^-$ (v=0) and $a^1\Delta_g$(v=0-2) are probed by the same process and the branching ratios for O(^{3}P$_j$) at the probe wavelengths are known for $X^3\Sigma_g^-$ (v=0) photodissociation[4]. By scaling each TKER distribution at the $X^3\Sigma_g^-$ (v=0) signal to the known j branching ratio and comparing the integrated $a^1\Delta_g$(v=0-2) peaks (in light of the preceding discussion), the data set yields a ratio of 55:35:10 for the $a^1\Delta_g$-state j=2:1:0 yield. An independent estimate of the $a^1\Delta_g$-state j=2:1:0 yield was obtained from a two-color experiment where signal at 0.78 eV TKER is created by 157nm dissociation of $X^3\Sigma_g^-$ (v=0) and probed by the REMPI detection laser, and the $a^1\Delta_g$ state signal is both created and probed by the REMPI laser. By scaling each TKER distribution at the 157nm signal to known branching ratios [6,34] a relative yield for j=2:1:0 of 58:36:6 was obtained. Each approach has challenges; the $X^3\Sigma_g^-$ (v=0) signal must be corrected for overlap by $X^3\Sigma_g^-$ (v=11) in the former method, while the second method requires the same spatial overlap of two laser beams for the three different measurements. Averaging results of the two approaches, we estimate the branching ratio for the v-state averaged $a^1\Delta_g$(v=0-2) state signal as 56 : 36 : 8, with at least 5% uncertainty for each value.The behaviour is similar to that of $X^3\Sigma_g^-$ (v=0) state, although the vibrationally resolved $a^1\Delta_g$ (v) data suggest significant deviations for each vibrational level. Note that the apparent overpopulation of the v=1 signal in the j=0 channel seen in Fig. 5 has only a small effect on the branching ratio due to the low yield of j=0.

3. The **wavelength dependence of the $a^1\Delta_g$(v=0) signal** can be qualitatively determined by comparing the $X^3\Sigma_g^-$ (v=0) and $a^1\Delta_g$(v=0) signals in Figs 4-7, where the same (mild) discharge conditions were used. For the photodissociation wavelength steps from 217 to 226 to 239 nm, the relative amount of $a^1\Delta_g$(v=0) signal compared to $X^3\Sigma_g^-$ (v=0) signal is increasing towards longer

wavelengths. This trend is also seen in data not presented here; at 200 nm there is no discernible $a^1\Delta_g$-state signal and a very weak signal at 205 nm. Figure 2 shows that the $a^1\Delta_g$(v=0) cross section also increases in the same wavelength range while the $X^3\Sigma_g^-$ (v=0) cross section decreases. This data suggests that the Chamberlain continuum shown in Fig. 2 is indeed relevant, *i.e.*, a continuum is being probed that peaks towards wavelengths longer than 239 nm. The data is not consistent with a continuum peaking in the deep UV-VUV region such as $1^3\Pi_u \leftarrow a^1\Delta_g$ or $B^3\Sigma_u^- \leftarrow a^1\Delta_g$ as discussed later in the text.

4. Data for the **angular anisotropy (β) for $a^1\Delta_g$ -state photodissociation** is presented in Table 1. The beta values obtained using the VH geometry do no relate to the $a^1\Delta_g$only but contain also other contributions. The effective beta values are roughly constantover the studied wavelength region, implicating that also the beta value for the $a^1\Delta_g$statewill be roughly constant. In our studies[9,10] of the photodissociation of van der Waals clusters containing O_2 we observed indirectly O_2 $a^1\Delta_g$ -state photodissociation with an angular anisotropy value of β=0.8, which is consistent with the values shown in Table 1. In principle, the beta values measured for $O(^3P_2)$ and $O(^3P_1)$ can be affected by atom alignment[38]. $O(^3P_0)$ can show no alignment, however, the beta values measured for j=0,1, and 2 are similar, suggesting that alignment effects, if present, are small. The preceding discussion about slicing with H polarization also supports a positive beta value, larger than β=0.6. At 226 nm an average over the $O(^3P_j)$ levels weighted by the j-level branching factor yields β=1.3±0.4 for $a^1\Delta_g$(v=0-2)and β=1.55±0.4 for $a^1\Delta_g$(v=0) only.

3.4 Discussion

In the results section it was shown that the discharge beam contains a large signal for $O(^3P_2)$ atoms, a trace but easily detectable amount of highly excited vibrational levels of ground state $X^3\Sigma_g^-$ O_2, a significant signal for the $a^1\Delta_g$ state compared to ground $X^3\Sigma_g^-$ (v=0) signal and no detectable O_2 $b\ ^1\Sigma_g^+$ state. Over the decreasing wavelength range 240-200 nm the $a^1\Delta_g$ -state signal relative to the $X^3\Sigma_g^-$ (v=0) signal decreases strongly, at 226 nm the $a^1\Delta_g$ (v=0-2) states averaged branching ratio percentage for $O(^3P_j$ j=2:1:0) is found to be 56 : 36 : 8 (±5%), and for 226 nm dissociation wavelength range the $a^1\Delta_g$ (v=0-2) states the j-state averaged β=1.3±0.4 and β=1.55±0.4 for $a^1\Delta_g$(v=0) only.

On energetic grounds, population of the $b\ ^1\Sigma_g^+$-state (v=0 at 1.63 eV) may be expected, especially since $X\ ^3\Sigma_g^-(v > 0)$ levels as high as v=16, which has 2.76 eV internal energy, are observed (Fig. 4). Studies by Setzer et al.[39]of fast flow discharges containing singlet O_2, however, indicate that while the $a^1\Delta_g$ -state of O_2 is not rapidly quenched by collisions, deactivation of the $b\ ^1\Sigma_g^+$-state is efficient. In support of collisional $b\ ^1\Sigma_g^+$-state deactivation we note that the introduction of extra water (which is usually already present in low amounts in gas handling systems) is found to increase the $a^1\Delta_g$-state population in the discharge. Adding excess water to the discharge was not found to be advantageous in this study because this also leads to OH production with additional O(^{3}P) photofragment signals from OH photodissociation[28]; these OH photodissociation signals overlap primarily the $X\ ^3\Sigma_g^-$(v>0) state signals.

3.4.1 Simple model to estimate σ_a/σ_X at 226 nm from measured signals.

Inspection of the data set of Fig. 3 with 70% depletion shows that comparing the relative intensity of the signal arising from the $a^1\Delta_g$(v=0) state, defined as S_{av0}^{on}, seen only with the discharge on, to the relative intensity of the signal S_{Xv0}^{on} arising from the $X\ ^3\Sigma_g^-$(v=0) state with the discharge on, yields the ratio of signals ($S_{av0}^{on}/S_{Xv0}^{on}$) ~4, and for the data set shown in Figs. 4,5 with 30% depletion ($S_{av0}^{on}/S_{Xv0}^{on}$)=1.3. We note that both channels are probed through the same 2+1 oxygen atom ionization process. Hence, the signal strengths reflect the product of the relative photodissociation cross sections and the relative populations. Upon 30% depletion of the ground state, this fraction is distributed over oxygen atoms (the cold signal in the centre) and $a^1\Delta_g$(v=0-2) state population. It is very difficult to assess the branching between these two channels as this implies knowledge of the $a^1\Delta_g$-state photodissociation cross section. However, it is noted that already with 30% depletion - implying that maximally the a-state population to X-state population is 1:2 - the signal strength of the $a^1\Delta_g$state is larger than that of the ground state by 30%. We conclude that the photodissociation cross section of the $a^1\Delta_g$state is at least 2.5 times as large. In the case of 70% depletion, if this 70% depletion ends up fully in the $a^1\Delta_g$ state, the conclusion is also that the photodissociation cross section is at least twice as large. From this simple observation, we conclude that the $a^1\Delta_g$ state photodissociation cross section is significantly larger than that of the ground state. We have ignored here the presence of the strong O(^{3}P) cold atom signal also created by the discharge, and point out that 70% (or even 30%) conversion of $O_2\ X^3\Sigma_g^-$ (v=0) to $O_2\ a^1\Delta_g$ is unlikely. From the above estimates,10% conversion (at 30% depletion), which is quite substantial,

would imply that the photodissociation cross section of the $a^1\Delta_g$ state is ~10 times larger than the prediction by theory.

From theory by Klotz and Peyerimhof[14]and Slanger and Saxon[15],the sum of the $A^3\Sigma_u^+$, $A'^3\Delta_u \leftarrow X^3\Sigma_g^-$ cross sections at 226 nm is ~4.6x10^{-24} cm^2 while the $A'^3\Delta_u$,$A^3\Sigma_u^+ \leftarrow a^1\Delta_g$ cross section sum is ~3.7x10^{-24} cm^2, yielding σ_a/σ_X = 0.8. A ten-fold increase in σ_a to 4x10^{-23}cm^2, for example, is still 20 times less than the upper limit of 8x10^{-22} cm^{2}determined in Ref. 13. Note that Saxon and Slanger[15]needed to rescale the *ab initio* theory down by a factor of 0.6 in order to match experimental measurements of σ_X. A theoretical revaluation of the total photodissociation cross section for the Chamberlain continuum, σ_a, is also necessary.

3.4.2 Adiabatic and sudden limits for O_2 photodissociation via Chamberlain continuum

As described in detail in Ref. 4, O_2 photodissociation dynamics can be described in two limiting cases, the sudden-recoil limit, and the adiabatic limit, corresponding to high and low fragment recoil velocity, respectively. In the sudden-recoil limit, the atomic multiplet distribution is often close to a statistical one, *i.e.* proportional to $2j+1$, the degeneracy of each j state, this yields for O(^{3}P$_j$ j=2:1:0) a 5:3:1 statistical population ratio. However, for an exact calculation of the fine-structure distribution in the sudden recoil limit, a frame transformation in which molecular eigen-states are expanded in atomic eigen functions is required[40]. The other extreme is fully adiabatic behavior. In this case the projection of the total angular momentum of the initial Born-Oppenheimer stateon the internuclear axis ,Ω, is conserved during dissociation. Dissociation at threshold is described by the adiabatic limit. An adiabatic correlation diagram[36]can be used to find the specific atomic fine-structure state that connects with the fine-structure level of the molecule. For both the Herzberg and Chamberlain continua, the adiabatic limit allows only O(^{3}P$_2$) production, while experimentally all three fine-structure states are observed. While our study of the Herzberg continuum[4] showed that the limiting case of sudden-recoil was also not reached, it was found useful in predicting the O(^{3}P$_2$) branching ratios and angular anisotropy parameters. In Ref. 4 a sudden limit analysis for the $A^3\Sigma_u^+$ state was presented. Because the $A'^3\Delta_u$ state is also important for the Chamberlain continuum, the results of a sudden limit treatment of theΩ=1,2, and 3levels of the $O_2A'^3\Delta_u$state described the Appendix are presented in Table 2. For the case of $A'^3\Delta_u$ Ω=3, is not possible to conserve Ω in the dissociation process, so this level cannot connect to O(^{3}P$_0$) in any combination of O(^{3}P$_0$) +O(^{3}P$_j$).

Table 3.2: Fine-structure branching ratios $P_\Omega(j)$ (Equ. A.5) for $O_2 A'^3\Delta_u$ in the sudden recoil limit

$A'^3\Delta_u\Omega \setminus O^3P_j$	j = 2	1	0
$\Omega = 1$	4/12	6/12	2/12
2	7/12	3/12	2/12
3	9/12	3/12	0

3.4.3 Comparison of Herzberg and Chamberlain continua

Branching ratios and beta values for photodissociation of O_2 via the Herzberg continuum $A^3\Sigma_u^+$, $A'^3\Delta_u, c^1\Sigma_u^+ \leftarrow X^3\Sigma_g^-$ and Chamberlain continuum, $A^3\Sigma_u^+, A'^3\Delta_u$, $c^1\Sigma_u^+, \leftarrow a^1\Delta_g$ at 226 nm are compared in Table 3 using the same format as Ref. 4.

Table 3.3: Beta values and $O(^3P_j)$ branching ratios for the Herzberg[4] and Chamberlain continua (this work) for photodissociation of $O_2 X^3\Sigma_g^-$ (v=0) and $O_2 a^1\Delta_g$(v=0) at 226 nm. Branching data is presented in the same format as Ref. 4.

$O(^3P_j)$	j=2	j=1	j=0
A,A',c←X			
β	0.64±0.08	0.53±0.09	0.37±0.24
branching	9.00±0.70	3.33±0.43	1.00±0.26
A',A',c←a			
β	1.7±0.3	1.3±0.4	1.5±0.6
branching	7.0±0.8	4.3±0.6	1.0±0.6

Inspection of the experimental values in Table 3 indicates a higher yield of $O(^3P_j)$ j=1,0 compared to $O(^3P_j)$ j=2 is produced by dissociation via the Chamberlain continuum compared to the Herzberg continuum. In the sudden limit analysis of the $A'^3\Delta_u$state (Table 2) an increased yield of $O(^3P_j)$ j=1,0 is predicted for pathways involving $\Omega = 2$ and 1. Assuming the $\Omega = 2$ pathway is most important (as discussed next), the branching ratios for the Chamberlain continuum are in closer agreement with the sudden limit model than those for the Herzberg continuum; this may reflect the additional 1 eV in total excess energy available for dissociation of the $a^1\Delta_g$-state compared to the $X^3\Sigma_g^-$-state for dissociation by the same photon energy (5.49 eV).

In terms of the β parameter, both the Herzberg and Chamberlain continua are forbidden transitions where spin-orbit coupling with optically allowed transitions is the main mechanism for acquiring transition strength. The allowed transition determines the parallel – perpendicular character of the transition while spin-orbit coupling between sub-states with the same initial and final Ω=Λ+Σvalues determines the weighting factor for each parallel or perpendicular pathway. For the Herzberg continua the dominant sources of transition strength are the Schumann-Runge $B^3\Sigma_u^- \leftarrow X^3\Sigma_g^-$ (parallel),and $A^3\Sigma_u^+ \leftarrow 1^3\Pi_g$ (perpendicular) transitions, where the overall positive beta character (Table 3) indicates that pathways involving the Schumann-Runge transition are strongest.

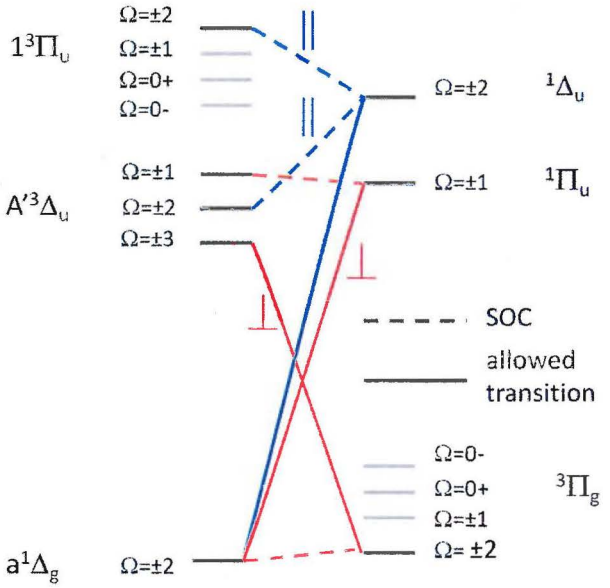

Figure 3.8: Pathways of acquiring transition strength for the $A'^3\Delta_u \leftarrow a^1\Delta_g$ transition from spin-orbit coupling (SOC) with allowed transitions, adapted from Klotz and Peyerimhof [14].

Pathways for gaining intensity for the forbidden $A'^3\Delta_u \leftarrow a^1\Delta_g$ Chamberlain continuum transition, adapted from Klotz and Peyerimhof[14], are shown in Figure 8. Since the $a^1\Delta_g$-state has only Ω=±2, its pathways are less numerous than those for the Herzberg continuum. For example, it is not possible to borrow intensity from the strong $B^3\Sigma_u^- \leftarrow X^3\Sigma_g^-$ parallel Schumann-Runge transition because the $X^3\Sigma_g^-$ state has no Ω=±2 values, these are needed for $a^1\Delta_g$ - $X^3\Sigma_g^-$ spin orbit coupling. Instead, parallel oscillator strength can be gained from the allowed $1^1\Delta_u \leftarrow a^1\Delta_g$ transition,

the $1^1\Delta_u$ state can spin-orbit couple with the $A'^3\Delta_u$final state, but not with the $A^3\Sigma_u^+$ state (not shown in Fig. 8) which has no $\Omega=\pm2$ values. Calculations by Klotz and Peyerimhof[14], and by Minaev[19], predict that the allowed $A'^3\Delta_u \leftarrow {}^3\Pi_g$ perpendicular transition with spin orbit coupling to $a^1\Delta_g(\Omega=3)$ is dominant, the parallel pathway with $\Omega=2$ is one third as strong, the allowed $a^1\Delta_g \leftarrow {}^1\Pi_u$ perpendicular transition with spin orbit coupling to $A'^3\Delta_u$ $\Omega=\pm1$ are insignificant, one-hundredth of the $\Omega=3$intensity. In addition, the $A^3\Sigma_u^+ \leftarrow a^1\Delta_g$ transition, which is a third as strong as the $A'^3\Delta_u \leftarrow a^1\Delta_g$ transition (Fig 2) can only borrow from allowed transitions of perpendicular character. Previous theory thus predicts a strongly perpendicular character for the Chamberlain continuum while our experiment indicates a strongly parallel nature characterized by beta larger than unity.

From Table 3 the $O(^3P_j$ j=2:1:0) branching ratios from the $A'^3\Delta_u\Omega=2$ state under the sudden approximation yields j 2:1:0 = 7:3:2. Since aβ value of ~ 1.3 indicates 77% parallel and 23% perpendicular character the perpendicular part appears to increase mainly the j = 1 yield relative to j=0, under the assumption of the sudden analysis. Because the sudden approximation does not quantitatively explain photodissociation in the Herzberg continuum, its application to the $a^1\Delta_g(\Omega=2)$ upper state of the Chamberlain continuum is quite qualitative. In accord with the strong parallel character observed in our experiment,it does indicate an increase in importance of the $O(^3P_j)$ j=0 stateas final product compared to the Herzberg continuum. This trend is in agreement with the j-state branching ratios found experimentally in this study. Not being in one of the limiting cases, we need accurate knowledge of the couplings between different electronic states at short and large internuclear separation for an accurate calculation of the β-parameters and branching ratios.

In summary, the cross section for the Chamberlain continua appears to be much stronger than that of the Herzberg continuum at 226 nm, in contrast to theory which predicts that the Herzberg continuum cross section should be slightly higher. With the additional result that the Chamberlain continuum has a strong parallel character where theory predicts perpendicular character, we can suggest that the parallel $\Omega=2$ pathway via the $^1\Delta_u$ state shown in Figure 8 may be more important than expected. In the calculations of Klotz and Peyerimhof[14] spin-rotation coupling was not considered. Our sample, however, should be quite rotationally cold, which suggests that spin-rotation coupling may not be important[4]. From energetic grounds we do not expect contributions from a different transition other than the Chamberlain continuum. For example, the threshold for the $B^3\Sigma_u^- \leftarrow a^1\Delta_g$ continuum is at 203 nm; calculations by Minaev[19] predict that this transition is equally strong as

the $A^3\Sigma_u^+ \leftarrow X^3\Sigma_g^-$ transition. However, we see no evidence for $a^1\Delta_g$-state dissociation at 200 nm; and at 205 nm only a weak signal is seen, consistent with the blue edge of the $A'^3\Delta_u \leftarrow a^1\Delta_g$ transition. Predissociation following bound-bound $B^3\Sigma_u^- \leftarrow a^1\Delta_g$ transitions, which have quite low Franck-Condon factors, do not yield peaks at the observed kinetic energy release. Minaev[19] also predicts that the $1^3\Pi_u \leftarrow a^1\Delta_g$ transition, which as shown in Fig. 8 has a parallel character, is especially strong; the $1^3\Pi_u$ state dissociates to D_0. This transition, however, should lie at much shorter wavelengths. Furthermore, we did not see any evidence for $a^1\Delta_g$-state dissociation to D_0 (or D_1) at 157 nm. The Chamberlain continuum with its unexpectedly large cross section and strongly parallel character appears to be the dominant dissociation pathway for the $a^1\Delta_g$ state in UV-VUV region.

3.5 Conclusions

Our study of a pulsed discharge beam of O_2 has revealed several surprising results. First, the discharge can be adjusted to remove from 30% to more than 70% of the initial $O_2 X^3\Sigma_g^-$ (v=0) molecule present in the beam. Surprisingly large populations of excited $a^1\Delta_g$-state in the v=0, 1 and 2 levels are also indicated, these populations may even exceed those observed for cold oxygen atoms. Due to their enormous photodissociation cross sections, we also observe trace amounts of highly vibrationally excited ground state molecules. While essentially no $b^1\Sigma_g^+$-state is formed, this may be consistent with the higher collisional quenching rate of the $b^1\Sigma_g^+$-state compared to the $a^1\Delta_g$-state.

From the predictions by theory of the strength of the $a^1\Delta_g$-state photodissociation cross section in the wavelength range 240-200nm, we should expect only a weak signal from $a^1\Delta_g$-state compared to that of $X^3\Sigma_g^-$ (v=0). However, the $a^1\Delta_g$-state signal is strong; a very simple model of the discharge shows that the photodissociation cross section must be at least but more probably more than 3 times stronger than theory predicts. Furthermore, the photodissociation image shows a strong parallel character, while theory predicts a predominantly negative character. While we do not expect these results to have much effect on models of the atmospheric photochemistry, where the fraction of $a^1\Delta_g$-state is only 10^{-5}, this work does call for a new *ab initio* calculation of the transition moments and intensity borrowing for forbidden transitions of $a^1\Delta_g$-state O_2. After so many decades of investigation, molecular oxygen, with its complex electronic structure and strongly forbidden transitions, still holds surprises.

27. G. BazalgetteCourrèges-Lacoste, J. P. Sprengers, J.Bulthuis, S.Stolte, T. Motylewski, and H. Linnartz, *Chem. Phys. Lett.*, **335**, 209 (2001).

28. D. C.Radenovic, A. J. A. vanRoij, D. A. Chestakov, A. T. J. B. Eppink, J. J. terMeulen, D. H. Parker, M. P. J. vanderLoo, G. C. Groenenboom, M. E. Greenslade, M. I. Lester, *J. Chem. Phys.*, **119**, 9341 (2003).

29. L. M. Janssen, M. P. J. vanderLoo, G. C. Groenenboom, S.-M. Wu, D. Č. Radenović, A.J. A. vanRoij, I.A. Garcia, D. H. Parker *J. Chem. Phys.*, **126**, 094304 (2007).

30. P. W. J. M. Frederix, C.-H. Yang, G. C. Groenenboom, D. H. Parker, K. Alnama, C. M. Western, A. J. Orr-Ewing, *J. Phys.Chem. A*, **113**, 14995 (2009).

31. R. Ogorzalek Loo, W. J. Marinelli, P. L. Houston, S.Arepalli, J. R. Wiesenfeld, and R. W. Field, *J. Chem. Phys.*, **91**, 5185 (1989).

32. M. E. Sanz, M. C. McCarthy,P. Thaddeus, *J. Chem. Phys.*, **119**, 11715 (2003).

33. V. Dribinski, A. Ossadtchi, V.A. Mandelshtam, and H. Reisler, *Rev. Sci.Instrum.*, **73**, 2634 (2002).

34. D.A. Chestakov, S-M. Wu,D. H.Parker,A.T.J.B. Eppink, and T.N. Kitsopoulos, *J. Phys. Chem. A*, **108**, 8100 (2004).

35. D. J. Leahy, D. L. Osborn, D. R. Cyr, D. M. Neumark, *J. Chem. Phys.*, **103**, 2495 (1995).

36. Y.-L. Huang, R. J. Gordon, *J. Chem. Phys.*, **94**, 2640 (1991).

37. R. P. Saxon and T. G. Slanger, *J. Geophys. Res.*, **96**, 17291 (1991).

38. M. Brouard, R. Cireasa,A. P. Clark,F.Quadrini and C. Vallance, *Phys. Chem. Chem. Phys.*, **8**, 5549 (2006).

39. K.D. Setzer, M. Kalb, and E.H. Fink, J. Mol.Spec.,**221,** 127 (2003).

40. S. J. Singer, K. F. Freed, and Y. B. Band, *Adv. Chem. Phys.*, **61**, 1 (1985).

41. M. C. G. N. van Vroonhoven and G. C. Groenenboom, *J. Chem. Phys.*, **116**, 1965 (2002).

Chapter 4

Photodissociation of $S_2(\tilde{X}\,^3\Sigma_g^-, \tilde{a}\,^1\Delta_g^+, \tilde{b}\,^1\Sigma_g^+)$ in the ultraviolet (320-205 nm) region

Abstract

Photodissociation of S_2 has been studied using velocity map imaging (VMI) in the ultraviolet region (320-205 nm). A pulsed electric discharge is used to produce $S_2\,\tilde{X}\,^3\Sigma_g^-$ triplet ground state as well as electronically excited singlet sulfur $S_2\,\tilde{a}\,^1\Delta_g^+(v=0)$ and $\tilde{b}\,^1\Sigma_g^+(v=0,1)$. In a previous paper [Frederix et al, J. Phys. Chem. A,**113**,14995 (2009)] we reported threshold photodissociation of $S_2\,\tilde{X}\,^3\Sigma_g^-$ in the 282-266 nm region. In the present study, $S(^3P_J)$ fine structure branching and angular distributions for photodissociation of S_2 ($\tilde{X}\,^3\Sigma_g^-$(v>0), $\tilde{a}\,^1\Delta_g^+$, and $\tilde{b}\,^1\Sigma_g^+$) via the $\tilde{B}\,^3\Sigma_u^+$ and $\tilde{B}''\,^3\Pi_u^+$ excited states are reported. In addition, photodissociation of $\tilde{X}\,^3\Sigma_g^-$ state S_2 to the second dissociation limit $S(^3P)+S(^1D)$ is characterized. The present results on S_2 photodynamics are compared to those of the well-studied isovalent molecule O_2.

4.1 Introduction

The free radical diatomic sulfur (S_2) has been observed in many environments such as dense molecular clouds[1], comets[2,3] , the atmosphere of Jupiter[4], and interstellar space. S_2 is also present in combustion processes[5], volcanic activity[6], in discharges containing sulfur compounds[7], and in sulfur-containing chemical lasers[8,9]. While the absorption spectrum of S_2 in the ultraviolet (UV) region is well studied,[10,11] the understanding of its photodissociation dynamics is far from complete. Furthermore, parallel research in our laboratory on the photodissociation of singlet molecular oxygen has given motivation to explore the chemistry of its analogous sulfur species, singlet diatomic sulfur S_2 $\tilde{a}\ ^1\Delta_g^+$ and $\tilde{b}\ ^1\Sigma_g^+$. Although singlet sulfur has been found to be involved in various physical and chemical processes,[12] relatively few studies[13,12] on its chemistry have been reported because of the difficulty of preparing sufficient concentrations of singlet sulfur. In our group we have also investigated the photodissociation of the low-lying metastable O_2 $\tilde{a}\ ^1\Delta_g^+$ state; also known as singlet oxygen, in the UV-region[14]. Because S_2 is electronically isovalent with O_2, it is also interesting to compare the photodynamics of singlet sulfur with those of singlet oxygen.

Recently, Frederix et al.[15] reported the near-threshold photodissociation of ground electronic state S_2 $\tilde{X}\ ^3\Sigma_g^-$ into two $S(^3P_2)$ atoms (the lowest energy dissociation limit) with subsequent detection of $S(^3P_J$, J=2, 1, and 0) fragments using the velocity map imaging technique[16], which measures the velocity (speed and angular distribution) of nascent state-selected photofragments. Rotationally cold S_2 was formed in a pulsed electric discharge of a mixture of H_2S seeded in Argon. An important result from this previous work was the revision of the S_2 bond energy by ~ -400 cm^{-1} to $\overline{D_0}$ = 35636.9 ± 2.5 cm^{-1} (4.418 eV) with respect to the lowest rovibrational level. A pump-probe method was used where one laser dissociated the S_2 molecule and a second laser state selectively ionized nascent $S(^3P_J$, J=2, 1, and 0) fragments by two-photon Resonance Enhanced Multi-Photon Ionization, abbreviated here as (2+1) REMPI. In Ref.15, the laser used for REMPI detection of $S(^3P_J)$ alone also created extra S^+ signals that could not be assigned to $S(^3P_J)$ atom formation from one-photon dissociation of ground electronic state S_2. In the present work we assign these signals to the photodissociation of singlet $\tilde{a}\ ^1\Delta_g^+$ and $\tilde{b}\ ^1\Sigma_g^+$, and observe dissociation of S_2 $\tilde{X}\ ^3\Sigma_g^-$ above the second dissociation limit using the two-color dissociation-detection technique.

4.1.1 Absorption Spectra of S_2 and O_2

Schematic potential energy curves scaled to the bond energy $\overline{D_0}$ for the electronic states of S_2 and, for later discussion, O_2, most relevant for this study are compared in Figure 1.[17] An important difference between S_2 and O_2 is the stronger bonding character of most S_2 bound states. The position of the $\tilde{B}\ ^3\Sigma_u^+$ curve in S_2,for example, shifts downward in energy compared to the same state in O_2 such that bound levels are present below the first dissociation limit, which is indicated by the lower dashed horizontal line in the figure. The $\tilde{B}''\ ^3\Pi_u^+$ state of S_2 also shifts downwards and acquires binding character.

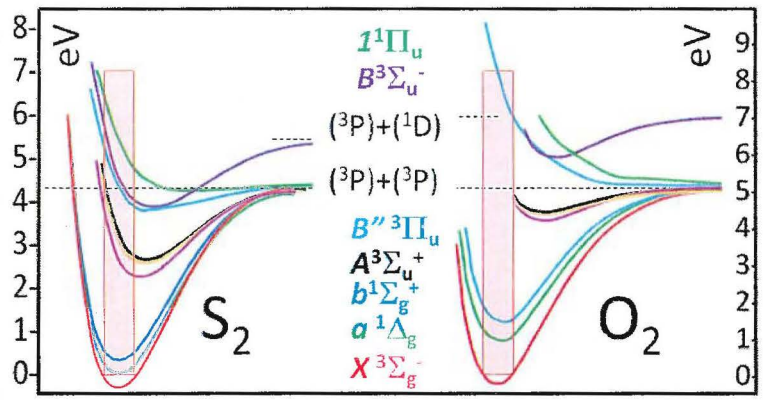

Figure 4.1: Potential energy curves for selected electronic states of S_2 and O_2, adapted from Refs. 11 and 15, and for O_2, adapted from Ref. 17. The two sets of curves are scaled arbitrarily on the vertical (energy) axis to the bond energy $\overline{D_0}$ and on the horizontal (atom-atom separation) axis to display the same width of the ground electronic state energy well. The curves are color labeled in their energy order at R_e, the equilibrium bond length of the ground electronic states. Only one Herzberg state, the $\tilde{A}\ ^3\Sigma_u^+$ is labeled, plots for the lowest energy $\tilde{c}\ ^1\Sigma_u^+$ Herzberg III (magenta color) and middle energy $\tilde{A}'\ ^3\Delta_u$ state (orange) curves are directly under the $\tilde{A}\ ^3\Sigma_u^+$ (black) curve. The lower (upper) horizontal dashed line indicates the first $\overline{D_0}$ (second, $\overline{D_1}$) dissociation energy of the molecule. The shaded rectangle indicates the region of Franck-Condon overlap.

Compared to O_2, the bound states of S_2 have a much more favorable Franck-Condon overlap (shown schematically by shaded rectangles in Fig. 1) with the lowest set of electronic states here after abbreviated as $\tilde{X}$, $\tilde{a}$, and $\tilde{b}$, in the UV region. Owing to the strict symmetry rules valid for homonuclear diatomic molecules, very few transitions between the electronic states of either molecule are electric dipole allowed. Starting from the ground electronic state, for both molecules the only allowed

transitions are: the $\tilde{B}\ ^3\Sigma_u^+ \leftarrow \tilde{X}\ ^3\Sigma_g^-$ transition (for O_2, this is the well-known Schumann-Runge transition) and the $\tilde{B}''\ ^3\Pi_u^+ \leftarrow \tilde{X}\ ^3\Sigma_g^-$ transition. The $\tilde{B}''\ ^3\Pi_u^+$ upper state of molecular oxygen lacks bonding character and lies higher in energy compared to the $\tilde{B}''\ ^3\Pi_u^+$ state of S_2. This places the $\tilde{B}''\ ^3\Pi_u^+ \leftarrow \tilde{X}\ ^3\Sigma_g^-$ transition of O_2 in the deep vacuum ultraviolet[18]. In S_2, both allowed transitions are observed in the ultraviolet region and the transition strengths and mixing of the two bound-bound transitions has been studied in detail. As pointed out by Green and Western[19], the molecular orbital configurations of the involved states are

$\tilde{B}\ ^3\Sigma_u^+$	$...5\sigma_g^{\ 2}\ 2\pi_u^{\ 3}\ 2\pi_g^{\ 3}$,
$\tilde{B}''\ ^3\Pi_u^+$	$...5\sigma_g^{\ 2}\ 2\pi_u^{\ 4}\ 2\pi_g^{\ 1}\ 5\sigma_u^{\ 1}$,
$\tilde{X}\ ^3\Sigma_g^-, \tilde{a}\ ^1\Delta_g^+, \tilde{b}\ ^1\Sigma_g^+$	$...5\sigma_g^{\ 2}\ 2\pi_u^{\ 4}\ 2\pi_g^{\ 2}$,

and while the $\tilde{B}\ ^3\Sigma_u^+ \leftarrow \tilde{X}$, $\tilde{a}$, $\tilde{b}$ are strong bonding-antibonding π_u-π_g transitions, the σ_u-π_g character of the $\tilde{B}''\ ^3\Pi_u^+ \leftarrow \tilde{X}$, $\tilde{a}$, $\tilde{b}$ transitions is inherently weak according to the propensity rules described by Mulliken[20,21]. Spin-orbit coupling is the main mechanism for gaining transition strength for all forbidden transitions of O_2[17]. Spin-orbit coupling is expected to be even stronger the S_2 than in O_2. Essentially all intensity of the $S_2\ \tilde{B}'' \leftarrow \tilde{X}$ transition is known[22] to arise from spin-orbit mixing of the $\tilde{B}$ and $\tilde{B}''$ states. This mixing is strong but complex and indirect. Direct spin-orbit coupling of the $\tilde{B}$ and $\tilde{B}''$states is not allowed because they differ in the occupation of two separate electron orbitals. Green and Western [19]were able to trace out the complex mixing patterns of the two states via analysis of rotational state perturbations across the bound-bound UV absorption spectrum.

Because $\mu(R)$, the transition dipole functions, are unknown it is not possible to predict S_2 absorption spectra from the potential energy curves shown in Fig. 1. Franck-Condon factors can be estimated however; these are useful in order to indicate the wavelength regions of interest for the different transitions, and are shown in Fig. 2. Our work concerns photodissociation following transitions from the three lowest electronic states to the optically allowed $\tilde{B}$ and $\tilde{B}''$ upper electronic states, and transitions from the ground state to the equivalents of the Herzberg states of S_2. Transitions from the S_2 $\tilde{a}$, $\tilde{b}$ states to the equivalent Herzberg states lie in the visible region, which was not studied in this work, and are not shown in Fig. 2. For selected transitions in the UV region, the Franck-Condon envelops are shown where the height (intensity) of the curves is arbitrarily scaled. The relative heights of the $\tilde{B} \leftarrow \tilde{X}$, $\tilde{B} \leftarrow \tilde{b}$ and $\tilde{A}\ ^3\Sigma_u^+ \leftarrow \tilde{X}$ curves in Fig. 2 are plotted to match those of the known absorption spectra of the O_2 molecule (Figure 2 of Ref. 15), when

multiplied by the factors $2 \cdot 10^6 : 10^4 : 1$, respectively, i.e., the maximum of the Schumann-Runge transition in O_2 is ~2 million times stronger than that of the $\tilde{A} \leftarrow \tilde{X}$ Herzberg I transition and ~100 times stronger than that of the $\tilde{B} \leftarrow \tilde{b}$ *"Parker"*transition[24].

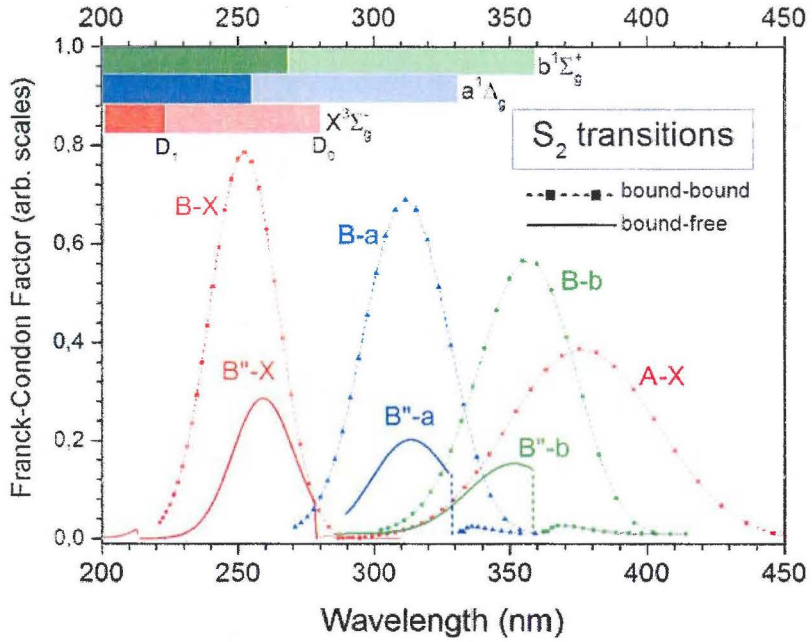

Figure 4.2: Simulated bound-bound (dashed lines) and bound-free (solid lines) transitions between selected potential energy curves shown in Figure 1, based only on Franck-Condon overlap, in the 200-450 nm range. Regions of continuous (bound-free) transition from the $\tilde{X}$, $\tilde{a}$, and $\tilde{b}$ states are marked as bars above the spectra, beginning at the first (light shading) and second (darker shading) dissociation limits, labeled $\overline{D_0}$ and $\overline{D_1}$, respectively, for transitions arising from the $\tilde{X}$-state. The relative heights of the curves are chosen only for clarity of display, these curves do not include the transition dipole $\mu(R)$, which can also change the shape of the curves if $\mu(R)$ varies over the Franck-Condon region, shown for the vibrational level v=0 as a shaded bar in Figure 1.

Although very weak, the $\tilde{A} \leftarrow \tilde{X}$ Herzberg I continuum of O_2 has a dominant role in ozone production in Earth's atmosphere. Franck-Condon factors for this continuum, which begins for photodissociation of S_2 $\tilde{X}$(v=0) below 280.61 nm, are strongly decreasing in S_2 instead of increasing as in O_2, which suggests that the Herzberg

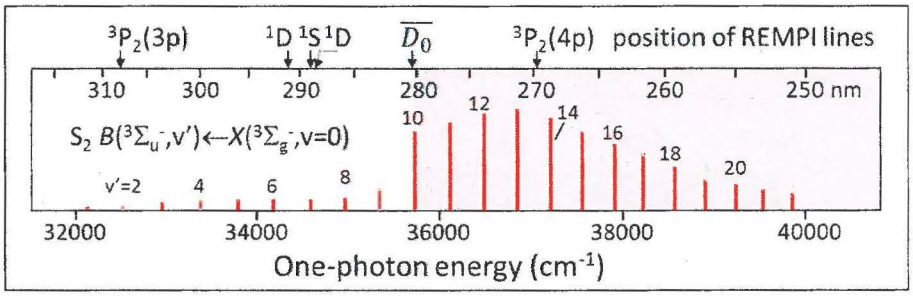

Figure 4.3: Schematic absorption spectrum for S_2 in the 315-245 nm region

continuum of S_2 is much weaker than that of O_2. As seen in the 230-280 nm wavelength region of Fig. 2, continuous absorption from the $\tilde{X}$ state to the $\tilde{B}''$ state (which is weak according to the Mulliken rules) is overlapped by more intense bound-bound transitions to the $\tilde{B}$ state. A simplified ultraviolet absorption spectrum of S_2, adapted from Herzberg [23] is shown in Figure 3. Note the differences between the actual absorption spectrum and the Franck-Condon Factor spectrum for the $\tilde{B}(v')\leftarrow \tilde{X}(v'')$ bands shown in Fig. 2. The $\tilde{B}(v')\leftarrow \tilde{X}(v'')$ bands preceding the 10-0 band are fairly weak while the 10-0 and higher energy bands have considerable intensity and peak at ~270 nm compared to the FCFs which peak ~250 nm in Fig. 2. The rotational envelop of the 10-0 band in Fig. 3 overlaps the onset of dissociation $\overline{D_0}$ in Fig. 2. Photodissociation of ground state S_2 is indicated by the shaded region in Fig. 3.

Transitions originating from the O_2 $\tilde{a}$ and $\tilde{b}$ states have been calculated by theory[24,25], such calculations have not been reported for S_2. In our analysis of S_2 we use what is known about the transition strengths for O_2 as a starting point for discussion.

4.1.2 Photodissociation of S_2 and O_2

Photodissociation of S_2 occurs in the regions of continuous absorption indicated in Fig. 2 by horizontal bars between $\overline{D_0}$ and $\overline{D_1}$ (light shading) and above $\overline{D_1}$ (dark shading). Bars are shown for the $\tilde{X}$, $\tilde{a}$,and $\tilde{b}$ initial states. Photo-dissociation of the ground state of S_2 to $\overline{D_0}$, for example, begins below 282 nm and limit $\overline{D_1}$, becomes energetically accessible below 223 nm.

Our most sensitive photodissociation experiment uses the same laser tuned to state-selective REMPI of nascent $S(^3P_J, J=2,1,0)$, $S(^1D_2)$ and $S(^1S_0)$ for photodissociation. VMI detection of the REMPI-produced ions

provides the speed and angular distribution of S-atom photofragments. The quantum state of one atom is state-specified by REMPI; from the measured speed distribution, momentum conservation yields the quantum state of the other atom. From the radial position the speed and kinetic energy of the nascent atom is determined, and the angular distribution of the photodissociation products is described by:

$$I(\theta) = \frac{1}{4\pi}[1 + \beta P_2(\cos\theta)]$$

where $P_2(x) = \frac{1}{2}(3x^2 - 1)$ is the 2nd order Legendre Polynomial, θ is the recoil angle with respect to the polarization axis and β is the anisotropy parameter $(-1 < \beta < 2)$. $I(\theta)$ is thus an important observable that can elucidate the amount of parallel (β =2) and perpendicular (β =-1) character in an electronic transition to a continuum state, information that is unattainable using conventional spectroscopic techniques.

REMPI wavelengths used to dissociate the S_2 beam and state-selectively probe nascent S atom products are indicated at the top of Figure 3. The longest REMPI wavelength, around 311 nm, for S(^{3}P) atoms can dissociate S_2 $\tilde{b}$ state (threshold 360 nm) and $\tilde{a}$ state (threshold 330 nm), and vibrationally excited $\tilde{X}$(v>5). In this paper we describe one-photon dissociation of S_2; multiphoton dissociation, which can also be detected by REMPI of S(^{1}D) and S(^{1}S) atoms around 290 nm is described in a separate paper[26]. One-photon dissociation and S($^3P_2$) REMPI via the 4p Rydberg state near 270 nm using a single laser was described in our earlier paper[15] on threshold dissociation of $S_2\tilde{X}$.

Our previous studies of O_2 photodissociation have shown that the strongest O-atom product signal results from passage through the second dissociation limit, $\overline{D_1}$. Even when one-photon dissociation of the ground state of O_2 is energetically not possible, two-photon dissociation of the X-state to $\overline{D_1}$ is the dominant signal when using a focused laser beam. Photodissociation of high lying states of O_2 such as high vibrational levels of the $\tilde{X}$ state, or of the metastable $\tilde{b}$ state[26] via $\overline{D_1}$was also observed even when the population of these levels is quite low.

We have recently reported a study of O_2 photodissociation in the UV region using a discharge where photodissociation of the a-state and trace amounts of vibrationally excited $\tilde{X}$(v>2) were observed[14]. In the present study, S_2 itself is produced in a discharge of H_2S or OCS, and it is expected that the low-lying excited singlet-spin states of S_2 will also be produced along with $\tilde{X}$ state. Discharges in O_2 and S_2 have been compared previously, for example by Setzer et al[27], who showed that population of the a-state is favored in O_2 discharges while b-state formation is favored in S_2 discharges.

4.2 Experiment

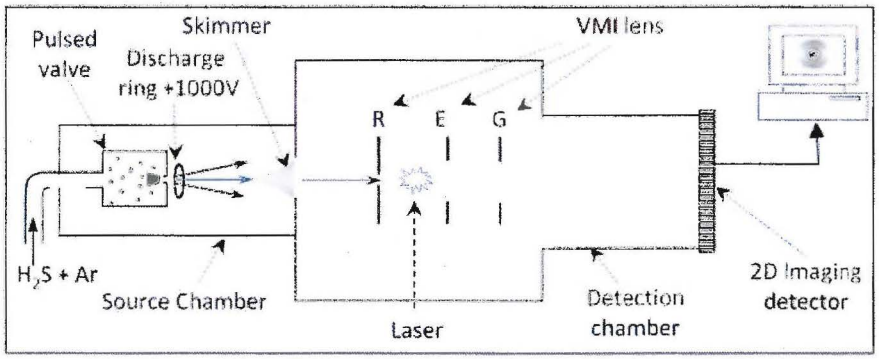

Figure 4.4: Schematic diagram of the VMI apparatus. See text for details.

The VMI experimental setup consists of a source chamber (typical background pressure ~10^{-7}mbar and 10^{-5} mbar with the molecular beam operating) and a detection chamber (~10^{-7} mbar with beam on or off). A pulsed discharge was used to produce S_2 radicals[28]. A mixture of 20% H_2S gas in argon at 2 bar was led to a pulsed valve (Jordan) with a 0.4 mm diameter orifice. This gas expands through the nozzle into the source chamber to produce a cold, pulsed molecular beam. Just in front of the nozzle, 2.5 mm downstream, a stainless steel ring (4 mm diameter, 0.5 mm thickness) is mounted. As each gas pulse passes, the voltage on the ring is pulsed to a positive high voltage (~1000 V) which produces an electrical discharge between the ring and the grounded nozzle. The production of S_2 radicals is dependent on the width, delay and voltage of the pulse applied to the ring. It is observed that a positive voltage (~1000V, 10 μs) is more suitable for a high production rate of S_2 radicals as compared to a negative voltage (more suitable for production of SH and singlet oxygen). A 0.5 mm diameter tungsten filament was placed adjacent to discharge ring and a current of around 1.5 A was passed through it. The glowing filament emits electrons that help initiate and stabilize the discharge. Under specific conditions, low-lying metastable S_2 $\tilde{a}$ and $\tilde{b}$ states are formed in this electric pulsed discharge. Like molecular oxygen O_2, vibrationally excited ground state sulfur is also populated when using this pulsed electric discharge.

S_2 molecules formed in the molecular beam are efficiently cooled in the supersonic expansion and propagate through a skimmer (2 mm diameter) 20 mm downstream from the nozzle. The beam is further collimated by a 2 mm hole in the center of the repeller electrode. In this standard VMI setup the electrostatic lens consists of three electrodes (repeller, extractor and ground electrode) with 20 mm inner diameter[18]. The interaction

between the molecular beam and laser beam takes place in the region between the repeller and extractor electrodes, in the detection chamber.

A frequency-doubled pulsed Nd:YAG laser (Spectra-Physics DCR-3A) operating at a repetition rate of 10 Hz is used to pump a dye laser (Spectra-Physics PDL-2) which is operated at various wavelengths by using a range of laser dyes. Subsequently, frequency doubling is achieved by an angle-tuned KDP/BBO crystal. During the experiments the wavelength was scanned in the ultraviolet region. About 3 to 4 mJ per pulse of polarized laser light (0.6 cm^{-1} linewidth) is focused into the interaction region by means of a 20 cm focal length lens. The ions created by (2+1) REMPI are extracted from the interaction region (between repeller and extractor) into the time-of-flight (TOF) tube. At the end of the TOF tube the ions are detected by an imaging detector, containing a dual chevron stack of microchannel plates (MCPs) and a phosphor screen.

Mass selection is achieved by gating the voltage on the front MCP at the arrival time of the ion of interest. A charged-coupled device (CCD) camera monitoring the phosphor screen captures the ion images appearing at each laser shot. The timings for laser, discharge, detector and valve are controlled by digital pulse generators with 10 Hz repetition rates. The CCD images are collected in a PC where the center of each event appearing in the images is registered and counted (running under Davis, LaVision). For a typical image data is collected over 15000 laser shots. Subsequent data analysis includes an Abel inversion routine (using the BASEX algorithm based on a basis set expansion method [29]. The Abel inverted images contain all relevant information to extract the full three-dimensional velocity distributions (i.e. speed and angular distributions).

For kinetic energy calibration, one-color images of $S(^3P)$ detection at 308.20 nm were employed. Three strong rings appear in the S^+ image corresponding to two-photon excitation of S_2 followed by dissociation to the first, second and fourth ($^3P_2+^3P_2$,$^3P_2+^1D$ and $^3P_2+^1S$, respectively) dissociation limits. The strong and sharp middle ring corresponding to ($^3P_2+^1D$) with a total kinetic energy release (TKER) value of 2.531 eV was used for calibration.

4.3 Results

A quadrant-symmetrized raw velocity map image of $S(^3P_2)$ atoms converted by (2+1) REMPI to S^+ ions using a tightly focused laser beam at 308.2 nm is shown in Figure 3.

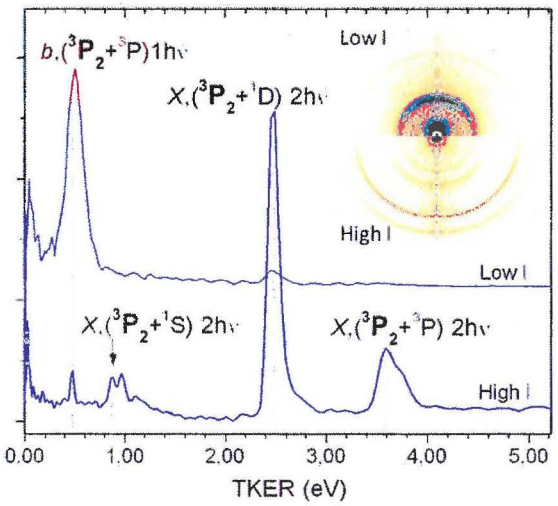

Figure 4.5: Raw S^+ image recorded at 308.21 nm, the (2+1) REMPI wavelength for ionization of S^3P_2 atoms. The laser polarization direction ***E*** *is parallel to the detector face and along the vertical axis of the figure. A color bar for conversion to signal intensity is given on the right side of the figure. For each labeled ring the detected atom is indicated by bold typeface.*

Four rings are assigned, the three outer rings correspond to two-photon dissociation of S_2 to the limits $\overline{D_0}$, $\overline{D_1}$, and $\overline{D_3}$ in decreasing radius, the ring labeled (^{3}P+^{1}D) is used to calibrate the energy scale of all other images, as discussed in the experimental section. The image shown in Figure 3 was taken under typical tight-focusing conditions where a 20 cm focal length spherical lens was positioned to focus the laser beam directly at the molecular beam. By moving the focus of the laser beam 1-2 cm away from the molecular beam and limiting the width of the electric discharge pulse forming the S_2 to only a few microseconds, the inverted image shown in the upper part of the inset of Figure 4 was obtained.

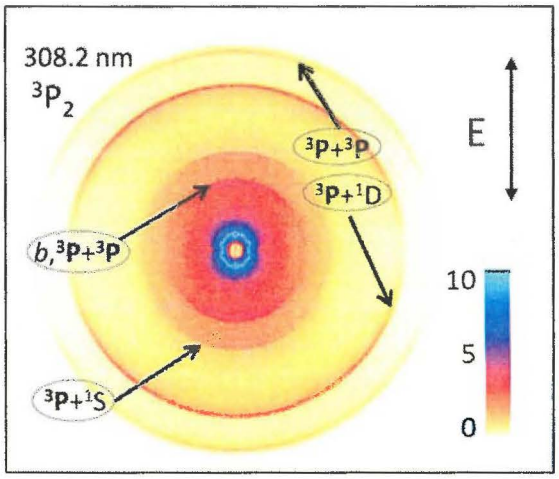

Figure 4.6: Total kinetic energy release curves obtained from S($^3P_2$) 308.2 nm images at high and low laser intensities. The inset shows the top (low intensity) and bottom (high intensity) of the inverted images for the two conditions for comparison. See Fig. 3 for polarization direction and color bar. Detected atoms are indicated by bold typeface.

For comparison, the lower part of the inset shows the inverted image taken under normal tight-focusing conditions as in Fig. 3. Integration around the angular distribution of the inverted images and division of the intensity at each pixel by the pixel radius yields the total kinetic energy release (TKER) curves shown in Fig. 4 for the low and high intensity 308.21 nm dissociation/detection processes.

Raw quadrant-symmetrized S^+ images taken under the low-intensity condition at the detection wavelengths for S($^3P_1$) and S($^3P_0$) are shown in Fig. 5 and the corresponding TKER curves in the 0-1.0 eV TKER energy range are plotted in Figure 6. While each distribution in Fig. 6 is plotted using the same calibration factor, the S($^3P_1$) and S($^3P_0$) curves are shifted to higher energy by the difference in the photon energy ($E_{h\nu}$($^3P_2$)-$E_{h\nu}$($^3P_{J=1,0}$) to compensate for the longer wavelengths needed for S($^3P_{J=1,0}$) resonance detection.

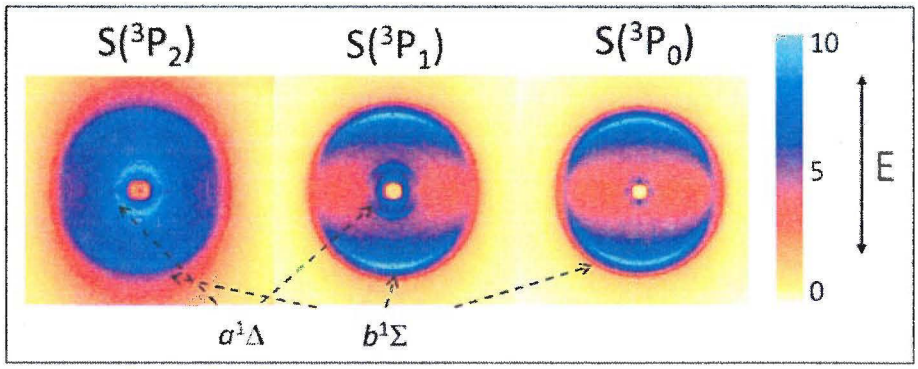

Figure 4.7: Raw symmetrized images of $S(^3P_J)$ atoms taken under low laser intensity conditions with a short discharge time.

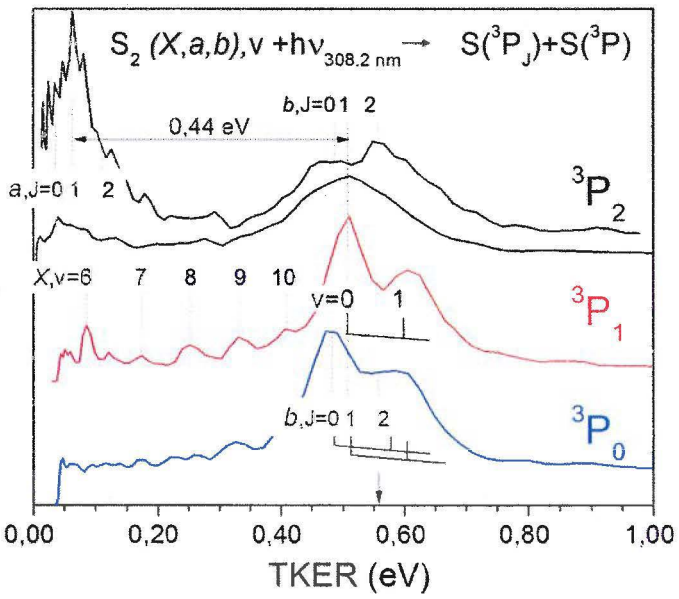

Figure 4.8: TKER curves for $S(^3P_J$, J=2,1,0) atoms formed under low laser intensity conditions. The J=1 and J=0 curves are shifted higher in energy by the one photon energy difference $(E_{h\nu}(^3P_2)$-$E_{h\nu}(^3P_{J=1,0})$ relative to the J=2 image. The vertical dashed lines mark the energy spacing of the J=2,1,0 states along with the addition of one vibrational quantum of S_2,X (v=1).

The upper trace of the $S(^3P_2)$ curve was obtained with a 1 μs discharge pulse, the other traces with a 3μs pulse. See text for more details.

In addition, a two-color image taken with the dissociation laser at 205.6 nm and the detection laser at the $S(^3P_2)$ wavelength of 308.2 nm is shown along with the TKER curve in Figure 7. Focused 205.6 nm radiation causes a very large and unstructured S^+ signal from the beam with the discharge on or off; this background, particularly at low TKER, is difficult to remove by subtraction.

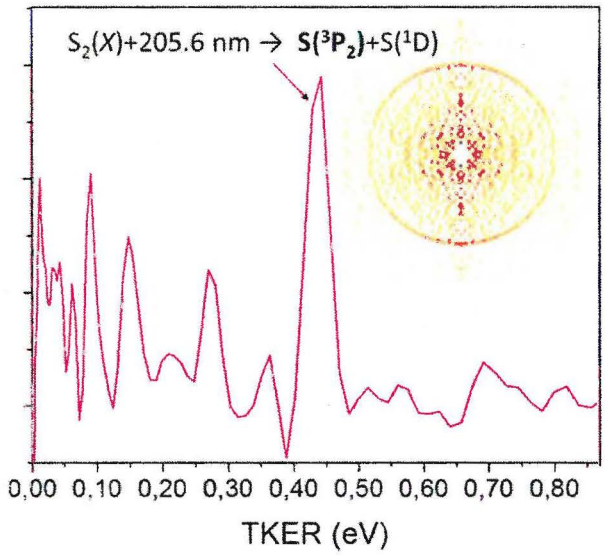

Figure 4.9: Background-subtracted two-color image with dissociation at 205.6 nm and detection of $S(^3P_2)$ at 308.2 nm.

4.4 Analysis

Despite the complex chemistry of the pulsed electric discharge in a H_2S/Ar mixture, with many possible sources of S^+ formation, all signals observed in this study, with the exception of the two-color 205.6 dissociation / 308.2 nm detection image of Fig. 7 can be attributed from their TKER positions to photodissociation of S_2 as the parent molecule. SH, predominant when using a negative high voltage discharge[30], yields S atoms with low TKER due to the mismatch in mass of ^{32}S and ^1H. Only regions near the center of the images (low TKER) can be contaminated with S from SH photodissociation. It is experimentally straightforward to distinguish the detection of nascent S atoms by (2+1) REMPI due to their

wide Doppler profiles which requires scanning the laser across the central detection wavelength. Other processes that create S^+ such as dissociation of S_2^+ or ionization of excited S* atoms are bound-continuum transitions and do not show such a Doppler effect. The sharp ring in Fig. 7, and all other rings observed in the other images presented arise from S_2, as shown in this section.

4.4.1. Photodissociation of S_2 $\tilde{X}\,^3\Sigma_g^-(v=0)$ at 205.6 nm

Inspection of Fig. 2 shows that absorption of a 205.6 nm (6.2 eV) photon by $S_2\tilde{X}$ should excite the molecule to the edge of the S_2 Schumann-Runge continuum, just above the $\overline{D_1}$ limit. An image of $S(^3P_2)$ fragments from excitationat this wavelength is presented in Figure 7. While the $S(^3P_2)$ signal is strongly overlapped by the photodissociation signal from H_2S (or OCS) present as the parent beam, one clear ring emerges at TKER=0.45 eV, which agrees well with the expected value for dissociation to $\overline{D_1}$, from $h\nu\text{-}\overline{D_1}$= 6.01-(4.418+1.145)=0.456 eV. The product angular distribution is strongly parallel with β=1.5±0.5 (Table 1) where the large uncertainty is due to the background subtraction problem. No signal was observed at 1.6 eV, the TKER corresponding to dissociation of $\tilde{X}$(v=0) to $\overline{D_0}$ products.

4.4.2. Photodissociation of S_2 $\tilde{X}\,^3\Sigma_g^-(v>5)$ around 310 nm

Figure 5 shows images from dissociation at the $S(^3P_J)$ REMPI detection wavelengths around 310 nm where a series of weak but sharp rings in the TKER region below 0.5 eV are observed, particularly in the $S(^3P_1)$ image. These are labeled $\tilde{X}$(v=6-10) in the TKER curves shown in Fig. 6 for $S(^3P_1)$, and are visible but weak in the $S(^3P_0)$ image and TKER curves. The energy positions of these peaks agree with the expected positions of the (2,1) channels for $S(^3P_1)$ detection. Beta parameters of the $S(^3P_1)$ images arising from photodissociation of $\tilde{X}$(v=6-10) are listed in Table 1.

Table 4.1: *Beta values and $S(^3P_J)$ branching ratios for this work for photodissociation of S_2 $\tilde{a}\ ^1\Delta_g^+$, $\tilde{b}\ ^1\Sigma_g^+$ and $\tilde{X}\ ^3\Sigma_g^-(v>5)$, at ~310 nm, and $\tilde{X}\ ^3\Sigma_g^-(v=0)$ at 205.6 nm.*

Diss. λ	S atom	β a-state	β b-state	β X-state
308.2 nm	$^3P_2$	0.6±0.15	0.93±0.05	
310.0 nm	$^3P_1$		0,66	v=6 0,65 v=8 0,52 v=9 0,55 v=10 0,50
311 nm	$^3P_0$		v=0 0.62 v=1 0.34	
205 nm	$^3P_2$			1.5±0.5

4.4.3 Photodissociation of S_2 $\tilde{b}\ ^1\Sigma_g^+$ around 310 nm

The strongest signals observed in Fig. 5 appear around 0.5 eV TKER. The $S(^3P_{1,0})$ TKER curves in Figure 6 have been shifted to compensate for the differences in the $S(^3P_J)$ REMPI wavelengths, so the pair-correlated peaks for the same final channel (e.g. $S(^3P_2)$ + $S(^3P_1)$, abbreviated hereafter as (2,1)) fall at the same TKER. Both the $S(^3P_2)$ and $S(^3P_1)$ curves are found to peak at TKER = 0.50 eV, which we assign as the position of (2,1). The $S(^3P_0)$ detection curve peaks then at the energy position of (2,0). Both the $S(^3P_1)$ and $S(^3P_0)$ curves show a clear extra peak higher by 0.09 eV which corresponds to the photodissociation of $\tilde{X}$(v=1). From these data we assign the position of (2,2) at TKER=0.56 eV as indicated by a vertical arrow in Figure 5. The precursor state leading to this TKER energy is determined from the equation TKER+D_0-hν= 0.56+4.418-4.023= 0.96 eV, which agrees well with the spectroscopic value of T_0 = 0.99 eV determined by Fink *et al* for the $\tilde{b} \rightarrow \tilde{X}$ transition. From the relative peak heights for $S(^3P_J)$ J=2, 1 and 0 detection it can be seen from Fig. 5 that J=1 and 0 are formed in significant fractions in the dissociation process, *i.e.*, the (2,2) channel is not the dominant product. The angular distribution of all three images (J=2 is shown in Fig. 4) is parallel with β values (Table 1) of 0.93, 0.66, 0.62, for $S(^3P_J)$ J=2, 1 and 0, respectively.

4.4.4 Photodissociation of the S_2 $\tilde{a}\ ^1\Delta_g^+$ around 310 nm

The upper $S(^3P_2)$ TKER curve in Fig. 6 was obtained using the shortest possible discharge pulse of 1 μs, where a substantial ring at low energy

(TKER ~ 0.06 eV) is observed. This ring decreases rapidly in strength as the length of the discharge increases. As indicated by the horizontal arrow in Fig. 6, the energy spacing between this low energy peak and the $\tilde{b}$ state peak matches the energy difference in T_0 values for the $\tilde{a}$, and $\tilde{b}$ states reported by Barnes et al.[13] No clear evidence was seen for this peak in the $S(^3P_0)$ image at the shortest discharge pulses. As was found for photodissociation of the $\tilde{X}$ and $\tilde{b}$ states, the strongest component of the $\tilde{a}$ state to S^3P_2 dissociation is the (2,1) channel. Analysis of the angular distribution, Table 1, yields a value of β=0.6.

4.5 Discussion

4.5.1 Composition the discharge beam

Electric discharges are known to produce beams of rotationally cold but vibrationally hot O_2[14], S_2[15], OH[31], SH[32], SO[33] and NO[34], with vibrational populations that can be described by temperatures of several thousand Kelvin. These temperatures apply to the distribution of highest vibrational levels, the lower levels $\tilde{X}$ (v=1-3) were found to have populations consistent with much lower temperatures. If we ignore Franck-Condon factors, the vibrational progression observed in Fig. 6 for $S(^3P_1)$ detection is roughly consistent with a temperature of 2000K.

Metastable singlet states of O_2 and S_2 are also produced in the pulsed discharge. S_2 $\tilde{a}$ state appears to be formed and then quenched early in the discharge while the $\tilde{b}$ state signal is less dependent on the length of the discharge pulse. In order to observe singlet sulfur signal it is necessary to lower the laser intensity, otherwise the signal becomes dominated by multiphoton dissociation. In our O_2 discharge study[14] we observed production of only the $\tilde{a}$ state. In different types of flow discharges studies of O_2 and S_2 the $\tilde{a}$ state of S_2 is found to be much more efficiently quenched to the ground state than the $\tilde{a}$ state of O_2[35,36]. Setzer and coworkers[27] found that the $S_2\tilde{b}$ state is more rapidly quenched than the $\tilde{a}$ state, in contrast to our pulsed discharge results. A simple explanation for the stability and relative strength of the S_2 $\tilde{a}$ and $\tilde{b}$-state signals we observe in this pulsed discharge study is not available at present.

4.5.2 Dissociation of S_2 $\tilde{X}$ to the $\overline{D_1}$ limit

Photodissociation of O_2 in the Schumann-Runge continuum has been studied in detail, making a comparison of our results for 205.6 nm photodissociation of S_2 interesting. In O_2, 99.5% of the products branch to $\overline{D_1}$, only 0.5% produces two $O(^3P)$ atoms via $\overline{D_0}$. The angular distribution of the $O(^3P+^1D)$ fragments lies parallel to the laser polarization direction,

characterized by the β parameter β=2.0. Dissociation in the S_2 Schumann-Runge continuum is found to be equivalent, within the measurement uncertainty and limited data ($S(^3P_2)$ detection only), to that of O_2.

In O_2 we also observed photodissociation of very high levels (up to v=16) of vibrationally excited ground state molecules[37,14]. They were easily detected at dissociation wavelengths too long for O_2v=0 photodissociation, and showed exclusive fragmentation to the $\overline{D_1}$ limit. Due to the extremely high cross section of the Schumann-Runge continuum of O_2, it is possible to detect extremely low populations of these states. Considering its position at the blue end of the B-X FCF curve, it is not expected that vibrationally excited $S_2\tilde{X}$v>0 species will have large photodissociation cross sections compared to Xv=0 at 206 nm. Excitation of $S_2\,\tilde{a}$ and $\tilde{b}$ to the allowed B, B" upper states has no FC intensity at 206 nm. Observation of the photodissociation of only $S_2\tilde{X}$v=0 can thus be expected, as is observed.

4.5.3 Dissociation of $\tilde{X}$ v to the $\overline{D_0}$ limit

The FCF curves in Fig. 2 suggest that photodissociation of $S_2\tilde{X}$ to $\overline{D_0}$ should be favorable in the 280-230 nm region. While the $\overline{D_0}$ threshold is 280 nm for $\tilde{X}$(v=0), at 310 nm photodissociation to $\overline{D_0}$ of $\tilde{X}$(v=6-10) is observed, with beta parameters consistent with photodissociation of $\tilde{X}$(v=0) in the 280-266 nm range, which covers similar excess energy. The (2,1) limit is favored, which is consistent with adiabatic dissociation on the $\tilde{B}^{"}$ PE curve[12]. The relatively strong $S(^3P_0)$ signal observed, however, shows clearly that non-adiabatic processes such as curve-crossing at long internuclear distances play an important role.

Our previous study[16] showed that photodissociation cross sections do not increase significantly when the dissociation wavelength is resonant with the $\tilde{B} \leftarrow \tilde{X}$ bound-bound transitions. This suggests that an underlying continuum contributes strongly to the photodissociation cross section. From Fig. 2 is it clear that the $\tilde{B}^{"} \leftarrow \tilde{X}$ transition has much larger FCFs than the $\tilde{A} \leftarrow \tilde{X}$ Herzberg continuum at 310 nm and shorter wavelengths. Western and coworkers[19] have shown that the transition strength of $\tilde{B}^{"} \leftarrow \tilde{X}$ is mainly due to indirect spin-orbit coupling with the $\tilde{B} \leftarrow \tilde{X}$ parallel transition. The observed positive beta parameter Table 1of β=0.6±0.1 for photodissociation of X v=6-9 is consistent with intensity borrowing from a parallel transition. These beta values agree well with $\beta(^3P_1)$=0.6 reported in ref. 16 for the roughly energetic equivalent dissociation of $S_2\,\tilde{X}$(v=0) at 266 nm.

The Herzberg continuum in O_2 is also characterized by a positive beta parameter, due again to intensity borrowing from the Schumann-Runge transition. Due to the better Franck-Condon overlap we suggest that the

$\tilde{B}'' \leftarrow \tilde{X}$ continuum is most important for the photodissociation of S_2 around 310 nm. At the shortest wavelength of 205 nm this continuum is no longer active as evidenced by the lack of products to the $\overline{D_0}$ limit. Inspection of Fig. 2 shows that the $\overline{D_1}$ limit is hardly accessible for any S_2 transition besides B-X. S^1D production via the Schumann-Runge continuum of S_2, with its poor Franck-Condon overlap (Fig. 2) appears to play a much less important role in S_2 photodissociation compared to O_2.

4.5.4 Photodissociation of Singlet Sulfur

Our limited data on photodissociation of the $S_2\tilde{a}$ state at 310 nm is consistent with photodissociation through the spin-forbidden $\tilde{B}'' {}^3\Pi_u^+ \leftarrow \tilde{a} {}^1\Delta_g^+$ continuum transition. Franck-Condon overlap for $\tilde{B} \leftarrow \tilde{a}$ and $\tilde{B}'' \leftarrow \tilde{a}$ is optimal at 310 nm, Fig. 2.and the accidental resonance of $S(^3P_2)$ REMPI with the $\tilde{B}(v=13) \leftarrow \tilde{a}(v=0)$ transition followed by predissociation may explain why the $\tilde{a}$-state channel is observable for $S(^3P_2)$ detection. The beta parameter for this process is also similar to that for above-threshold $\tilde{B}'' \leftarrow \tilde{X}$photodissociation. While Franck-Condon factors for the $\tilde{B},\tilde{B}'' \leftarrow \tilde{a}$ transitions are small at 266 nm excitation (Fig,2), the absence of signal for this process[16] is more likely due to photodissociation of the small $\tilde{a}$ state population compared to the $\tilde{X}(v=0)$ photodissociation, which is energetically possible at the shorter wavelength.

Photodissociation of the $O_2\tilde{b}$ state[17] has been found to pass exclusively through the $\overline{D_1}$ limit via the spin forbidden $\tilde{B} \leftarrow \tilde{b}$ continuum[16]. Franck-Condon overlap for this transition in S_2 with the $\overline{D_1}$ limit is essentially zero, however, as seen in Fig. 2. Instead, the spin- and parity forbidden $\tilde{B}'' \leftarrow \tilde{b}$ transition may be responsible. According to the FCF curves in Fig. 2 the B"-b continuum should be accessible at 310 nm. As discussed above, forbidden transitions in both S_2 and O_2 are predominantly due to spin-orbit coupling with the allowed $\tilde{B} \leftarrow \tilde{X}$ parallel transition. The mixing process should result in a positive beta character, which is observed.

4.6 Conclusion

The photochemistry of S_2 is found in this work to be rather different from that of its electronic analog O_2. This difference is presumed to be due Franck-Condon overlap (Fig. 2) which, for example, greatly diminishes the importance of the Schumann-Runge and Herzberg continua of S_2. Instead, an underlying continuum with a parallel character, presumably the $\tilde{B}'' \leftarrow \tilde{X}$ continuum with intensity borrowing from the parallel $\tilde{B} \leftarrow \tilde{X}$ transition has a more important role in the photodissociation of S_2 compared that of O_2.

Unlike O_2, photodissociation of $S_2\tilde{X}\ ^3\Sigma_g^-(v>0)$, and $\tilde{b}\ ^1\Sigma_g^+$ in the near UV region around 310 nm is efficient through the $\overline{D_0}$ limit. For both molecules, the $\tilde{a}\ ^1\Delta_g^+$ state is found to photodissociate to $\overline{D_0}$. In the deep UV region at 206 nm where photodissociation of S_2 through the equivalent of the Schumann-Runge continuum is possible, similar branching ratios and angular distributions to those of O_2 are observed. Extensive calculations have been reported on the absorption and photodissociation properties of O_2, most of which, but not all (see Ref. 14) agree well with experiment. We hope the (limited) experimental data on S_2 photodissociation presented here will stimulate advanced calculations, for example on the transition moments and spin-orbit coupling strengths, on S_2.

References

1. H. Liszt, Astrophys. J. **219**, 454 (1978).
2. M. Ahearn, D. Schleicher and P. Feldman, Astrophys. J. **274**, L99 (1983).
3. R. Grim and J. Greenberg, Astron. & Astrophys. **181**, 155 (1987).
4. K. Noll, M. McGrath, L. Trafton, S. Atreya, J. Caldwell, H. Weaver, R. Yelle, C. Barnet and S. Edgington, Science **267**, 1307 (1995).
5. A. Fowler and W. Vaidya, Proceedings of the Royal Society of London. Series A **132**, 310 (1931).
6. J. R. Spencer, K. L. Jessup, M. A. McGrath, G. E. Ballester and R. Yelle, Science **288**, 1208 (2000).
7. G. Lakshminarayana and C. G. Mahajan, J. Quant. Spect. & Rad. Trans. **16**, 549 (1976).
8. V. Baboshin, S. Dobychin, V. Zuev, L. Mikheev, A. Pavlov, A. V. e. Startsev and V. Fokanov, Soviet Journal of Quantum Electronics **7**, 1183 (1977).
9. S. R. Leone and K. G. Kosnik, Applied Physics Letters **30**, 346 (1977).
10. M. D. Wheeler, S. M. Newman and A. J. Orr-Ewinga, J. Chem. Phys. **108**, 6594 (1998).
11. B. Meyer, T. V. Oommen and D. Jensen, J. Phys. Chem. **75**, 912 (1971).
12. W. C. Swope, Y. P. Lee and H. F. Schaefer, J. Chem. Phys. **70**, 947 (1979).

13. I. Barnes, K. H. Becker and E. H. Fink, Chem. Phys. Let. **67**, 314 (1979).

14. Z. Farooq, D. A. Chestakov, B. Yan, G. C. Groenenboom, W. J. van der Zande and D. H. Parker, Phys. Chem. Chem. Phys. **16**, 3305 (2014).

15. P. W. Frederix, C.-H. Yang, G. C. Groenenboom, D. H. Parker, K. Alnama, C. M. Western and A. J. Orr-Ewing, J. Phys. Chem. A **113**, 14995 (2009).

16. A. T. J. B. Eppink, B. Buijsse, M. H. M. Janssen, W. J. van der Zande and D. H. Parker, J. Chem. Phys. **108**, 1305 (1998).

17. B. F. Minaev, Phys. Chem. Chem. Phys. **1**, 3403 (1999).

18. A. T. J. B. Eppink and D. H. Parker, Rev. Sci. Instrum. **68**, 3477 (1997).

19. M. E. Green and C. M. Western, J. Chem. Phys. **104**, 848 (1996).

20. R. S. Mulliken, J. Chem. Phys. **7**, 14 (1939).

21. R. S. Mulliken, J. Chem. Phys. **8**, 234 (1940).

22. J. M. Dyke, L. Golob, N. Jonathan and A. Morris, J. Chem. Soc. Fara, Trans. 2: Mol. & Chem. Phys. **71**, 1026 (1975).

23. G. Herzberg, *Molecular spectra and molecular structure. Vol. 1: Spectra of diatomic molecules*. (1950).

24. B. Lewis, S. Gibson, T. Slanger and D. Huestis, J. Chem. Phys. **110**, 11129 (1999).

25. R. Klotz and S. D. Peyerimhoff, Mol. Phys. **57**, 573 (1986).

26. Z. Farooq and D. H. Parker, J. Chem. Phys., Submitted (2015).

27. K. D. Setzer, M. Kalb and E. H. Fink, J. Mol. Spec. **221**, 127 (2003).

28. M. Van Beek and J. Ter Meulen, Chem. Phys. Lett. **337**, 237 (2001).

29. A. O. Vladimir Dribinski, Vladimir A. Mandelshtam and Hanna Reisler1 Rev. Sci. Instrum. **73**, 2634 (2002).

30. R. A. Rose, A. J. Orr-Ewing, C.-H. Yang, K. Vidma, G. C. Groenenboom and D. H. Parker, J. Chem. Phys. **130**, 034307 (2009).

31. D. C. Radenovic, A. J. van Roij, D. A. Chestakov, A. T. Eppink, J. J. ter Meulen, D. H. Parker, M. P. van der Loo, G. G. Groenenboom,

M. E. Greenslade and M. I. Lester, J. Chem. Phys. **119**, 9341 (2003).

32. L. M. Janssen, M. P. van der Loo, G. C. Groenenboom, S.-M. Wu, D. Radenovic, A. J. van Roij, I. A. Garcia and D. H. Parker, **126**, 094304 (2007).

33. M. E. Sanz, M. C. McCarthy and P. Thaddeus, J. Chem. Phys. **119**, 11715 (2003).

34. G. Bazalgette Courrèges-Lacoste, J. P. Sprengers, J. Bulthuis, S. Stolte, T. Motylewski and H. Linnartz, Chem. Phys. Lett. **335**, 209 (2001).

35. R. Donovan, D. Husain and P. Jackson, Trans. Faraday Soc. **64**, 1798 (1968).

36. O. Strausz, R. Donovan and M. D. Sorgo, Berichte der Bunsengesellschaft für physikalische Chemie **72**, 253 (1968).

37. S.-M. Wu, D. Chestakov, G. C. Groenenboom, W. J. van der Zande, D. H. Parker, G. Wu, X. Yang and C. Vallance, Molecular Physics **108**, 1145 (2010).

Chapter 5

Multi-photon dissociation of molecular oxygen O_2 via two-photon resonant Rydberg states in the UV region

Abstract

Photodissociation and photoionization of O_2 and subsequent photodissociation of O_2^+ in the wavelength region from 200 to 240 nm is reported using resonance enhanced multiphoton ionization (REMPI) and velocity map imaging detection. A series of two-photon allowed Rydberg states with principle quantum number n=3-11 converging to the ground electronic state of $O_2^+(X\ ^2\Pi_g)$ are used as doorway states to reach the region of super-excited states of O_2 in the three-photon energy range of 16.5-20 eV. A detailed analysis of the kinetic energy release and anisotropy parameters of photofragments extracted from velocity map images reveal competition between neutral dissociation and autoionization and leads to identification of different O^+ formation channels. Moreover, the measurement of anisotropy parameters for each channel gives additional information on the symmetry of electronic states involved in absorption process. Formation followed by dissociation of vibrationally excited O_2^+ is the strongest channel over the full wavelength range studied. Ground and vibrationally excited $O_2^+(\ ^2\Pi_g\ ,a\ ^4\Pi_u\ ,A\ ^2\Pi_u)$ are formed and dissociated to ionic products via one and two-photon processes. Neutral dissociation to form electronically excited atoms is important at longer wavelengths and becomes noticeably less important at shorter wavelengths. These results agree with and expand on a previous study from our lab of O^+ formation at a single (2+1) REMPI wavelength and the results obtained in this study are found to complement our study of the electronically analogous counterpart S_2 where most of S^+ ions arise from electronically excited S^* atoms.

5.1 Introduction

Above the Schumann-Runge continuum, at energies higher than 9.5 eV, molecular oxygen exhibits a complex absorption spectrum dominated by Rydberg states correlating to the higher excited states of the O_2^+ ion (Figs. 1.1 and 1.3 of this thesis). Following absorption, the molecule can undergo many processes including photoionization (for photon energy > 12.097 eV), photodissociation to neutral O atoms where one of the O atoms is electronically excited (>14.263 eV) and ion-pair dissociation (>17.27 eV), as outlined in Chapter 1 of this thesis. When the energy of an electronic state of a neutral atom or molecules exceeds the first ionization energy the state is called a superexcited state[1]; these are typically Rydberg states that converge to internally excited states of the ion, as well as valence excited states lying above the ionization energy. Superexcited states can arise from the excitation of electrons from orbitals more strongly bound than the highest occupied molecular orbital (HOMO). The presence of many rapid decay channels often causes their lifetimes to be very short. Superexcited states can autoionize and dissociate into neutral fragments but also couple with each other and then decay. While it is expected that a vast number of superexcited states exist in polyatomic molecules, bound Rydberg states are the states that can be most easily observed and characterized.

The concept of superexcited states were suggested by Platzman in the early 1960s[1] and confirmed by Hatano experimentally in the 1990s.[2,3] Since then, much progress has been made in understanding the dynamics of superexcited states, especially those of O_2, by means of studies using synchrotron radiation, spectroscopy of fluorescence radiation, imaging techniques and modern spectroscopy techniques such as zero kinetic energy (ZEKE) spectroscopy and mass-analyzed threshold ionization (MATI)[4,5,6,7,8]. Superexcited states give fundamental test cases for probing short-lived intermediates which show complex decay behavior due to competition between autoionization and neutral dissociation. This competition is an extra tool for investigating molecular superexcited states since it cannot be seen in a superexcited atom[9]. Autoionization (pre-ionization) and pre-dissociation have long been recognized as competitive channels for the decay of superexcited states. However, both processes are usually considered independently within the framework of the Born-Oppenheimer separation of nuclear and electronic motion[10,11,12,13]. Processes other than autoionization and neutral dissociation such as emission of fluorescence and ion pair formation are possible, although their contribution is found so far to be small.[6]

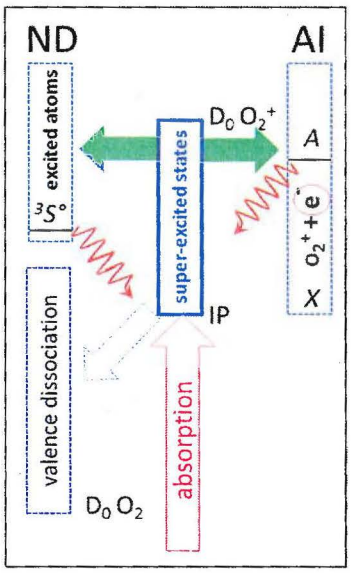

Figure 5.1: Schematic diagram for measurements (in red) probing the dynamic properties of super-excited states of O_2.

Measurements, highlighted in red, used previously to characterize super-excited states of O_2 are shown schematically in Figure 5.1. *Absorption spectra* with increasingly higher resolution over the years have been reported[14], tracing out the position, strength, and line-width of the superexcited states. After excitation, two main exit channels are indicated: ND – neutral dissociation – where the molecule dissociates to one ground (or 'valence') state O atom ($O\,1s^2 2s^2 2p^4$ (^{3}P, ^{1}D, or ^{1}S) plus an electronically excited atom, where the lowest energy possibility is the $O(1s^2 2s^2 2p^3 3s)^5S°$+ $O(^3P)$ pair. In the case of ND, it is possible to measure *fluorescence* at 130 nm in the vacuum ultraviolet from O atoms produced in the $O(1s^2 2s^2 2p^3 3s)^3S°$ state[15], or emission of higher states to this or the lower energy^{5}S° state in the visible region[16]. Detection of dissociation to two valence atoms requires an advanced pulsed laser detection method such as laser induced fluorescence (LIF) or resonance enhanced multiphoton ionization (REMPI).[17]

The other exit channel, labeled AI in fig. 5.1, indicates (Auto)-Ionization, where O_2^+ and an electron are formed. In this case it is possible to measure the total *electron yield* (photoionization spectrum)[14], the dispersed electron kinetic energy spectrum[18] or the yield of near-zero kinetic energy electrons[19](threshold electron spectrum). Ionization can produce O_2^+ in the $X^2\Pi$ ground electronic state but also in increasingly higher excited states, the lowest lying being the $a^4\Pi$ and $A^2\Pi$ states. As the *A*-state emits *fluorescence* down to the ground state in the ultraviolet

region, studies with emission detection (also sensitive to the polarization of the emission with respect to the direction of the excitation light polarization) have been reported [20]. Note that the threshold for O^+ formation is 17.27 eV, where the (O^+,O^-) ion pair can be formed. Our group has studied ion pair production using femtosecond laser excitation[21] , this process is not observed under the conditions of present study.

In this work superexcited states lying between the IP of O_2 and the first dissociation limit of O_2^+ are studied; but super-excited states also extend too much higher energy. The energy region of superexcited states in $O_2$is accessed here by three-photon excitation, where the energy sum of the first two photons is resonant with an allowed two-photon transition to a Rydberg state of the molecule. In this chapter it will be shown that detailed information on superexcited state dynamics is obtained from imaging the O^+ ions that are observed which is complementary to that obtained following direct one-photon excitation. The three-photon (or XUV) region is not continuously accessable in this work, instead specific wavelengths can only be probed when Rydberg states are found at the two-photon level. However, there are numerous such 'doorway' states.

Several Rydberg series converging to excited states of the O_2^+ ion have been identified using XUV spectroscopy (see Chapter 1 and Fig. 1.3 of this thesis). In contrast, only the lower members of the series converging to the ground state of O_2^+(abbreviated now as R-X)have previously been identified.[22,23,24]. In the last few decades the low-lying *gerade* R-X states of O_2 have been assigned experimentally. Park *et al.*[25] and Chupka *et al* [26] reported (2+1) REMPI studies of the *4s-3d* and *5s-4d* Rydberg complexes using tunable pulsed laser radiation in the 235-215 nm region. Later, Pratt *et al.*[27] continued the observations of Rydberg states further to higher energies up to the $O_2^+X^2\Pi_g(v^+=0)$ ionization threshold. REMPI spectra were obtained in the region 215—200 nm and exhibited a number of transitions to *ns* and *nd* Rydberg states with n = 5-9 and $v' = 0$ and $v' = 1$, as well as transitions to the previously unobserved *5s-4d*,$v' = 3$ levels.[27] In Fig. 5.2.a the positions of these previously assigned Rydberg states are indicated; these states at the two-photon level are used as doorway states for reaching superexcited states at the three-photon level.

Competition between neutral dissociation and autoionization in O_2 is not yet fully understood, especially in the energy region well beyond the ionization potential (IP). This is due to low cross sections and the experimental difficulties to observe all major product channels. Synchrotrons sources are typically used to study O_2 superexcited states, where it is possible to detect a) direct absorption, b) ionization (electrons, and O^-,O^+, and O_2^+ ions); and c) fluorescence from electronically excited

O_2^+ and electronically excited (O*) atoms. Absolute cross sections for 'total' dissociation (difference between absolute absorption and ionization cross sections) and ionization are shown in panels c) and d) of Fig. 5.2, which were reported in 1993 by Holland et al[14]. The resolution of these spectra have been improved recently with, more powerful and very narrow-bandwidth synchrotron studies. In addition, studies with tunable high-resolution VUV-XUV lasers of O_2 using sum and difference frequency four-wave mixing have been reported. Most recently, the group of Mo have combined VMI detection with tunable XUV excitation, detecting O^- from ion-pair dissociation[28], and electronically excited O^* atoms from neutral dissociation[29]. This latter study is particularly relevant to this chapter: using XUV generation from table-top pulsed dye lasers it is possible to synchronize the XUV with a tunable UV pulse for REMPI product detection; this is not possible in synchrotron sources which usually operate in a free-running mode.

In panel b) of Fig. 5.2 results from Ukai et al[30] are shown where VUV emission at 130.4 nm was used to detect ND processes in O_2. As seen from Figure 1.4 of Chapter 1, which shows the energy level structure of the O atom, the $3p\,^5P°$ state can radiate to the $3s\,^5S°$ state by emission of 777 nm, and the 3p ^3P state can radiate to the $3s\,^3S$ state by emission at 845 nm, where the later state then emits rapidly to the ground state in the VUV at 130.4 nm. Previous emission studies detecting VUV radiation are thus sensitive only to the 3s $^3S°$and 3p ^3P states, the quintet states remained unprobed. Recently, Karawajczy et al [16] reported studies of the IR-visible emission In the XUV region below 20 eV. These authors show the n=3s ($^5S°$,$^3S°$) and n=3p (^5P,^3P) atoms are the main excited atom products of ND, and concluded that dissociation to the 3s $^5S°$ state is the strongest channel below 20 eV. This is somewhat in contrast to the the results of the 'total' dissociation spectrum of O_2 reported by Holland et al, panel c)[14] of Fig. 5.1, which suggests that the n=3s $^3S°$ channel is strongest.

This study uses a focused laser operating in the 200-240 nm region (6.1 – 5.1 eV), which has sufficient energy and flux to detect all four excited states by one-photon ionization. However, only the O 3s $^5S°$ state is metastable and is thus likely to be ionized with the highest probability. Mo and coworkers[29] using a UV laser operating in the 220 nm region at >1 mJ/pulse and focused with a 30 cm lens (quite similar conditions as this study) have shown that photoionization of the 3p ^3P level is saturated thus emission to the 3s $^3S°$ level can be ignored. Under typical conditions the ionization step should also be saturated and that the raw data measured in this study is representative for the $^3P/^3S°$ yield ratio.

In addition, it is expected that the measured yield ratios between quintet and triplet state products are also at least qualitatively representative of the actual yields.

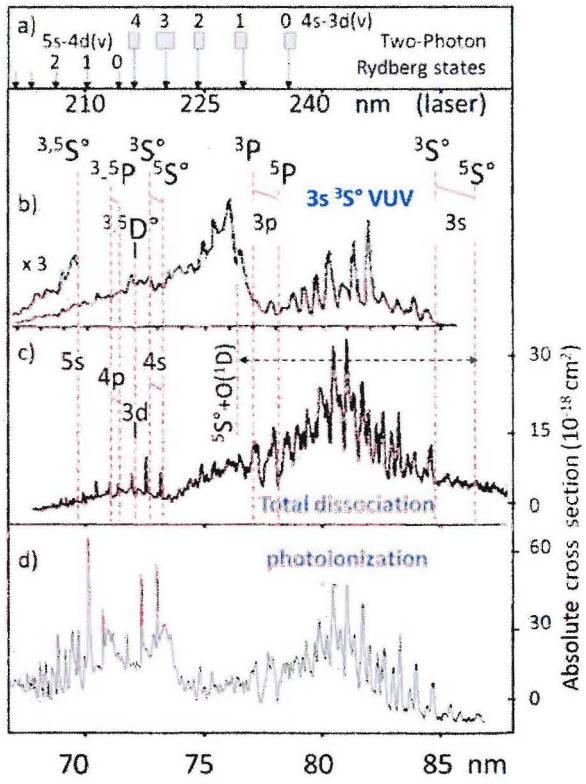

Figure 5.2: Ionization and dissociation channels for O_2 in the 68-87 nm region (~18-14 eV). Panel a): positions of the two-photon Rydberg states used in this study. For the 4s-3d (v=0-4) series a number of different electronic states are probed, the boxes above each arrow indicates the wavelength ranges (see also Table 1). Vertical lines in panels b) and c) indicate the positions where each product (e.g. the lowest energy n=3s ($^5S°$,$^3S°$)) channel opens, with O ...$2p^4\,^3P$ as co-product. Panel b) shows results of Ukai et al (Ref. 30) who detected O 3s $^3S°$ emission at 130.2 nm, while the lower panel shows the total photodissociation cross section from Holland et al. Note that O 3s $^3S°$ emission detection does not distinguish between the O^3P and O^1D co-product channels, and that the total dissociation cross section increases significantly at the threshold for the O $^5S°$+O^1D channel at 77 nm. Panels c) and d) show the total dissociation and photoionization yields, respectively. Both are taken from Holland et al*

(Ref. 14) who reported the absolute cross sections indicated on the right vertical axes.

Velocity map imaging (VMI) combined with REMPI studies[17, 31] has the advantage that all product channels including photoelectrons, O_2^+, O^+,O^- and excited O* atoms can be efficiently detected. In addition, the technique is ideally suited for simple diatomic molecules such as O_2 because the large vibrational spacing and limited number of possible atomic product states results in a unique KER for each final quantum state channel. The present work builds on a previous study in the ultraviolet (UV) region by Eppink and Parker[32] who studied the competition between autoionization and neutral dissociation of superexcited state of molecular oxygen which was accessed via (v=2, N=2) level of the 3dπ($^3\Sigma_g^-$) two-photon Rydberg state at 11.02 eV. This article describes autoionization and neutral dissociation of superexcited states reached via a full range of *ns* and *nd* Rydberg states up to n=11. A comparison of the photodynamics of the superexcited states of O_2 with those of the isovalent S_2 molecule is presented in Chapter 6 of this thesis.

5.2 Experiment

The velocity map imaging apparatus has been described in detail elsewhere[33] so only a brief overview will be given here. The experimental setup consists of differentially pump source and detection vacuum chambers, a pulsed valve (Jordan), laser beam and electrostatic lenses. The pulsed valve (operated at 10 Hz) has a nozzle with a 0.4 mm diameter which produces a pulsed supersonic expansion of pure O_2 that is skimmed (with a 2mm skimmer) 20mm downstream from the nozzle. This collimated beam is directed parallel to the axis of a time-of-flight (TOF) mass spectrometer. At an additional 100mm downstream the molecular beam passes through a 1mm hole in the repeller electrode and enters the region between the repeller and extractor electrodes, where it is crossed at right angles with the photolysis/ionization laser beam. In the VMI experimental setup, the electrostatic lens consists of three electrodes (repeller, extractor and ground electrode) which are flat plates with central holes to allow the molecular beam to pass through them. The electrostatic lens is set to project all ions of the same velocity to the same point on the 2D detector, independent of their position of formation.

A dye laser pumped by a frequency doubled or tripled pulsed Nd:YAG laser (Continuum Surelite) operating at a repetition rate of 10 Hz produced wavelengths between 225 and 200nm by using different mixtures of dyes like Rhodamine 6G, Sulforhodamine B, DCM and Fluorescence 548. A mixture of Sulforhodamine B and DCM dyes was also used in order to cover wavelengths between 600 and 625 nm.

Subsequently, the output of the dye laser (Radiant Dye Narrow Scan) was frequently doubled and tripled by focusing into a KDP crystal and a beta barium borate (ß-BaB2O4, BBO) crystal respectively. Later on, the fundamental laser beam was separated from the frequency-doubled and tripled beam by a Pellin-Broca prism. The frequency tripled laser beam with approximately 1mJ power is focused with a 15cm lens onto the molecular beam and ions are extracted towards a pulsed (dual MCP with phosphor screen) imaging detector read by a charge-coupled device CCD camera. The MCPs are pulsed on to coincide with the arrival time of the desired ion mass, which yields mass selectivity for O^+. All the timing was controlled by three delay/pulse generators running at 10 Hz. The data acquisition was performed using DaVis software (LaVision) with add in image analysis and event counting[31] routines. Typically, 5000 laser shots were used to produce the final raw (crush) images which were then inverted using a basis set expansion algorithm based on the original BASEX method[34]. From the inverted images the ion speed and angular distributions are extracted.

$O(^3P_2)$ detection (2+1) REMPI wavelength (225.65 nm) was used for calibration, following dissociation of O_2 at one-photon and two-photon levels. One-photon dissociation in the Herzberg continuum leads to the $O(^3P_2)+O(^3P_j)$ channel where the O atom total kinetic energy release is 0.38eV, and two-photon dissociation leads to $O(^3P_2)$ $+O(^1D_2)$, and $O(^3P_2)+O(^3P_j)$, where the O atom kinetic energy release (KER)is 3.91 and 5.88eV, respectively. The values of TKER are determined from TKER = $h\nu - D_0 - E_{int}$(atoms) where D_0 = 5.117 eV is the bond dissociation energy for O_2 and E_{int} is the internal energy of the product atoms. The two-photon ^{1}D channel is used for initial calibration of the images.

5.3 Results

5.3.1 Overview and assignment of the images

A sample of O^+images taken at various two-photon resonances in the energy region of 10.5-12.3 eV at two-photons, 15.8-18.3 eV at three-photons, over the laser wavelength range of approximately 200-240 nm (also indicated in panel a) of Fig. 5.2) is shown in figure 5.3. Images are labeled by their three-photon energy; the doorway state of each image is found in Tables 1 and 2. These two dimensional velocity mapped images yield a wealth of information on the dynamics of autoionization and dissociation of neutral O_2 as well as O_2^+. Most of the rings seen in the images show a parallel character, the strongest images correspond to excitation to the v=2 level of the various Rydberg states excited, in accord with Franck-Condon overlap, and the image size does not simply increase with photon energy since, as shown in this section, dissociation at higher

energies occurs to higher-lying limits where the atomic products contain increasing internal energy.

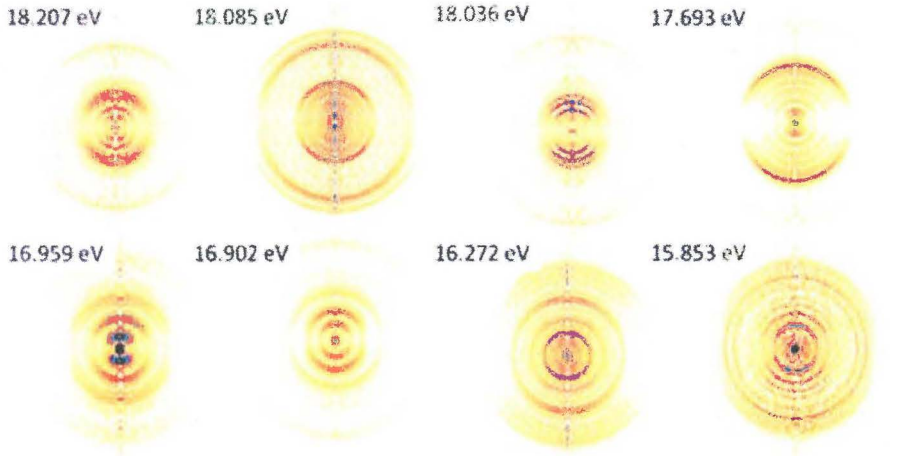

Figure 5.3: A sample of inverted velocity mapped O^+ images in the wavelength range 200-240 nm. Images are labeled by their three-photon energy with more details in tables 5.1-2. The laser polarization lies along the vertical axis of this figure.

An overview of the ionization/dissociation pathways for forming O^+ when molecular oxygen is excited at different wavelengths in the region 200 to 235nm is given in figure 5.4. Two mechanisms, indicated by their available kinetic energy $E_{avail}(3)$ and $E_{avail}(4)$ explain the observed rings: (1), $E_{avail}(3)$, electronically excited oxygen atoms are formed by predissociation of the superexcited states at the three-photon level, and the atoms are then ionized by an additional laser photon, or (2) $E_{avail}(4)$, O_2^+ ions formed by autoionization at the three-photon level are subsequently photodissociated by absorbing one or two more photons. If the laser wavelength is tuned to a REMPI line of the O ($^3P,^1D,^1S$) valence atoms then O^+ atoms are also detected for dissociation at the one- or two-photon level with $E_{avail}(1,2)$. Only the lowest dissociation limit, L1, of O_2^+ is shown in Fig. 5.4. Following literature conventions (and to avoid confusion with the O_2 dissociation limits $D_{0\text{-}6}$) the O_2^+ dissociation limits below 27 eV are labeled by L1-L6 in Table 5.1 along with the molecular states that correlate adiabatically with each limit. Like O_2, O_2^+ has a plethora of excited electronic states as is evident in Table 5.1.

Table 5.1. *Dissociation limits of* O_2^+ *and the correlating molecular states.*

O_2^+ Dissociation Limits	Products	Energy (eV)	Moleculare State
L1	$O^+(^4S)+O(^3P)$	18.733	$^{2,4,6}(\Sigma^+,\Pi)_{g,u}$
L2	$O^+(^4S)+O(^1D)$	20.700	$^4(\Sigma^-,\Pi,\Delta)_{g,u}$
L3	$O^+(^2D)+O(^3P)$	22.057	$^{2,4}(\Sigma^-,\Sigma^+,\Pi,\Delta,\Phi)_{g,u}$
L4	$O^+(^4S)+O(^1S)$	22.923	$^4\Sigma^-_{g,u}$
L5	$O^+(^2P)+O(^3P)$	23.750	$^{2,4}(\Sigma^-,\Sigma^+,\Pi,\Delta)_{g,u}$
L6	$O^+(^2D)+O(^1D)$	24.025	$^2(\Sigma^-,\Sigma^+,\Pi,\Delta,\Phi,\Gamma)_{g,u}$

Assignment of almost all of the peaks in the TKER curves is straight forward using the energy positions of the O* states listed in the NIST atomic data website and the positions of the $O_2^+(X,a,A)$ state vibrational levels listed by Akahori et al.[19] Peak TKER positions for dissociation of the super-excited state at 3hν to an excited atom channel are calculated by $3h\nu-E(O^*)-D_{0,1}$ (where D_0= 5.117 eV and D_1=1.967+D_0 for the $O(^1D)$ coproduct is used), and the O_2^+ vibrational level dissociation peaks are calculated for each dissociation limit L*i*(*i=1-6*) by $E(O_2^+,v)+(1 \text{ or } 2)*h\nu-Li$. As the photon energy increases the vibrational progressions for $O_2^+(X,a,A)$ states dissociating to the different L1-L6 limits give a large number of possible final product channels. In almost all cases, however, the accuracy of the TKER value of each peak (±0.002 eV) extracted from velocity mapped inverted images is sufficient to uniquely determine the active channel.

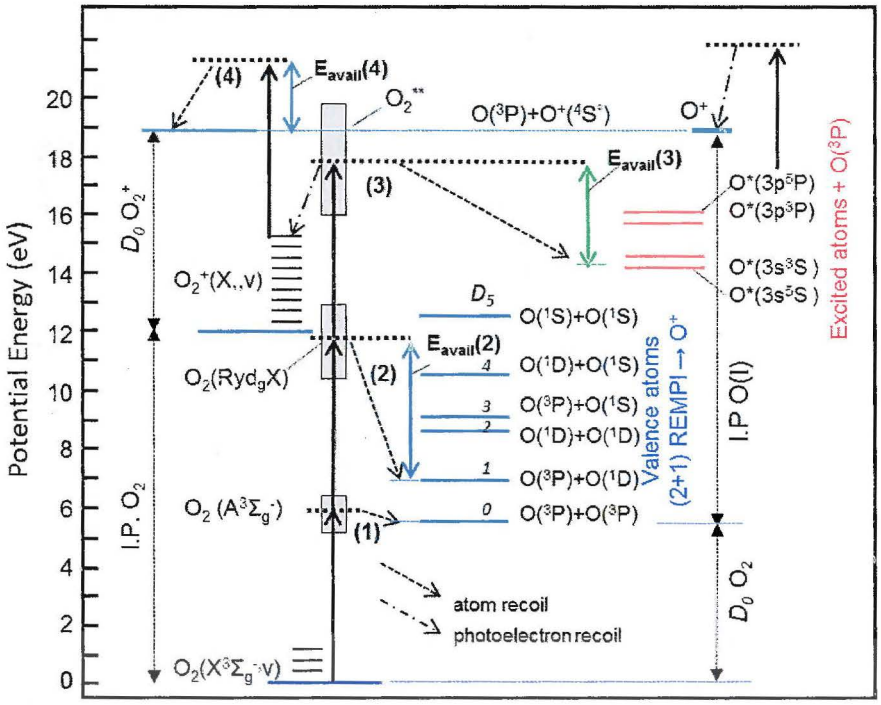

Figure 5.4: Schematic energy level diagram showing multiple photon excitations toselect O_2 and O_2^+ electronic states and dissociation limits. Vertical black arrows indicate the energy of a 220 nm photon, which exceeds D_0 at the one-photon level. The energy difference $E_{avail}(1,2)$ appears as O atom kinetic energy release. At the two-photon level, Rydberg states converging to $O_2^+X(^2\Pi_g)$ are energetically accessible. The processes that determine the speed and angular distributions of the measured O^+ ions are labeled E_{avail} and shown with green double headed arrows. Excitation to a superexcited state labeled O_2^{**} at the three-photon level leads to (auto) ionization to $O_2^+X(^2\Pi_g)$ or higher states can take place along with (pre)dissociation to an O excited atom limit, E_{avail} (3). Ion pair formation, threshold 17.27 eV is not shown in this figure. In order to form O^+ ions, photoionization of O* or photodissociation (4) of O_2^+ is found to be necessary.*

5.3.2 Doorway levels: Two-photon allowed Rydberg states of O_2

In the first step of the excitation process, Rydberg states of O_2 are accessed by simultaneous absorption of two photons. A group of two-photon resonant Rydberg states of n=3-11 of *nd* and *ns* series converging

to $X\ ^2\Pi_g$ states of O_2^+ ions have been selected.[25,26,27 ,35,36] Owing to the large number of electronic states (Fig 1.4) arising from coupling of an *nd* electron with the $O_2^+(X^2\Pi_g)$ ion core and to spin orbit interaction mixing the singlet and triplet levels, this was a complex assignment. Most of the two-photon MPI signals in the *3d* region belong to transitions to upper states of Σ symmetry. In this work, the Rydberg states listed in table 1 are accessed. With a cold molecular beam, in almost all cases the (lowest) N=1 rotational level is excited via a Q-branch transition. A more detailed study of the rotational state dependence of the observed 0^+ signals is progress.

Table 5.2: *Measured two-photon resonant low lying (4s-3d) Rydberg states of molecular oxygen. Images taken at the wavelengths tagged by red are described in detail in the text.*

Rydberg state	Vibrational energy level	One-photon wavelength (nm)	On-photon energy (eV)	Two-photon Energy (eV)	Two-photon Energy (cm^{-1})	Three-photon energy (eV)	Figure number
$4d\pi\ ^3\Sigma_1^+$	$(v=1)$	215.958	**5.741**	11.482	92611	17.223	5.17
$4d\pi\ ^3\Sigma_0^-$	$(v=1)$	216.297	**5.732**	11.464	92466	17.196	5.16
$4d\pi\ ^3\Sigma_1^-$	$(v=1)$	216.410	5.729	11.458	92417	17.187	
$3d\pi\ ^1\Sigma_0^+$	$(v=3)$	219.320	**5.653**	11.306	91191	16.959	5.15
$3d\pi\ ^3\Sigma_1^+$	$(v=3)$	220.059	**5.634**	11.268	90885	16.902	5.14
$3d\pi\ ^3\Sigma_1^-$	$(v=3)$	220.568	5.621	11.242	90675	16.863	
$3d\pi\ ^1\Sigma_0^+$	$(v=2)$	223.762	**5.542**	11.084	89401	16.626	5.13
$3d\pi\ ^1\Delta_2$	$(v=2)$	223.995	5.535	11.070	89226	16.605	
$3d\pi\ ^3\Sigma_1^+$	$(v=2)$	224.523	5.522	11.044	89078	16.566	
$3d\pi\ ^3\Sigma_0^-$	$(v=2)$	224.848	5.514	11.028	88949	16.542	
$3d\pi\ ^3\Sigma_0^-$	$(v=2)$	224.869	**5.5135**	11.027	88941	16.541	5.12
$3d\pi\ ^3\Sigma_1^-$	$(v=2)$	224.995	**5.510**	11.021	88891	16.532	5.11
$3d\pi\ ^1\Sigma_0^+$	$(v=1)$	228.410	**5.428**	10.856	87562	16.272	5.9
$3d\pi\ ^3\Sigma_1^+$	$(v=1)$	229.213	5.409	10.818	87255	16.227	
$3d\pi\ ^3\Sigma_0^+$	$(v=1)$	229.353	5.406	10.811	87199	16.217	
$3d\pi\ ^3\Delta_3$	$(v=1)$	229.510	**5.402**	10.804	87142	16.206	5.8

Rydberg state	Vibrational energy level	One-photon wavelength (nm)	On-photon energy (eV)	Two-photon Energy (eV)	Two-photon Energy (cm^{-1})	Three-photon energy (eV)	Figure number
$3d\pi\ ^3\Delta_2$	$(v = 1)$	229.608	**5.395**	10.790	87029	16.185	5.7

The pattern of higher-lying Rydberg states is relatively simple in appearance with the exception of the region between 96000 and 96500, where there are number of overlapping bands. In this study images at some unassigned O^+ producing resonances in this region are obtained, their one-photon energy is indicated in the text. Pratt et al.[27] assigned most of the higher lying two-photon resonant Rydberg states of molecular oxygen. The spin-orbit splitting ($X\ ^2\Pi_{1/2g} - X\ ^2\Pi_{3/2g}$) between two states with different Ω, but the same n and v, is around 200 cm^{-1}. Here, superexcited states have been accessed via these two-photon higher-lying Rydberg states, as listed in table 5.3.

Table 5.3: *Observed two-photon resonant higher Rydberg states of molecular oxygen.[27,37] Images taken at the wavelengths tagged by red are described in detail in the text, their figure numbers are also listed.*

Rydberg state (n,v)	Symmetry Ω		One-photon wavelength (nm)	One-photon Energy (eV)	Two-photon Energy (cm^{-1})	Three-photon Energy (eV)	Figure number
Unassigned			200.822	6.1737	99588	18.521	5.23
Unassigned		–	203.281	6.099	98386	18,297	
(10,1)		3/2	**203.348**	6.097	98353	18,291	5.22
(11,1)		1/2	203.381	6.096	98337	18,288	
(6,2)		3/2	203.482	6.093	98289	18,279	
(10,1)		1/2	203.783	6.084	98144	18,252	
(9,1)		3/2	203.883	6.081	98095	18,243	
(6,2)		1/2	**204.286**	6.069	97902	18,207	5.21
(8,1)		1/2	**205.029**	6.047	97547	18,141	5.20
Unassigned		–	205.662	6.0284	97248	18,085	
(7,1)		1/2	206.120	6.015	97031	18,045	
(5,2)	$^1\Sigma_g^+$	3/2	206.223	6.012	96982	18,036	

Rydberg state (n,υ)	Symmetry Ω		One-photon wavelength (nm)	One-photon Energy (eV)	Two-photon Energy (cm^{-1})	Three-photon Energy (eV)	Figure number
(5,1)	$^1\Sigma_g^+$	3/2	**210.245**	5.897	95135	17,693	5.19
(5,0)	$^1\Sigma_g^+$	3/2	**214.463**	5.781	93256	17,343	5.18

5.3.3 TKER curves and peak assignments

A large number (>40) of O^+ images were measured and analyzed across the 240-200 nm laser wavelength range. In this section, total kinetic energy release (TKER) curves are shown for a range of images over the full wavelength range in order to illustrate their trends. Raw images for each doorway state are first quadrant symmetrized and then inverted, and the TKER curves are extracted and calibrated as described in Section 5.2. For determining branching between AI and ND the full angular distribution is integrated and deconvoluted. ND, when observed, often shows an angular distribution characterized by a low (β<1) beta parameter (Chapter 1), while AI almost always shows a more positive beta parameter (β>1). When ND is present two TKER curves are usually displayed: for the vertical (θ=0-30°) and horizontal (θ=60-90°) angular regions of each image, otherwise, the TKER curve shown is for the full angular range.

As the first example, TKER curves for the lowest energy doorway state, $3d\pi^3\Sigma_{0g}^-$(v=0) at 234.547 nm, (5.286 eV, 10.572 eV, or 15,853 eV = 85270 cm^{-1} at the one- two- and three-photon levels, respectively, Table 5.2), are shown in Fig. 5.5.

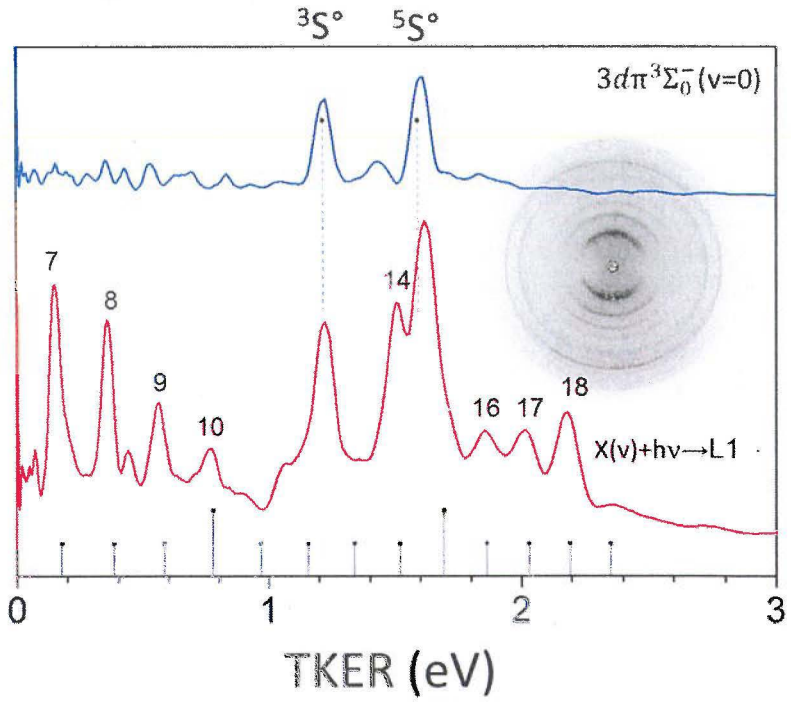

Figure 5.5: TKER curves and gray-scale raw image for O^+ formation via the $3d\pi\ ^3\Sigma_{0g}^-(v=0)$ Rydberg state at 234.547 nm or 5.286 eV. Darker regions in the image correspond to stronger signal. The laser polarization lies in the plane of the image in the vertical direction. The red (blue) curve is obtained by integrating the inverted image over the vertical 0-30° (horizontal θ=60-90°) angular regions. The vertical axis relative scale is arbitrary; branching ratios between different channels AI and ND are described later in the text. ND products, n=3s ($^5S°$,$^3S°$), labeled on the top axis are clearly seen in the horizontal profile. The AI channel appears most strongly in the vertical profile where O^+ from photodissociation to the lowest limit O_2^+ [X(v)+hν→ L1=18.733 eV], Table 5.1; v is labeled in black above selected peaks. A stick spectrum near the lower horizontal axis indicates the position of the O^+ peak created by photodissociation of the labeled $O_2^+X(v)$ state to the L1 limit. For the AI channel the maximum possible $O_2^+X(v)$ state that can be formed by AI at the three-photon level is X(v=18), and photodissociation by 5.286 eV photons of $O_2^+X(v)$ is possible for all v states with v>6.

Note that even though the image shown in Figure 5.5 is taken at the lowest energy doorway state, the *n=3s*($^5S°$,$^3S°$) O atom ND products are formed significantly (>1 eV TKER) above threshold. Unfortunately, this is also higher in energy than the 14.6-15.2 eV range studied by Zhou et

al,[29] who used direct XUV excitation with imaging detection of the *n=3s* ($^5S°$,$^3S°$) ND products, which makes direct comparison with their results difficult. O_2 has lower-lying *n=3p* molecular Rydberg states but these are two-photon forbidden and cannot be used as doorway states to the three-photon level. The lowest molecular Rydberg states, the two-photon allowed *n=3s* $C^3\Pi$ and $d^1\Pi$ states require lower energy photons that do not cause O^+ formation.

At a slightly shorter in wavelength, via the $^3\Sigma_1^+$(v=0) state at 234.236 nm, the O*^{5}P channel becomes visible in the TKER curve and shows a strongly negative beta parameter, Figure 5.6. This is typical of the excited atom channels, the most anisotropic character is observed near threshold.

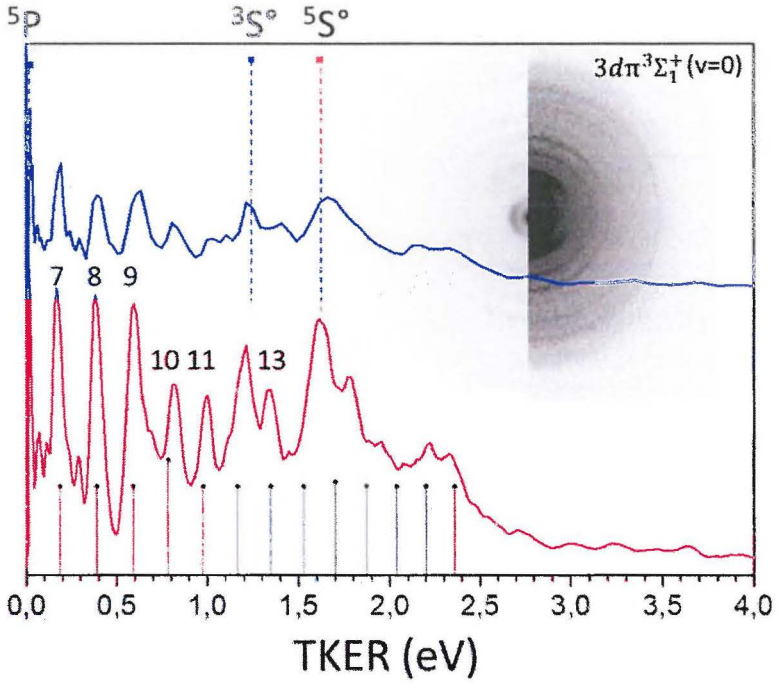

Figure 5.6: TKER curves and gray-scale image for O^+ *formation via the* $3d\pi\ ^3\Sigma_1^+(v=0)$ *Rydberg state at 234.236 nm or 5.293 eV. The raw image is split and shown at two intensity levels so that the strongest peak (the low velocity O*^{5}P excited atom signal) with strong negative anisotropy of is on-scale. See the caption of Fig. 5.5 for more details.*

Moving to the 3s-4d (v=1) manifold, TKER curves and O^+ and photoelectron images taken at 229.608 nm, 5.395 eV, are shown in Figure

5.7 for the $3d\pi^3\Delta_2$ (v=1)state. This is the longest wavelength where a photoelectron image with a good signal to noise ratio could be obtained. In the higher electron energy region a trace of the time-of-flight (TOF) electron spectroscopy data of Colson and coworkers[25] is included. While the electron TOF data is limited to 3 eV and above, its resolution is superior, but the result agrees well with the photoelectron imaging data. It is clear from these curves that the main photoelectron signal is due to direct ionization to O_2^+X (low v) levels with a clear propensity for $\Delta v=0$ production. The autoionization signal represented by the O_2^+(high v) levels is a small but still significant fraction of the total signal. Note that O^+ cannot be formed from the photodissociation of O_2^+X (v<6). The area of the peaks corresponding to the $O^*{}^5S^\circ$ state are used to scale the O^+ and e⁻ TKER curves, which are integrated over the full angular distribution.

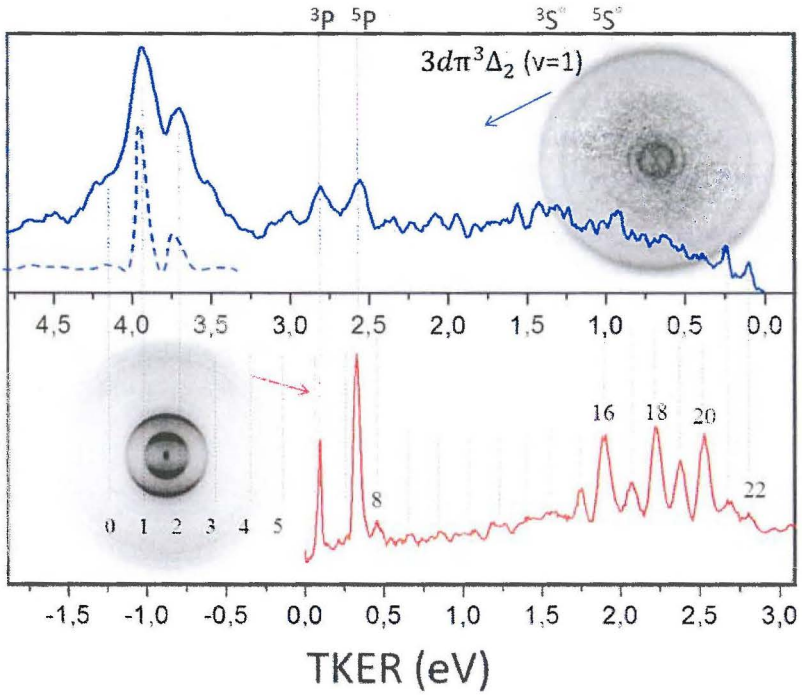

Figure 5.7: TKER curves and gray-scale images for O^+ *(red curve)and e⁻ (blue curve) formation via the* $3d\pi\,{}^3\Delta_1$ *(v=1) Rydberg state at 229.608 nm or 5.395 eV. See the caption of Fig. 5.4 and the text concerning the photoelectron image analysis and scaling for more details.*

The relative scaling of the two curves is still qualitative, but the electron image indicates a relatively smooth distribution of O_2^+X (high v) levels is created but the O^+ signal is modified by the Franck-Condon factors for

overlap of the $O_2{}^+X$ (high v) levels with the dissociation continuum, possibly the repulsive wall of the $A^2\Pi_u$ state, which correlates with limit L1 (see the PE curves in Chapter 1 and Table 5.1).

At shorter wavelengths in the 3s-4d (v=1) manifold there is sufficient energy at the three-photon level to access the $O_2{}^+a$(v=0) state, which lies close in energy to $O_2{}^+X$ (v=21). Just above the threshold, no a-state evidence for formation or dissociation is seen in the images shown in Fig. 5.7, taken at $3d\pi\ ^3\Delta_1$ (v=1) Rydberg state at 5.395 eV. The O^+ image taken at very slightly higher energy of 5.402 eV, via the $3d\pi\ ^3\Delta_3$ (v=1) Rydberg state at 229.510 nm shown in Figure 5.8 shows new peaks in the 0.5-1.5 TKER region not seen in Fig. 5.7. The same peaks are seen and are more easily analyzed at the next step up in energy via the $^1\Sigma_0{}^+$(v=1) state 228.410 nm, 5.428 eV shown in Fig. 5.9. In both figures 5.8 and 5.9, strong peaks are observed near TKER = 1 eV. In Fig. 5.9 two peaks can only be assigned to photodissociation of the$O_2{}^+a$ (v=1) state to the L2 limit at 20.700 eV, and at slightly higher TKER, two-photon dissociation of $O_2{}^+X$ (v=1) to the L3 limit at 22.057 eV. In both of these peaks in Fig. 5.9 Δv=0 propensity appears to favor production of the v=1 of the X- and a-state from the two-photon Rydberg state. For the $O_2{}^+a$(v) state, formation of $O_2{}^+a$(v=2) is energetically not possible by excitation at the three-photon energy of 16.272 eV; and furthermore, no signal is observed for dissociation of $O_2{}^+a$(v=0), which could most simply indicate that it is not formed to any significant extent, since Δv=-1. Similar conclusions can be made for Fig. 5.8 where the lower energy peak is again assigned to photodissociation of $O_2{}^+a$ (v=0) to the L2 limit at 20.700 eV and the higher peak to two-photon dissociation of $O_2{}^+X$(v=1) to the L3 limit at 22.057 eV. For the photon energy used to create the O^+ image shown in Fig. 5.8, only $O_2{}^+$a(v=0) can be formed.

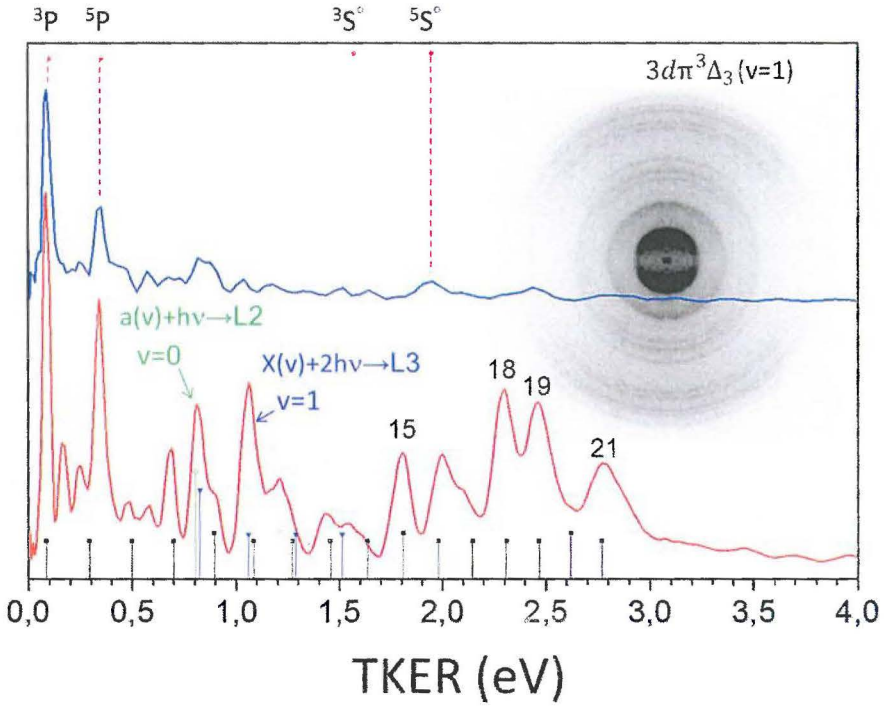

Figure 5.8: TKER curves and gray-scale image for O^+ *formation via the* $3d\pi\ ^3\Delta_3$ *(v=1) Rydberg state at 229.510 nm or 5.402 eV.*

Two-photon dissociation of O_2^+X(low v) to the L3 limit is weak in most cases, with the exception of signals seen in Figs. 5.8 and 5.9 but is also observed in other images taken at higher laser intensity, also when the lower-lying C- and d- $^{3,1}\Pi_g$ states are probed.

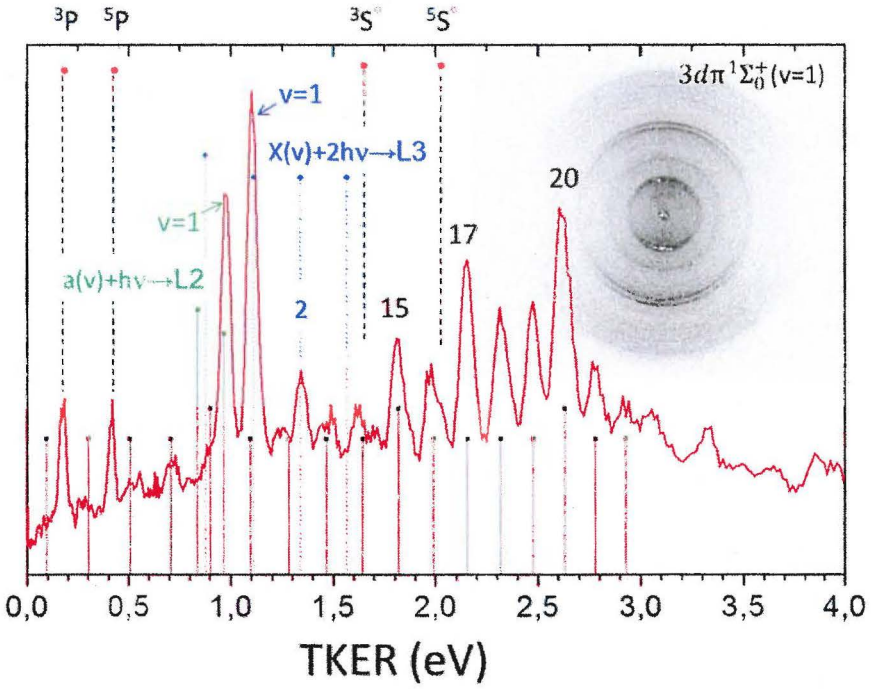

Figure 5.9: TKER curves and gray-scale image for O^+ formation via the $3d\pi\ ^1\Sigma_0^+(v=1)$ Rydberg state at 228.410 nm or 5.428 eV.

The strongest signals for 2+1 REMPI of O_2 is via Rydberg states of the 3s-4d(v=2) manifold, particularly for states of $^3\Sigma_g$ character which are directly two-photon allowed. Spin-orbit mixing provides significant transition strength to the $^1\Sigma_g$ states in this region. Figure 5.10 shows an overview of TKER spectra taken at various close-by resonances in the lower energy part of the v=2 region, under conditions where the rotational temperature of the molecular beam was higher than normal in order to detect higher rotational states than N=1. The resonances shown cover the two-photon energy range of 88,935 to 88,841 $cm^{-1}$and include the $3d\pi\ ^3\Sigma_0^-$, $^3\Sigma_1^-$ and the $^3\Delta_2$ (v=2) Rydberg states. As can be seen in Fig. 5.10, the basic pattern of the TKER curves are quite similar, with some variation in the amount of AI vs ND, and more variation in the relative yields of the ND atoms, in particular the ratio of O* ^{3}P to O* ^{5}P.

The previously reported [32] O^+ image taken at the $3d\pi\ ^3\Sigma_1^-(v=2)$ state at 224.995 nm (blue curve in Fig. 5.10) is shown in more detail, with better TKER resolution in Fig. 5.11. Almost all peaks not assigned to ND are due to photodissociation of O_2^+ to the L1, 18.733 eV limit. In contrast to the 3s-4d(v=1) data, the 3s-4d(v=2) images shown in Figs. 5.10, 5.11 and

5.12 show little or no signal for photodissociation of the *a*-state. At the photon energy used for Fig. 5.10, the O(^{1}D) co-product channel opens for ND to the n=3s^5S° atom product

In all images analyzed in the 226-215 nm region, the fraction of O(^{1}D) coproduct yield in the ND channel is found to be significant.

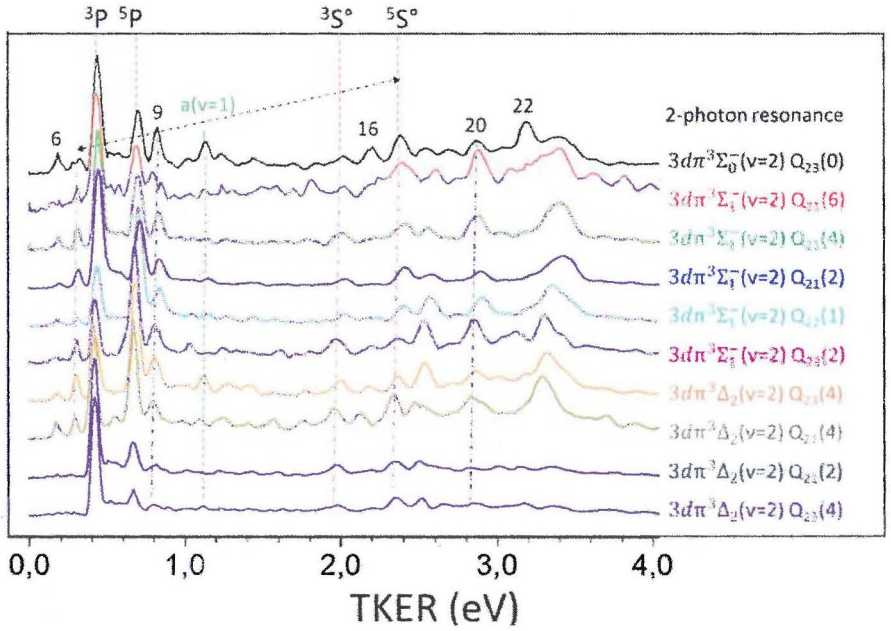

Figure 5.10: TKER curves for a series of near-by peaks in the REMPI spectrum of O_2 in the region covering 88,935 cm^{-1} (upper curve) to 88,841 cm^{-1} (lower curve). The energy spacing is irregular, thus also the shift in peak positions with increasing photon energy. The absolute signal level is arbitrary; each TKER curve is scaled to its highest peak. Ro-vibronic assignments for each resonance are given to the right side of each curve, where in the subscript $Q_{ij}(J)$, i refers to the F manifold (F=1,2,3) of the upper electronic state, j to the ground electronic state.A diagonal double headed arrow indicates the position of the O(^{1}D) co-channel.

Fig. 5.12 shows another set of images for both photoelectrons and O^+ ions, in this case for formation via the 3dπ $^3\Sigma_0^-$(v=2) Rydberg state at 224.869 nm or 5.5135 eV, the black curve in Fig. 5.10. The strong transition used in Fig.5.11 originates from the lowest (F3) N=1 spin-rotation manifold of the molecule, which has the most population in a rotationally cold supersonic expansion. In the case of Fig. 5.11 it is apparent that the population of O_2^+(v) levels created by AI (from in the photoelectron signal)

is quite similar to the pattern for photodissociation of O_2^+ seen in the O^+ signals.

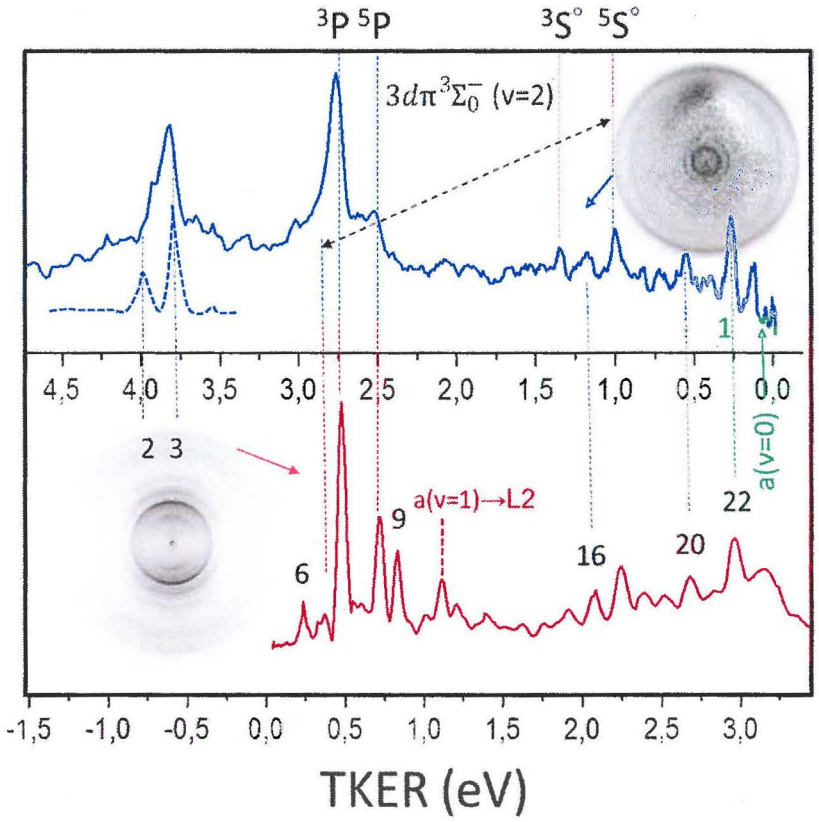

Figure 5.11: TKER curves and gray-scale image for O^+ formation via the $3d\pi\ ^3\Sigma_1^-(v=2)$ Rydberg state at 224.995 nm or 5.5105 eV. A diagonal double headed arrow indicates the position of the $O(^1D)$ co-channel.

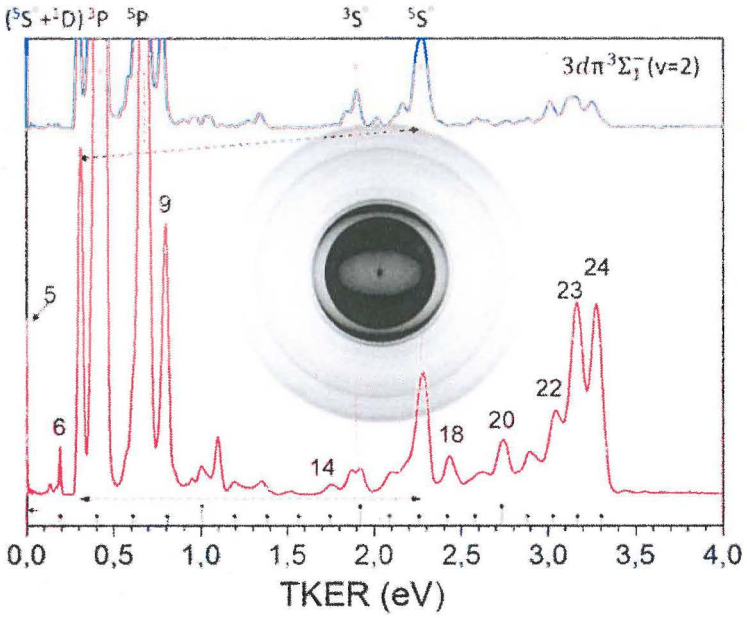

Figure 5.12: TKER curves and gray-scale imagesfor O^+ *(red curve)and* e^- *(blue curve) formation via the* $3d\pi\ ^3\Sigma_0^-$ *(v=2) Rydberg state at* **224.869** *nm or 5.5135 eV. See the caption of Fig. 5.4 and the text concering the photoelectron image analysis and scaling for more details.*

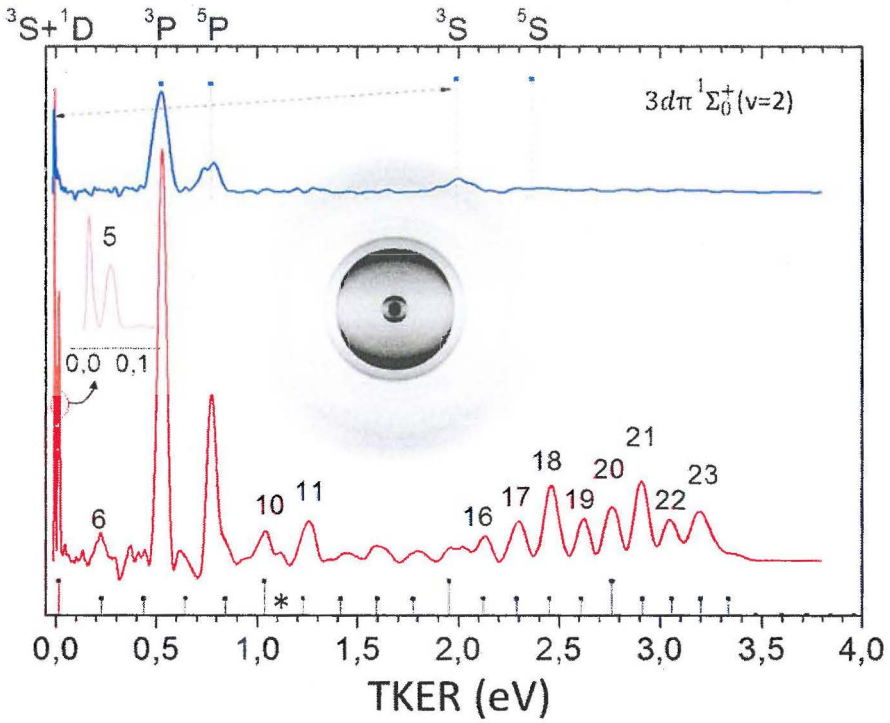

Figure 5.13: TKER curves and gray-scale images for O^+ *formation via the* $3d\pi\ ^1\Sigma_0^+$ *(v=2) Rydberg state at* **223.762***nm or 5.542 eV. The small peak indicated by an asterisk is at the correct energy for two-photon dissociation of* O_2^+ *(v=0) to the L3 limit.*

An image taken at the highest energy in the 3dπ(v=2) Rydberg manifold is shown in Fig. 5.13. At this energy photodissociation of O_2^+(v=5) is possible and observed along with the (^{1}D) coproduct chanel of the O* ^{3}S excited atom. A very small peak is seen for photodissociation of a(v=0) and the a(v=1) peak may underly the X(v=11) peak in the TKER curve.

Two 3s-4d (v=3) images are shown in Figs. 5.14 and 5.15. Characteristic for both is the dominance of ND above AI.

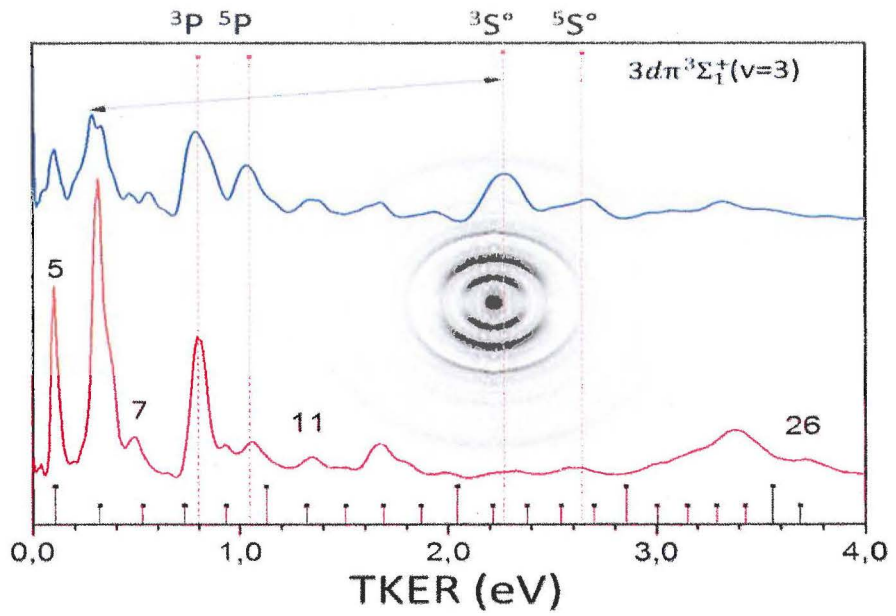

Figure 5.14: TKER curves and gray-scale images for O^+ *formation via the* $3d\pi\ ^3\Sigma_1^+(v=3)$ *Rydberg state at* $220.059nm$ *or 5.6334 eV. Note the dominance of the ND channels.*

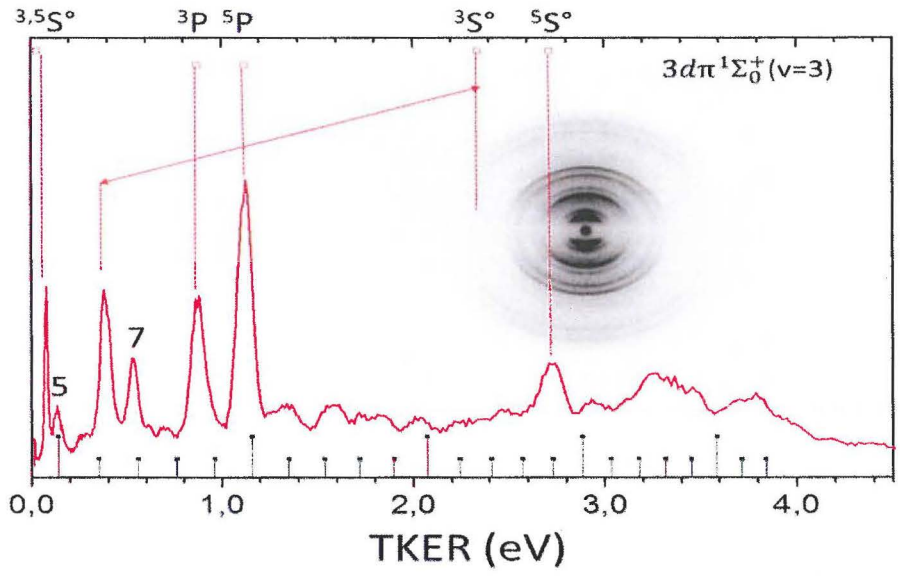

Figure 5.15: TKER curves and gray-scale images for O^+ *formation via the* $3d\pi\ ^1\Sigma_0^+$ *(v=3) Rydberg state at* **219.320** *nm or* **5.653** *eV. Full angular integration of the image indicates a 50% yield for ND.*

Continuing on to the highest energy images where ND is observed, TKER curves for the $4d\pi\ ^3\Sigma_0^-$ (v=1) state at 216.297 nm or 5.732 eV, the $4d\pi\ ^3\Sigma_1^+$(v=1) state at 215.598 nmor 5.741 eV,and the *6s-5d* $^1\Sigma_g^+$ *(v=1, Ω=3/2) state at 214.463 nm or 5.781 eV* are shown in Fig. 5.16, Fig. 5.17, and Fig. 5.18, respectively. ND to the n=3s (^{5}S°,^{3}S°) O* atom with O(^{1}D) co-product is observed along with the next higher excited atoms O*^{5}D° and the O*^{3,5}S° doublet. Photodissociation of O_2^+ to its L3 limit (O^+ (^{2}D)+O(^{3}P) at 22.057 eV) is now observed and is quite intense (v peaks for this limit are labeled in blue) and dissociation to the L1 limit is weak (again, these peaks are labeled in black). In the region of Figs. 5.16- 5.18 the threshold for formation of the $O_2^+A(^2\Pi_u)$ state is reached and evidence for formation and dissociation of this state to the L3 limit is seen in the images, especially for the O^+ image shown in Fig. 5.17. No indications are seen in the images for photodissociation of the $O_2^+A(^2\Pi_u)$ state to the L2 limit.

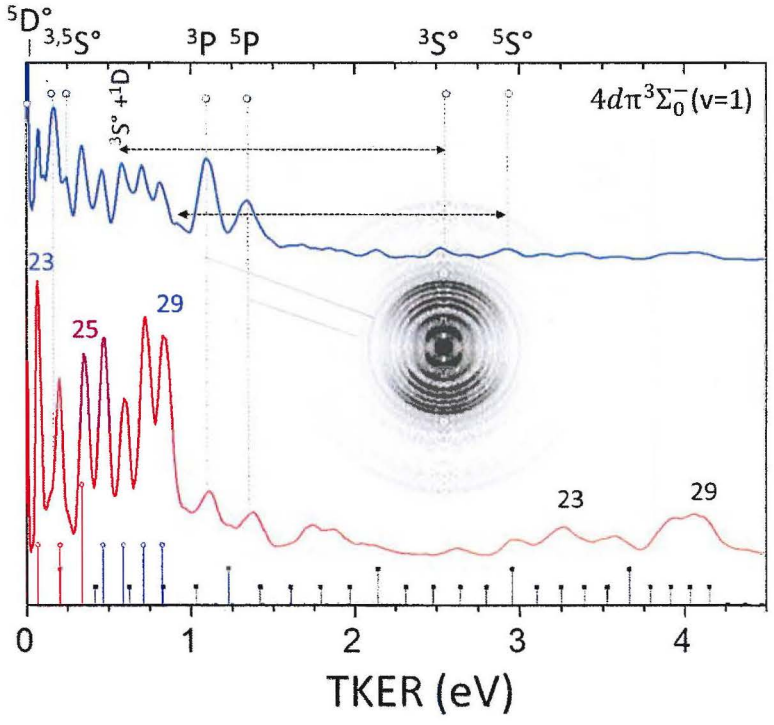

Figure 5.16: TKER curves and gray-scale inverted image for O^+ *formation via the* $4d\pi\ ^3\Sigma_0^-$ *(v=1) state at 216.297 nm or 5.732 eV. The sharp set of peaks labeled by the v number in blue below TKER = 1 eV are due to photodissociation of* $O_2^+X(v)$ *to the L3 limit at 22.057 eV.*

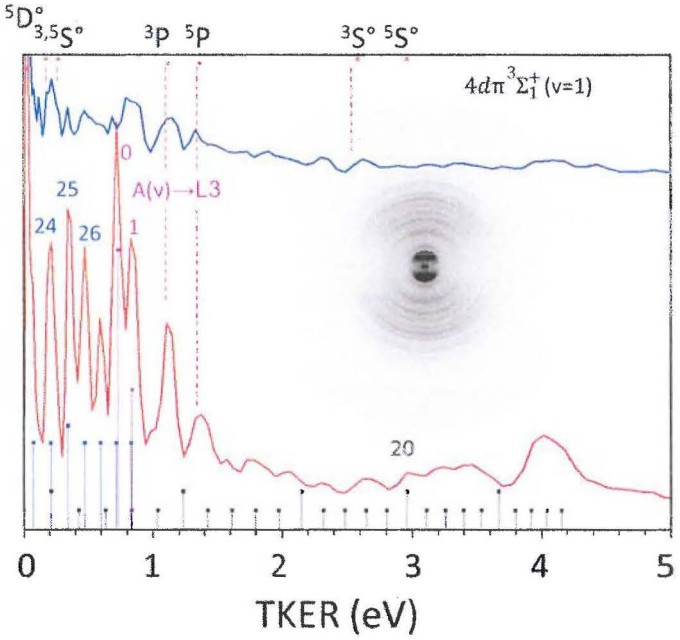

Figure 5.17: TKER curves and gray-scale inverted image for O^+ *formation via the* $4d\pi\ ^3\Sigma_1^+$*(v=1) state at 215.598 nm or 5.741 eV.*

TKER curves for the next higher image at 5.897 eV, shown in Fig. 5.19 continue the same trend in the photodissociation of O_2^+ but show no evidence for ND. At 5.897 eV the image shown in Fig. 5.19 via the 6s-5d $^1\Sigma_g^+$ (v=1, Ω=3/2)) state at 210.245 nm shows essentially the same pattern for AI and O_2^+ photodissociation as Figs. 5.16 and 5.17, but no longer any ND products.

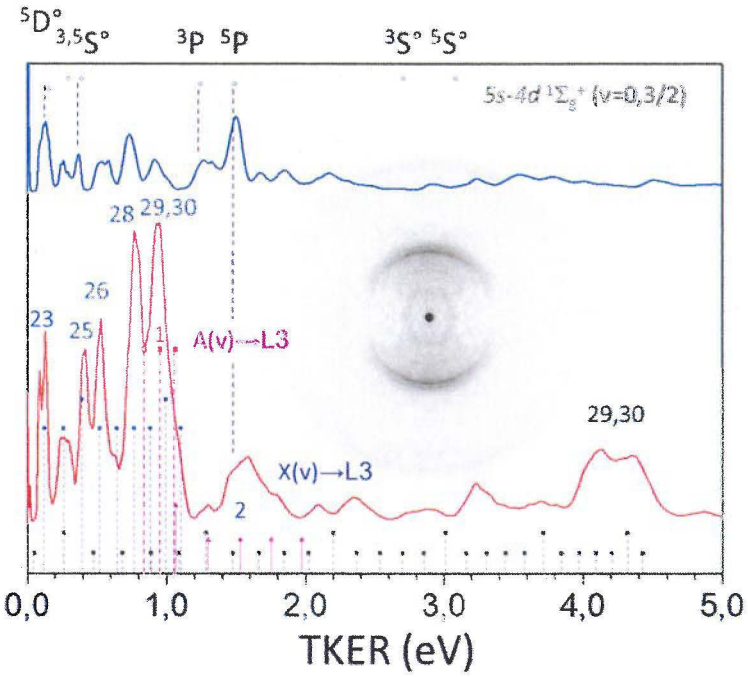

Figure 5.18: TKER curves and gray-scale raw image for O^+ formation via the 6s-5d $^1\Sigma_g^+$ (v=1, Ω=3/2)) state at 214.463 nm or 5.781 eV.

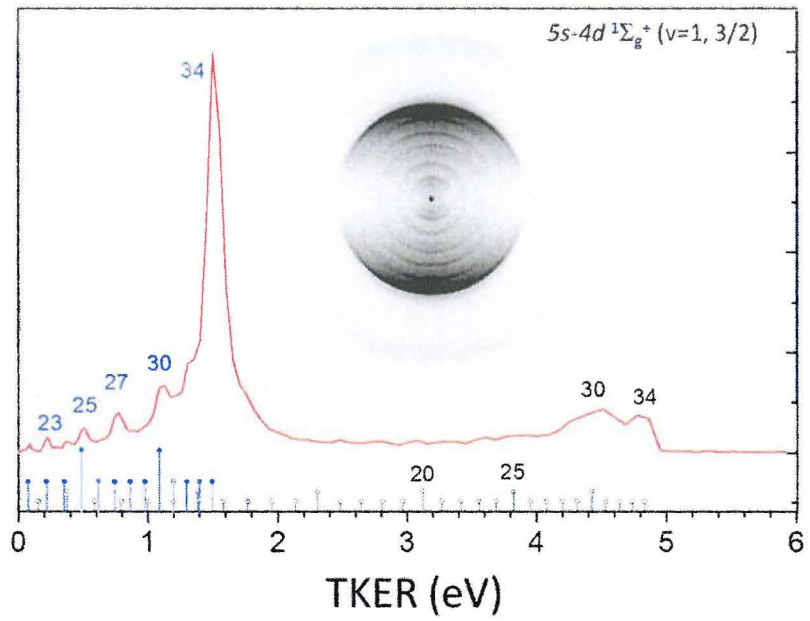

Figure 5.19: TKER curves and gray-scale raw image for O^+ formation via the 6s-5d $^1\Sigma_g^+$ (v=1, Ω=3/2)) state at 210.245 nm or 5.897 eV.

Between 216 and 205 nm only AI is observed, leading to production of a wide range of O_2^+ (v) levels with the significant signals for the highest possible v levels, where one-photon dissociation of these high v levels leads to the assigned O^+ peaks. Below 206.6 nm, the two-photon energy exceeds the IP of O_2 at 12.079 eV. The first image measured after crossing this threshold is shown in Fig. 5.20, taken at two-photon excitation via the 8s-7d $^1\Sigma_g^+$ (v=1, Ω=1/2)) state at 205.029 nm(6.047 eV). Only O_2^+(v=0) can be formed at this energy and surprisingly, the full O^+ signal is due to two-photon dissociation of O_2^+ (v=0) to the L4 and L5 limits at 22,057 and 23.750 eV, respectively. At slightly shorter wavelengths, however, formation and one-photon dissociation of O_2^+ (high v) levels, the typical signature of AI, is again dominant, as illustrated in Fig. 5.21 for the *the 6s-5d* $^1\Sigma_g^+$(v=2, Ω=1/2)) state at 204.029 nm(6.069 eV). At this energy, dissociation of O_2^+ X(v=37-41) to the L5 limit at 23.025 eV and O_2^+X(v=38,39) to the L6 limit at 24.025 eV is also observed.

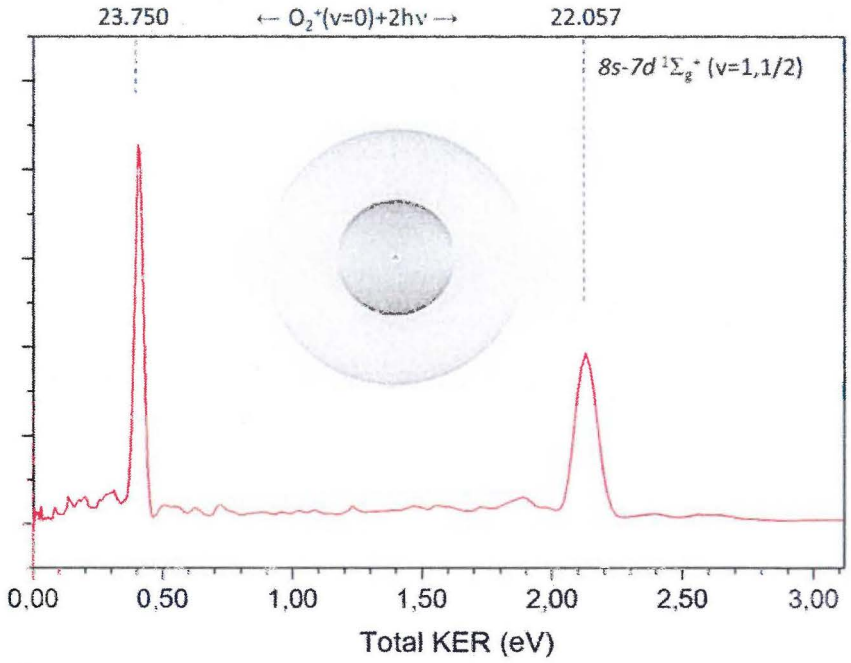

Figure 5.20: TKER curves and gray-scale image for O^+ formation via the 8s-7d $^1\Sigma_g^+$ (v=1, Ω=1/2)) state at 205.029 nm (6.047 eV).

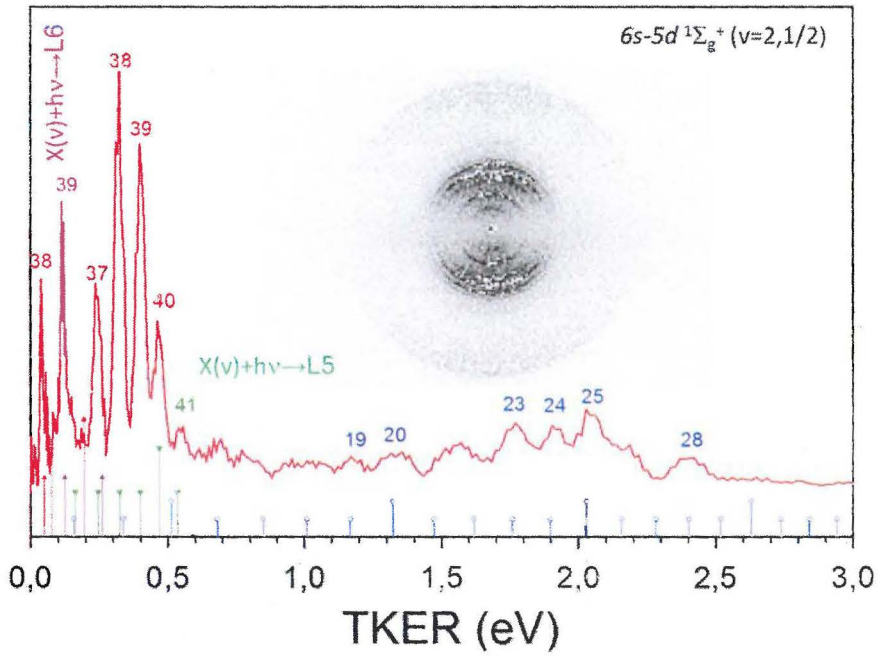

Figure 5.21: TKER curves and gray-scale image for O^+ formation via the 8s-7d $^1\Sigma_g^+$(v=1, Ω=1/2)) state at 204.029 nm(6.069 eV).

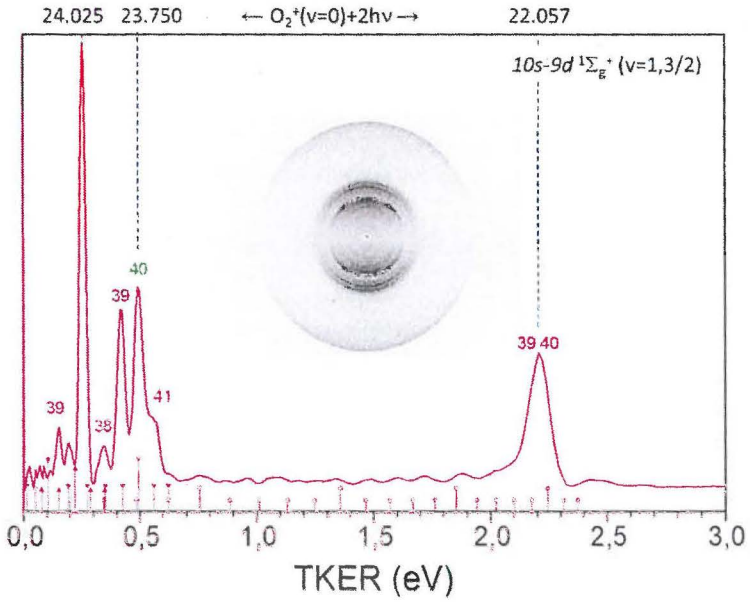

Figure 5.22: TKER curves and gray-scale image for O^+ formation via the 10s-9d $^1\Sigma_g^+$(v=1, Ω=3/2)) state at 203.348 nm(6.097 eV).

One-photon dissociation of O_2^+X(high v) levels and two-photon dissociation of O_2^+X(low v) levels occurs simultaneously at the shorter wavelengths, causing overlap of peaks, as illustrated in the O^+ image obtained via *the 10s-9d* $^1\Sigma_g^+$(v=1, Ω=3/2)) state at 203.348 nm(6.097 eV) shown in Fig. 5-22.

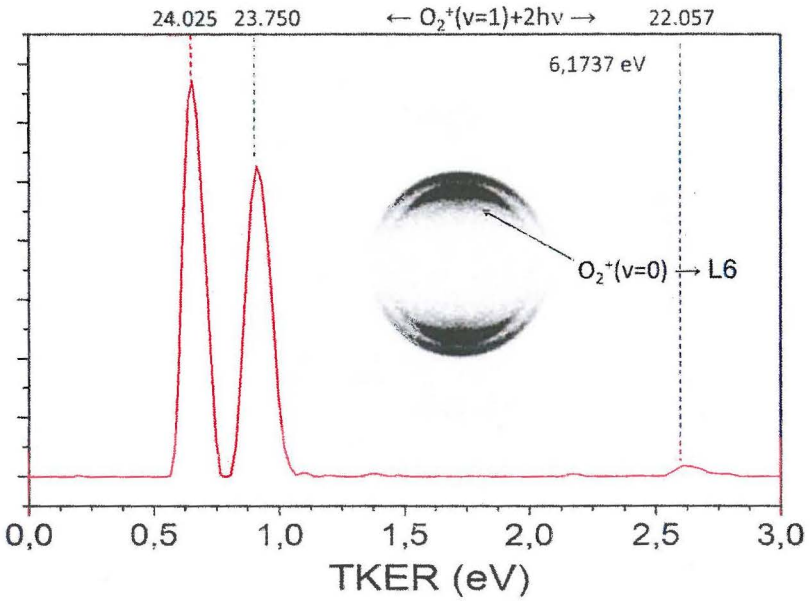

Figure 5.23: TKER curves and gray-scale image for O^+ formation via an unassigned resonance at 200.822 nm (6.1737eV). A very weak ring at lower velocity in the image is assigned to photodissociation of O_2^+X(v=0) to the L6 limit at 24.025 eV.

The shortest wavelength image measured in this work is shown in Fig. 5.23, taken at an unassigned resonance at 6.1737 eV; the two-photon energy of which slightly exceeds the formation energy of O_2^+X(v=1). Now, two-photon dissociation of O_2^+ X(v=1) is seen almost exclusively, similar to the two-photon dissociation of O_2^+X(v=0) seen in Fig. 5.19.

The trends observed in the 200 nm region are also seen at shorter wavelengths. Fig. 5.24 shows data from a previous study by Bakker et al[38] for O+ formation at 193.2 nm, using an injection-seeded tunable ArF excimer laser set off-resonance from any one-photon absorption to the B-state of O_2. O_2^+ formation in the X(v=0-2) states are observed by both

direct one-photon dissociation form $O_2^+(v>0)$ to the L1 limit, and, as in Figs. 5.19-5.21, two-photon dissociation of $O_2^+X(v)$ to the L6 and L3 limits.

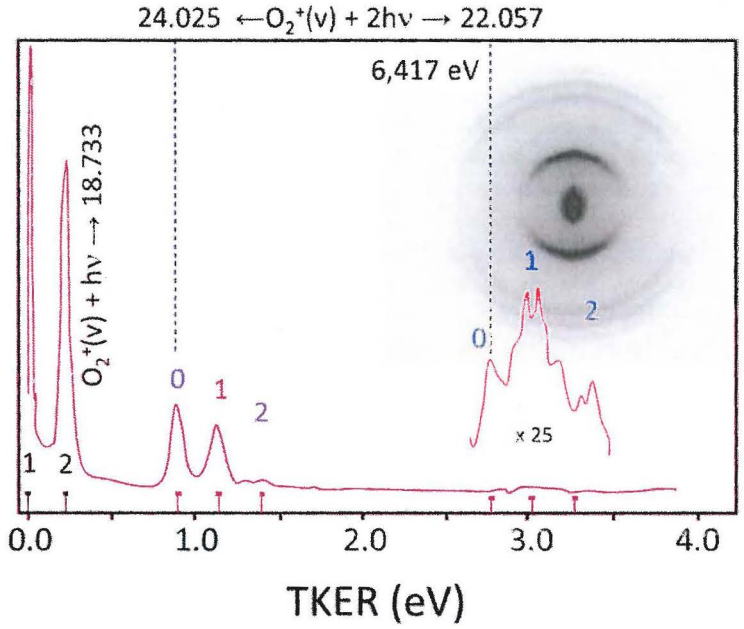

Figure 5.24: TKER curves and gray-scale image for O^+ formation at 193.2 nm or 6.417 eV using a tuneable ArF excimer laser.

5.3.4 Image resolution and calibration aspects

Because the set of O^+ images shown in Figs. 5.5- 5.24 contain many sharp and well-spaced rings, they are quite useful in calibrating the velocity scale (m/s per pixel) of a VMI apparatus; this holds especially for the image shown in Fig. 5.11 which has been assigned previously.[32,33] This resonance produces one of the strongest set of O^+ signals in the full O_2-X Rydberg series. Now that essentially all peaks in the TKER curves are assigned for all the doorway states in this study, it is useful to discuss why the images are so sharp and the limitations that arise in resolution and peak assignment.

The individual peaks labeled in the TKER curves shown in Figs. 5.5 - 5.24 for O_2^+ X-state dissociation can be used for calibration. Their exact energies can be calculated using the energy positions of the X-state levels from Akahori et al[19] by the simple equation TKER = Energy(X,v)+hν-Li, where hν is the laser photon energy, and Li is the dissociation limit (either L1, L3, L5 or L6). In several figures *a* $^4\Pi$–state and $A^2\Pi$–state

peaks are labeled, but because of possible overlap they cannot be used for calibration. Peaks are also labeled for two-photon dissociation of O_2^+ (low v) levels, these are less reliable due to possible electron recoil effects, as follows: three-photon excitation has been found to occur even in cases where the two-photon energy exceeds the ionization potential at 12.079 eV (e.g. Fig. 5.22). Ionization from any three-photon level to the lowest vibrational levels of the O_2^+X state will create fast photoelectrons with TKERs of up to 6.5 eV. Taking the conditions for Fig. 5.11 ($h\nu$=5.5013 eV) as an example, ionization to O_2^+v=0 occurs with TKER= 4.4512 eV. Momentum conservation results in an O_2^+ ion recoil velocity of $v_{O2+}=(m_e/m_{O2+}) \cdot v_e = (m_e/m_{O2+}) \cdot (2TKER/m_e)^{½}$= 22 m/s. Without recoil, two-photon photodissociation of O_2^+ to the L3 limit produces O^+ ions with TKER = 1,025eV, which is 3517 m/s. Adding the ion recoils in both directions results in velocities of 3495 and 3537 m/s or a TKER of 1,013-1,037 eV, and thus an energy splitting of the peak due to ion recoil of 0,026 eV, which is larger than the typical resolution of extracted from the images. This is of course the maximum effect, when the electron recoil is in the same direction as the ion recoil, as discussed in more detail in Ref.39. [39] The effects of ion recoil are most clearly seen in low-velocity rings when image slicing is used, this will be discussed in more detail in a future publication.

From the above discussion it is clear that ion-recoil, which often determines the resolution of an image, is not a serious problem for most of the O+ rings. The highest velocity sharp rings shown in Figs. 5.11 and 5.13 are from photodissociation of high vibrational levels of O_2^+X, which are thus formed with very low ion recoil.

For the excited atom channels, the TKER is easily calculated from TKER = $3h\nu$-E O*-D_0, where the E O* energies are listed in the NIST atomic data base. Ion recoil for O+ from the O* or ND channel is also relatively small, in the range of 5-10 m/s, where the largest ion recoil effect arises from ionization of the highest lying O* atom, which is formed with the lowest TKER following ND from the three-photon super-excited state. Excited atom channels, with both O(^{3}P) and O(^{1}D) co-products can also be used for velocity calibration.

Other advantages for using O_2 for apparatus calibration are: O_2 is an inexpensive, clean, and pure gas that can be introduced in high conentrations without problems with cluster formation. Only ~ 1mJ of laser light is needed, and the image can easily be adjusted to fill the detector. As shown here, resonances throughout the 234-200 nm region can be chosen, so that a dye change is not usually necessary.

5.3.5 O^+ formation via related processes in other studies of O_2.

Two other unpublished studies of O_2 photodissociation are mentioned here where O^+ formation due to the same processes as described in this paper are observed.

Figure 5.25 shows a set of O^+ images taken at the resonances of the lower-lying 3s $^3\Pi$ (v=0-3) Rydberg states of O_2. In these two-color experiments the first laser is tuned to the Rydberg state and a second, detection laser was set to ionize O($^3P_2$) atoms via 2+1 REMPI at 225.65 nm. No O+ signal is observed with the first laser only. The main two-color signals arise from detection of O(^{3}P) formed by two-photon dissociation of O_2 to dissociation limits D_0 and D_1, but there is also signal clearly seen in the C(v=2 and 3) images at low kinetic energy that arises from a different process. This lower energy peak depends on the presence of the 225 nm laser, but not on it being resonant with O($^3P_2$) REMPI, the signal is stronger at shorter wavelengths off-resonance. Most interestingly, the anisotropy of this lower energy peak does not depend on the polarization direction of the 225 nm laser. The peak also disappears when the 225 nm laser is delayed by more than 50 ns after the first laser. All together, this evidence requires that the origin of the low energy peak is an O* atom formed by ND, which can only take place at the four-photon level, for the *C* 3s $^3\Pi$(v=2) TKER curve shown this corresponds to 17.256 eV. From the TKER this peak can definitely be assigned to ionization of the O*(4s ^{5}S°) atom, the anisotropy of which is determined by the first laser, and the lifetime on the tens of nanoseconds scale is due to emission. Note that this O* atom formation is also observed in Figs. 5.17 and 5.18, which correspond to similar total energy as Fig. 5.25. While formation of O* is caused by the 305-280 nm laser, it appears that these atoms are not ionized efficiently at this wavelength as this requires two-photon ionization, while the 225 nm (and shorter) wavelengths cause efficient one-photon ionization.

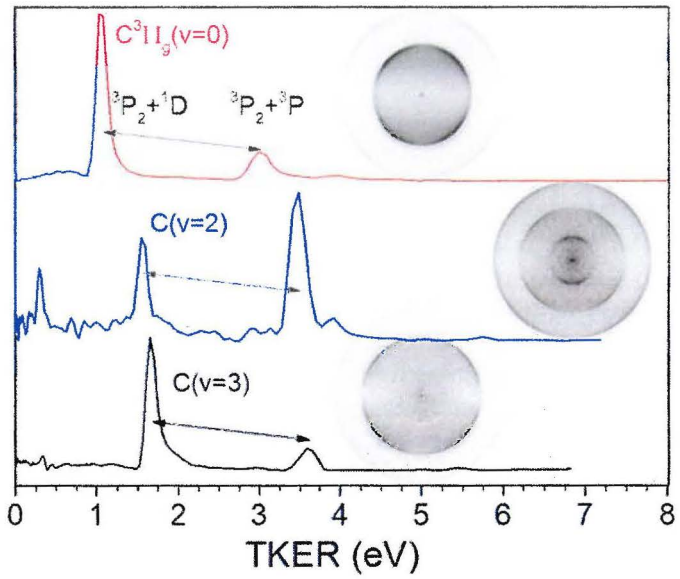

Figure 5.25: Gray-scale images and TKER curves for photodissociation of the lowest energy $C^2\Pi(v=0\text{-}3)$ Rydberg states at 305.3 nm, 287.6 nm, and 280.1 nm, respectively, followed 10 ns later by $O(^3P_2)$ REMPI detection at 225.6 nm. The D_0 and D_1 dissociation channels are connected by double headed arrows. Note the extra peak at low kinetic energy in the (v=2 and 3) curves, which is assigned to ionization of the $O^*(4s\ ^5S^\circ)$ atom formed in conjunction with an $O(^3P)$ atom.

Another related signal was observed in a previous study[40] of the photodissociation of discharge-excited O_2 molecules at 157 nm, shown in Fig. 5.25. An electric discharge takes place during the pulsed supersonic expansion of O_2 and results in the formation of singlet O_2 (chapter 3 of this thesis) along with the production of vibrationally excited ground-state O_2 . A F_2 laser operating at 7.865 eV (157.6 nm) causes photodissociation and second laser tuned to the 2+1 REMPI line of $O(^1D)$ causes ionization 10 ns after the 157 nm laser. With the 205 nm laser blocked, no O^+ signal is observed, and with both lasers on but the discharge off, no additional signal is observed from the 157 nm laser. With the discharge on an additional signal at 0.06 eV is observed when tuned to $O(^1D)$ detection, this signal is not observed when the detection laser is tuned to the $O(^3P)$ REMPI line at 225.6 nm. Based on its TKER, this peak can be uniquely assigned to two-photon dissociation of $O_2X(v=5)$ to form $O^*{}^3S^\circ + O(^1D)$ an energy of 16,605 eV, similar to that of Fig. 5.11. This $O(^1D)$ channel is active in Figs. 5.11 and 5.12, at similar energies. Considering the low intensity of the 157 nm laser (~100 μJ/pulse) it is not

surprising that the more intense (~2 mJ/pulse) 205 nm laser causes ionization of the O* atom. The pulsed electric discharge is known to produce vibrationally excited O_2 X(v>0) states. It may also be expected that two-photon excitation of X(v>5) to form O* by ND should also take place, but these signals lie beneath peaks from the 205 nm laser-only signal and, if present, do not rise above the background subtraction noise in the image.

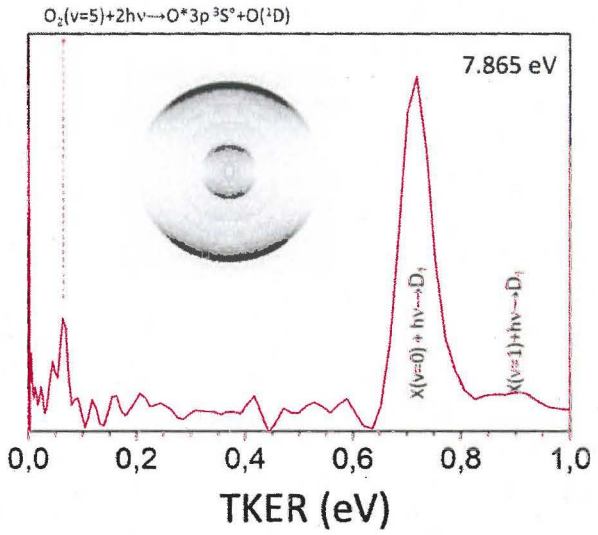

Figure 5.26: Gray scale difference image [(157 nm+205 nm) – 205 nm] for discharge-excited O_2 dissociated by a F_2 laser at 157 nm and probed 10 ns later by a laser tuned for 2+1 REMPI of $O(^1D)$ atoms at 205.3 nm. The large peak at 0.7865 eV is due to one-photon dissociation at 157 nm of O_2 to the D_1 limit.

5.3.6 Angular distributions of the ND and AI channels

The angular distribution of products from one-photon dissociation is described by $I(\theta) = \frac{1}{4\pi}[1 + \beta P_2(\cos\theta)]$, where $P_2(x) = \frac{1}{2}(3x^2 - 1)$ is the 2nd order Legendre Polynomial, θ is the angle with respect to the polarization axis and β is the anisotropy parameter $(-1 < \beta < 2)$ with the limiting values corresponding to a pure perpendicular $(\Pi - \Sigma)$ and parallel $(\Sigma - \Sigma, \Pi - \Pi)$ transition, respectively. Determination of anisotropy parameter for different channels predicts information on the symmetry of excited states and nonadiabatic interactions involved in the absorption process[41,42,43,44,45]. For almost all of the signals observed the simple one-photon formula is sufficient to describe the measured angular distributions, but the limiting values of β=+2 or -1 are not expected due to

the multiphoton excitation scheme, and especially due to overlapping final states at the three-photon level. In addition, the value of β can also be lowered by non-axial recoil for state lifetimes on the same time-scale as rotation. Anisotropy parameters of photofragments resulting from neutral distribution and dissociation of O_2^+ ions were measured and reported over the 200−240 nm wavelength for channels that are not strongly overlapped by other signals. Due to these problems in overlap and to imperfectly round images, the beta values reported have large uncertainty ranging from ± 10 to 50%.

Beta values for ND channels are listed in Table 5.4, and selected beta parameters for non-overlapped peaks labelled in the Figs. 5.4-5.21 for AI from the $O_2^+X(v)$ state to the L1 and L3 limits are tabulated graphically in Figs. 5.26 and 5.27, respectively.

Table 5.4: *Anisotropy parameter β for O* atoms measured at the indicated photodissociation energies.*

Energy (eV)	3s ^{5}S + ^{3}p	3s ^{3}S + ^{3}p	3p ^{5}p + ^{3}p	3p ^{3}p + ^{3}p	3s ^{5}S + ^{1}D	3s ^{3}S + ^{1}D
5.741	–	–	1,0	1,1	–	–
5.732	1,0	0,8	0,8	0,7	1,3	0,6
5.634	0,5	-0,1	0,8	1,4	–	1,8
5.542	–	0,4	1,5	1,2	–	1,5
5.522	1,4	1,2	1.5	1,3	0,8	–
5.510	1,0	0,7	1,9	1,3	1,1	–
5.428	–	-0,1	0,8	1,2	–	–
5.402	−0,2	–	0,7	0.8	–	–
5.395	0.4	0.2	−0,7	1.11	–	–
5.286	−0,5	−0,2	–	–	–	–

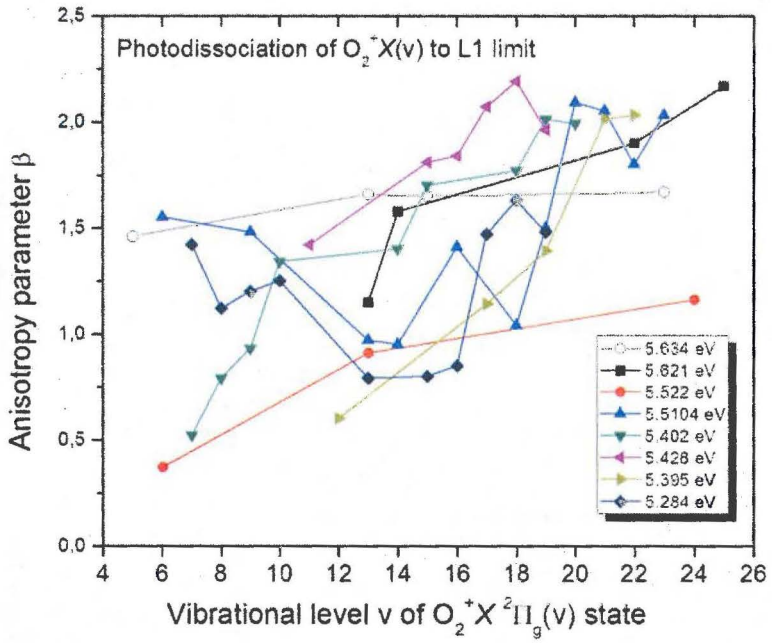

Figure 5.26: Beta values for photodissociationof O_2^+ X(v) levels to the L1 limit at the indicated wavelengths

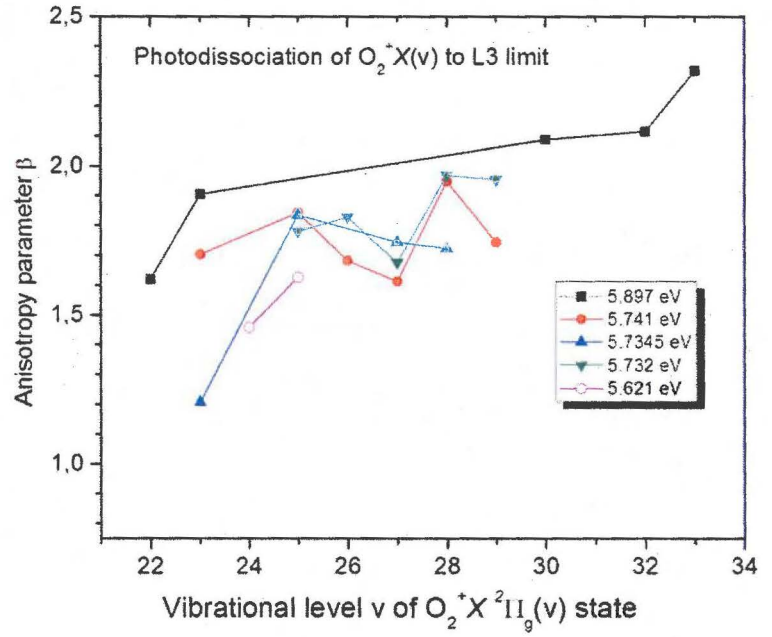

Figure 5.27: Beta values for photodissociation of $O_2^+X(v)$ levels to the L3 limit at the indicated wavelengths indicated.

5.3.7 Branching ratios between AI and ND

Branching ratios between autoionization and neutral dissociation are shown graphically in figure 5.28. These values are only indicative because it was not possible to keep the laser power constant over the entire range; some transitions were quite weak and noisy, especially after inversion, and because of strong overlap of the ND and AI peaks. Ratios were estimated from TKER curves integrated over the full angular distributions (not those shown in Figs. 5-25) by adding up peak areas for ND and AI peaks separately. No ND signals were observed below 214 nm (Fig. 5.18). Autoionization is found to be dominant over the full wavelength range 214-240 nm and the proportion of auoionization phenomenon oscillates between 90 and 50 percent in this range.

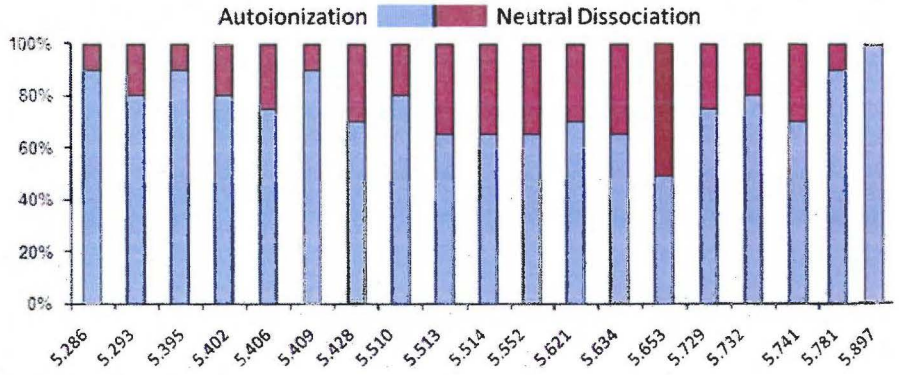

Figure 5.28: Branching ratios between autoionization (blue color) and neutral dissociation (red color) in the photon energy range from 5.3-5.9 eV, corresponding at the three-photon energy to 15.9 - 17.7 eV or three-photon wavelength 78 - 70 nm.

5.4 Discussion

The results obtained in this study can be described as measurements of branching ratios and beta values for the product channels of three processes, as shown schematically in Fig. 5.29. Each process is monitored by imaging of O^+ ions or electrons; the effects and limitations of the measurement method are first discussed. Competition between AI and ND are then discussed, based on a simple model described in Ref. 46 [46]. The section concludes with discussion of each process, ND, AI and photodissociation of O_2^+.

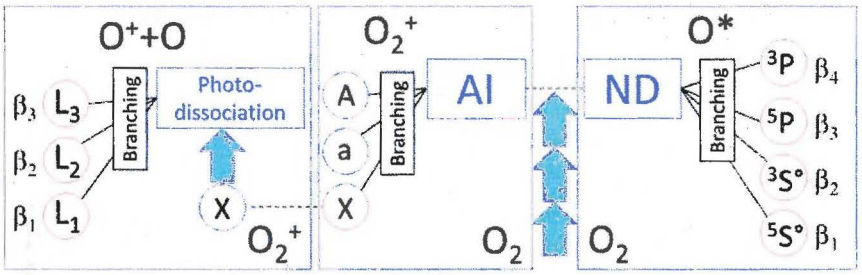

Figure 5.29: Schematic overview of results. Three-photon excitation of O_2 through two-photon doorway Rydberg states populates superexcited states that either undergo neutral dissociation (ND) to form O excited atoms, with each O* channel characterized by an anisoptropy parameter β; or autoionization (AI) to form an electron and three possible O_2^+ electronic states. Photodissociation of O_2^+ produces O^++O products at 6 possible dissociation limits L1-L6, each characterized by an anisotropy parameter β.*

5.4.1 Detection of ND and AI in O_2 by O^+ formation

O^+ product angle-velocity distributions are used in this study to uniquely determine whether AI or ND has taken place following three-photon excitation of O_2 via two-photon allowed O_2 R-X Rydberg states. No evidence is seen for O^+ formation via ion-pair dissociation (threshold 17.27 eV) by either detection of O^- or by detection of electrons by photodetachment of O^-. Referring back to Fig. 1, the O^+ product angular distribution can be expected to be determined by the super-excited state since the detected O* atom has been 'tagged' in its formation from that state and is simply ionized later on during the 5 ns laser pulse. This is confirmed in the two-laser data described in Fig. 5.25, the angular distribution of the O* signal is determined by the laser that causes excitation to the Rydberg state and is not sensitive to the polarization of the ionizing laser. ND can create polarized O* atoms, however, and weak polarization has been detected via their optically emission (indicated in Fig. 5.1) following one-photon excitation by synchrotron radiation. The angular distribution of the O* channel can thus be affected by this polarization on formation, but this was not detectable, for example, in the measurements described in Fig. 5.25.

In contrast to ND, the angular distribution of the O^+ product from AI is determined by primarily by photodissociation of O_2^+ and less so by the super-excited state. This is confirmed in two-laser experiments (not shown) where the angular distribution of O^+ from O_2^+ dissociation does indeed depend directly on the polarization of the laser driving the

photodissociation step. Ionization from the super-excited state can, however, lead to of the O_2^+ product alignment, which has been observed in studies of the polarization of O_2^+ A-state emission (see Fig. 5.1) to the ground-state of O_2^+ following synchrotron excitation to the super-excited state in the 20-25 eV range. This study is at lower energy where A-state formation is quite minor (Figs. 5.17 and 5.18). Since A-state products of AI have been found to show alignment, the beta parameter for dissociation of O_2^+ in the X-state may also be affected by pre-alignment from the AI process. For this reason, and due to near-overlap problems, the beta parameters discussion in the following is at a qualitative level.

5.4.2 Simplified Mechanism for ND and AI

Ehresmann and coworkers[46] have suggested a mechanism for ND from the lowest-lying I, I', I" superexcited states of O_2, which is shown schematically in a highly simplified form on the right side of Fig. 5.29. Following their discussion, a possible mechanism for AI is shown on the left side of the figure.

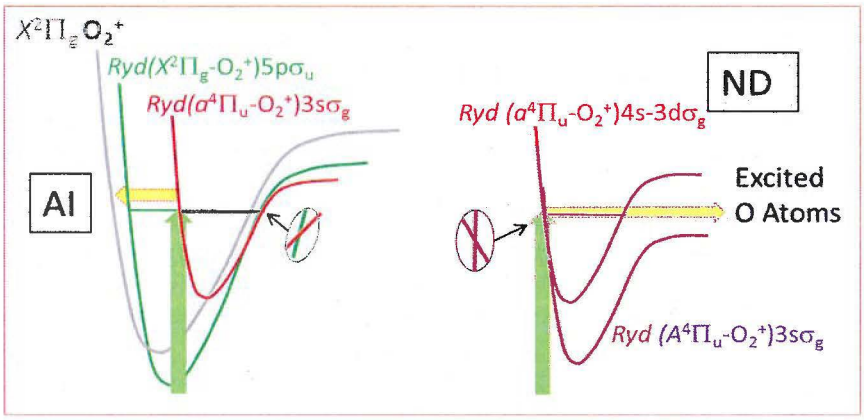

Figure 5.30: Simplified mechanism for AI and ND from the lower super-excited states of O_2, following ref.[46] See also Chapter 1 of this thesis.

The key aspect of the ND mechanism is excitation to a region of near-perfect overlap of the inner wall of a potential energy curve of a lower quantum number Rydberg state of O_2 converging to the higher-lying A-state of O_2^+ with the inner wall of a potential energy curve of a higher quantum number Rydberg state converging to the lower-lying a-state of O_2^+. The R-A state is dissociative at the point of excitation and correlates adiabatically with O* $^3S°$ production. Similarly, in the AI process, overlap of the outer wall of the same upper state (red curve in Fig. 5.29) with the outer wall of a higher quantum number Rydberg state converging to the

ground electronic state of O_2^+ takes place. Coupling of this lower R-*X* state, which has a high vibrational energy at the crossing point, with the nearby $O_2^+ X$ state leads due to favorable Franck-Condon overlap to production of a wide range of $O_2^+X(v)$ levels

For the ND channel, it should be pointed out that a large number of optically allowed 'upper' Rydberg-*a* states and 'lower'-lying Rydberg-X states besides the two curves shown in Fig. 5.29 for ND are possible. In addition, a full manifold of repulsive states correlating with the bound states exists, where curve crossing of states of the same symmetry will thus take place. With weak mixing (Chapter 1) branching to different final O* states can be expected. As the excitation energy increases, dissociation should favor the limit nearest threshold; while higher in energy, branching between the lowest and next higher limit can be expected, as shown schematically on the left side of Fig. 5.30. Spin-orbit coupling will mix states of different symmetry and eventually all energetically available O* limits will become open. In the expected case overlap of two allowed states of different symmetry (right side of fig. 53), all final channels become accessable.

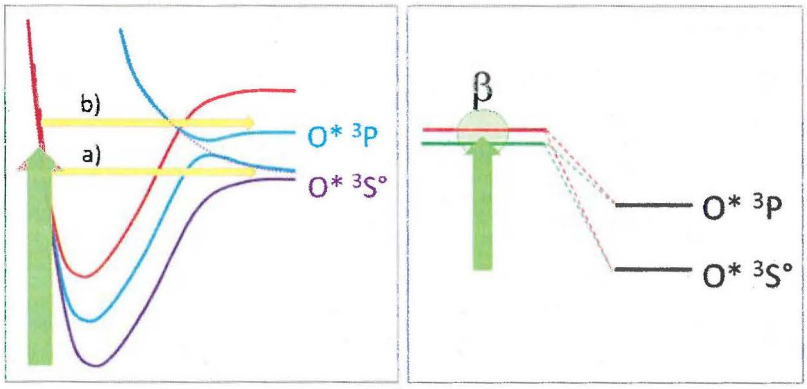

Figure 5.31: Complexity added to Fig. 5.30; on the left side the effect of crossing of two states of the same symmery leads to different O limits. a) Excitation near threshold leads to formation of O* at the closest liait, while b) above threshold branching between the upper and lower limits depends on the amount of state mixing at the crossing point. On the right side two states of different symmetry overlap and are both excited, leading to a mixed beta value between -1<β<2. Due to spin-orbit mixing, both final O* channels become possible from the starting state.*

Over the higher energy range of this study the near-perfect overlap mechanism should allow production of the higher O* products, which are observed in previous one-photon studies and now in the present three-

photon study. In the following sections, discussion of the reported results will be based loosely on the overlap model.

5.4.3 General overall trends from the data

General trends in the TKER distributions are observed as the wavelength decreases: At long wavelengths, 240-215 nm, ND is important, and channels with $O(^3P)$ and $O(^1D)$ as copartner are observed when energetically possible, but $O(^3P)$ formation is in general stronger. At wavelengths shorter than ~214 nm only AI was observed. At still shorter laser wavelengths, as soon as the photon energy is high enough to drive two-photon ionization (λ<207 nm), then production of O_2^+ at the two-photon level becomes dominant, and O^+ formation takes place by two-photon dissociation of O_2^+. At the shortest wavelength studied, 193 nm, one-photon dissociation of the lowest vibrational levels of O_2^+X (low v) to the L1 limit becomes energetically possible and produces the strongest O^+ signal.

5.4.4 One-photon versus Three-photon excitation

Before discussion of the observed trends it is useful to compare the three-photon excitation pathway used in this work with direct one-photon excitation. A simple schematic diagram is shown in Fig. 5.26 for illustration.

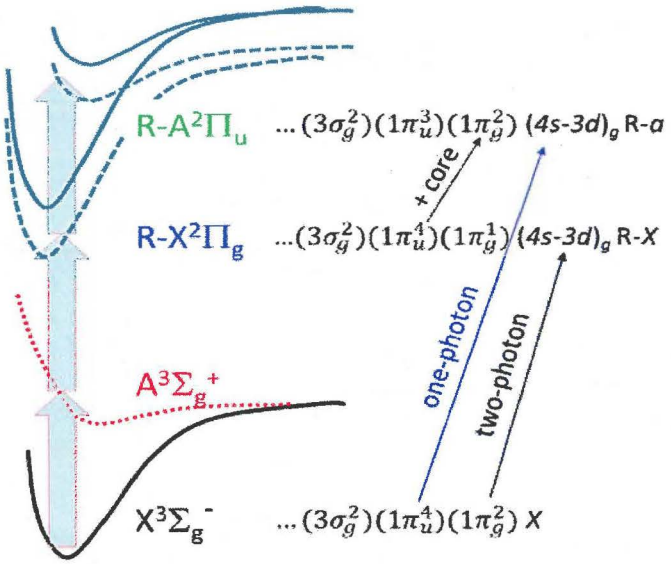

Figure 5.32: Molecular orbital configurations involved in one- and three-photon excitation to the $^3\Pi_u$ I, I', and I" (4s-3d) Rydberg states.

The main super-excited states of O_2 that lead to ND and AI have been identified as the $^3\Pi_u$ *I, I', and I"* (4s-3d) Rydberg states converging to the O_2^+a-state. As indicated in Fig. 2.26, the same MO configuration can be accessed by two-photon excitation to the (4s-3d) Rydberg states converging to the ionic ground state followed by core excitation of the $1\pi_u^4 1\pi_g^2$ configuration to the $1\pi_u^3 1\pi_g^1$ configuration, which corresponds in the ion to the strong, optically allowed X→A second negative system in the UV region of the spectrum. Both the A and a electronic states of O_2^+ belong to the $1\pi_u^3 1\pi_g^1$configuration. It can thus be expected that the results observed with three-photon can be at least compared with caution with those for direct one-photon excitation. The angular distribution anisotropy can in any case be expected to differ as the two-photon step involves a mixed parallel-perpendicular character coupled with a core excitation with parallel character, while the direct one-photon excitation should at first sight be either pure parallel or perpendicular transitions to $^3\Sigma_u$ or $^3\Pi_u$ super-excited Rydberg state, respectively, where a perpendicular transition is expected for the $^3\Pi_u$ symmetry *I, I', I'* states. This is indeed the case observed [29] by detection of O* atoms.

5.4.5 Competition between AI and ND

The TKER curves shown in Figs. 5.5-5.22 correspond to three-photon wavelength ranging from 78 to 67 nm. Inspection of Fig. 5.2 (b , c) shows that with direct one-photon excitation, ND rapidly decreases below 71 nm, which is consistent with the present three-photon excitation data as summarized in Fig. 5.28, where the last measurable ND signal was observed at 5.873 eV, equivalent to 71.4 nm on the three-photon level. Note that detection of $n=3s^5S°$ or $^3S°$ by emission, Fig. 5.2, does not distinguish between the O(^{3}P) and O(^{1}D) product channels. In the present data the O*+O(^{1}D) channel is indeed observed, particularly nearby threshold, but is found to be minor in comparison with the O*+O(^{3}P) channel. From the branching ratios shown in Fig. 5.28, it is also apparent that AI (detected by O^+ formation) is stronger than ND, as long as the photoionization of O* is saturated, as should be the case in this experiment. The actual ratio favors AI even more, since O^+ formation is in the present case not possible for the lowest X(v) vibrational levels, which are the most strongly populated; this is seen clearly in the photoelectron spectra shown in Figs. 5.5 and 5.12. Note that photoelectron images collect electrons from any ionization process including that from background at other masses. An advantage to electron imaging is that slicing is not possible, these images are always perfectly crushed at the detector. O^+ images are quite selective forO_2 processes, but partial slicing of the image is inadvertent, this will under-count the fastest particles and can thereby affect the ND: AI branching ratios.

Photoelectron images are more direct indicators of the competition between AI and ND, again assuming that O* photoionization is saturated. The two electron images shown in Figs. 5.5 and 5.12 show that 'direct' ionization (Δv =0-2) is stronger than AI, this is also the case for electron images now shown here. Branching ratios between ND and AI obtained from the electron images are found to agree qualitatively with those from the O^+ images, supporting the conclusion that ionization (AI and direct) is stronger than ND across the energy range studied.

5.4.6 Neutral Dissociation

O* 3s ^{3,5}P and ^{3,5}S° are the primary products observed in this study; this is consistent with the results of Ref 47 [47]. Inspection of Figs. 5.5-5.25 shows that the O* ^{3,5}P product yield is larger than that of the ^{3,5}S° atoms, although a quantitative ratio is not possible due to overlap with the AI signals and to partial slicing as mentioned above. Within the O* ^{3,5}P product group, the relative yield of O* ^{3}P versus O* ^{5}P varies widely, as is particularly apparent in Fig. 5.10, which shows TKER curves over a range of dissociation energies. A similar variation in yield between O* ^{3}S° and ^{5}S° was observed in Ref. 29 at lower energies where only O* ^{3,5}S° products were energetically possible. This is in accord with previous observations that the complex spectral pattern of the super-excited states determines the ND branching ratios. These spectral patterns, which include overlap of different super-excited states of different $^3\Sigma_u$ and $^3\Pi_u$ symmetry and result in the range of beta values measured. In Fig. 5.27 the beta parameter data from Table 5.4 is plotted two ways: first as a function of the excitation photon energy, and the second as a function of the TKER of each individual ND peak.

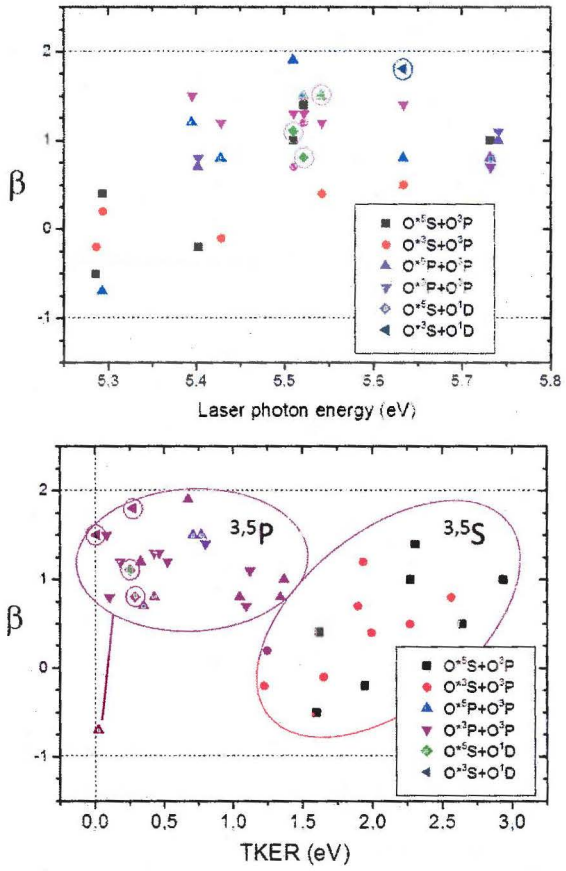

Figure 5.33: Angular anisotropy parameter beta, β, values for each ND product channel as a function of the laser photon energy (upper panel) and the TKER for each individual peak (lower panel). Data points for production of O(^{1}D) coproducts are circled.

The upper plot in Fig. 5.27 shows a general increase in beta as the laser photon energy increases. This may be consistent with the picture that towards higher photon energy the dissociation process becomes predominantly parallel and/or more rapid compared to molecular rotation. From the lower plot it is clear that the O* ^{3,5}P products show a higher (more positive) average beta value which appears to depend less on the available energy. There is one exception, however, where very close to threshold the beta parameter for the O*^{5}P+O(^{3}P) product is strongly negative (Fig. 5.6). In contrast, the O* ^{3,5}S products betas

increase in general from negative values near threshold towards positive values as the available energy increases.

Another interesting aspect of the ND beta values is branching for a given O* product state between the O(^{3}P) and O(^{1}D) product channels. For the limited data shown in the upper panel of Fig. 5.27 it appears that the two different channels have different beta parameters, suggesting that the channel selection occurs at the moment of optical excitation instead of branching taking place later on to O(^{3}P) versus O(^{1}D) channels. This is most apparent in the lower panel of Fig. 5.27 which shows that the channels with O(^{1}D) products, data points for which are circled in the figure, fall in the grouping of O* ^{3,5}P products, even though their co-partners are O* ^{3,5}S products. This again supports the idea that final channel is determined at the moment of optical excitation.

5.4.7 Autoionization

Analysis of the O^+ from photodissociation of O_2^+ data shows that the dominant product of AI in this study is the $O_2^+ X$ (v) state. Direct ionization to the *X*, and to less extent, the *a*, and *A* states, with Δv equal to zero or a small integer observed for one-photon excitation outside the region of the near-perfect overlap described in the model of section 5.4.2. In the region studied here where the overlap model applies, the general results for AI are in agreement with this model, where only O_2^+X(v) in a wide range of v is predicted. A limited amount of *a*-state (low v) and *A-state* (low v) is observed, but this could be due to direct ionization. Figure 5.34 shows an excitation spectrum of O2, taken from Ref. 20, in the 17.0-18.6 eV region, where fluorescence emission and its polarization is measured. Most of the peaks in the fluorescence yield spectrum are assignable to transitions to superexcited R-b and R-B Rydberg states, the structure in the polarization spectrum was not possible to fully assign. Positions of the images described in Figs. 17-19 are indicated in the figure. Peaks in the TKER curves for these figures, and for an image taken at 5.729 eV (not shown) all include signals from formation and dissociation of A-state molecules. Further above threshold no formation of A-state was observed in the TKER curve shown in Fig. 5.19, even though this energy position at three-photons corresponds to a peak in A-state yield. This could indicate a weak photodissociation cross section or a much stronger yield of X-state O_2^+. Note that since the O_2^+ a-state does not fluoresce, an excitation spectrum for a-state formation similar to that of Fig. 5.34 is not available.

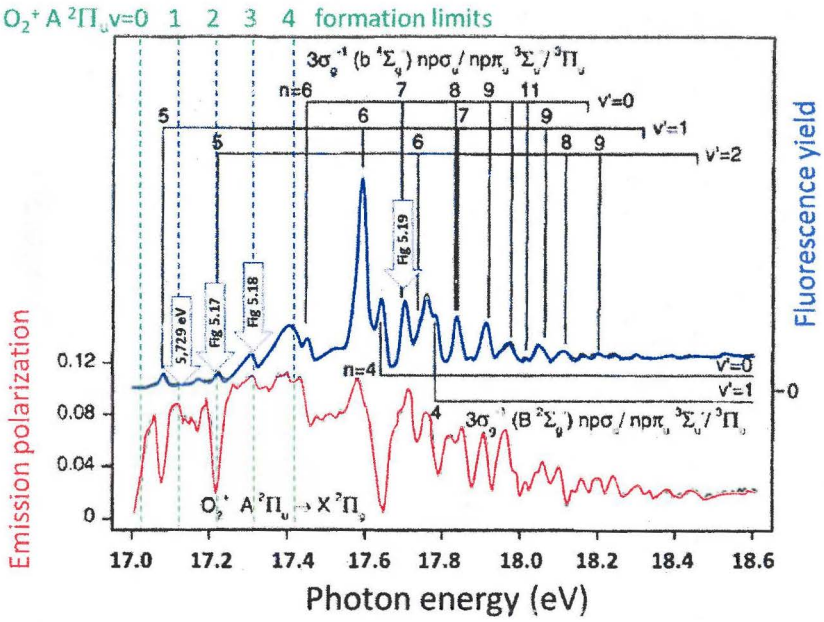

Figure 5.34: Excitation spectrum of O_2 with detection of emission from the O2+ A-state, copied from Holland et al. The energy thresholds for production of $O_2^+ A(v=0\text{-}4)$ are shown as dashed vertical lines, and the positions of three-photon excitation in this study are indicated by arrows.

5.4.8 Two-photon ionization of O_2

The data shown in Figs. 5.20-5.24 is taken in regions where the two-photon energy exceeds the IP of O_2. While it was not possible to obtain a reliable two-photon O_2^+ ionization yield spectrum it is useful to consult the one-photon ionization yield spectrum reported by Holland [14] for similar cold molecular beam conditions as the present study, which is shown in Fig. 5.35.

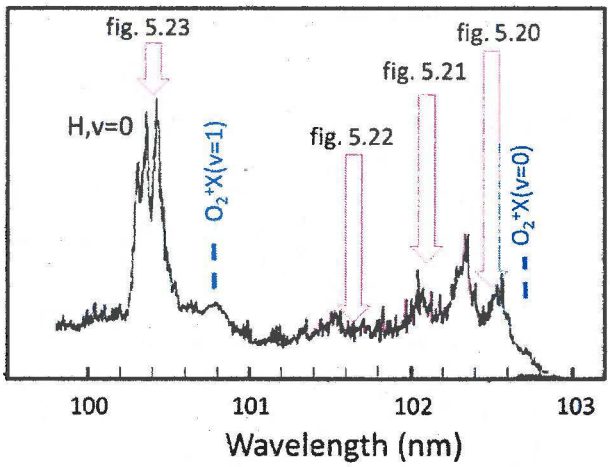

Figure 5.35: One-photon Ionization yield spectrum of O_2 copied from Holland et al.[14] The energy thresholds for production of $O_2^+X(v=0,1)$ are shown as dashed vertical lines, and the positions of two-photon excitation in this study are indicated by arrows.

While the ionization yield spectra for one- versus two-photon excitation will be necessarily quite different, the presence of autoionizing Rydberg-states that re more intense than the underlying ionization continuum is also expected for the two-photon case. Not that Fig. 5.23 shows almost exclusive production of O_2^+ X v=1 while Fig. 5.21 shows exclusive production of O_2^+X v=0, in agreement with their positions above threshold. However, Figs. 5.20 shows no indication of O_2^+Xv=0 formation and Fig. 5.22 shows a O_2^+ X (v=0) signal and much stronger signals due to photodissociation of O_2^+X (high v) states. Clearly, a two-photon ionization yield spectrum in this region would be useful to assign the autoionizing states responsible for O_2^+ (low v) production.

5.4.9 *Photodissociation of O_2^+*

In all images, formation of O_2^+X is dominant, with production of a very wide range of vibrational levels. Formation of $O_2^+a(^4\Pi_u)$ and $O_2^+A(^2\Pi_u)$ is observed (via O^+ production) only in small ranges near their energetic thresholds. Photodissociation of the O_2^+X state is observed to the L1, L3, L5 and L6 limits, no measurable signal was observed for dissociation to the L2 or L4 limits. In contrast, photodissociation of $O_2^+a(^4\Pi_u)$ state was only observed to the L2 limit, while the $O_2^+A(^2\Pi_u)$ was observed to dissociate only to the L3 limit.

Electric dipole transitions can excite $O_2^+X(^2\Pi_g)$ to states of $^2\Sigma_u^-$, $^2\Sigma_u^+$, $^2\Pi_u$ and $^2\Delta_u$ symmetry. According to the adiabatic photodissociation correlation rules, table 5.1, states of these molecular orbital symmetries are found in each of separated atom limits L1, L3, L5 and L6. Photodissociation of O_2^+ to the limits observed is thus consistent with spin-conserving dipole photoexcitation. L2 and L4 can only be reached via excitation of a quartet excited states, such as $O_2^+a(^4\Pi_u)$. For the photon energy needed for the production of $O_2^+a(^4\Pi_u)$ near its energy threshold, only photodissociation of L2 is possible, dissociation to the L4 limits lies too high in energy. The rather large difference in nergy between L1and L3, 3.324 eV, explains why dissociation of $O_2^+X(^2\Pi_g)$ to L3 only appears at laser photon energy of 5.7 eV (Fig. 5.16) and higher.

When several limits are energetically possible, branching to the highest energy limit, yielding the lowest TKER, is observed to be favored. At higher photon energies, increasingly higher vibration levels of the X-state are formed, and at the outer turning points of the X-state potential energy curve these states have increasing larger Franck-Condon overlap with repulsive states correlating to the higher limits L5, L6 etc. This may explain the fact that both one photon dissociation of X (high v) competes with two photon dissociation X (low v) states which are assumed to have much higher population. Such competition is seen very clearly in Fig.5.21.

Two photon dissociation of the lowest vibrational levels of the $O_2^+X(^2\Pi_g)$ is observed at many of laser wavelengths studied here when using higher laser intensity. The $O_2^+A(^2\Pi_u)\leftarrow X(^2\Pi_g)$ transition is a strongly allowed parallel transition, and at the intensity of the focused laser beams used here power broadening will take place and exact resonance at first photon is probably not necessary. The second photon can excite states of $^2\Sigma_g^-$, $^2\Sigma_g^+$, $^2\Pi_g$ and $^2\Delta_g$ symmetry. Excitation by the second photon to a Σ or Δ state should yield a mixed parallel-perpendicular transition with a $\sin^2\theta\cos^2\theta$ angular 'quadrupole' distribution such as that seen for the higher energy two/photon channels in Fig. 5.25, while a parallel-parallel two photon transition should yield a $\sin^4\theta$ angular distribution and a beta parameter greater than 2. This latter condition is observed for all two photon signals, suggesting the two photon transition pathway is $O_2^+(^2\Pi_g)\leftarrow O_2^+A(^2\Pi_u)\leftarrow O_2^+X(^2\Pi_g)$ where the upper state could be $2(^2\Pi_g)$ state [48] which correlates with the L3 limit, the limit observed experimentally for this channel.

Beta parameters for one photon dissociation of $O_2^+X(^2\Pi_g)$ to the L1 and L3 limits are plotted in Figs. 5.26 and 5.27, respectively, as a function of the initial vibrational level. Large variations are observed for different

pathway states, but general trend seen is that beta increases with initial vibrational level, and often exceed 2, which usually indicates for one photon dissociation alignment of the initial state. Pre-alignment of $O_2^+A(^2\Pi_u)$ has been observed previously as polarization of emission A-state molecules formed by ionization, as discussed earlier. Such alignemnet is expected for X-state molecules and the trend suggests that the alignment varies from perpendicular to the laser E field polarization for production of low v molecules to parallel for high-v molecules. This must be seen as a qualitative observation because the three photon ionization process itself can easily produce pre-selction and thus alignment of O_2, which will bias the ionization –induced alignment.

5.5 Conclusion

Velocity map imaging of O^+ ions and electrons formed by 2+1 REMPI of O_2 via the lowest Rydberg states is shown to yield a wealth of information on superexcited states and their dynamics, where a number of genral trends are observed. Over the entire energy region studied here, ionization to form $O_2^+X(^2\Pi_g)$ in a wide range of vibrational levels is the strongest channel, where direct ionization to form low low v-lelvels is observed by photoelectron imaging to be stronger that auto-ionization, which forms a full ensemble of v-levels, and particularly the highest-v levels. In the lower energy range, fully consistent the range observed for one-photon absorption in the XUV region of 70 to 75 nm, neutral dissociation to form electronically excited atoms, particularly the *3s* $^5S°$, $^3S°$ and *3p* $^5P°$, $^3P°$ states is observed with formation of both O ^3P and O ^1D co-partner atoms. At the high laser intensity needed for (2+1) REMPI, saturation of the ionization step to form O^+ from the electronically excited O^* atom is observed, consistent with a previous VMI study using XUV excitation and imaging detection. Assuming saturation of the O^* ionization shows from the comparison of the photoelectron and O^* images that a large fraction of the O_2^+ ions are photodissociated by the laser light. O_2^+ photodissociation occurs to the limits L1, L3, L5 and L6 in our energy range, each limits contains states that are optically allowed from the ground state of the ion. Angular distributions suggest a strong alignment effect in the ionization process to form $O_2^+X(^2\Pi_g)$. Small amounts of $O_2^+($ $a\ ^4\Pi_u$) and $O_2^+(\ A\ ^2\Pi_u)$ states these dissociate to the L2 and L3 limits, respectively.

Future experiments to further clarify the identity of the super excited state could make use of 2+1 REMPI, Where Glab et al.[49] have shown an example using the $3d\pi\ ^3\Sigma_0^-(v=0)$ Rydberg state. A continuous scan of the last photon should trace out the identity of the super excited state. A more quantitative comparison of a wider set of photoelectron images is

also in progress along with higher resolution slice imaging studies. While at present it is possible to assign essentially all observed O^+ signals, by slicing it should be able to improve the quality of the observed beta values by further decreasing the amount of overlap of signals.

References:

1. R. L. Platzman, Rad. Res. **17**, 419 (1962).
2. Y. Hatano and K. Kuchitsu, Elsevier, Amsterdam, 151 (1994).
3. Y. Hatano, Rad. & Envir. Biophys. **38**, 239 (1999).
4. U. Masatoshi, J. Elec. Spec. & Rel. Pheno. **79**, 423 (1996).
5. D. Song, A. Azarm, Y. Kamali, K. Liu, A. Xia, Y. Teranishi, S.-H. Lin, F. Kong and S. L. Chin, J. Phys. Chem. A **114**, 3087 (2010).
6. K. Noriyuki, U. Masatoshi and H. Yoshihiko, J. Phys. B: Atom., Mol. & Opt. Phys. **30**, 2319 (1997).
7. K. Muller-Dethlefs and E. W. Schlag, Annu. Rev. Phys. Chem. **42**, 109 (1991).
8. J. E. LeClaire, R. Anand and P. M. Johnson, J. Chem. Phys. **106**, 6785 (1997).
9. R. L. Platzman, J. Phys. Radium **21** (1960).
10. P.-M. Guyon and I. Nenner, Appl. Opt. **19**, 4068 (1980).
11. C. Jungen, J. De Chim. Phys. Et De Physi.-Chemi Biologi. **77**, 27 (1980).
12. A. Giusti-suzor and H. Lefebvre-Brion, Chem. Phys. Let. **76**, 132 (1980).
13. K. Kirby, S. Guberman and A. Dalgarno, J. Chem. Phys. **70**, 4635 (1979).
14. D. M. P. Holland, D. A. Shaw, S. M. McSweeney, M. A. MacDonald, A. Hopkirk and M. A. Hayes, Chem. Phys. **173**, 315 (1993).
15. H. Liebel, R. Müller-Albrecht, S. Lauer, F. Vollweiler, A. Ehresmann and H. Schmoranzer, J. Phys. B: Atomic, Mol. & Opt. Phys. **34**, 2581 (2001).
16. A. Karawajczyk, P. Erman, E. Rachlew-Källne, J. R. i. Riu, M. Stankiewicz, K. Y. Franzén and L. Veseth, Phys. Rev. A **61**, 032718 (2000).

17. M. N. R. Ashfold, N. H. Nahler, A. J. Orr-Ewing, O. P. J. Vieuxmaire, R. L. Toomes, T. N. Kitsopoulos, I. A. Garcia, D. A. Chestakov, S.-M. Wu and D. H. Parker, Phys. Chem. Chem. Phys. **8**, 26 (2006).

18. J. Rius i Riu, A. Karawajczyk, M. Stankiewicz, K. Yoshiki Franzén, P. Winiarczyk and L. Veseth, Chem. Phys. Let. **333**, 91 (2001).

19. T. Akahori, Y. Morioka, T. Tanaka, H. Yoshii, T. Hayaishi and K. Ito, J. Chem. Phys. **107**, 4875 (1997).

20. D. A. Shaw, D. M. P. Holland, E. E. Rennie and L. G. Shpinkova, J. Phys. B: Atom., Mol. & Opt. Phys. **38**, 173 (2005).

21. A. V. Baklanov, L. M. C. Janssen, D. H. Parker, L. Poisson, B. Soep, J.-M. Mestdagh and O. Gobert, J. Chem. Phys. **129**, 214306 (2008).

22. P. H. Krupenie, J. Phys. & Chem. Refer. Data **1**, 423 (1972).

23. O. Edqvist, E. Lindholm, L. Selin, H. Sjogren and L. Asbrink, Arkiv For Fysik **40**, 439 (1970).

24. O. Edqvist, E. Lindholm, L. E. Selin and L. Åsbrink, Phys. Let. A **31**, 292 (1970).

25. H. Park, P. J. Miller, W. A. Chupka and S. D. Colson, J. Chem. Phys. **89**, 6676 (1988).

26. R. J. Yokelson, R. J. Lipert and W. A. Chupka, J. Chem. Phys. **97**, 6153 (1992).

27. S. T. Pratt, J. L. Dehmer and P. M. Dehmer, J. Chem. Phys. **93**, 3072 (1990).

28. C. Zhou and Y. Mo, J. Chem. Phys. **139**, 084314 (2013).

29. Y. Zhou, Q. Meng and Y. Mo, J. Chem. Phys. **141**, 014301 (2014).

30. M. Ukai, N. Kouchi, K. Kameta, N. Terazawa, Y. Chikahiro, Y. Hatano and K. Tanaka, Chem. Phys. Let. **195**, 298 (1992).

31. B.-Y. Chang, R. C. Hoetzlein, J. A. Mueller, J. D. Geiser and P. L. Houston, Rev. Sci. Instrum. **69**, 1665 (1998).

32. D. H. Parker and A. T. J. B. Eppink, J. Chem. Phys. **107**, 2357 (1997).

33. A. T. J. B. Eppink and D. H. Parker, Rev. Sci. Instrum. **68**, 3477 (1997).

34. V. Dribinski, A. Ossadtchi, V. A. Mandelshtam and H. Reisler, Rev. Sci. Instrum. **73**, 2634 (2002).

35. R. Ogorzalek Loo, W. J. Marinelli, P. L. Houston, S. Arepalli, J. R. Wiesenfeld and R. W. Field, J. Chem. Phys. **91**, 5185 (1989).

36. R. J. Yokelson, R. J. Lipert and W. A. Chupka, J. Chem. Phys. **97**, 6144 (1992).

37. J. S. Morrill, M. L. Ginter, E. S. Hwang, T. G. Slanger, R. A. Copeland, B. R. Lewis and S. T. Gibson, J. Mol. Spec. **219**, 200 (2003).

38. B. Bakker and D. Parker, J. Chem. Phys. **112**, 4037 (2000).

39. D. H. Parker, R. F. Delmdahl, B. B. L. G. Bakker and H.-P. Loock, J. Chinese Chem. Soc. **48**, 327 (2001).

40. Z. Farooq, D. A. Chestakov, B. Yan, G. C. Groenenboom, W. J. van der Zande and D. H. Parker, Phys. Chem. Chem. Phys. **16**, 3305 (2014).

41. A. S. Bracker, E. R. Wouters, A. G. Suits, Y. T. Lee and O. S. Vasyutinskii, Phys. Rev. Let. **80**, 1626 (1998).

42. A. S. Bracker, E. R. Wouters, A. G. Suits and O. S. Vasyutinskii, J. Chem. Phys. **110**, 6749 (1999).

43. T. P. Rakitzis, S. A. Kandel, A. J. Alexander, Z. H. Kim and R. N. Zare, Science **281**, 1346 (1998).

44. T. P. Rakitzis and R. N. Zare, J. Chem. Phys. **110**, 3341 (1999).

45. G. G. Balint-Kurti, A. J. Orr-Ewing, J. A. Beswick, A. Brown and O. S. Vasyutinskii, J. Chem. Phys. **116**, 10760 (2002).

46. P. V. Demekhin, V. L. Sukhorukov, H. Schmoranzer and A. Ehresmann, J. Chem. Phys. **132**, 9 (2010).

47. A. Ehresmann, H. Liebel, H. Schmoranzer, O. Wilhelmi, B. Zimmermann and K. H. Schartner, J. Phys. B: Atomic, Mol. & Opt. Phys. **37**, 389 (2004).

48. N. H. F. Beebe, E. W. Thulstrup and A. Andersen, J. Chem. Phys. **64**, 2080 (1976).

49. W. L. Glab, P. M. Dehmer and J. L. Dehmer, J. Chem. Phys. **104**, 4937 (1996).

Chapter 6

Multiphoton dissociation of molecular sulfur S_2 via two resonant states in the UV region

Abstract

The multiphoton dissociation dynamics of molecular sulfur (S_2) in the ultraviolet range of 205-300 nm is studied using velocity map ion imaging (VMI). In this one-color experiment, molecular sulfur (S_2) is generated in a pulsed discharge and then photodissociated by UV radiation. At the three-photon level, superexcited states are accessed via two different resonant states: the B (v=8-11) valence states at one-photon level and a Rydberg state at the two-photon level. Among the decay processes of these superexcited states, dissociation to electronically excited S atoms is dominant as compared to autoionization to ionic states $S_2^+(X\,^2\Pi_g)$ at wavelengths $\lambda < 288$ nm. The anisotropy parameter extracted from these images reflects the parallel character of these electronic transitions. In contrast, autoionization is found to be particularly efficient at the S(^{1}D) and S(^{1}S) detection wavelengths around 288nm. Information obtained from the kinetic energy distributions of S atoms has revealed the existence of vibrationally excited $S_2^+(X\,^2\Pi_g$ (v>11)) which dissociates to ionic products following one-photon absorption. This work reveals also many interesting features of S_2 photodynamics compared to those of electronically analogous O_2.

6.1 Introduction

Sulfur (S_2) molecules are of astrophysical significance, as they are found in the atmospheres of some comets[1] and dense molecular clouds.[2] The emission and absorption spectra of S_2 is observed in the atmospheres of Jupiter [3] and its satellite[4], which confirm the presence of these molecules in planetary atmospheres. S_2 molecules can also be found in various natural and industrial plasmas containing sulfur compounds.[5] The S_2 molecule is widely observed in shock tubes, flames, and discharges[6] and is an important ingredient in sulfur lamps.[7] The compound is hazardous and also a pollutant in the atmosphere; hence the photodissociation phenomenon of S_2 is a significant topic.

While molecular sulfur has been studied extensively over the last decades, its photoexcitation dynamics are still unclear due to its complexity and to spin-orbit coupling between its manifold of states. Our laboratory studies of S_2 use a discharge system in which diatomic sulfur is produced in the discharge and then allowed to interact with intense laser light. In our study the transitions of S_2 are detected via the speed and angular distribution of S atom photofragments using the velocity map imaging (VMI) technique. Frederix et al.[8] studied the photodissociation of S_2 at one-photon level with subsequent detection of $S(^3P_j)$ fragments using VMI where the bond energy of S_2 was significantly revised to a value of 4.418 eV. Later, we investigated the photodissociation of singlet sulfur S_2 $\tilde{a}\ ^1\Delta_g^+$ and $\tilde{b}\ ^1\Sigma_g^+$ (i.e. the metastable singlet states of S_2), in single laser experiment.[9] The main goal of this work is to extend the study of photodissociation of S_2 at multi photon levels in order to explore various dynamical processes in S_2.

Exposure of S_2 to high intensity light from a focused, pulsed, tunable dye laser, such as that needed for (2+1) REMPI detection of S atoms, can lead to multiphoton ionization of S_2, as first reported by Dyke and coworkers[10], and in detailed studies by Western and coworkers[11], who showed that three-photon ionization can be resonance enhanced at the one-photon level via the $\tilde{X}\ ^3\Sigma_g^- - \tilde{B}\ ^3\Sigma_u^-$ and $\tilde{X}\ ^3\Sigma_g^- - \tilde{B}''\ ^3\Pi_u^+$ bands, and at the two-photon level by the $(3d\pi)^3\Delta_g$ Rydberg state and the $2\ ^5\Sigma_g^-$ ion-pair state. We may thus expect that stepwise multiple photon photodissociation of S_2 is a means of producing S atoms. Autoionization followed by photodissociation of the S_2^+ ion via the continuum of the strong $X(^2\Pi_g)$ – $A(^2\Pi_u)$ transition leads to neutral S atoms in combination with S^+ ions, which are detected in our experiment. In O_2,[12] the main channel for production of O^+ ions when using (2+1) REMPI via a manifold of Rydberg states was the formation of O_2^+ in a wide range of vibrational levels, followed by photodissociation of O_2^+ to form O^+ ions. A secondary process was formation of electronically excited O atoms after absorption of three-

photons (competing with O_2^+ formation); these excited atoms are immediately ionized to O^+ by the intense UV laser field. Alongside the observation of S^+ from 2+1 REMPI of neutral (valence) atoms we can thus expect production of S^+ by following production and ionization of electronically excited atoms, and by photodissociation of S_2^+ ions, where the latter two processes can take place on- and off-resonance with S-atom 2+1 REMPI lines.

6.2 Experiment

A standard VMI setup contains ion optics (for the extraction field), a time of flight (TOF) tube and a 2-dimensional position sensitive detector, which consist of two microchannel plates and a phosphor screen followed by a charge-coupled device (CCD) camera. The power of VMI is its ability to extract ions with the same velocity vector using ion optics and to focus them onto the same pixel position at the 2-D detector, irrespective of the position where these ions were formed.[13] A schematic diagram of our experimental set up to obtain velocity mapped images is illustrated in figure 1.

In a high vacuum setup, a discharge of H_2S was used to produce molecular sulfur (S_2). H_2S gas is seeded in argon in a 20% ratio with a backing pressure of 2 bar, and the molecular beam is created by a pulsed valve (Jordan) with 0.4 mm diameter orifice. This gas expands through the nozzle into the source chamber to produce a cold, pulsed molecular beam. Just in front of the nozzle, 2.5 mm downstream, a stainless steel ring (4 mm diameter, 0.5 mm thickness) is mounted. As each gas pulse passes, the voltage on the ring is pulsed to a positive high voltage (~1000 V) which produces an electrical discharge[14] between the ring and the grounded nozzle for the production of S_2. The production of S_2 radicals is dependent on the width, delay and voltage of the pulse applied to the ring. It is observed that a positive voltage (~1000V, 10 μs) is more suitable for a high production of S_2 radicals as compared to a negative voltage (which is more suitable for the production of SH[15]). In addition, a filament is placed adjacent to the ring discharge and a current of around 1.5 ampere is passed through it. This glowing filament emits electrons which help to initiate and stabilize the discharge.

The molecular beam of S_2 passes through one conical skimmer (2 mm diameter) 20 mm downstream from the nozzle and is directed towards the detector. After passing through a 2mm diameter hole in the center of the repeller, the molecular beam is crossed orthogonally by laser light between repeller and extractor electrodes of the velocity mapped imaging TOF source as shown in figure.

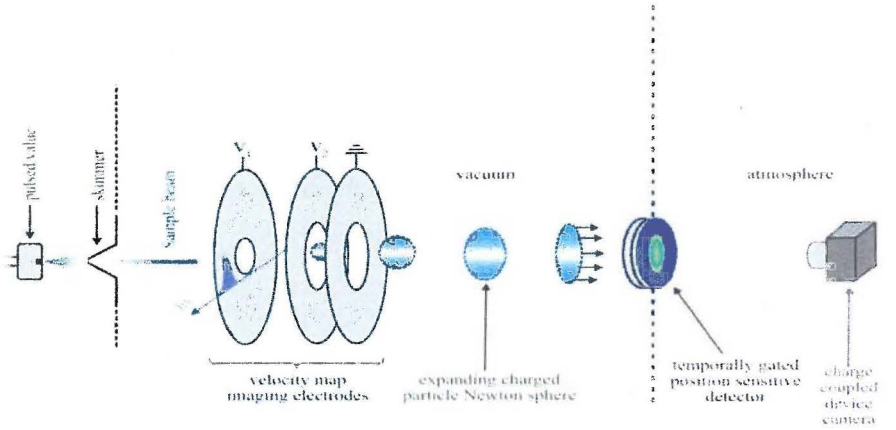

Figure 6.1: Schematic diagram of velocity map imaging experimental set up.

In the experiment, the output of a frequency doubled dye laser (Spectra-Physics PDL-2) pumped by the second harmonic of a pulsed Nd:YAG laser (Spectra-Physics DCR-3A,10 Hz) is operated at various wavelengths by using different mixtures of dyes such as Rhodamine 6G, sulforhodamine B, DCM and Fluorescence 548. Subsequently, frequency doubling is achieved by an angle-tuned KDP/BBO crystal, producing ~4mJ/pulse in the observed wavelength range. A Pellin-Broca prism was used to separate the second harmonic light from the fundamental. Finally, ~3 to 4 mJ per pulse of polarized laser light (0.6 cm^{-1} line width) is focused into the interaction region by means of a positive focal length lens. During the experiments the wavelength was scanned in the range between 300 nm and 205 nm. The ions created by UV laser radiation are extracted from the interaction region (between repeller and extractor) into the time-of-flight (TOF) tube.

To record the two-dimensional VMI images, an ion imaging detection system is employed at the end of the TOF tube which comprises a matched pair of MCP plates coupled to a P46 phosphor screen. The images are recorded using CCD camera mounted behind the phosphor screen captures the ion images on the phosphor screen at each laser shot. The MCPs can be gated with a high voltage pulse to allow only the ions of interest to be detected. The timings for laser, discharge, detector and valve are controlled by digital pulse generators with 10 Hz repetition rates. The CCD images are collected in PC and for each image data is collected over a 15000 laser shots. The images are further analyzed via Davis 62. The S^+ velocity map images are quadrant-symmetrized prior to extending the kinetic energy and angular distributions. S^+ ion images are inverted using the BASEX method.[16]

For kinetic energy calibration, one color images for S(^{3}P) detection at 308.20 nm were employed. Three strong rings appear in the S^+ image corresponding to two-photon excitation of S_2 followed by dissociation to the first, second and third ($^3P_2$+$^3P_2$, $^3P_2$+^{1}D and $^3P_2$+^{1}S, respectively) dissociation limits. The strong and sharp middle ring corresponding to $^3P_2$+^{1}D with a total kinetic energy release (TKER) value of 2.531 eV was used for calibration.

6.3 Results

Velocity mapped images of S^+ ions arising from multistep dissociation of S_2 were recorded in the wavelength region of 205-300 nm. An overview of the possible ionization/dissociation pathways when molecular sulfur is excited at different wavelengths in the region 205 to 300 nm is given in figure 2. The energy range studied here is indicated in Figure 2 as a gray-shaded region of 3.97-4.66 eV for one-photon excitation, 7.94-9.32 eV for two-photon excitation, and 11.91-13.98 eV for three-photon excitation. Neutral dissociation products are indicated in Figure 2 as *valence atoms* (S(^{3}P, ^{1}D, and ^{1}S, from the S(..3S23p^4) configuration), and electronically *excited atoms* (e.g., the lowest is S(..$3s^2 3p^3(^4S°)4s$ ^{5}S°, J=2), indicated as S*(^{5}S), at 6.524 eV above the S($^3P_2$) covalent state.

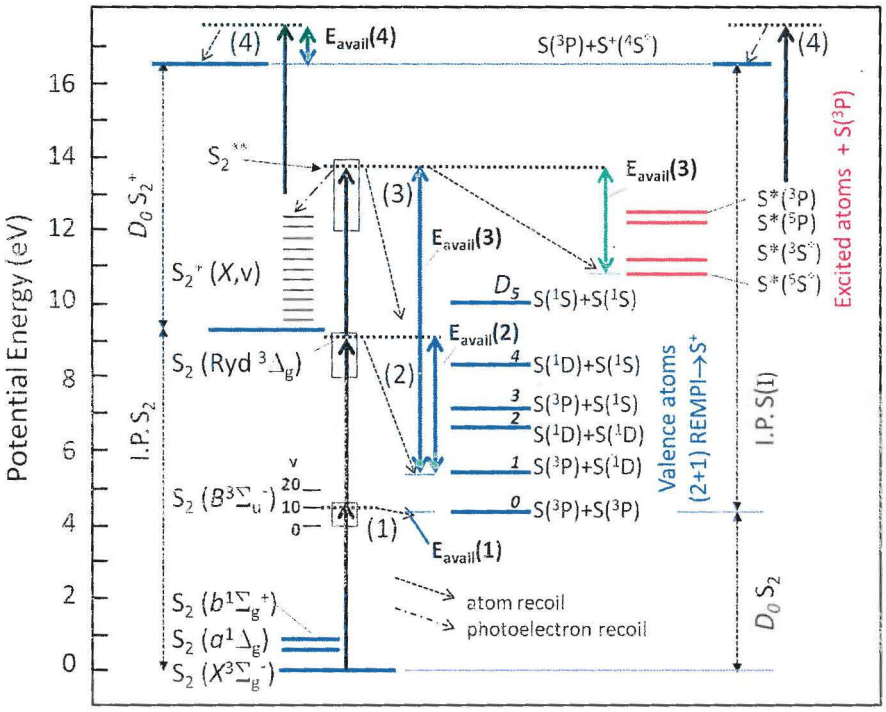

*Figure 6.2: Energy level diagram showing the positions of selected S_2 and S_2^+ electronic states and dissociation limits $D_{0\text{-}5}$ to neutral 'valence' atoms and to excited Rydberg states (in which case the partner is an $S(^3P_2)$ atom). Vertical black arrows indicate the energy of a 280 nm photon, which is just above D_0 at the one-photon level. The energy difference $E_{avail}(1\text{-}2)$ appears as S atom kinetic energy release. The gray-shaded region indicates the energy ranges covered by 320-266 nm photons. In the region at the one-photon level are the strong Schumann-Runge $X(^3\Sigma_g^-)$-$B(^3\Sigma_u^-)$ transitions shown in Fig. 2. At the two-photon level, dissociation limits $D_{4\text{-}0}$ are energetically accessible, the $(3d\pi)^3\Delta_g$ Rydberg state and 2 $^5\Sigma_g^-$ ion-pair states lie in this region. Excitation to a superexcited state labeled S** at the three-photon level leads to dissociation to valence atoms or to (auto)ionization to $S_2^+X(^2\Pi_g)$ or higher energy states can take place along with (pre)dissociation to an S* excited atom or valence atom limit. In order to form S^+ ions, photoionization of S* or photodissociation of S_2^+ is necessary. The processes that determine the speed and angular distributions of the measured S^+ ions are labeled E_{avail} and shown with green double headed arrows.*

6.3.1 Superexcited state autoionization vs. excited atom formation

At the three-photon level, superexcited states of S_2 can be accessed via the B state, the upper state of the Schumann-Runge transition at one-photon level and via Rydberg states at two-photon level. These superexcited states of S_2 can either dissociate into electronically excited fragments followed by ionization of these fragments or they can autoionize, followed by photodissociation of S_2^+. Such processes can compete at similar rates.

In the UV wavelength region, images were recorded under tight focusing conditions. In our previous two-color study we reported images taken with the dissociation laser in the 281-266 nm region at low laser intensity and the detection laser tightly focused for $S(^3P_J)$ detection around 308 nm. With tight focusing in the region below 288 nm, strong S^+ images were found at or near the wavelengths corresponding to the $X(^3\Sigma_g^-)$-$B(^3\Sigma_u^-)(v')$ bands shown schematically in the energy level diagram of Figure 2,, and in Figure 3 of Chapter 4. The inverted images and TKER curves for the images taken at wavelengths resonant with the B(v'=8-11) bands are shown in Figure 3. The starting points of the TKER curves are shifted relative to each other in this figure by three times the photon energy difference. Two main channels are identified in the TKER distributions, where three-photon excitation forming superexcited S_2^{**} followed by predissociation appears to be the strongest channel here. This involves the formation of electronically excited S atoms $S^*($ ....$(^4S^0)$ 4p $^5P)$, $S^*($ ....$(^4S^0)$ 4p $^3P)$, $S^*($ ....$(^4S^0)$ 4s $^3D)$, S^*(....$(^4S^0)$ 3d $^5D)$, S^*(....$(^4S^0)$ 3d $^3D^0)$,

$S^*(....(^4S^0)5s\ ^5S^0)$, $S^*(3s\ 3P^{53}P^0)$ atoms which autoionize, producing equal amount of S^+ atoms and electrons. The other process, autoionization following three-photon absorption, producing $X^2\Pi_g(v)$ states of S_2^+followed by one or two-photon dissociation of S_2^+ ions to $S^+(^4S)+S(^3P)$ and $S^+(^4S)+S(^1D)$ dissociation channels is a weaker channel in this observed wavelength range.

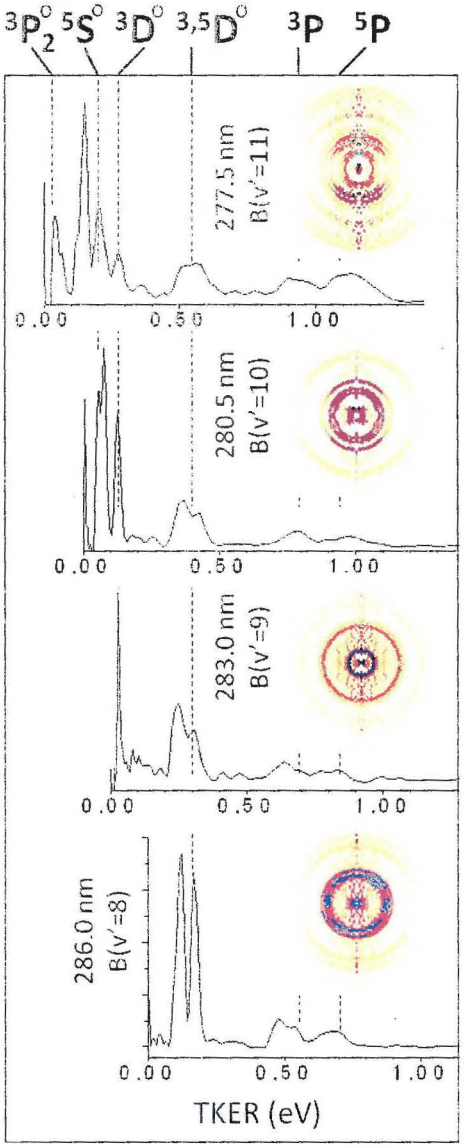

Figure 6.3: S^+ images taken at the indicated wavelengths in the 286-277 nm region along with the corresponding TKER curves. For each image the laser wavelength and the vibrational level of the $X \rightarrow B(v')$ one-photon transition excited at this wavelength are labeled. Vertical dashes lines indicate the TKER for the $S(^3P_2)+S^{**}$ ($S^{**}= {}^3P_2^o, {}^5S^o$, ${}^{3,5}D^o, {}^3P, {}^5P$ excited atoms), in most cases a stronger peak at lower energy corresponding to $S(^3P_1)+S^{**}$ is also present. The TKER curves are shifted to lower energy by $\Delta 3h\nu$ with respect to the 277.5 nm curve.

6.3.2 Two- and three-photon dissociation of S_2 in $S(^1D)$ and $S(^1S)$ detection

Continuing to increasingly longer wavelengths, velocity map images for $S(^1S)$ and $S(^1D)$ detection were recorded in the wavelength region above 286 nm. TKER curves for the $S(^1S)$ and $S(^1D)$ images at 288.27 nm and 288.19 nm are plotted, respectively in Figure 6 along with the TKER curve for $S(^1D)$ detection at 291.30 nm.

While at present we have no quantitative theory to predict or describe two-photon dissociation of S_2, we can most simply compare the trends observed in S_2 with those for O_2. While two-photon dissociation occurs most likely at all laser wavelengths used, we can only detect the neutral valence atoms formed at the REMPI wavelengths indicated in Fig. 4. These neutral atoms have a distinct signature in their S^+ Doppler profile, where the image intensity along the laser propagation direction changes with wavelength.

$S(^1D)$ detection

$S(^1D)$ images recorded at the REMPI wavelengths 291.30 nm and 288.19 nm via the S $..3s^23p^3(^2D^\circ)4p\ ^1F$ state and the S $..3s^23p^3(^2D^\circ)4p\ ^1P$ state, respectively. At both wavelengths products formed via the dissociation limits D_1 and D_2 are observed for both two-photon and three-photon dissociation. We should point out that for the high kinetic energy resulting from three-photon dissociation it will not be possible to crush the Newton sphere, which implies that the actual signal could be significantly stronger than the observed signal for these fragments. For the two-photon dissociation signal D_3 appears to be significantly weaker for photodissociation at the REMPI ^1P resonance compared to ^1F resonance detection, an effect also observed in O_2.

$S(^1S)$ detection

Nearby the known 2+1 REMPI line for $S(^1D)$ detection at 288.19 nm a strong ring with the clear Doppler signature of a bound-bound transition

of a fast neutral atom appears in the S^+ image at the resonant wavelength 288.27 nm. TKER analysis (Fig. 4) shows that this strong signal corresponds energetically exactly to the $^1S + {}^3P$ (D_3) channel. REMPI detection of $S(^1S)$ atoms have been reported previously at numerous resonances in the 295 nm region,[17] where assignment of the upper resonant state was not possible. As previously, the upper resonant state of this newly identified REMPI process cannot be reliably assigned. There is no evidence for formation of the $^1S + {}^1D$ (D_4) channel, the $^1S + {}^1S$ (D_5) channel is not energetically accessible at this wavelength.

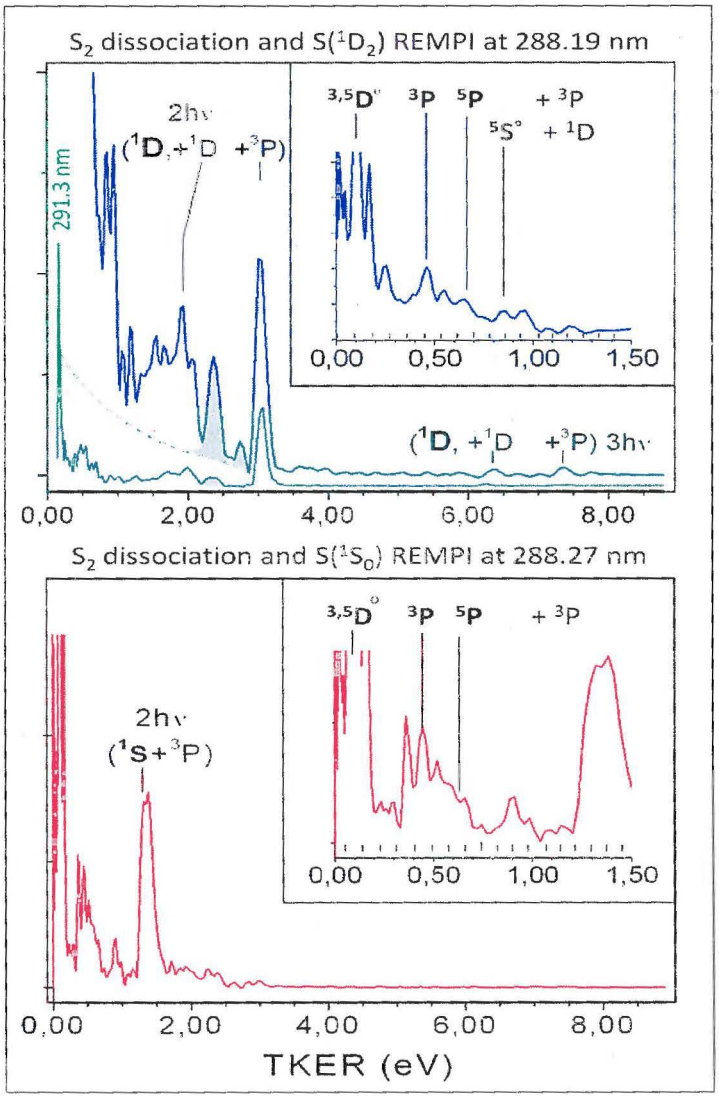

Figure 6.4: Upper panel; TKER curves for S(^{1}D) (2+1) REMPI detection at 291.30 and 288.19 nm (image shown in Figure 3. Lower panel; TKER curves for S(^{1}S) detection at 288.27 nm. Detected atoms are indicated by bold typeface.

6.3.3 One-photon dissociation of the S_2^+ molecular ion

Several rings are observed at the same velocity in the S(^{1}D) and S(^{1}S) detection image and the most prominent of these peaks at higher TKER are indicated by shaded peaks in the TKER curves for the S(^{1}D) images in Figure 4. In the TKERs of Fig. 4, this series of shaded peaks is attributed to $S^+(^4S)+S(^3P)$ products. These rings appears in the S(^{1}D) and S(^{1}S) detection images and also appear weakly in the images shown in Fig. 3, taken at dissociation wavelengths in (near)resonance with the B(v=8-11) levels. Peaks in the TKER 0.2-1.0 eV region which are not labeled in Fig. 4 also belong to this group of rings, all of which show maximum intensity along the direction of the electric field of the linearly polarized dissociation laser. We assign this set of peaks to photodissociation of the ground electronic state of the S_2^+ ion for the following reasons. First, signal at the expected arrival time of the S_2^+ mass is observed under our conditions in the TOF mass spectrum, confirming that S_2^+ is present. Second, the TKER of the peaks observed is consistent with S_2^+ photodissociation at the wavelengths used in this study, as discussed next, and finally, the parallel nature of the angular distribution (positive beta parameter) is that expected for photodissociation of ground electronic state S_2^+(($X^2\Pi$) to the repulsive wall of the strong, dipole allowed $X(^2\Pi_g)\rightarrow(^2\Pi_u)$ transition.

In similar studies of O_2 photodissociation, the most prominent O^+ signals arise from one-photon dissociation of O_2^+ populated in a wide range of vibrational levels in the ground electronic state due to autoionization from a core-excited state at the three-photon level. The same process, as discussed later, is also expected for S_2. Figure 5 shows a schematic of the energetics of S_2^+ formation and photodissociation at the energy of 4.301 eV (288.27 nm), S(^{1}S) detection in Fig. 3.

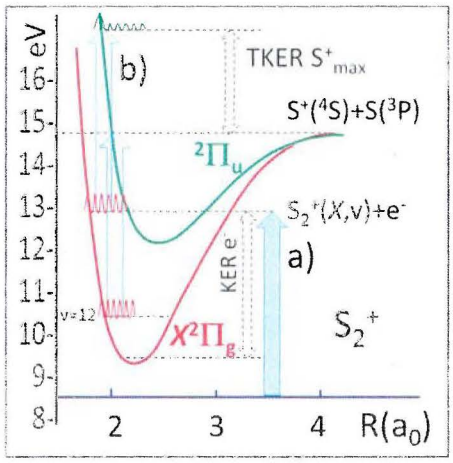

Figure 6.5: Schematic diagram of S_2^+ ion formation and photodissociation at 288.27 nm.

At this wavelength the energy sum of three-photons (3hν=12.903eV) (at the point labeled **(3)** in Fig. 2)is needed to exceed the S_2 ionization potential of 9.360 eV, leaving an excess energy of 3.54 eV. All $S_2^+(X)$ vibrational levels from v=0 up to v=~45 are energetically accessible; the electron carries off the remaining energy. D_0 of the S_2^+ ion is 5.418eV, which restrictsS_2^+ photodissociation by a 4.301 eV photon to the v=12 and higher vibrational levels. The highest kinetic energy release for S^+ ions corresponds to four-photon excitation, yielding a TKER of 2.42 eV, which agrees well with that of the highest energy shaded peak in Fig. 4. The maximum TKER corresponds thus to photodissociation of $S_2^+(X,v=45)$ and nearly zero TKER to photodissociation of $S_2^+(X,v=12)$, and thus 33 different rings between 0 and 2.43 TKER . In principal the apparatus could resolve this many rings, but because both final products have multiple fine structure states, and because of the presence of vibrationally excited S_2 which leads to extra rings, reliable assignment of vibrational quantum numbers to the observed peaks is not possible. The peak height distribution for photodissociation of the set of vibrational states will be governed by the Franck-Condon overlap between the S_2^+ vibration wavefunction and the continuum wavefunction arising at the repulsive wall of the $^2\Pi_u$ state, as shown in Fig. 5. Since the photon energy is constant, progression up the vibrational ladder from v=12 to v=45 will reflect the positions of the nodes and peaks in the ground state wavefunctions, but this pattern is convoluted with the variation in initial population of the vibrational states, leading to a complex intensity pattern. Compared to O_2, the formation and photodissociation of S_2^+ is

relatively much weaker than excited atom formation/ionization, in part due to the high D_0 value of S_2^+ in relation to the photon energy. Detection of S_2^+ is limited to v>11 at the typical 288 nm wavelength, making lower vibrational levels invisible for S^+ detection.

6.3.4 *Relative strengths of the multi-photon dissociation channels*

By comparing signal strengths measured under the same laser conditions it is possible to compare the relative probabilities for photodissociation and S^+ formation for one- and multiple photon excitation of S_2. At wavelengths shorter than 280 nm direct one-photon dissociation of ground electronic state should be the dominant channel. In a previous paper[8] we reported S^+ production following excitation at 269.277 nm, resonant for 2+1 REMPI detection of $S(^3P_2)$ atoms via the $4p(^3P_2)$ Rydberg state. All signal corresponded to one-photon dissociation to D_0; no signals for two-photon dissociation (to ^3P products) or to photodissociation of S_2^+ ions were observed. In our other study (described in Chapter 4) on of the S_2(a,b) state around 310nm [18] one-photon dissociation is also the stronger channel compared to two-photon dissociation processes. At the ^1S and ^1D REMPI wavelengths longer than 280 nm two-photon dissociation was found to be stronger than three-photon dissociation to S^{**} or dissociation of S_2^+. When the valence atom products were not ionizable, S^{**} production by three-photon excitation was found to be stronger than autoionization to form S_2^+.

6.4 *Discussion*

We have observed the dissociation dynamics of superexcited states S^{**}formed at the three-photon level via the $B(^3\Sigma_u^-)$ state at one-photon level and Rydberg state at two-photon level; these state lead to formation of electronically excited S^* atoms and autoionization. Dyke et. studied the dynamics of superexcited states for molecular sulfur and compared the autoionization and electronically excited S atoms results for ground state of molecular sulfur $S_2\tilde{X}\ ^3\Sigma_g^-$. From our analysis of TKER distributions it is clear that the dynamics is dominated by the pathway yielding electronically excited atoms $S^*(\ldots.(^4S^0)\ 4p\ ^5P)$, $S^*(\ldots.(^4S^0)\ 4p\ ^3P)$, $S^*(\ldots.(^4S^0)\ 4s\ ^3D)$, $S^*(\ldots.(^4S^0)\ 3d\ ^5D)$, $S^*(\ldots.(^4S^0)\ 3d\ ^3D^0)$, $S^*(\ldots.(^4S^0)5s\ ^5S^0)$, $S^*(3s\ 3p^5{}^3P^0)$ from dissociation of the S_2^{**} state, which are subsequently ionized with a fourth photon. Curve crossing from repulsive states, or the repulsive wall of overlapping bound Rydberg states as in O_2, leads to excited atom production[19] and it appears to be active in case of molecular sulfur. Evidence from S^+ images taken at different vibrational levels (v=8-11) of the B state suggests that excited atom formation is a general process and not the result of a coincidental resonance. It is also observed

that S^+ ions are not the result of ion pair formation (threshold =12.65 eV)[20] or from non-resonant S atom multiphoton ionization.

Autoionization $S_2^{**} \rightarrow S_2^+$, followed by photodissociation which yields S^+ ions was not observable at wavelengths $\lambda > 288$ nm.Weak photodissociation signals of S_2^+ were observed in this study at wavelengths$\lambda < 288$ nm. This is due to the high D_0 value of S_2^+ in relation to the photon energy; the ionic state is quite strongly bound, so only vibrational levels with $v>11$ ($S_2^+(X\ ^2\Pi_g)$ can be dissociated at 288 nm. In general, transitions between the excited state and a bound ionic state are not possible either, since the excitation energy must be exactly in resonance with the bound ionic state. This can easily be seen from energy conversation: there is no open channel available to carry away the energy if the transition is not resonant.[21]

One-photon dissociation of S_2^+ ($X^2\Pi_g$) to the lowest ion dissociation limit, $S^+(^4S)+S(^3P)$,has been observed around 288 nm. $^2\Pi_{g,u}$ states correlate with this limit $S^+(^4S)+S(^3P)$ [22] and the $X(^2\Pi_g) \rightarrow (^2\Pi_u)$ transition is a dipole allowed and strong transition. The ground ionic state of S_2^+ ($X^2\Pi_g$) photodissociates most likely on the repulsive wall of the $^2\Pi_u$ state. This results in a parallel transition, which is indeed observed in the S+ product angular distribution.

In contrast to O_2,[12] however, most of the S^+ ions came from electronically excited S atoms and a small amount resulted from photodissociation of S_2^+. Although O_2 is electronically analogous to S_2, there are many significant differences in the electronic structure of the two molecules. The upper level of the well known SR bands, the $B(^3\Sigma_u^-)$ state is located at lower energy in S_2 with bound levels lying below the first dissociation limit. Also, O_2^+ is in proportion less strongly bound compared to S_2^+ such that lower vibrational levels could be dissociated.

The measurement of β for any product channel provides information on the symmetry of the electronic states involved in the absorption process and their lifetime with respect to rotation. The extreme values of β (-1 for a perpendicular bound free transition and +2 for parallel bound free transition) can only be obtained if a single state is excited and the dissociation lifetime of the excited state is much shorter than the rotation period of the parent molecule. An isotropic distribution is characterized by β =0. At all three wavelengths 277.5 nm, 280.5 nm and 286 nm, the β values for all channels were found to be fluctuate markedly in the studied wavelength region and values ranging from almost β=0.65 upto 2 were found. These measured values of β would imply a parallel transition. Photo-alignment in multiphoton excitation steps through the Rydberg state must influence the product angular distribution. In fact, just as in O_2, anisotropy parameter values $\beta > 2$ have been observed in S_2 at 277

nm. This trend is always possible because we deal with many photons. We expect that the overall process dominated by an allowed one-photon step, but it can happen that a previous photon causes alignment of the molecule, which affects the dissociation steps. At 283 nm dissociation, the peaks corresponding to ^5D and ^3D are closer to isotropic distribution. Several explanations are possible including excitation of multiple states, saturation due to higher laser flux , and a long-lived precursor state. It should also be mentioned that the Doppler effect and axis alignment due to photo-selection also influence the observed angular distribution anisotropy. For more progress an accurate knowledge of couplings between different electronic states is needed to explain the trends in β.

6.5 Conclusion

The multiphoton excitation dynamics of S_2 has been characterized using velocity map imaging over a wide range of wavelengths in the UV region. A single laser operating in UV region is used for both photodissociation of S_2 and simultaneous detection of the S^+ photoproducts via (2+1) REMPI. Superexcited states are accessed via two different resonant states, the B (v=8-11) valence states at the one-photon level and the 3dπ ($^1\Delta_g$) Rydberg state at the two-photon level. Neutral dissociation (excited atom production) is dominant at the excitation energy equivalent of three-photon absorption at wavelength $\lambda < 288$ nm. In comparison, most of the O^+ ions come from dissociation of O_2^+ instead of electronically excited atoms. One-photon dissociation of $S_2^+(X)$ has also been observed at longer wavelengths $\lambda > 288$ nm where (2+1) REMPI of S(^{1}D) and S(^{1}S) takes place.

References:

1. S. J. Kim, M. F. A'Hearn, D. D. Wellnitz, R. Meier and Y. S. Lee, Icarus **166**, 157 (2003).

2. G. Mitchell, Astrophys. J. **287**, 665 (1984).

3. K. Noll, M. McGrath, L. Trafton, S. Atreya, J. Caldwell, H. Weaver, R. Yelle, C. Barnet and S. Edgington, Science **267**, 1307 (1995).

4. P. Geissler, A. McEwen, C. Porco, D. Strobel, J. Saur, J. Ajello and R. West, Icarus **172**, 127 (2004).

5. L. St-Onge, N. Sadeghi, J. P. Booth, J. Margot and C. Barbeau, J. App. Phys. **78**, 6957 (1995).

6. G. Lakshminarayana and C. Mahajan, J. Quant. Spec. & Rad. Trans. **16**, 549 (1976).

7. C. Johnston and H. van der Hdjden, J. Phys, D: Appl. Phys. **37**, 211 (2004).

8. P. W. Frederix, C.-H. Yang, G. C. Groenenboom, D. H. Parker, K. Alnama, C. M. Western and A. J. Orr-Ewing, J. Phys. Chem. A **113**, 14995 (2009).

9. Z. Farooq and D. H. Parker, J. Chem. Phys., Submitted (2015).

10. M. Barnes, J. Baker, J. M. Dyke and R. Richter, Chem. Phys. **166**, 229 (1992).

11. M. J. Cooper and C. M. Western, Chem. Phys. Let. **267**, 365 (1997).

12. D. H. Parker and A. T. J. B. Eppink, J. Chem. Phys. **107**, 2357 (1997).

13. A. T. J. B. Eppink and D. H. Parker, Rev. Sci. Instrum. **68**, 3477 (1997).

14. M. Van Beek and J. Ter Meulen, Chem. Phys. Lett. **337**, 237 (2001).

15. R. A. Rose, A. J. Orr-Ewing, C.-H. Yang, K. Vidma, G. C. Groenenboom and D. H. Parker, J. Chem. Phys. **130**, 034307 (2009).

16. V. Dribinski, A. Ossadtchi, V. A. Mandelshtam and H. Reisler, Rev. Sci. Instrum. **73**, 2634 (2002).

17. C. L. Liao and C. Y. Ng, J. Chem. Phys. **84**, 778 (1986).

18. W. A. Chupka, J. Chem. Phys. **87**, 1488 (1987).

19. W. C. Lineberger and B. W. Woodward, Phys. Rev. Let. **25**, 424 (1970).

20. J. M. Dyke, L. Golob, N. Jonathan and A. Morris, J. Chem. Soc. Fara, Trans. 2: Mol. & Chem. Phys. **71**, 1026 (1975).

21. N. P. L. Wales, E. de Beer, N. P. C. Westwood, W. J. Buma, C. A. de Lange and M. C. van Hemert, J. Chem. Phys. **100**, 7984 (1994).

22. K. Wang and V. McKoy, J. Chem. Phys. **95**, 4977 (1991).

Summary

The central goal of this thesis is to examine the photodissociation dynamics of molecular oxygen (O_2) and molecular sulfur (S_2) by detecting the speed and angular distributions of photofragment atoms using the velocity map imaging (VMI) technique. Molecular oxygen and molecular sulfur are the key species in the chemistry of planetary atmospheres but due to their complex electronic structure, their photodissociation properties are still not well understood. The photodissociation of molecular oxygen and molecular sulfur have been one of the central research topics in the Parker group at the Radboud University of Nijmegen for more than a decade. As a continuation, this thesis focuses on investigation of the bound-free transitions of metastable states $\left(a^1\Delta_g, b^1\Sigma_g^+\right)$ of molecular oxygen and molecular sulfur in the ultraviolet (UV) region. Multiphoton excitation of a molecule often results from exposure to intense UV laser light. Multiphoton dissociation of O_2 and S_2 taking place via two-photon resonant Rydberg states in intense UV laser beam have also been probed and are described in last two chapters of this thesis. A comparison of the photodynamics of O_2 with those of electronically analogous S_2 molecule is also topic of discussion throughout the thesis.

First, a brief description of photodissociation dynamics of molecular oxygen (O_2) and molecular sulfur (S_2) and the general motivation of our particular studies is outlined in the introduction. The important features of O_2 and S_2 in and beyond the simple valence MO picture are also explained here. The second chapter is devoted to the description of the apparatus and experimental techniques used in this work. background information regarding VMI and experimental details about lasers, the vacuum set up, molecular beam configuration, discharge, time of flight (TOF) detection scheme and calibration procedures have been given in details here. The majority of experimental work presented in this thesis has been performed in the UV region.

Despite their obvious importance in a wide range of systems, a very few experimental studies of the photodissociation dynamics of the metastable states of O_2 and S_2 have been reported. A simple ring-type pulsed discharge is used to produce singlet oxygen and singlet sulfur. Part of this thesis work deals with excitation of these $\left(a^1\Delta_g, b^1\Sigma_g^+\right)$ metastable states of O_2 and S_2. Chapter 3 is about the UV photodissociation of singlet oxygen $O_2\left(a^1\Delta_g\right)$ in the energy region from 200 to 240 nm by VMI. Transition of $O_2\left(a^1\Delta_g\right)$ via the Chamberlain continua, which is a forbidden transition, is a complex process, where spin-orbit coupling with optically allowed transitions is the main mechanism for acquiring transition strength. One-color and two-color experiments were performed to dissociate singlet oxygen $O_2\left(a^1\Delta_g\right)$ via the Chamberlain continua $\left(A^3\Sigma_u^+, A'^3\Delta_u \longleftarrow a^1\Delta_g\right)$ with subsequent detection of $O\left(^3P_{j=0,1,2}\right)$ fragments atoms. A small amount of highly excited vibrational levels of ground state $O_2\left(X^3\Sigma_g^-(v>0)\right)$ are detected but no $\left(b^1\Sigma_g^+\right)$ state is formed, which may be due to higher collisional quenching rate of the $\left(b^1\Sigma_g^+\right)$ state compared to $\left(a^1\Delta_g\right)$ state. From our experimental results, the cross section for the Chamberlain continua appears to be much stronger the cross section predicted by theory. The anisotropy parameter for photodissociation $\left(a^1\Delta_g\right)$ state suggests a parallel character of the transition.

Chapter 4 deals with the photodissociation of $S_2\left(a^1\Delta_g, b^1\Sigma_g^+\right)$ in the ultraviolet wavelength region (320-205nm). We probed the photodissociation of singlet sulfur $S_2\left(a^1\Delta_g, b^1\Sigma_g^+, X^3\Sigma_g^-(v>0)\right)$ via $B^3\Sigma_u^+$ and $B''^3\Pi_u^+$ excited states using velocity map imaging. Branching ratios over the three fine- structure $S\left(^3P_j\right)$ with $j=2,1,0$ were obtained in a one-laser experiment. The photochemistry of S_2 is found in this study to be rather different from that its electronic analog O_2. Unlike O_2, photodissociation of $S_2\left(b^1\Sigma_g^+, X^3\Sigma_g^-(v>0)\right)$ in near UV wavelength region is efficient through D_0 limit. While for both molecules $a^1\Delta_g$ is efficient through D_0 limit.

In the second part of the thesis we presented new experiments on multiphoton dissociation of O_2 and S_2 in a wide range of Ultraviolet wavelengths. The various decay processes in multiphoton dissociation is topic of discussion in last two chapters of thesis. Chapter 5 is about the

multiphoton dissociation of molecular oxygen via two photon resonant Rydberg states in the wavelength region from 200 nm to 240 nm using VMI technique. A series of two-photon allowed Rydberg states with principle quantum number n=3-11 converging to ground electronic states of O_2^+ are used as doorway states to reach the region of superexcited states of O_2. Competition between autoionization and neutral dissociation have been observed in this study and discussed according to a simple model described by Ehresmann and coworkers. A number of general trends are observed. Over the entire energy region studied here, ionization to form $O_2^+\left(X^2\Pi_g\right)$ is dominant with production of a very wide range of vibrational levels. Formation of $O_2^+\left(A^2\Pi_u\right)$ and $O_2^+\left(a^4\Pi_u\right)$ is observed only in a narrow range of photon energy near their energetic thresholds. Ground and vibrationally excited O_2^+ are dissociated to ionic products via one and two-photon processes. Angular distributions suggest a strong alignment effect in the ionization process to form $O_2^+\left(X^2\Pi_g\right)$. Neutral dissociation to form electronically excited atoms is efficient for longer dissociation wavelengths and noticeably less efficient at shorter wavelengths. Branching ratios between ND and AI obtained from electron images are found to agree qualitatively with those from the O^+ images, supporting the conclusion that ionization (AI and direct) is stronger than ND across the energy range studied. In addition, this set of O^+ images contains many sharp and well spaced rings, they are quite useful in calibrating the velocity scale of a VMI apparatus.

Finally, the last chapter of thesis presents the multiphoton dynamics of molecular sulfur S_2 in the UV- visible region (205-300 nm). In single laser experiment, an electric pulsed discharge has been used to produce molecular sulfur S_2. At the three photon level, superexcited states of S_2 are reached via two different resonant states: B (v=8-11) valence state at one photon level and Rydberg state at two photon level. In decay processes, neutral dissociation is appeared to be dominant as compared to autoionization to ionic states $S_2^+\left(X^2\Pi_g\right)$. Vibrationally excited $S_2^+\left(X^2\Pi_g, v\rangle 11\right)$ has been observed which dissociated to ionic products via one photon process.

In conclusion we studied the photodissociation phenomenon of O_2 and S_2 molecules including their metastable states in a wide range UV region. Despite their familiarity and years of rigorous study, molecular oxygen and molecular sulfur, with their complex electronic structures and strongly forbidden transitions, still yield remarkable surprises.

Samenvatting

De hoofddoel van deze proefschrift is onderzoek te doen na de dynamica van moleculair zuurstof (O_2) en moleculair zwavel (S_2) door de snelheid- en hoekverdeling van de fotodissociatie fragmenten te detecteren met Velocity Map Imaging (VMI) techniek. Moleculair zuurstof en zwavel zijn één van de belangrijkste deeltjes in de chemie in planetaire atmosferen. Wegens de complexe elektronische structuur van deze moleculen zijn de fotodissociatie eigenschappen niet helemaal begrepen. Meer dan een decennium lang is het bestuderen van fotodissociatie van moleculair zuurstof en zwavel een lange project in de groep van prof. David Parker aan de Radboud Universiteit Nijmegen. Om meer specifiek te zijn; in de proefschrift zal de onderzoek na niet-gebonden overgangen van metastabiele toestanden $\left(a^1\Delta_g, b^1\Sigma_g^+\right)$ van moleculair zuurstof en zwavel in het ultraviolet (UV) regio behandeld worden. Meervoudige foton excitatie vindt plaats in een molecuul wanneer het interactie heeft met een intense UV lichtpuls van een laser. De meervoudige foton dissociatie van O_2 en S_2 vindt plaats via een twee-foton resonante Rydberg toestand, dit is beschreven in de laatste twee hoofdstukken. Zwavels elektronische structuur is analoog aan die van zuurst of, de vergelijkingen in de foton dynamica zal door het gehele proefschrift bediscussieert worden.

In de introductie zal een korte beschrijving van de fotodissociatie dynamica van moleculair zuurstof (O_2) en zwavel (S_2) en de algemene motivatie van het project beschreven worden. Ook zal hier de belangrijke kenmerken van O_2 en S_2 en de valentie MO diagram van deze moleculen in meer detail besproken worden. In hoofdstuk 2 wordt het apparaat en experimentele technieken besproken, onder andere: achtergrond informatie over VMI, experimentele details over de lasers die gebruikt zijn, het vacuüm systeem, de moleculaire bundel configuratie, de ontladingsbron, de vluchttijd (time-of-flight [TOF]) detectie schema en de kalibratie procedures. Een grote gedeelte van de experimenten zijn uitgevoerd in het UV gebied.

De fotodissociatie dynamica van de metastabiele toestanden van O_2 en S_2 zijn belangrijk in veel verschillende systemen. Ondanks ze voor verschillende systemen belangrijk zijn is er niet veel bekend over de fotodissociatie dynamica. In de proefschrift zal een gedeelte toegekend worden aan het beschrijven van het produceren van singlet zuurstof en zwavel $\left(a^1\Delta_g, b^1\Sigma_g^+\right)$. De singlet toestanden worden geproduceerd door gebruik te maken van een pulsende ringvormige ontladingsbron. In hoofdstuk 3 wordt de fotodissociatie van singlet zuurstof $O_2\left(a^1\Delta_g\right)$ in de energie gebied van 200 – 240 nm door gebruik te maken van VMI behandeld. De overgang van $O_2\left(a^1\Delta_g\right)$ via het Chamberlain continuüm, wat een verboden overgang is, door spin - baan koppeling is het alsnog mogelijk om de overgang te kunnen maken. Eén en twee kleur experimenten zijn uitgevoerd voor het dissociëren van singlet zuurst of $O_2\left(a^1\Delta_g\right)$ via het Chamberlain continuüm $\left(A^3\Sigma_u^+, A'^3\Delta_u \longleftarrow a^1\Delta_g\right)$ waarbij de O ($^3P_{j=0,1,2}$) fragment atomen worden gedetecteerd. Een kleine hoeveelheid van hoog geëxciteerde vibrationele levels in de grondtoestand van $O_2\left(X^3\Sigma_g^-(v>0)\right)$ zijn gedetecteerd maar de $\left(b^1\Sigma_g^+\right)$ werd niet waargenomen, dit kan komen doordat de er meer botsingen plaats vindt met de $\left(b^1\Sigma_g^+\right)$ ter vergelijking met de $\left(a^1\Delta_g\right)$ toestand. Uit experimentele data blijkt dat de 'cross-section' voor de Chamberlain continuüm veel hoger is dan de waardes bepaald met theorie. Uit de anisotrope parameter voor fotodissociatie van $\left(A^3\Sigma_u^+, A'^3\Delta_u \longleftarrow a^1\Delta_g\right)$ blijkt dat deze overgang een parallelle karakter te hebben.

In hoofdstuk 4 zal de fotodissociatie van $S_2\left(a^1\Delta_g, b^1\Sigma_g^+\right)$ in de ultraviolet golflengte gebied (205 – 320 nm) behandeld worden. Fotodissociatie van singlet zwavel $S_2\left(a^1\Delta_g, b^1\Sigma_g^+, X^3\Sigma_g^-(v>0)\right)$ werd gedetecteerd met VMI via de aangeslagen toestanden $B^3\Sigma_u^+$ en $B''^3\Pi_u^+$. De verhouding tussen de drie fijn structuren van $S\left(^3P_j\right)$ met j = 2,1,0 werd bepaald met de één-kleur laser experiment. Uit deze studie blijkt dat de fotochemie van S_2 heel anders is dan de elektronische analoog O_2. Bij zwavel is de $S_2\left(b^1\Sigma_g^+, X^3\Sigma_g^-(v>0)\right)$ dichtbij de UV licht gebied efficient te zijn om door D_0 limiet te gaan. Alhoewel, voor beiden moleculen is de $a^1\Delta_g$ toestand dat door de D_0 limiet efficiënt te zijn.

In het tweede gedeelte van de proefschrift zal nieuwe experimenten van meerdere fotonen dissociatie processen van O_2 en S_2 in een wijde gebied

van ultraviolet golflengtes gepresenteerd worden. De verschillende verval in de meerdere fotonen dissociatie processen zal bediscussieerd worden in de laatste twee hoofdstukken van de proefschrift. In hoofdstuk 5 wordt de detectie van de meerdere fotonen dissociatie proces van moleculair zuurstof via twee-foton resonante Rydberg toestanden in het gebied van 200 tot 240 nm met VMI besproken. Een serie van twee-foton toegestane Rydberg toestanden met de kwantum nummer n = 3 -11 na de grondtoestanden van O_2^+ wordt gebruikt als tussen toestanden om het gebied van super geëxciteerde toestanden van O_2 te bereiken. De competitie tussen auto-ionisatie (AI) en neutrale dissociatie (ND) is geobserveerd in deze studie en het wordt behandeld met een simpele model dat beschreven is door Ehresmann en collega's. Een aantal algemene trends zijn als volgt waargenomen: Over het gehele energie bereik, wat in deze studie is gebruikt, is ionisatie van O_2 om $O_2^+\left(X^2\Pi_g\right)$ te vormen het dominantst, hierbij werden veel verschillende vibrationele toestanden waargenomen. De formatie van $O_2^+\left(A^2\Pi_u\right)$ en $O_2^+\left(a^4\Pi_u\right)$ is alleen geobserveerd in een kleine gebied van foton energie dichtbij hun energetische drempel. Grond en vibrationeel geëxciteerde O_2^+ zijn gedissocieerd na ion producten via één en twee-foton processen. Uit de hoekverdeling van de fragmenten suggereert dat er een sterke uitlijn effect in het ionisatie proces van $O_2^+\left(X^2\Pi_g\right)$ te zijn. De neutrale dissociatie mechanisme waar uiteindelijk elektronische geëxciteerde atomen uit vormt is veel efficiënter bij een langere dissociatie golflengte en minder efficiënt bij een kortere golflengte. De verhoudingen tussen het ND en AI mechanisme wat volgt uit het detecteren van de elektronen is consistent met het resultaat dat uit de O^+ plaatjes volgt. Door de vele scherpe en goed gescheiden ringen kan de set van O^+ plaatjes ook zeer goed gebruikt worden om de snelheidsschaal van de VMI apparaat te kalibreren.

In de laatste hoofdstuk wordt de meerdere fotonen dynamiek in zwavel S_2 in het UV/VIS gebied (205 – 300 nm ß is gewoon UV?) behandeld. In het experiment waar maar een één-kleur laser wordt gebruikt is er gebruik gemaakt van de elektrische pulserende ontladingsbron om moleculair zwavel S_2 te vormen. Wanneer drie fotonen zijn geabsorbeerd dan is het mogelijk om de super geëxciteerde toestanden van S_2 te bereiken dat via twee verschillende resonante toestanden kan gaan: via de B (v = 8-11) valentie toestand door het absorberen van één foton en/of de Rydberg toestand wanneer er twee fotonen worden geabsorbeerd. Uit het verval proces blijkt de neutrale dissociatie dominanter te zijn dan auto-ionisatie na de ionische $S_2^+\left(X^2\Pi_g\right)$ toestand. De vibrationele geëxciteerde

$S_2^+\left(X^2\Pi_g, v\rangle 11\right)$ toestand is geobseveerd wat vervolgens dissocieert in ion producten na het absorberen van één foton.

Uit de studie kan geconcludeerd worden dat de fotodissociatie van O_2 en S_2, inclusief de meta stabiele toestanden, in een wijde UV bereik is bestudeerd. Ondanks de gelijkheden en na vele jaren het bestuderen van deze moleculen, geeft het nog steeds verassende resultaten. Dit allemaal wegens de complexe elektronische structuur en verboden overgangen.

Publications

- Photodissociation of Singlet Oxygen in the UV region
  Zahid Farooq, Dimitri A. Chestakov , Bin Yan, W.J. van der Zande, G.C. Groenenboom and D. H. Parker
  Phys. Chem. Chem. Phys., 2014,**16**, 3305-3316

- Photodissociation of S_2 ($\tilde{X}\,^3\Sigma_g^-$, $\tilde{a}\,^1\Delta_g^+$, $\tilde{b}\,^1\Sigma_g^+$) in the ultraviolet (320-205 nm) region
  Zahid Farooq and D. H. Parker, to be submitted

- Multi-photon dissociation of molecular oxygen O_2 via two-photon resonant Rydberg States in the UV region,
  Zahid Farooq, Andre Eppink, Zhichao Chen and D. H. Parker, to be submitted

- Multiphoton dissociation of molecular sulfur S_2 via two resonant states in the UV region
  Zahid Farooq and D. H. Parker, to be submitted

Acknowledgment

I would like to thank all the people who contributed in some way to work described in this thesis.

First and foremost, I feel great honour in expressing my deepest sense of gratitude to my reverend Supervisor Prof. Dr. D.H. Parker. Dave, without your constant encouragement and support, this thesis would not have happened. Thanks a lot for your patience, kindness and help.

Besides my supervisor, I would like to thank the rest of my thesis committee: Prof. dr. W.J. van der Zande, Prof. dr. ir. G.C. Groenenboom and Prof. dr. C. Western (University of Bristol, UK) for their help and insight comments in my work.

Special thanks to Andre Eppink, who was very affectionate and cooperative during my research work. I greatly benefited from keen scientific insight, his tendency for solving seemingly intractable practical difficulties and his ability to put complex ideas into simple terms.

I was fortunate to have chance to work with Dr. Alexey V. Baklanov in project of molecular cluster formation. You taught me a lot regarding different laboratory techniques in this project.

I feel highly obliged to Leander, Peter and Cor for their daily basis technical support over the entire period of my research work. I offer my sincerest words of thanks to them.

I also want to acknowledge Magda, Secretary of our department for her cooperation and help.

I also would like to thank my fellow labmates in Nijmegen: Konstantin, Pim, Chung Hsin, Zhichao, Eric, Gautam, Ashim, Bin Yan, Chandan, George, Jolijn and Sasha. It was nice to work with you all.

Thanks a lot Roy for translating the Summary of this thesis into Dutch (Samenvatting).

It was also nice to see you around: Afric, Frans, Simona, Mehrnoosh, Denis, Malik and Chris.

I am grateful to my HEC friends for making my life feeling like home in Nijmegen. My Pakistani friends include Ghulam Rabbani, Muhammad Kaleem, Zafar Iqbal, Faisal Wali, Waseem Akhtar, Afsheen Api, Ammir Aslam, Kaleem (lent) Muhammad Imran, Shazia, Abid Sindhu, Waqas Goraya, Mesha Saeed, Hina , Maliha and Sadia Saeed. The list remains incomplete without the description of my best friends Syed Saiden Abbas and Arslan Klair, with whom I spent most part of my stay in Netherlands. Waqar Aslam and Muhammad Ali, I am highly indebted to you for providing me moral assistance whenever I need it.

No words to describe my sweet sensations of respect about my mother because without her shadow of love, perhaps, it could be impossible to attain this target. A lot of joy and moral support always encouraged me, giving by my whole family until this stage has come.

Last but not the least, I also grateful to the Higher Education Commission, Pakistan for the financial assistance.

Zahid Farooq
Pakistan June 2015